# Next-Generation Electronics for the Read-Out of Micro-Pattern Gaseous Detectors

Dissertation

zur
Erlangung des Doktorgrades (Dr. rer. nat.)
der
Mathematisch-Naturwissenschaftlichen Fakultät
der
Rheinischen Friedrich-Wilhelms-Universität Bonn

vorgelegt von

Lucian Simon Scharenberg

aus
Speyer

Bonn 2022

Angefertigt mit Genehmigung der Mathematisch-Naturwissenschaftlichen Fakultät der Rheinischen Friedrich-Wilhelms-Universität Bonn.

Diese Dissertation wurde im Rahmen eines Wolfgang-Gentner-Stipendiums am CERN (europäisches Forschungszentrum für Teilchenphysik) in Genf angefertigt. Die Betreuung erfolgte durch Dr. Eraldo Oliveri.

| | |
|---|---|
| 1. Gutachter: | Prof. Dr. Klaus Desch |
| 2. Gutachter: | Prof. Dr. Ian C. Brock |

| | |
|---|---|
| Tag der Promotion: | 24.01.2023 |
| Erscheinungsjahr: | 2023 |

In Gedenken an

Dr. Ferdinand Josef Scharenberg

# ABSTRACT

Developed by the RD51 collaboration, the Scalable Readout System (SRS) is widely used for the read-out of Micro-Pattern Gaseous Detectors (MPGDs). With different front-end Application-Specific Integrated Circuits (ASICs) integrated into the SRS and its capability to read out small R&D set-ups up to mid-size experiments, the SRS functions as a multi-purpose read-out system. One of the ASICs integrated into the SRS is the VMM3a, which was specifically developed for the read-out of gaseous detectors. Due to its rich feature set and high configurability, it is the ideal candidate to further enhance the multi-purpose character of the SRS and move it into its next era.

In the scope of this thesis, the capabilities of the VMM3a front-end of the RD51 Scalable Readout System (VMM3a/SRS) were explored for the charge read-out of MPGDs. This includes characterisation studies and the evaluation and improvement of calibration procedures to understand and optimise the system response. There it was found that the time resolution of VMM3a/SRS is better than 2 ns and that it allows to read-out detectors with trigger rates in the MHz regime. Furthermore, it was explored how different measurement types can benefit from the capabilities of VMM3a/SRS. As such, various kinds of X-ray imaging studies were performed with a single-detector set-up. In addition, a new beam telescope with VMM3a/SRS read-out was built for the RD51 collaboration, which meant the read-out of multiple detectors at the same time. This allowed to demonstrate that VMM3a/SRS can be used as an integrated read-out system, which provides position, time and energy information at the same time. In addition to the characterisation measurements, also different applications of VMM3a/SRS were demonstrated, such as the possibility to resolve argon fluorescence interactions inside gaseous detectors and use these interactions to determine the electron drift velocity. Ultimately, the newly built beam telescope was used in the NA61/SHINE experiment at CERN, demonstrating that VMM3a/SRS can be successfully operated in particle physics experiments.

# PUBLICATIONS

*Methods and results presented in this thesis have been partially published in articles and proceedings of peer-reviewed journals:*

L. SCHARENBERG ET AL.: *Gaseous detector studies with the VMM3a ASIC and the Scalable Readout System*, Journal of Instrumentation **15** (2020) C08026.
DOI: `https://doi.org/10.1088/1748-0221/15/08/C08026`.
Proceeding of the *International Conference on Instrumentation for Colliding Beam Physics (INSTR20)*, Novosibirsk, Russia, 24–28 February 2020.

L. SCHARENBERG ET AL.: *Resolving soft X-ray absorption in energy, space and time in gaseous detectors using the VMM3a ASIC and the SRS*, Nuclear Instruments and Methods in Physics Research A **977** (2020) 164310.
DOI: `https://doi.org/10.1016/j.nima.2020.164310`.

L. SCHARENBERG ET AL.: *X-ray imaging with gaseous detectors using the VMM3a and the SRS*, Nuclear Instruments and Methods in Physics Research A **1011** (2021) 165576.
DOI: `https://doi.org/10.1016/j.nima.2021.165576`.

D. PFEIFFER, L. SCHARENBERG, P. SCHWÄBIG ET AL.: *Rate-capability of the VMM3a front-end in the RD51 Scalable Readout System*, Nuclear Instruments and Methods in Physics Research A **1031** (2022) 166548.
DOI: `https://doi.org/10.1016/j.nima.2022.166548`.

# PRESENTATIONS

*Methods and results presented in this thesis, as well as work performed in the scope of this thesis, have been partially shown on the following conferences, workshops, meetings and seminars:*

L. SCHARENBERG ET AL.: *Exploring VMM3a and SRS Features using GEMs and X-Rays*, RD51 Collaboration Meeting, 21–23 October 2019, CERN, Geneva, Switzerland.
URL: `https://indico.cern.ch/event/843711/contributions/3613185/`

D. PFEIFFER, L. SCHARENBERG ET AL.: *Studies on the Rate-Capability of the VMM3a within the SRS*, RD51 Mini Week, 10–13 February 2020, CERN, Geneva, Switzerland.
URL: `https://indico.cern.ch/event/872501/contributions/3741492/`
*Presentation together with Dorothea Pfeiffer*

L. SCHARENBERG ET AL.: *Gaseous Detector Studies with the VMM3a ASIC and the SRS*, International Conference on Instrumentation for Colliding Beam Physics (INSTR20), 24–28 February 2020, Budker Institute of Nuclear Physics, Novosibirsk, Russia.
URL: `https://indico.inp.nsk.su/event/20/contributions/809/`

L. SCHARENBERG ET AL.: *Improving the position response of MPGDs*, RD51 Collaboration Meeting and Topical Workshop on 'New Horizons in Time Projection Chambers', 05–09 October 2020, Galician Institute of High Energy Physics (IGFAE), Santiago de Compostela, Spain (virtual meeting).
URL: `https://indico.cern.ch/event/889369/contributions/4044539/`

L. SCHARENBERG ET AL.: *S-curve noise measurements with VMM3a/SRS*, RD51 Mini Week and Workshop on 'Gaseous Detector Contributions to PID', 15–19 February 2021, CERN, Geneva, Switzerland (virtual meeting).
URL: `https://indico.cern.ch/event/989298/contributions/4226168/`

L. SCHARENBERG ET AL.: *A simple method to improve the position resolution*, Spring Meeting of the German Physical Society (DPG-Frühjahrstagung), 15–19 March 2021, Technical University of Dortmund, Dortmund, Germany (virtual meeting).

L. Scharenberg: *Exploring next-gen readout electronics for MPGDs*, 7th EIROforum School on Instrumentation, 07–11 June 2021, Institut Laue-Langevin (ILL), Grenoble, France (virtual meeting).
*Video Presentation*

L. Scharenberg et al.: *High-rate X-ray measurements with VMM3a/SRS*, RD51 Collaboration Meeting and Topical Workshop on 'Front End Electronics for Gas Detectors', 14–18 June 2021, CERN, Geneva, Switzerland (virtual meeting).
url: `https://indico.cern.ch/event/1040996/contributions/4406960/`

L. Scharenberg et al.: *Position reconstruction studies with GEM detectors and the charge-sensitive VMM3a ASIC*, 12th International Conference on Position Sensitive Detectors (PSD12), 12–17 September 2021, University of Birmingham, Birmingham, United Kingdom.
url: `https://indico.cern.ch/event/797047/contributions/4455967/`
*Poster Presentation*

L. Scharenberg: *A new ASIC for (gaseous) detectors – Exploring the VMM3a front-end in the RD51 Scalable Readout System*, 20th Gentner Day, 27 October 2021, CERN, Geneva, Switzerland.
url: `https://indico.cern.ch/event/1082756/contributions/4590587/`

L. Scharenberg: *VMM3a/SRS software installation and operation overview*, RD51 Collaboration Meeting and Topical Workshop on 'Wide Dynamic Range Operation of MPGDs', 15–19 November 2021, CERN, Geneva, Switzerland (virtual meeting).
url: `https://indico.cern.ch/event/1071632/contributions/4615369/`
*Online Tutorial*

L. Scharenberg: *First characterisation study for front-end and data acquisition systems aimed at future micro-pattern gas detectors*, AIDAinnova Newsletter 'On Track', 30 November 2021, CERN, Geneva, Switzerland.
url: `https://aidainnova.web.cern.ch/taxonomy/term/56`
*Newsletter article*

L. Scharenberg: *Developing a general-purpose readout system for gaseous detectors*, CERN EP-DT Training Seminar, 08 December 2021, CERN, Geneva, Switzerland.
url: `https://indico.cern.ch/event/1102899/`

L. Scharenberg: *Common DAQ Developments: RD51 SRS & BNL/ATLAS VMM3a*, AIDAinnova 1st Annual Meeting, 28–31 March 2022, CERN, Geneva, Switzerland.
URL: `https://indico.cern.ch/event/1104064/contributions/4785093/`

L. Scharenberg et al.: *Latest experiences and first test beam results using VMM3a/SRS*, RD51 Collaboration Meeting, 13–17 June 2022, CERN, Geneva, Switzerland.
URL: `https://indico.cern.ch/event/1138814/contributions/4921252/`

L. Scharenberg et al.: *Next-generation electronics for the gaseous beam telescope of RD51*, 10th Beam Telescopes and Test Beams Workshop (BTTB10), 20–24 June 2022, University of Salento, Lecce, Italy.
URL: `https://indico.cern.ch/event/1058977/contributions/4632034/`

# CONTENTS

# INTRODUCTION

The conceptualisation and construction of particle physics experiments involve typically the use of new detector technologies. The development of new detector technologies is at the same time interconnected with the development of new read-out technologies and vice versa. A prominent technology used in particle physics experiments are ***M**icro-**P**attern **G**aseous **D**etectors* (MPGDs). To cope with new experimental requirements, they have been recently integrated into three large high-energy physics experiments, ATLAS [1, 2], CMS [3, 4] and ALICE [5, 6] at CERN. MPGDs enable a large area coverage (up to hundreds of square metres), a high rate-capability (several MHz/cm$^2$ and beyond), radiation hardness, radiopurity and low material budget, while at the same time preserving good spatial resolutions (better than 100 µm) and time resolutions (typically a few nanoseconds, but technologies exist which enable picosecond resolution [7]).

Many ***R**esearch and **D**evelopment* (R&D) activities on MPGDs are concentrated within the RD51 collaboration [8, 9]. As part of these activities, the RD51 collaboration developed the ***S**calable **R**eadout **S**ystem* (SRS) [10] for the charge read-out of MPGDs. With its approach to read out small laboratory R&D detectors up to mid-size experiments, it gained remarkable popularity within the MPGD community, since its introduction in 2009. At the same time, it allowed to read out different MPGD technologies, such that it was also used in the development process for the MPGD upgrades of the LHC experiments, where the final electronics were not yet available.

After its introduction, various front-end ***A**pplication-**S**pecific **I**ntegrated **C**ircuits* (ASICs) have been integrated into the SRS. One of the ASICs is the ATLAS/BNL VMM3a [11] from the ATLAS ***N**ew **S**mall **W**heel* (NSW) upgrade [2], which was specifically designed to read out gaseous detectors. It allows to handle the experimental needs, targeting in particular a high rate-capability, nanosecond time resolution, as well as the ability to handle different detector capacitances, meaning different detector sizes and types of read-out electrodes. With the integration of the VMM3a into the SRS [12], the VMM3a front-end of the SRS (VMM3a/SRS) is intended to move the SRS and thus the charge read-out of MPGDs to its next era.

In this thesis, the capabilities of VMM3a/SRS are explored with three main goals. The first goal is to characterise the combination of the VMM3a ASIC and the RD51 SRS and to understand if it allows to satisfy the experimental needs. The second goal is to understand what the system can provide to explore new features of MPGDs. The third goal is to demonstrate that VMM3a/SRS can function as a multi-purpose integrated read-out system with a wide range of gaseous detector applications. Starting with a review of the working principle and basic quantities in the behaviour of gaseous detectors (chapter 1) and a description of the components of the VMM3a front-end and its integration into the SRS (chapter 2), the electronics capabilities, especially the ones of the VMM3a ASIC are explored (chapter 3). There it is e.g. shown that the VMM3a provides time resolutions between 0.5 ns and 2 ns and that the rate-capability lies in the MHz regime. Also, the optimisation procedures that are necessary for the use in experiments are included in this chapter. While the characterisation studies make mainly use of measurements with calibration pulses, the next part of the thesis focuses on measurements with particle detectors, beginning with the presentation of the two experimental set-ups built for this purpose in the scope of this thesis (chapter 4). On the one hand, a single detector set-up for X-ray imaging studies and on the other hand a new beam telescope for the common RD51 test beam activities. The measurements which have been performed (chapter 5) explore the different essential detector parameters, spatial resolution, time resolution and energy resolution, as well as the rate-capability of the read-out system. It is investigated how the electronics' properties affect the measurement of these detector parameters and at the same time, it is investigated how they can be (potentially) improved. It is shown that VMM3a/SRS can record particle interactions with several MHz interaction rate. The electronics time resolution allows to intrinsically measure the time resolution of the particle detectors, which is between 8 ns and 12 ns. A large fraction of the chapter is spent on spatial resolution studies, with the goal of understanding if a hardware feature of the VMM3a allows to improve the measured spatial resolution. Furthermore a simple modification of the centre-of-gravity position is investigated to improve the accuracy of the position reconstruction. In the end, it was possible to obtain spatial resolutions better than 50 μm using the beam telescope and minimum ionising particles. The thesis is closed with the presentation of three different applications of VMM3a/SRS (chapter 6). The system is used for detector studies by resolving argon fluorescence interactions and measuring the electron drift velocity, it is shown that VMM3a/SRS can be used for quality assurance measurements of MPGDs and ultimately, the successful operation of the RD51 VMM3a/SRS beam telescope in the NA61/SHINE experiment for neutrino physics [13, 14] is presented.

The collaborative activities to further develop and improve the read-out system, have been carried out within a sub-working group of RD51, the so-called *Working Group 5.1*, of which I am the convener. As part of this work, also training sessions with other groups have been organised to teach the use of VMM3a/SRS and a user guide that includes a tutorial video was written. The collaboration with other groups also showed the wide range of (intended) applications of the VMM3a front-end of the SRS, with the list neither being complete nor comprehensive. While some of the projects in the following are still in the evaluation phase, others use VMM3a/SRS already as a running system. One of its applications outside of the use for R&D purposes is the read-out of novel neutron detectors [15–17]. It is also used in different kinds of tracking systems. Tracking systems based on ***T**ime **P**rojection **C**hambers* (TPCs) include nuclear physics experiments such as the MAGIX experiment [18] or medical physics applications [19]. The use of VMM3a/SRS in transversal tracking detectors for high-energy physics is for example studied for the AMBER experiment [20]. Other applications include the read-out of TPCs for dark matter searches [21], muon tomography [22] and tracking with straw tubes [23]. This indicates the multi-purpose character of VMM3a/SRS and its application range for new particle physics experiments.

*Chapter 1*

# PARTICLE DETECTION WITH GASEOUS DETECTORS

The detection of particles is based on their interaction with matter. In the following, the concepts for particle detection with gaseous detectors are introduced, utilising the specific example of a ***Gas Electron Multiplier*** (GEM) [24] detector (figure 1.1), which was used for the measurements in this thesis.

First, the to-be-detected particle deposits energy inside the detection volume by ionising the gas atoms. Here it has to be differentiated between charged particles (section 1.1) and neutral particles, specifically photons (section 1.2). To observe the particle interaction, the created electron-ion pairs are separated and the electrons are transported towards the read-out structure by an applied electric field (section 1.3). Due to the low material density of the gas as active medium, the number of created electron-ion pairs is in most cases too small for a direct measurement of the charge signal. Thus an amplification of the original charge signal is required, which is achieved by means of electron avalanches (section 1.4). Afterwards, the electrons induce a signal on the read-out anode such that it can be acquired by the front-end electronics (section 1.5).

For a detailed and more comprehensive description, including other (gaseous) detectors as well as a mathematical derivation of the presented content, the reader is referred to [26, 27]. These are also the sources for all the information provided in the following unless stated differently.

## 1.1 CHARGED PARTICLES

Charged particles traverse the gas volume and/or ionise and excite the gas atoms along their path. Due to their low mass, it is important to differentiate between electrons and significantly heavier particles, for example, muons or pions. Hence, in the following, the mean energy loss of heavy particles by collisions with the outer shell electrons of the target material is presented (section 1.1.1). Afterwards, considerations on the statistical fluctuations of the energy loss are shown (section 1.1.2).

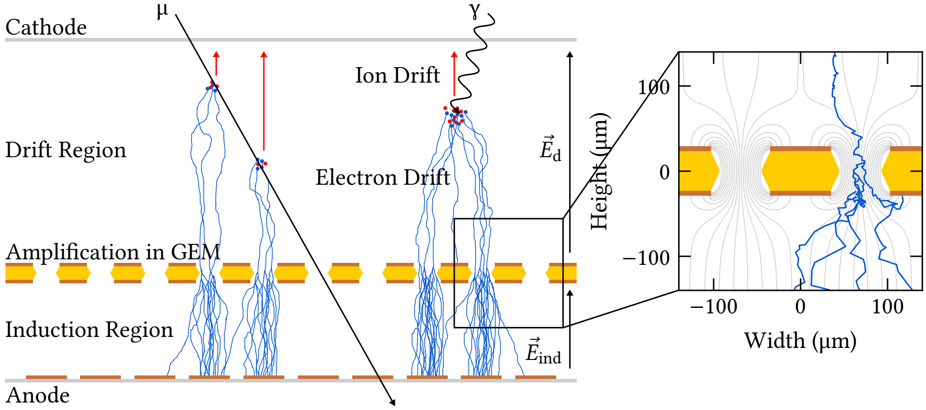

*Figure 1.1* – Schematic illustration of a GEM-based gaseous detector. The particles interact in the drift region. After the charge separation due to an electric field $\vec{E}_\mathrm{d}$, the electrons drift towards the amplification structure, while the ions drift towards the cathode. The amplification structure consists of at least one GEM foil, with the amplification taking place inside the conical holes of the GEM (highlighted on the right). After the amplification, the electrons are extracted from the holes and induced on the read-out anode. Adapted from [25].

### *1.1.1 Energy Loss of Heavy Particles*

The maximum energy, which can be transferred from an interacting particle with mass $M$ to one of the shell electrons with mass $m_\mathrm{e}$ in a single collision is given by [26]

$$T_\mathrm{max} = \frac{2m_\mathrm{e}c^2(\beta\gamma)^2}{1 + 2\gamma\dfrac{m_\mathrm{e}}{M} + \dfrac{m_\mathrm{e}^2}{M^2}} \,, \tag{1.1}$$

with $\beta = v/c$ and $\gamma = 1/\sqrt{(1-\beta^2)}$ being the Lorentz factors. Here, $v$ is the velocity of the incident particle, $p = \beta\gamma Mc$ its momentum, $E = \gamma Mc^2$ its energy and $c$ is the speed of light. In case of heavy particles with $M \gg m_\mathrm{e}$ this expression simplifies to $T_\mathrm{max} \approx 2m_\mathrm{e}c^2(\beta\gamma)^2$.

In addition to the maximum energy loss in a single collision, the mean energy loss per path length can be calculated. It is given in terms of the Bethe-Bloch formula [26]:

$$-\left\langle\frac{\mathrm{d}E}{\mathrm{d}x}\right\rangle = Kz^2\frac{Z}{A}\rho\frac{1}{\beta^2}\left[\frac{1}{2}\ln\left(\frac{2m_\mathrm{e}c^2(\beta\gamma)^2T_\mathrm{max}}{I^2}\right) - \beta^2 - \frac{\delta(\beta\gamma)}{2} - \frac{C(\beta\gamma, I)}{Z}\right] \,. \tag{1.2}$$

Here, $K = 4\pi N_\mathrm{A} r_\mathrm{e}^2 m_\mathrm{e}c^2$ with Avogadro's number $N_\mathrm{A} = 6.022\times10^{23}\,\mathrm{mol}^{-1}$, the classical electron radius $r_\mathrm{e} \approx 2.8\,\mathrm{fm}$, the charge of the incoming particle $z$, the atomic number $Z$ and the mass number $A$ of the medium with mass density $\rho$ and the mean ionisation energy $I$. It can be approximated with $I \approx 17.7\,Z^{0.85}\,\mathrm{eV}$. In addition,

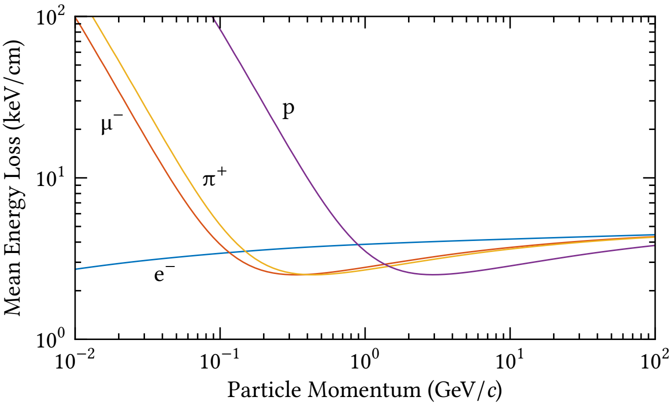

*Figure 1.2* – Dependence of the mean energy loss on the particle's momentum, calculated for different particles in pure argon at 293.15 K and 1013.25 hPa. The calculations were performed with Garfield++ [29, 30], using its interface to Heed++ [31, 32].

equation (1.2) contains with $\delta(\beta\gamma)$ an expression for the density correction and with $C(\beta\gamma, I)/Z$ an expression for the shell correction. The density correction is important at high particle energies, due to the resulting polarisation of the medium and thus smaller contributions to the energy loss of the interacting particles from the electric field of far electrons [28]. The shell correction is important for low energies, where the shell electrons cannot be treated as stationary collision targets anymore [28].

In figure 1.2, the mean energy loss is illustrated for different particles. Knowing the particle's momentum allows to identify different particle types. However, when the energy loss is expressed as a function of $\beta\gamma = p/(Mc)$, so normalised by the particle's mass, as it is the case in equation (1.2), it is found that the curves overlap. Combining this with a normalisation by the medium's mass density, $-\langle \mathrm{d}E/\mathrm{d}x\rangle \rightarrow -\langle \mathrm{d}E/\mathrm{d}x\rangle/\rho$, the following expression is found [26]:

$$-\frac{1}{\rho}\left\langle\frac{\mathrm{d}E}{\mathrm{d}x}\right\rangle\bigg|_{\beta\gamma\approx 3.5} \approx 1.5\,\frac{\mathrm{MeV\,cm^2}}{\mathrm{g}}\ . \tag{1.3}$$

It defines the ***M**inimum **I**onising **P**article* (MIP), so the minimum of each curve (figure 1.2). This definition allows also to distinguish between the low momentum region with $\beta\gamma < 3$ and the MIP region for $\beta\gamma > 4$. Despite the relativistic rise, where $-\langle \mathrm{d}E/\mathrm{d}x\rangle \propto \ln(\gamma)$ the energy loss is still minimal compared to the low momentum region, where $-\langle \mathrm{d}E/\mathrm{d}x\rangle \propto 1/\beta^2$. It should be noted that the Bethe-Bloch formula is valid in the range $0.1 \lesssim \beta\gamma \lesssim 1000$, where especially at higher momenta radiative losses (Bremsstrahlung), become the major source of energy loss, which is however not included in the underlying formalism [25].

### 1.1.2 Statistical Considerations

The Bethe-Bloch equation (1.2) describes the mean energy loss per unit path length of a particle in a medium. In case of argon as detection medium ($\rho = 1.66\,\mathrm{g/l}$ at ***N**ormal **T**emperature and **P**ressure* (NTP), i.e. 293.15 K and 1013.25 hPa [25]), a MIP loses on average approximately 2.5 keV/cm. This can be correlated to the mean number $N_0$ of electron-ion pairs created by a traversing particle via

$$N_0 = \frac{\Delta E}{W_\mathrm{i}} \;, \tag{1.4}$$

with $\Delta E$ the lost energy of the particle and $W_\mathrm{i}$ the average energy to create an electron-ion pair. For argon, with $W_\mathrm{i} = 26\,\mathrm{eV}$ [25], around 100 electron-ion pairs are created by a MIP per centimetre path length.

However, the energy loss distribution (figure 4.12) is highly asymmetric, with the mean energy loss being driven by single encounters with high energy loss. In these encounters, the so-called *delta electrons* are liberated. Thus, the most probable energy loss of a particle along a path $\Delta x$ becomes important for particle detection, which is much smaller. It can be expressed via the most probable value of the *Landau distribution* [26]

$$\Delta E_\mathrm{mp} = \xi \left[ \ln\left( \frac{2 m_\mathrm{e} c^2 (\beta\gamma)^2}{I} \right) + \ln\left( \frac{\xi}{I} \right) + 0.2 - \beta^2 - \delta(\beta\gamma) \right] \;, \tag{1.5}$$

with

$$\xi = \frac{1}{2} K z^2 \frac{Z}{A} \rho \frac{1}{\beta^2} \Delta x \;. \tag{1.6}$$

The quantities are the same as in equation (1.2). For argon, it is found that the most likely energy loss for MIP is 0.6 keV/cm corresponding to 23 electron-ion pairs per centimetre.

In addition to the strong fluctuations in the energy loss per ionising collision, also the number of created electron-ion pairs can fluctuate. It follows a Poisson distribution, where the total number of ionising collisions along a path $L$ is on average $L/\lambda$, with the mean free path $\lambda = 1/(n\sigma)$, $n$ the number density in the medium and $\sigma$ the cross-section [33]. It should be however noted that the number of ionising encounters from the MIP with the argon atoms is about a third smaller than the number of created electron-ion pairs [26]. This is because the MIP creates ionisation clusters, where the other electron-ion pairs of the cluster are created e.g. by ionising collisions from an initial ionisation electron [33].

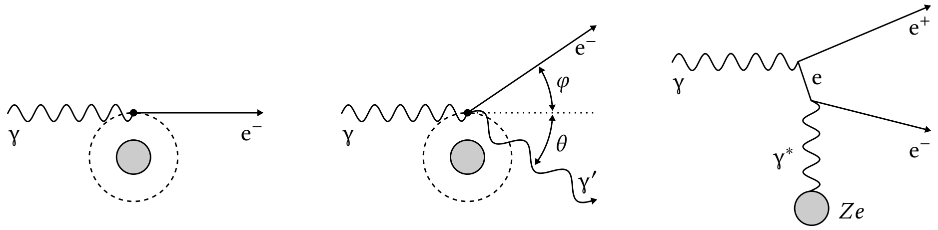

*(a)* – Photoelectric effect. *(b)* – Compton effect. *(c)* – Pair production.

*Figure 1.3* – Illustration of the three main photon interaction processes with matter. While the photoelectric effect and the Compton effect are interactions of a photon $\gamma$ with a shell electron $e^-$, in case of the pair production, the photon interacts with a virtual photon $\gamma^*$ from the field of an atomic nucleus with charge $Ze$. Adapted from [26].

## 1.2 PHOTON INTERACTIONS

In the following, the three most prominent types of photon interactions are presented: the photoelectric effect, the Compton effect and pair production (figure 1.3). The interaction behaviour of photons with matter can be described by [26]

$$I(x) = I_0 e^{-\mu x} \, , \tag{1.7}$$

where $I(x)$ is the intensity of a photon beam after length $x$, $I_0$ the initial beam intensity and $\mu$ the attenuation coefficient. The latter is the inverse of the absorption length $\lambda$ in the medium and can be related to the interaction cross-section $\sigma$ via the mass absorption coefficient (figure 1.4) [26]:

$$\mu_\mathrm{m} = \frac{\mu}{\rho} = \frac{1}{\lambda\rho} = \frac{N_\mathrm{A}}{A}\sigma \, . \tag{1.8}$$

Here $\rho$ is the mass density and $A$ the relative atomic weight.

Equation (1.7) shows the difference between photon interaction and charged particles. Charged particles continuously lose energy while traversing the medium, without substantial intensity losses, until a relatively sharp stop after a finite length is reached. In contrast, photons are absorbed (photoelectric effect and pair production) or deflected from the photon beam (Compton effect), as soon as they interact with matter.

### 1.2.1 *Photoelectric Effect*

In the photoelectric effect, a photon liberates an atomic shell electron, by transferring its energy at once. The kinetic energy of this photoelectron is

$$E_\mathrm{kin} = E_\gamma - E_\mathrm{b} \, , \tag{1.9}$$

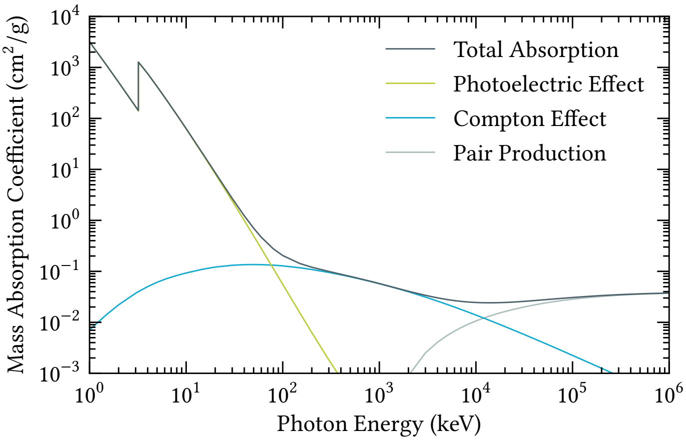

*Figure 1.4* – Energy dependence of the mass absorption coefficient in pure argon. At low photon energies in the X-ray regime, as it holds for this thesis, the photoelectric effect dominates, while at higher energies, first the Compton effect becomes relevant and then the pair production dominates. Data from [34].

where $E_\gamma$ is the energy of the photon and $E_\mathrm{b}$ the binding energy of the electron. Depending on the energy of the photon, either an outer shell electron (UV photon, 3 to 120 eV [35]) or an electron from the most inner shell (X-ray photon, 120 eV to 120 keV [35]) is liberated.

The range $r$ of each (photo)electron with energy $E_\mathrm{kin}$ in a gas with density $\rho$ can be described by the empirical relation [33]

$$r(E_\mathrm{e}, \rho) = \frac{k_1}{\rho} E_\mathrm{e} \left(1 - \frac{k_2}{1 + k_3 E_\mathrm{e}}\right) , \tag{1.10}$$

with $k_i$ being the empirical constants ($k_1 = 0.537 \times 10^{-3}\,\mathrm{g/cm^2\,keV^{-1}}$, $k_2 = 0.982$, and $k_3 = 3.123 \times 10^{-3}\,\mathrm{keV^{-1}}$). From this, it is found that for example, a photoelectron with 2.7 keV (section 4.2.1) has a track length of 220 µm in Ar/$CO_2$ (70/30 %) with a density of 1.716 g/l at NTP [25].

The energy and material dependence of the photoelectric effect is described by its cross-section [26]

$$\sigma_\mathrm{ph} \propto \frac{Z^a}{E_\gamma^b} , \tag{1.11}$$

with $a$ being between 4 and 5 and $b \approx 3.5$. For a constant photon energy, the absorption increases rapidly for materials with higher atomic number $Z$, while it drops significantly for higher energies in the same material (figure 1.4). At the same time, when the photon energy is fixed, the cross-section for an interaction with the most inner shell electron is the largest; requiring that the binding energy is still smaller than the photon energy. This is the reason for steps in the mass absorption coefficient, the so-called absorption edges. For argon, the absorption edge from the most inner shell electron is at 3.2 keV (figure 1.4), which is the corresponding binding energy [36].

### 1.2.2 *Other Photon Interactions*

In addition to the photoelectric effect, two other prominent photon interactions can take place inside a detector. The first one is the Compton effect, which is the scattering between a photon and an outer shell electron. The binding energy of the electron with respect to the photon's energy can be neglected and the electron can be assumed as quasi-free. From the kinematics of this process (figure 1.3b), the following energy relation can be derived [26]:

$$E_{\gamma'} = \frac{E_\gamma}{1 + \frac{E_\gamma}{m_\mathrm{e} c^2} \left(1 - \cos\theta\right)} \; . \tag{1.12}$$

Here, $E_\gamma$ is the energy of the photon before the scattering, $E'_\gamma$ is the one after the scattering and $\theta$ is the scattering angle of the photon. In the case of backscattering, $\theta = 180^\circ$, the energy transfer to the electron becomes maximal.

The other effect that can take place is pair production. It means the conversion of a photon, inside the electric field of a charge carrier, into an electron-positron pair (figure 1.3c). For this, it is required that the photon energy exceeds the mass at rest of the two created particles, i.e. the mass of an electron and a positron [26]:

$$E_\gamma > 2 m_\mathrm{e} c^2 \; . \tag{1.13}$$

Usually, pair production takes place in the field of the atomic nucleus (except for very light elements), which also means that the recoil energy which is transferred to the nucleus can be neglected, due to the high nucleus mass.

## 1.3 CHARGE TRANSPORT

After the initial ionisation process, the electron-ion pairs are separated by an external electric field. This imposes a drift motion (section 1.3.1) on the charge carriers along the electric field and transports the electrons towards the read-out anode. In addition to the superimposed directional drift, the electrons and ions follow a random thermal motion, leading to their diffusion (section 1.3.2). This is the result of the density gradient between charge carriers and the surrounding gas and does not require an external field.

### 1.3.1 Particle Drift

In moderate electric fields $\mathcal{O}(1\,\mathrm{kV/cm})$ charged particles drift with a constant average velocity $w$. Their motion can be understood as an equilibrium between acceleration and energy gained due to the electric field and energy loss due to collisions with the surrounding gas atoms.

The condition for this equilibrium in an electric field with strength $E$ can be described via [33]

$$\Lambda\epsilon = qEw\tau \ , \tag{1.14}$$

where $\epsilon$ is the energy of the charge carrier with charge $q$ obtained through the field, $\Lambda$ the fractional energy loss during a collision and $\tau$ the average time between two collisions. For the drift velocity itself, the following general expression can be obtained by solving the Boltzmann transport equation [26]:

$$\vec{w} = \frac{q\vec{E}}{m}\left[\frac{2}{3}\left\langle\frac{\lambda}{v}\right\rangle + \frac{1}{3}\left\langle\frac{\mathrm{d}\lambda}{\mathrm{d}v}\right\rangle\right] = \pm\mu\vec{E} \ . \tag{1.15}$$

Here, $\lambda$ is the mean free path between collisions, $v$ the instantaneous velocity of the charge carrier and $\mu$ the mobility, with the sign being defined by the charge of the particle. For ions, equation (1.15) simplifies to [26]:

$$\vec{w}_{\mathrm{ion}} = \frac{e\vec{E}}{m}\tau = \mu\vec{E} \ . \tag{1.16}$$

This is because for ions, the interaction cross-section $\sigma \propto 1/\lambda$ is almost energy-independent. Hence, the collision time and $\tau = \mathrm{d}\lambda/\mathrm{d}v$ can be assumed to be constant.

For electrons, the situation is more complex. Their cross-section is highly energy-dependent (figure 1.5). Thus, electron velocities are typically calculated numerically, e.g. with Magboltz [37, 38], with the corresponding cross-sections as input parameters. For some gases, this was done in this thesis (figure 1.6). For a typical drift field of around 2.4 kV/cm, an electron drift velocity of about 6.5 cm/µs is expected in a gas mixture of $\mathrm{Ar/CO_2}$ (70/30 %).

### 1.3.2 Diffusion

The liberated electrons and the ions in the gas follow a random thermal motion, described by the Maxwell-Boltzmann distribution. Their mean instantaneous velocity

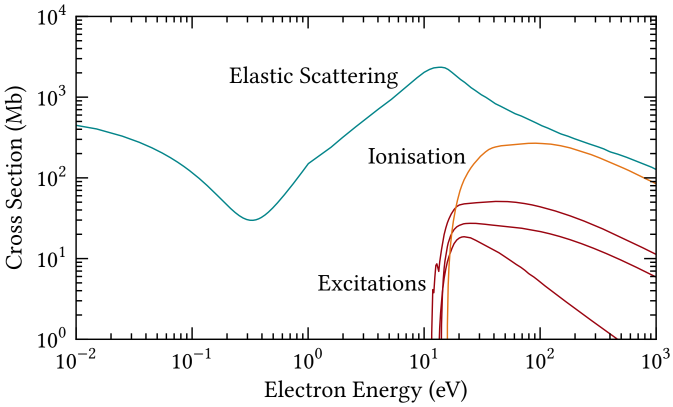

*Figure 1.5* – Energy dependence of the electron cross-section in argon. The data are the input parameters used for the Magboltz calculations [37, 38].

is then given by [28]

$$\langle v \rangle = \sqrt{\frac{8 k_{\mathrm{B}} T}{\pi m}} \,, \tag{1.17}$$

with $k_{\mathrm{B}} = 8.617 \times 10^{-5}$ eV/K Boltzmann's constant, $T$ the temperature of the gas and $m$ the particle's mass. The mean instantaneous velocity for an electron at 20 °C is found to be $10^5$ m/s, which is slightly larger than the drift velocity, but in the same order of magnitude.

Due to a density gradient between the electron-ion pairs and the surrounding gas, the electrons and ions diffuse, which can be described by [28]

$$\frac{\mathrm{d}N}{\mathrm{d}x} = \frac{N_0}{\sqrt{4\pi D t}} \exp\left(-\frac{x^2}{4Dt}\right) \,. \tag{1.18}$$

Here $\mathrm{d}N/\mathrm{d}x$ denotes the number of particles found in the space element $\mathrm{d}x$ after some time $t$ in a distance $x$ from the origin of the charge cloud containing $N_0$ particles. The width of the charge cloud after time $t$ along $x$ is given by $\sigma_x = \sqrt{2Dt}$, with the diffusion coefficient $D$. For drifting charge clouds, this expression can be related to the drift length $L$, the drift field $E$ and the drift velocity $w$ by using equation (1.15) and $w = L/t$ [33]:

$$\sigma_x = \sqrt{\frac{2DL}{\mu E}} = \tilde{D}\sqrt{L} \,. \tag{1.19}$$

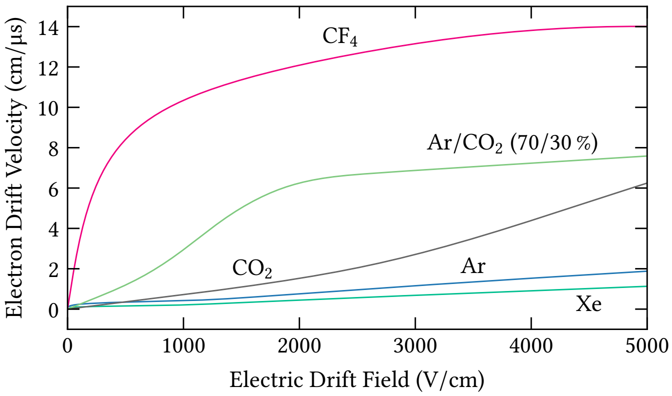

*Figure 1.6* – Calculated electron drift velocity at NTP depending on the electric drift field for various gases. The calculations were performed with Garfield++ [29, 30], using its Magboltz [37, 38] interface.

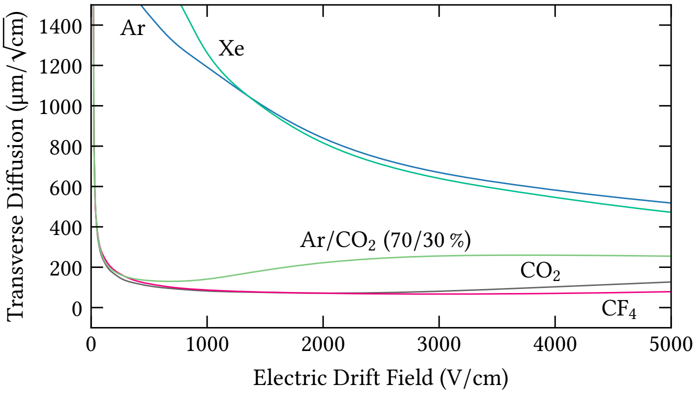

*Figure 1.7* – Calculated transverse diffusion at NTP depending on the electric drift field for various gases. The calculations were performed with Garfield++ [29, 30], using its Magboltz [37, 38] interfact.

Here, $\tilde{D}$ is the diffusion coefficient for a drifting charge cloud (figure 1.7). From the dependence of equation (1.19) on the mobility, it can be seen that the situation for electron and ion diffusion is similar to their drift; while for ions, a simple analytical expression is sufficient, the diffusion coefficient for electrons has to be calculated numerically. For the here described detector filled with Ar/$CO_2$ (70/30 %) and a total height of 9 mm, the diffusing charge cloud has a width of $\sigma = 240\,\mu\mathrm{m}$, assuming a typical drift field of 2.4 kV/cm and that the ionisation takes place immediately after the cathode and is initially point-like.

After the drift, the electrons reach the read-out anode. However, due to the small number of the initial ionisation electrons, their induced electronic signal is typically too low for a direct measurement. Thus, it has to be amplified, for which gas amplification by means of an electron avalanche is used.

During the drift, the electrons collide with the surrounding gas atoms. In-between the collisions, the electrons gain kinetic energy because of the acceleration in the electric field. If the electric field and hence the gained energy is large enough (exceeding the ionisation potential of the gas atoms), the drifting electron can ionise the gas atoms at the time of the collision. With the mean free path $\lambda_\mathrm{i}$ between two ionising collisions, the first Townsend coefficient $\alpha = 1/\lambda_\mathrm{i}$ can be defined, which describes the number of created secondary electron-ion pairs per unit path length.

In a high electric field $\mathcal{O}(50\,\mathrm{kV/cm})$, the first electron ionises a gas atom after a length of $1/\alpha$. Due to the high field, both electrons gain enough energy between the next collision with other gas atoms to ionise them as well. This process continues and leads to an electron avalanche, where $N$ electrons liberate $\mathrm{d}N$ more electrons after a path length $\mathrm{d}x$:

$$\mathrm{d}N = N\,\alpha\,\mathrm{d}x\ . \tag{1.20}$$

Integration leads to the gain factor $G$, which is defined as the ratio between the number of electrons in the avalanche $N(x)$ after length $x$ and the initial number of electrons $N_0$:

$$G = \frac{N(x)}{N_0} = \mathrm{e}^{\alpha x}\ . \tag{1.21}$$

However, the mean free ionisation path and hence the Townsend coefficient depends on the electric field, which itself depends on the position. Thus, the general expression for the gain factor is given by [26]

$$G = \frac{N(x)}{N_0} = \exp\left[\int_{x_\mathrm{i}}^{x_\mathrm{e}} \alpha\big(E(x)\big)\,\mathrm{d}x\right]\ , \tag{1.22}$$

with $x_\mathrm{i}$ the start position and $x_\mathrm{e}$ the end position of the amplification path.

Depending on the strength of the gas amplification, different operation modes can be defined [26]. The mode used in this thesis is the *proportional mode*, which means that the number of electrons arriving at the read-out anode is proportional to the energy deposited by the interacting particle inside the detection volume. This is achieved with gain factors between $10^3$ and $10^5$. Another aspect of the avalanche process is the so-called *quenching*. When the gas atoms, which have been ionised and excited during the avalanche procedure de-excite, they can emit UV photons, which themselves can ionise other gas atoms, with the liberated electrons being then able to ionise further gas atoms. As this can lead to a chain reaction and a discharge which could in the worst case destroy the detector of the read-out electronics, it is essential to absorb the UV photons created during the avalanche process. For this, a molecular gas (e.g. $CO_2$) is added to the gas inside the detector (e.g. argon). With its rotational and vibrational modes, the molecules can absorb the UV photons without releasing an electron and hence quench the discharge development [27].

## 1.5 Signal Induction

After multiplying the initial charge, the electrons are collected on the read-out anode. It is found, that the signal charge on the anode $\mathrm{d}Q_\mathrm{s}$, which is induced by a charge $q$ that moves a distance $\mathrm{d}r$ [26], is

$$\mathrm{d}Q_\mathrm{s} = -q\frac{\vec{E}}{V}\mathrm{d}\vec{r}\,, \tag{1.23}$$

with $\vec{E}$ the field between the anode and in the case of a GEM-based detector (figure 1.1) the bottom electrode of the GEM. The induced signal does not depend on the applied voltage $V$ between the electrodes but only on the detector and read-out geometry, as $|\vec{E}| \propto V$.

The quantity $\vec{E}/V = \vec{E}_\mathrm{w} = -\nabla\phi_\mathrm{w}$ from equation (1.23) is called the *weighting field*, with the corresponding weighting potential $\phi_\mathrm{w}$. From this, the induced signal current can be calculated via [26]

$$I_\mathrm{s} = -\frac{\mathrm{d}Q_\mathrm{s}}{\mathrm{d}t} = q\vec{E}_\mathrm{w}\vec{w}\,, \tag{1.24}$$

where $\vec{w} = \mathrm{d}\vec{r}/\mathrm{d}t$ is the drift velocity of $q$. As this expression is only geometry-dependent, it can be generalised to a multi-electrode system. Due to superposition, it is possible to calculate the signal current on an electrode $k$, by keeping this electrode on voltage $V_k = 1\,\mathrm{V}$ with all other electrodes being grounded. This leads to the Shockley-Ramo theorem [26], which states that the signal current that a moving charge $q$ induces on an electrode $k$ is given by

$$I_{\mathrm{s},k} = q\vec{E}_{\mathrm{w},k}\vec{w}\,. \tag{1.25}$$

Multi-electrode systems are used in the case of position-sensitive detectors (section 4.1). Once the signals are collected by the read-out geometry, they can be further processed by the front-end electronics (chapter 2).

*Chapter 2*

# VMM3a Front-End of the Scalable Readout System

To read the detector signals and process them for the analysis, dedicated read-out electronics are needed. The front-end processing follows usually the same principles (figure 2.1). As the first stage of the processing chain, a preamplifier is used which amplifies the detector signals generated by the incident radiation on its input. The second stage is a shaper, which shapes the preamplifier output, filters the signals and reduces e.g. the impact of electronic noise. The resulting output is then compared to a previously defined reference voltage in the discriminator. When the output signal exceeds the reference voltage, the signal processing is continued. The most prominent form of this continued processing is the digitisation of the signal in amplitude and time with ***A****nalogue-to-****D****igital* ***C****onverters* (ADCs). The digital signals can then be handled by the corresponding back-end electronics.

For the use in experiments, the signal processing is typically implemented on ***A****pplication-****S****pecific* ***I****ntegrated* ***C****ircuits* (ASICs). In the first part of this chapter, the VMM3a ASIC and its front-end processing components are reviewed (section 2.1). This is followed by a description of the back-end electronics, specifically the RD51 ***S****calable* ***R****eadout* ***S****ystem* (SRS) and the integration of the VMM3a into the SRS (sections 2.2 and 2.3).

## 2.1 VMM3a Front-End ASIC

The VMM3a [11] is a 64-channel front-end ASIC, which was developed at the ***B****rookhaven* ***N****ational* ***L****aboratory* (BNL) for the ***N****ew* ***S****mall* ***W****heel upgrade* (NSW) [2] of the ATLAS experiment [1] at CERN. Being the production version of a family of VMM ASICs [11], the VMM3a is used to read out the ***Micro****-****Me****sh* ***Ga****seous* ***S****tructure* (MicroMegas) [39] and *small-strip* ***T****hin* ***G****ap* ***C****hamber* (sTGC) [40] detectors of the NSW. This specific design to read out gaseous detectors and its rich set of features made the VMM3a also interesting for applications beyond the ATLAS muon system. Hence, the VMM was integrated into the SRS [12, 41], to provide a general-purpose

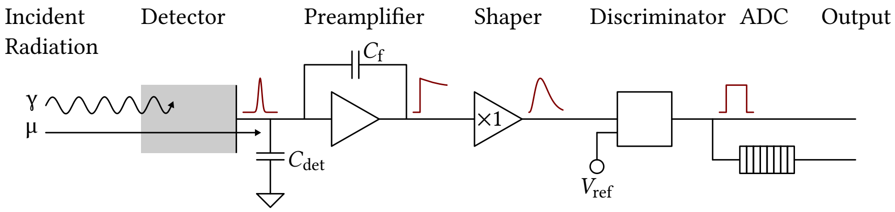

*Figure 2.1* – Illustration of a typical front-end electronics signal processing chain. Adapted from [26].

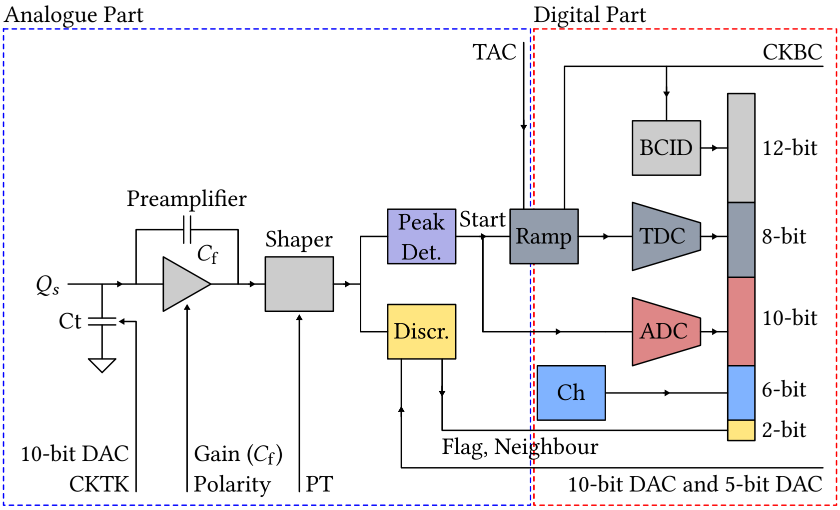

*Figure 2.2* – Block diagram of a VMM3a read-out channel, showing the relevant components for the VMM3a front-end of the SRS, with the adjustable peaking time (PT), the adjustable gain via the feedback capacitance $C_\mathrm{f}$, the TAC slopes for the voltage ramp of the input DACs. Adapted from Hans Muller [42].

read-out system for gaseous detectors. While this is described in the later sections of this chapter, in the present section the VMM3a itself is described.

Each VMM3a channel combines an analogue and a digital part for the signal processing (figure 2.2). The analogue part starts with a preamplifier (section 2.1.1), followed by a shaper and a discriminator (section 2.1.2) and a peak finder. The output of the peak finder provides the charge and the time information of the shaper output, which is then digitised in the digital part (section 2.1.3). In addition, the configuration logic for the signal handling is contained in the periphery of the chip. This includes global (common to all channels and the entire ASIC) control signals, like for example various clocks, and adjustments to the analogue part via ***Digital-to-Analogue Converters*** (DACs). Global inputs are for example the test pulse clock or the common discriminator level. Individual inputs for each channel are for example the

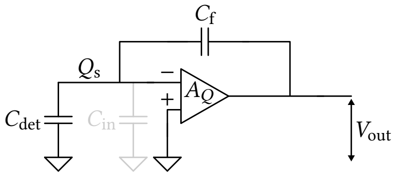

*Figure 2.3* – Illustration of the circuitry of a CSA. Adapted from [26].

channel-by-channel discriminator level trimming, the enabling of the test capacitor or the individual masking of channels. The periphery contains also a temperature sensor and an analogue monitoring output, giving direct access to each selectable analogue signal.

### *2.1.1 Preamplifier*

The VMM uses a ***C**harge-**S**ensitive **A**mplifier* (CSA) as a preamplifier (figure 2.3). With such an amplifier, the signal charge $Q_s$ from the read-out electrode (section 1.5) is converted to an output voltage $V_{out}$. Both quantities are related via [26]

$$V_{out}(t) = -\frac{Q_s(t)}{C_f} , \tag{2.1}$$

with $C_f$ the value of the feedback capacitor. This value defines also the charge amplification $A_Q = |V_{out}/Q_s| = 1/C_f$.

In case of the VMM3a, this value can be adjusted to 0.5, 1.0, 3.0, 4.5, 6.0, 9.0, 12.0 and 16.0 mV/fC [11], allowing a wide range of applications. Driven by the needs of the NSW, the amplifier was also designed to cope with a large range of input capacitances $C_{in}$ (few pF to 1 nF) and both, positive and negative input signal polarities [43].

### *2.1.2 Shaper and Discriminator*

The output of the CSA is filtered by a third-order ‘semi-Gaussian’ shaper (figure 2.4), which is described in detail in [11]. It ensures that the peak amplitude of the voltage output $V_{shaper}(t)$ is proportional to the input charge $Q_s(t)$. In a simplified way, the shaper can be understood as a combination of a high-pass and $n$ low-passes, with $n = 3$ for the VMM3a. As result [26],

$$V_{shaper}(t) = V_{out}(t)\, A(t) , \tag{2.2}$$

where

$$A(t) \propto \frac{1}{n!} \left(\frac{t}{\tau}\right)^n \exp\left(-\frac{t}{\tau}\right) \tag{2.3}$$

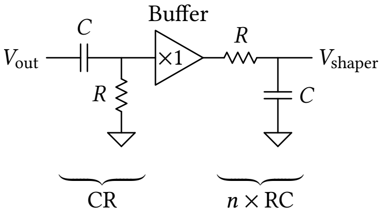

*Figure 2.4* – Illustration of an $n^{\mathrm{th}}$-order shaper consisting of a high-pass (CR) and $n$ low-passes (RC). Located after the preamplifier, the CSA's output signal $V_{\mathrm{out}}$ is the input of the shaper, which has its own output signal $V_{\mathrm{shaper}}$. Adapted from [26].

is the shaper pulse form, with the shaping time of the filter $\tau$ and $t_{\mathrm{peak}} = n\tau$ its peaking time. In the case of the VMM3a, the peaking time can be adjusted to values of 25, 50, 100 and 200 ns [11]. The shaper contains also a mechanism to stabilise the baseline of the output to 160 mV [11].

After the shaper, a discriminator is used. The value of the corresponding ***Th**reshold **L**evel* (THL) is first set by a common 10-bit DAC to all channels of one VMM and then fine adjusted with a 5-bit DAC trimmer for each channel individually [11]. The discriminator can be considered as one of the most important functionality parts, as other features rely heavily on it. One of them is the self-triggered continuous read-out mode with integrated zero-suppression used for the SRS. In this mode, the self-triggering is performed on the threshold level, meaning that a signal is only digitally processed and acquired if it surpasses the THL. The THL is also the starting point of the ***N**eighbouring-**L**ogic* (NL). It means that if a signal on channel $k$ surpasses the THL, the further signal processing (i.e. peak finding and digitisation) on the two adjacent channels $k \pm 1$ will be triggered as well, even if the signal on these two channels does not surpass the THL. Here it is important to note that the VMM3a is designed in such a way, that the neighbouring-logic trigger signal can be also passed between two adjacent VMMs [11]. It should be mentioned that the NL is an optional feature, which is turned off by default and has to be explicitly turned on by the user.

### *2.1.3 Timing and Signal Digitisation*

When the signal amplitude surpasses the threshold level, the electronics proceeds with the digitisation of the shaper output. For this, the peak amplitude of the shaper pulse has to be found as a measure of the charge information of the signal (figure 2.5). Once identified by a peak finder, the baseline-subtracted[1] amplitude of the ***P**eak **D**etector **O**utput* (PDO) is transferred to a 10-bit two-stage current-mode domino

---

[1] Technically, not the baseline of each channel is subtracted, but 150 mV are subtracted from the peak amplitude. The difference between this value and the actual baseline is implicitly subtracted during the ADC correction procedure (section 3.2).

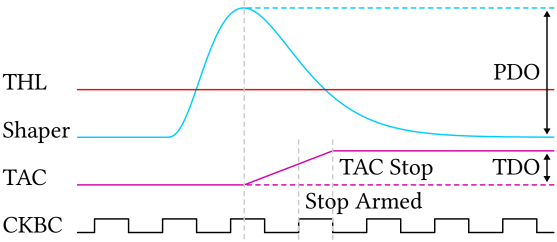

*Figure 2.5* – Timing diagram of the VMM3a's analogue part, illustrating the timing-at-peak procedure. The output of the shaper has to cross the THL in order to trigger further processing to happen. This includes the peak finding, with the amplitude of the peak being transferred to the charge ADC via the PDO. The coarse timestamp of the signal is given by the CKBC value of the peak. The fine timestamp is determined with a voltage ramp that is started once the peak is found. The stop of the voltage ramp is armed at the rising edge of the next CKBC value and then stopped at the falling edge of that CKBC value. The value of the voltage ramp is then transferred via the TDO to the timing ADC. Adapted from [11].

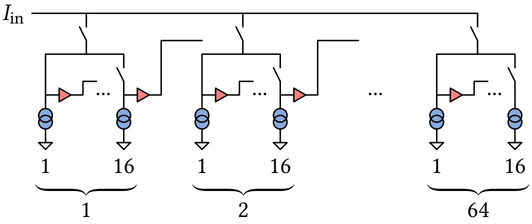

*Figure 2.6* – Working principle of the two-stage current-mode domino ADC, with its 64 *macro cells* in the first stage and the 16 *micro cells* per macro cell in the second stage. Adapted from [11].

ADC [11] (figure 2.6). This clockless ADC has a minimum dead time of 250 ns which is dominated by the ADC conversion time [11].

To get access to the time of the peak, a coarse 12-bit timestamp and a fine 8-bit timestamp are used. The coarse timestamp is given by a Gray counter, which counts the clock cycles of the so-called ***Bunch Crossing Clock*** (CKBC), which is active throughout the entire operation of the VMM3a. The output is the so-called ***Bunch Crossing ID*** (BCID)[2]. Once the peak amplitude is found, the corresponding BCID is stored (the last CKBC signal before the peak was found). To get timestamps with higher precision than the one defined by the CKBC frequency, a voltage ramp with constant slope is started at the time of the peak finding. The voltage ramp, which has adjustable slopes of 60, 100, 350 and 650 ns [11], is stopped at the falling edge of the

---

[2] In the name choice, the origin of the VMM ASIC from the ATLAS experiment becomes evident. However, the CKBC is not fixed to the ATLAS machine clock, but it is implemented as reference clock with an adjustable clock frequency.

next CKBC signal (figure 2.5)[3]. The signal from this ***T**ime-to-**A**mplitude **C**onverter* (TAC) is the ***T**ime **D**etector **O**utput* (TDO), which is processed by an 8-bit two-stage current-mode domino ADC. As a result, the precise time of the peak is given by [41]

$$t_{\text{chip}} = \text{BCID} \times \frac{1}{f_{\text{CKBC}}} + \left(1.5 \times \frac{1}{f_{\text{CKBC}}} - \text{TDC} \times \frac{\text{TAC Slope}}{255}\right) \tag{2.4}$$

and is called *chip time*.

It should be noted that for both, the ADC and the TDC, a value aggregation was observed, leading to an equivalent number of bits of 8-bit for the ADC and 6.5-bit for the TDC [11]. Furthermore, it should be noted that the VMM supports in addition to the here described *timing-at-peak* also *timing-at-threshold*, with the TAC ramp being started as soon as the shaper output surpasses the threshold level. However, it was observed that timing-at-threshold in the VMM3a is afflicted with some issues [11], making it unsuitable for the measurements performed in this thesis (section 3.4.3).

## 2.2 RD51 Scalable Readout System

The ***S**calable **R**eadout **S**ystem* (SRS) [10] is a multi-purpose and highly versatile read-out system, which was developed by the RD51 Collaboration for the read-out of ***M**icro-**P**attern **G**aseous **D**etectors* (MPGDs). It was proposed in 2009, with first systems being successfully used for experiments in 2010. The goal of the SRS is to provide a common and scalable read-out structure, that can be used independently of the detector type, starting from a few read-out channels and going to several thousand. As such, it should handle different experiment sizes, from small R&D set-ups to medium-sized experiments with $\mathcal{O}(\text{m}^2)$ sized detectors or detector modules. Various read-out ASICs have been integrated into the SRS, leading to another adaption to different detector technologies and experimental needs. The APV25 [10, 44], the Timepix [45, 46] and the VMM3a [11, 12] ASICs can be considered as the most successful examples in terms of integration.

To achieve this goal, the SRS implements the approach described in the following (figure 2.7)[4]. At the beginning of the read-out chain sits the *Hybrid PCB* (stage A), a ***P**rinted **C**ircuit **B**oard* (PCB) that contains the front-end ASIC, the connector to plug it onto the detector and additionally required electronics (e.g. signal drivers or power regulators). In terms of read-out stages, the VMM3a ASICs (A.1), the link between

---

[3] Hence, the TAC slope has to have at least the length of 1.5 CKBC periods.

[4] A common approach is to lead the signals collected with the read-out electrodes out of the active detector area via traces on the read-out board and to connect the front-end electronics there with a plug connection. This approach however does not work when the charge collection electrode and the front-end electronics are combined within a single ASIC, as for example in the Timepix [45]. For such a case, a slightly different approach was found, preserving the scalability concept [46].

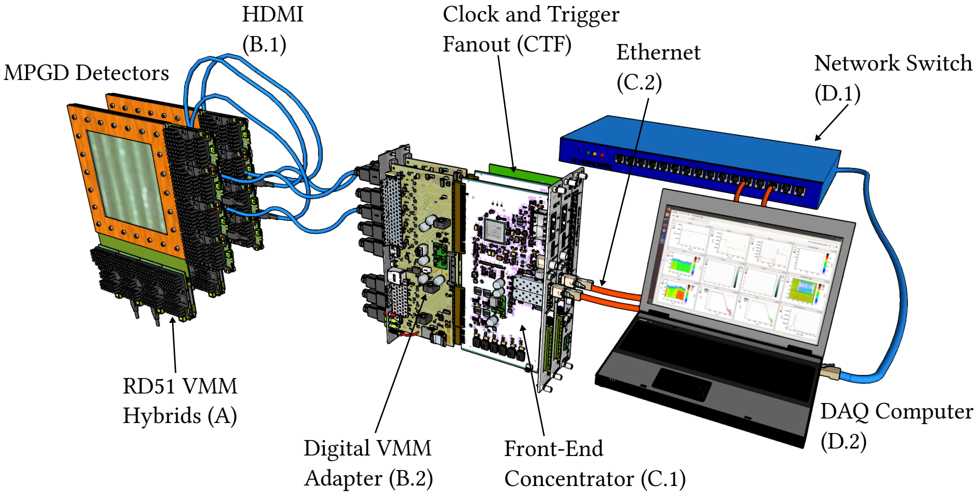

*Figure 2.7* – Illustration of the different read-out stages of the SRS with its VMM3a front-end. Stage A on the detector level consists of the RD51 VMM Hybrid. This is followed by stage B, with the HDMI cable (B.1) and the ASIC-specific adapter card (B.2). The adapter card is connected to the Front-End Concentrator card (C.1), which sends via Ethernet (C.2) the data to a switch (D.1) and from there to the DAQ computer (D.2). In case multiple Front-End Concentrator cards are used, the CTF card is used to provide a common clock. Adapted from Hans Muller [41, 42].

the ASICs and the digital read-out part (A.2) and the digital read-out part itself (A.3) on the Hybrid should be mentioned. This Hybrid PCB is connected via HDMI cables to an ASIC-specific adapter card (stage B). This is also the first scalability option, with the *adapter card* having eight HDMI ports. The adapter card is connected via PCIe to the ***F**ront-**E**nd **C**oncentrator* (FEC) card (stage C). The FEC card in terms of hardware is common to all ASICs, containing an ASIC-specific firmware, which provides common components (e.g. the network communications block). This is the second scalability option, using multiple FEC-adapter-card combinations. The data output of the FECs is transmitted via Ethernet, allowing to use a standard commercial network switch to combine the network stream and send the data to the ***D**ata **A**cquisition* (DAQ) computer (stage D). In order to ensure that the FECs operate synchronously in a multi-FEC system, the ***C**lock and **T**rigger **F**anout* (CTF) card exists, which provides a common clock for the FECs.

## 2.3 INTEGRATION OF THE VMM3A INTO THE SRS

After the general overview of the SRS structure, in the present section, the specific components of the VMM3a front-end of the SRS, here called *VMM3a/SRS*, are described. Following the read-out scheme, from the VMM3a towards the DAQ com-

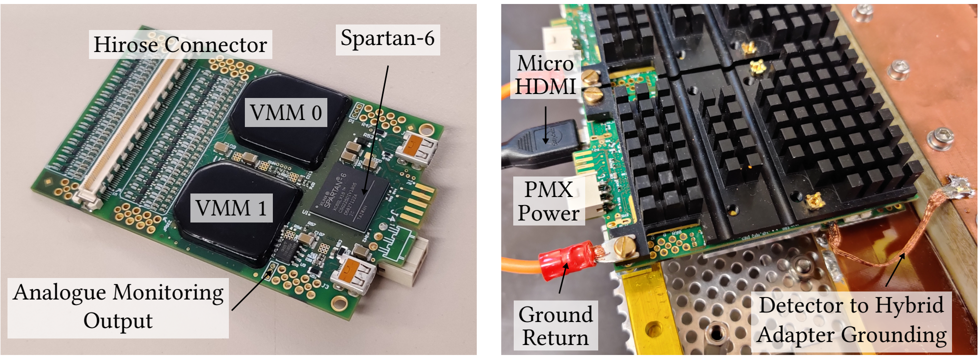

*(a)* – Bottom side without cooler.

*(b)* – Hybrid on detector.

*Figure 2.8* – Photographs of the RD51 VMM Hybrid. In one case (a), the bottom side without a cooler is shown, in the other case (b), the top side of the Hybrid with a passive cooler is shown while being connected to the detector.

puter, the hardware, firmware and software are presented. More information can be also found in [12, 41, 47]. It should be noted that the VMM contains different read-out modes [11], with the *non-ATLAS continuous mode* being used in the SRS implementation and described in the following. It should be further noted that all the components (hardware, firmware and software) were subject of continuous improvements throughout the course of this thesis with only the latest version being presented here.

### 2.3.1 RD51 VMM Hybrid

The *RD51 VMM Hybrid* is a PCB with an area of $5 \times 8\,\mathrm{cm}^2$ (figure 2.8). It carries two VMMs in order to match the typical 128-channel count of the SRS Hybrid PCBs and the MPGD connectors[5]. Additional components on the Hybrid are ***L**ow-**D**ropout* ***O**verlap* —

---

[5] Hirose FX10A-140P/14-SV1

[6] The typical voltages applied to the LDOs are $V_{\mathrm{P1}} = 3.05\,\mathrm{V}$ to $3.35\,\mathrm{V}$ and $V_{\mathrm{P2}} = 1.75\,\mathrm{V}$ to $2.05\,\mathrm{V}$, which are regulated down to $V_{\mathrm{P2}} = 1.2\,\mathrm{V}$ for the VMMs and some of the FPGA's components and $V_{\mathrm{P1}} = 2.5\,\mathrm{V}$ for the other FPGA components and the other electronics on the Hybrid.

[7] Texas Instruments ADS1015-BQDGSR-Q1

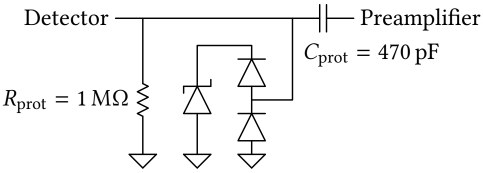

*Figure 2.9* – Illustration of the spark protection circuit used on the RD51 VMM Hybrid in front of inputs of each VMM channel. The diodes are the Onsemi NUP4114. Adapted from Hans Muller [42].

on the same PCB but that they can be also transmitted between two hybrids[8]. The most important component besides the VMMs is however the Xilinx Spartan-6 ***F**ield **P**rogrammable **G**ate **A**rray* (FPGA)[9]. It is used to provide the necessary clocks (e.g. for timing), read out the data transmission lines of the VMM3a and configure the VMMs.

From the Spartan-6 FPGA, the digitised detector signals are then sent via HDMI cables to the ***D**igital **VMM** Adapter* (DVMM) card. Despite having two HDMI ports on the Hybrid, only one is used, with the second one not being implemented in the firmware and serving purely as a hardware redundancy; originally the second port was indented for a master/slave operation [12], but this option was never realised, due to the high data rates achievable with VMM3a/SRS. The two I$^2$C lines of the HDMI cable are used to communicate with the external ADC. From the four differential pairs of the HDMI cable, two are used to send the acquired data from the VMMs to the DVMM and the FEC (one pair per ASIC). The two other differential pairs are used to send signals from the FEC to the VMMs, with the clock differential pair being used for a synchronised base clock and the configuration/trigger pair being used to send the configuration of the VMM3a as well as trigger signals (e.g. start and stop of the data acquisition). With the exception of the clock, all signals on the differential pairs are 8b/10b encoded.

All the clock signals needed by the VMM3a are generated by the Spartan-6 FPGA from the base clock of the FEC. The clock signals are the ***B**unch **C**rossing **C**lock* (CKBC), the ***T**est **P**ulse **C**lock* (CKTP), the ***D**ata **T**ransmission **C**lock* (CKDT) and the ***T**oken **C**lock* (CKTK). The latter are both needed for the read-out of the VMM channels (figure 2.10). The data stream from the VMM3a consists of 38-bit long hits (table 2.1). A hit is a digitised version of a shaper pulse from one read-out channel. Each hit is multiplexed onto two data lines ($data_0$ and $data_1$) per channel. With the hit being fully digitised, a token flag is raised during the multiplexing which means

---

[8] This can be achieved via Samtec MMCX-J-P-H-ST-TH1 connectors on the Hybrid, which are plugged to the same connector type on the read-out board. This however required a new detector read-out board design, which was not available during the scope of this thesis.

[9] Xilinx Spartan-6 LX FPGA XC6SLX16-2CSG225C

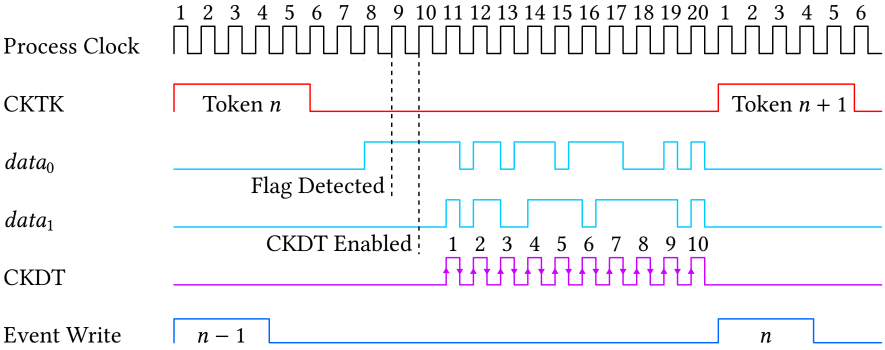

*Figure 2.10* – Timing diagram of the read-out process of the VMM3a in the non-ATLAS continuous mode, with one read-out cycle being shown in case of dual edge transmission. The process clock of the Spartan-6 can be maximally operated with 180 MHz, while the token clock CKTK can maximally be operated with 1/20th of the process clock, i.e. 9 MHz. The data transmission clock CKDT can be as fast as the process clock. Adapted from [41].

*Table 2.1* – Format of a 38-bit VMM3a hit. Adapted from [41].

| Name | Length (bit) | Value range |
|---|---|---|
| Data flag | 1 | Always 1 |
| Over-threshold flag | 1 | Over threshold: 1<br>Below threshold (requires NL on): 0 |
| Channel number | 6 | 0 to 63 |
| ADC (PDO) | 10 | 0 to 1023 |
| TDC (TDO) | 8 | 0 to 255 |
| BCID (Clock counter) | 12 | 0 to 4095 |

that a channel with raised flag needs to be read out. To be read out, first the CKTK loops in a round-robin-like scheme over the channels with raised token flag. After arriving at one of the tokens, the data transmission is started via the CKDT. Here the option exists to transfer the data with dual edge transmission, meaning that the bits of the hit are transferred at the rising and falling edge of the CKDT. After the data transfer, two bits are added to the hit such that it is 40-bit long for the 8b/10b encoding. Here it should be noted that each VMM3a channel contains a 4-hit deep ***First-In-First-Out*** (FIFO) buffer to store the hits. This FIFO is not accessible in the non-ATLAS continuous mode [11, 41, 47], meaning that as long as the hit is not read out, no other hit can be stored in this buffer and will be lost.

In terms of maximum data transfer rates, various limits were discovered. It was for example found out that the VMM3a cannot operate with CKDT frequencies larger than 180 MHz, as this leads to corrupted data transfers [47]. In addition, it is required

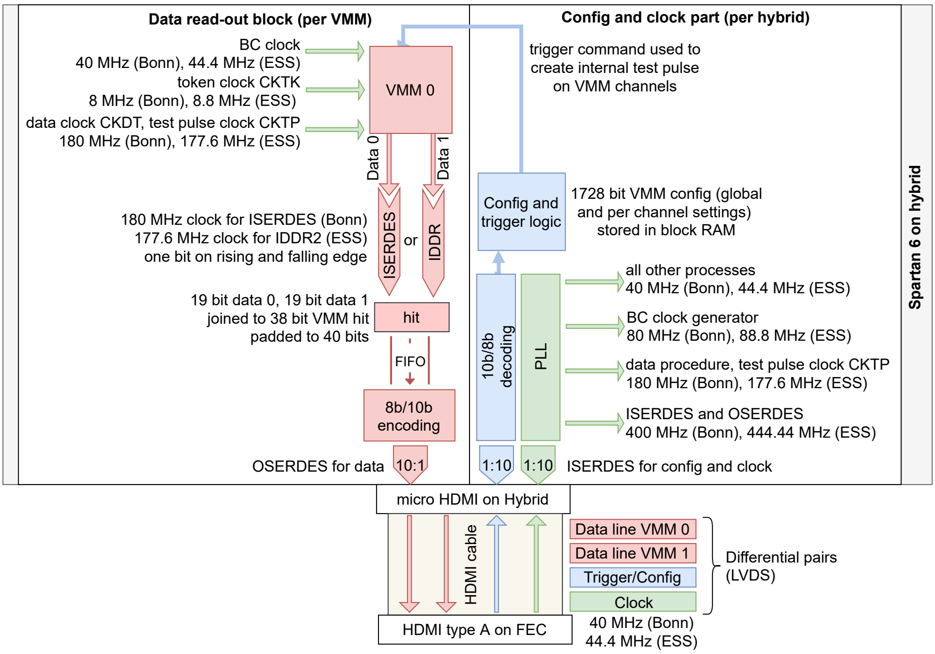

*Figure 2.11* – Schematic illustration of the working principle of the RD51 VMM Hybrid firmware, for both firmware versions. The read-out block (left) exists twice, one block per VMM. Taken from [41].

that the token has to be at least 28 ns long [47], otherwise the flag will not be detected (figure 2.10). The enabling of the CKDT after the flag detection needs another clock cycle of the process clock. Considering these three points, the maximum frequency for the CKTK is a twentieth of the process clock, i.e. 9 MHz, which assumes that the data transmission is performed in dual edge mode.

This read-out procedure, as well as all the other data and signal handling on the Spartan-6 FPGA, is implemented in two firmware versions: the *Bonn Firmware* and the *ESS Firmware*. While the Bonn firmware offers a higher configurability, the ESS firmware is more adjusted to the experimental needs of the ***E****uropean* ***S****pallation* ***S****ource* (ESS); both versions have been tested and successfully used in the scope of this thesis and their general working principle is de-facto identical (figure 2.11). One of the main differences lies in the base clock, which affects all other clocks as they are derived from it. The Bonn firmware operates with a base clock of 40 MHz (clock period of 25 ns), while the ESS firmware uses $44.\bar{4}$ MHz (clock period of 22.5 ns)[10].

---

[10] The 40 MHz clock originates from the VMM3a at ATLAS, where the bunch clock is 40.08 MHz [1], while the VMM3a at ESS will make use of half of the ESS facility clock of 88.053 MHz [11]. Here the implementation with 22.5 ns clock period was the first implementation step to get closer to this value.

For the Bonn firmware, the CKBC can be adjusted to values of 2.5, 5, 10, 20, 40, 80 and 160 MHz[11], while for the ESS firmware it is fixed to $44.\bar{4}$ MHz. The CKDT can be adjusted to values of 22.5, 45, 90 and 180 MHz in case of the Bonn firmware, while for the ESS firmware it is fixed to $177.\bar{7}$ MHz.

Due to the different base clocks, also the CKTK which is derived from it differs. While the maximum for the Bonn firmware is 8 MHz, it is $8.\bar{8}$ MHz for the ESS firmware. With the read-out procedure being performed via the token passing, the CKTK frequency corresponds also to the maximum possible hit rate that can be read out from the VMM3a. After the hits have been read out, they are stored in a 1024-hit deep FIFO on the FPGA, before being sent to the DVMM/FEC via the HDMI cable. To send the data, they are first 8b/10b encoded and afterwards serialised with a ***Ser****ialiser/****Des****erialiser* (SERDES) on the Spartan-6. The SERDES can operate at much higher frequencies than the other components on the Spartan-6, allowing them to operate at 400 MHz for the Bonn firmware and $444.\bar{4}$ MHz for the ESS firmware. These frequencies are the ones needed to match the maximum CKTK frequency. In the case of an 8 MHz CKTK, 8 Mhits/s can be read out. With the 40-bit long hit, this corresponds to a maximum data rate of

$$\nu_{\text{max}} = 40\text{-bit} \times 8\,\text{Mhits/s} = 320\,\text{Mbps}\,, \tag{2.5}$$

which after the 8b/10b encoding becomes 400 Mbps.

In order to match the maximally theoretical possible hit rate per VMM of 9 Mhits/s, derived from the maximal value of the CKTK, the maximum theoretical SERDES clock would need to be 450 MHz. This would in addition require a base clock of 45 MHz.

### *2.3.2 Digital VMM Adapter Card*

After being sent out from the hybrid, the hits arrive via the HDMI cables at the DVMM card (figure 2.12). Each DVMM contains eight HDMI ports, meaning that up to eight Hybrids can be read out at once. With the VMM3a sending and receiving only digital signals, there is no need for further data processing on the adapter card and the signals are simply forwarded between Hybrid and FEC via a PCIe connector. The DVMM is in addition used to provide the power needed by the Hybrids in a simple and direct way, instead of using external power supplies.

With HDMI cables of 2 m length, the power is directly provided over the HDMI cable itself. This avoids any additional other cables, with the exception of a strong ground return cable to the SRS crate (section 2.3.4). If the experimental set-up

---

[11] Here it should be noted that not every frequency works reliably. For frequencies up to $44.\bar{4}$ MHz, a stable operation was found, while with a CKBC of 160 MHz BCIDs were lost. The exact frequency at which the system becomes unstable was not determined.

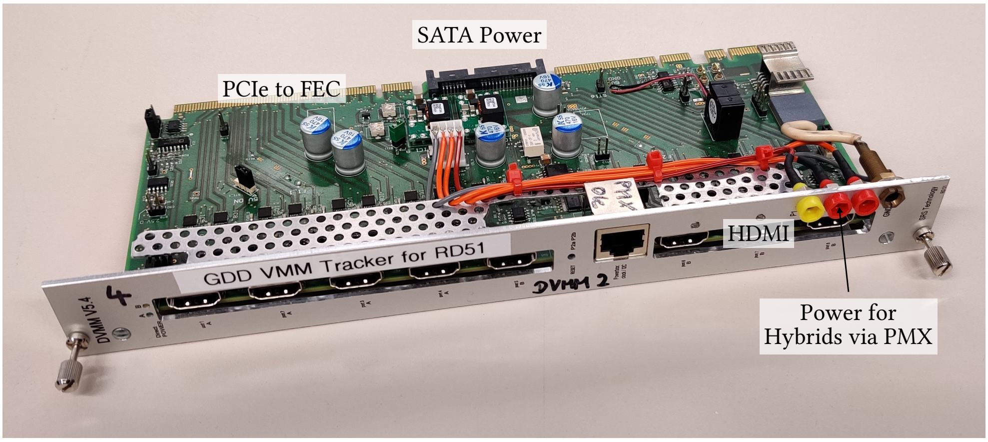

*Figure 2.12* – Photograph of the ***Digital VMM*** *Adapter* (DVMM).

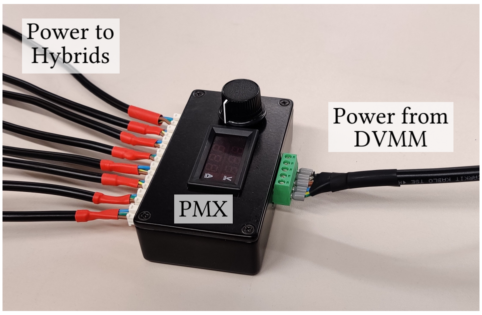

*Figure 2.13* – Photograph of the PMX box, with the single power cable coming from the DVMM card and the power being distributed within the PMX to up to eight Hybrids.

requires the use of longer HDMI cables, the power loss over the thin HDMI fibres would exceed the power needed by the Hybrid. For that case, the so-called ***Power Multiplexer*** (PMX) exists (figure 2.13). When using the PMX, the power provision over the HDMI cables is bypassed with connectors on the front panel of the DVMM. There, a long low resistivity cable can be connected between the DVMM and the PMX box that is located closer to the detectors, from which the power is distributed to up to eight Hybrids. This method allowed e.g. to operate Hybrids with 5 m long HDMI cables. However, the strong ground return cable is still required to avoid ground shifts due to the high added currents[12].

---

[12] The current needed by each Hybrid is around 2 A.

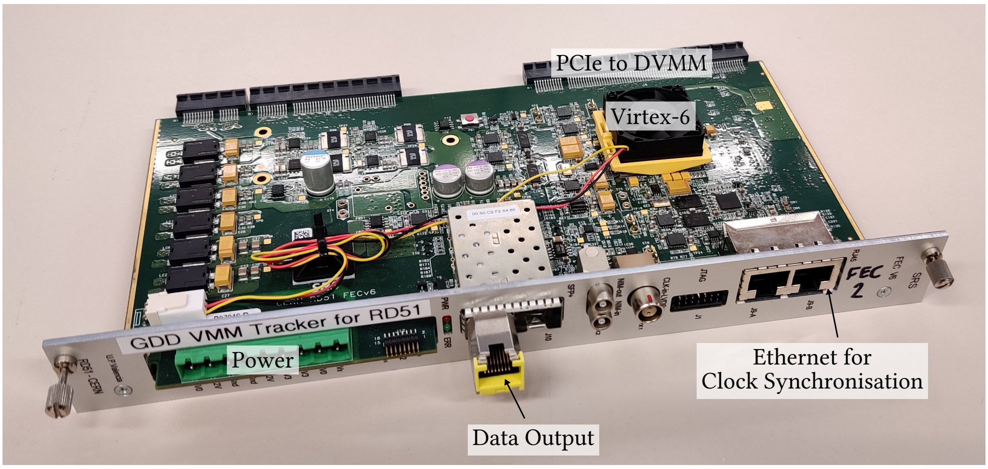

*Figure 2.14* – Photograph of the SRS ***F**ront-**E**nd **C**oncentrator* (FEC).

### *2.3.3 Front-End Concentrator Card*

Following the DVMM, the FEC (figure 2.14) combines the data stream from up to eight Hybrids and directs the data towards the DAQ computer via Ethernet. In the other direction, the FEC leads the control signals towards the VMMs and provides the base clocks for the Spartan-6 FPGAs. For this, a Xilinx Virtex-6 FPGA[13] is used on the FEC. Before being sent to the DAQ computer, the VMM data undergo some additional processing on the FEC (figure 2.15). The working principle of this FEC firmware is identical for both, the Bonn and the ESS firmware versions, with the only difference being the base clock.

As the first step, the data are 8b/10b decoded in the FPGA. This also reduces the data rate which needs to be handled on the FEC by 20 % per Hybrid. In the second step, each hit is provided with an additional timestamp and position information, enlarging the hit length to 48-bit. The extra timestamp is necessary because the chip time from equation (2.4) gets reset with every BCID counter overflow after 4096 bunch crossing periods. The extra position information is the VMM-ID because when send out from the Hybrid, a hit does not contain the information from which VMM and hence from which rough position in the detector it was sent.

The attachment of the additional timestamp and the VMM-ID to the hit works as follows. First, a 42-bit long timestamp with the resolution of the base clock frequency (25 ns or 22.5 ns) is generated on the FEC. This timestamp overflows about every 1.2 days, which should be sufficiently long for most data-taking runs. The timestamp is not added to each hit (for bandwidth purposes) but sent only every 16 BCID

---

[13] Xilinx Virtex-6 LXT FPGA XC6VLX130T-1FFG784C

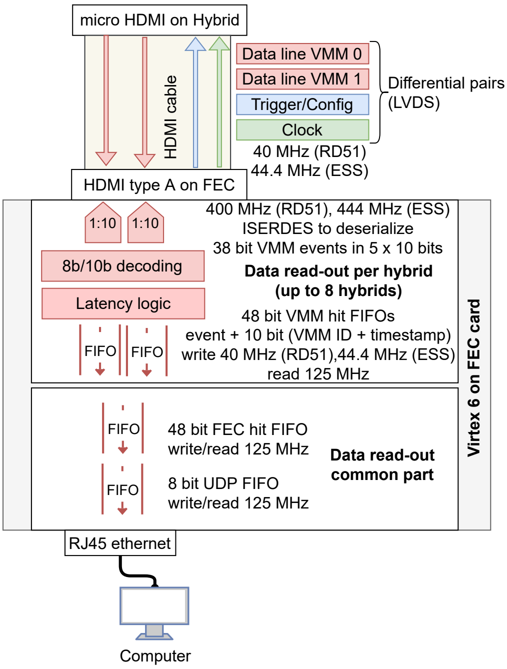

*Figure 2.15* – Schematic illustration of the data processing on the FEC. The read-out block exists for each connected hybrid (top), while the data output block (bottom) is common to the entire FEC. Taken from [41].

counter overflows as a so-called *Marker*. It is sent for each configured VMM, with the 5-bit long VMM-ID being added to the Marker, as well as a 1-bit flag, which is always set to 0 for a Marker and set to 1 for a hit. The VMM-ID is also added to the 38-bit long hit (with the two added zeros for the 8b/10b encoding being removed). Further, the information at which of the 16 BCID counter overflows the hit occurred is added. This 5-bit information is called *Offset*. As the last step, the 48-bit long hits and Markers are sent out from the FEC, going through several FIFOs. Reflecting the VMM-ID, each hit is written into a specific VMM data FIFO (one FIFO per VMM) using the base clock. From there, the hits are read into a common FEC hit FIFO with a 125 MHz clock using a fair scheduler. In the end, the 48-bit hits are split into six individual bytes and written to the UDP FIFO, again with a 125 MHz clock, defined by the 1 Gbps Ethernet connection.

The timestamping of the hits with the Offsets and Markers is performed by the *FEC Latency Logic* (figure 2.16). The necessity of this logic is illustrated with the following example. The example itself and the description of the latency logic afterwards are both taken from [41]. For all the descriptions, it is assumed that the CKBC is identical to the base clock. The example consists of three hits that arrive at roughly the same

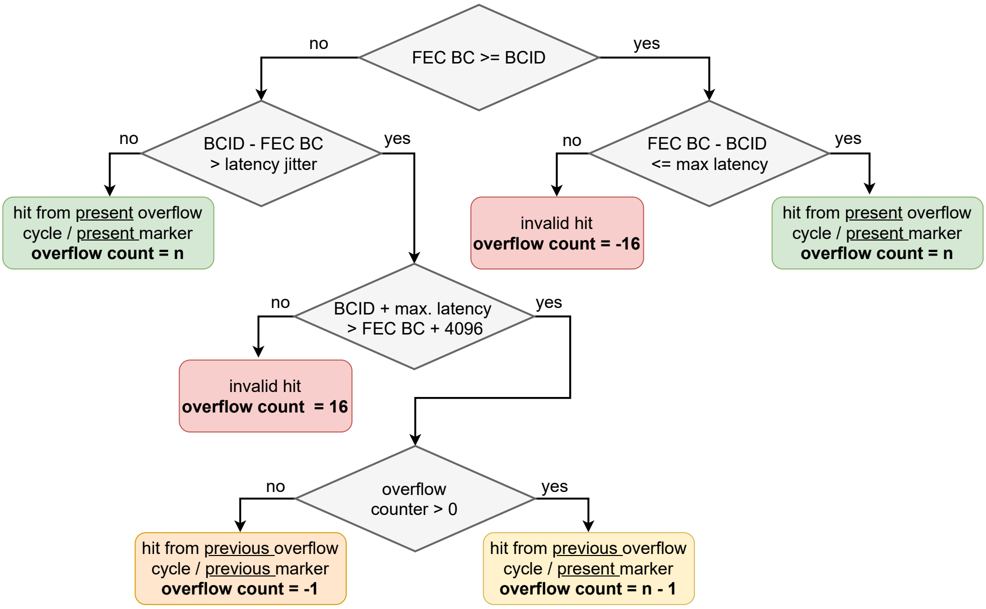

*Figure 2.16* – Illustration of the FEC latency logic. First, the BCID is compared with the FEC BC. Afterwards, either the latency jitter or the maximum latency is used for further comparison. If the comparison conditions are met, the hit is part of the present Overflow Count. If the conditions are not met, this means that the FEC BC did overflow during the read-out of hits from the previous overflow cycle. It is also possible that none of the conditions are fulfilled, which means that the hit is invalid. This case should however not occur with correctly working hardware and correct latency settings. Taken from [41].

time at the VMM. Channel 2 has a BCID of 0 and is already part of the next Offset, while channels 1 and 63 are still in the previous Offset with BCIDs of 4095. Now, due to the round-robin-like read-out scheme, channel 2 would get the same Offset assigned as the previously read out channel 1, meaning that it would be considered as arriving 4094 clock cycles earlier.

To ensure that each hit gets a correct Offset assigned and to avoid the behaviour described in the example, a CKBC-like clock and a corresponding counter are used to count the BCID overflows (called *FEC BC*) on the FEC level. This counter and the BCID need to be matched which by default is not the case, due to the time it takes to transmit and process the signals and data between FEC and Hybrid. Hence, the counter on the FEC has to be shifted by a certain amount of clock cycles, the so-called *Reset Latency*. For 2 m long HDMI cables, the Reset Latency was found to be 47 clock cycles [41]. This means that for example a hit with BCID 100 would be found with an FEC BC of 147 if the FEC BC would not be shifted by 47 clock cycles. This shift is applied to all timed control signals.

In addition to the Reset Latency, a *Latency Jitter* is implemented, to cope with a slight clock jitter between BCID and FEC BC which can still occur. It is typically set to 4 clock cycles [41]. Moreover, a *Maximum Latency* is added, arising from the CKTK, due to which a hit is read out only every five BCID counts. Consequently, with 64 hits being digitised at almost the same time (one hit per channel), the last hit arrives 320 clock cycles after the first hit.

Having these latencies established, the Latency Logic adds an *Overflow Counter* to the hit, which is based on the Offset and in fact replaces the Offset in the data output (figure 2.16). With this, the FEC timestamp of a VMM hit is given by [41]

$$t_{\mathrm{FEC}} = \frac{\mathrm{Marker}}{f_{\mathrm{CKBC}}} + \mathrm{Overflow\ Counter} \times \frac{4096}{f_{\mathrm{CKBC}}} \,, \tag{2.6}$$

and the full hit timestamp being

$$t_{\mathrm{hit}} = t_{\mathrm{FEC}} + t_{\mathrm{chip}} \,, \tag{2.7}$$

where $t_{\mathrm{chip}}$ is the chip time from equation (2.4).

### 2.3.4 SRS PowerCrate 2k

With the hits being processed on the FEC and grouped in UDP frames, they are sent out via Ethernet to the DAQ computer. If multiple FECs are used, the clocks of the FECs have to be synchronised, which is done via the CTF card, which sends a common clock to all FECs used in the read-out system. For housing the FECs, the CTF card and to provide the power to them, as well as to the other components like the Hybrids via the DVMM, everything can be inserted into the SRS PowerCrate 2k (figure 2.17). In addition to the PowerCrate 2k, which can house two FECs[14] and one CTF, also the SRS EuroCrate exists, which can house up to eight FECs and one CTF. The PowerCrate contains also the mounting points for the strong ground return cables from the Hybrids. To group the data stream from the multi-FEC system, a network switch[15] is used. The UDP packages are then sent from the switch to the network card[16] of the DAQ computer.

### 2.3.5 Control, Read-Out and Monitoring Software

On the DAQ computer, the settings of the read-out system are controlled, and the SRS data are monitored and stored. In this section, the software components developed for VMM3a/SRS are presented, with the goal of describing, which component is

---

[14] Hence the name *2k*, as it supports up to 2048 VMM read-out channels.

[15] Netgear® GS110MX

[16] Intel® Ethernet Network Adapter X710-T2L

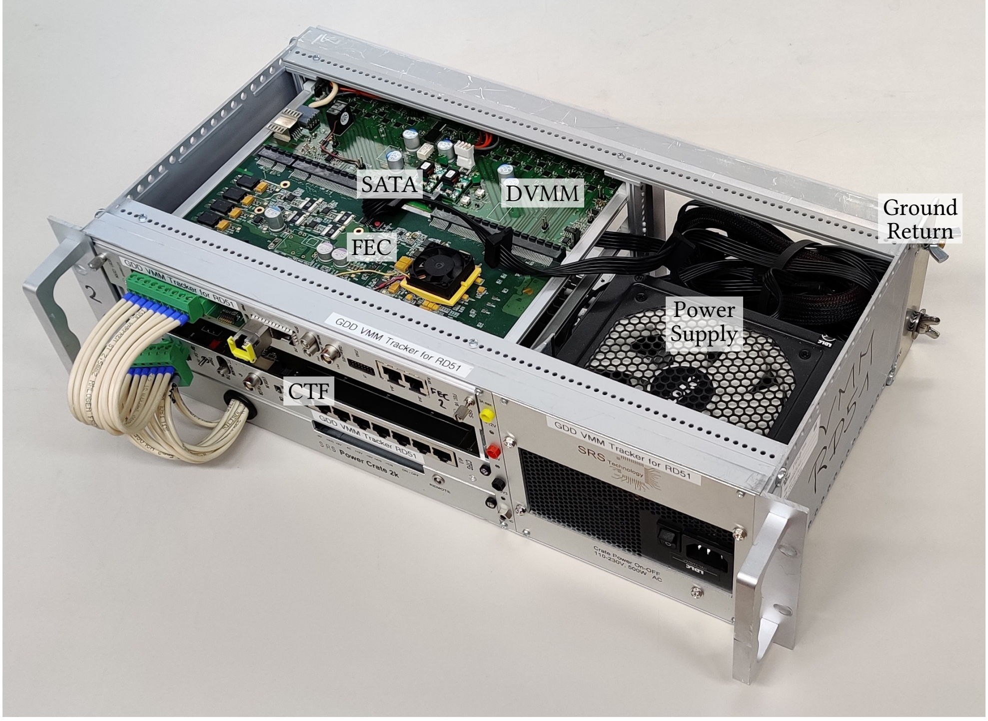

*Figure 2.17* – Photograph of an SRS PowerCrate 2k, equipped with a single FEC/DVMM combination and a CTF card. The ground return indicates the mounting points of the ground return lines from the Hybrids.

used for which purpose. For a detailed description of the software operation and installation, the reader is referred to the user guide [48] and the tutorial video [49] created in the scope of this thesis.

*vmmdcs:* the slow control software [50] is used to set the system parameters and define the chip settings, such as the number of FECs used, their IP addresses, the HDMI ports of the DVMM at which Hybrids are connected, the peaking time of the shaper, the channels which should be masked, etc. In addition, the slow control software contains the calibration module, with which the measurements to optimise the system response are performed (chapter 3).

*Wireshark plug-in:* Wireshark [51] is a network protocol analyser, allowing to monitor the network packages arriving at any network port of the DAQ computer. For the data arriving from the SRS, a plug-in exists to view the raw hit data from the FEC without any post-processing, giving direct access to e.g. the ADC values, the VMM-ID or the BCID.

*tcpdump:* to permanently store the SRS data, tcpdump [52] is used. It takes the UDP packages arriving at the DAQ computer and writes them directly into `.pcapng` files on the hard drive, again without any post-processing. This is an efficient method for high-rate acquisition, allows a later inspection of the data with Wireshark and preserves the raw data structure, as it is the data stream directly from the VMMs and the FEC, without any calibrations applied.

*ESS DAQ and Daquiri:* in addition to the very basic data monitoring via Wireshark, a more sophisticated online monitoring tool, called *Daquiri* [53] exists. Daquiri is founded on the *ESS DAQ* [54], which receives the UDP packages and performs an online reconstruction and analysis of the data, providing information such as the event rate, the particles position or its energy. This information is then visualised by Daquiri.

*vmm-sdat:* the last part of the software is the ***VMM3a/SRS*** ***D**ata* ***A**nalysis* ***T**ool* (vmm-sdat) [55]. Once the data have been acquired with tcpdump, vmm-sdat performs the offline cluster reconstruction (section 4.2.2) and applies the optimisation data. It reads the `.pcapng` files from tcpdump and creates a `.root` file, with the corresponding ROOT trees [56], giving access to the particle's interaction position in the detector, its arrival time and its energy. With this goal of extracting all the relevant information from the raw data and organising them per detector/read-out layer used in the experimental set-up, vmm-sdat can be seen as the most important interface between the data acquisition and the detector-based physics analysis.

Chapter 3

# SYSTEM CHARACTERISATION AND OPTIMISATION

When performing measurements and R&D work of any sort, it is important to understand the response of the entire experimental set-up. This means especially the detectors to be used and the read-out system. To find and understand possible peculiarities of the read-out system, it is important to read out detectors with a well-known behaviour. At the same time, especially to optimise and calibrate the electronics, well-defined test or calibration pulses are used, as it simplifies the experimental set-up and reduces the amount of possible error sources.

In the present chapter, the understanding and the optimisation of the performance from VMM3a/SRS are described. The calibration of the Digital-to-Analogue Converters, including the threshold calibration is presented at the start (section 3.1). It is followed by the calibration of the digitisation output, specifically the channel ADCs for the charge measurement (section 3.2) and the channel TDCs with the BCID for the time measurement (section 3.3). In both cases the calibration is used to correct the output. Afterwards, time resolution studies of the electronics using test pulses are presented (section 3.4). Subsequently, results of the electronics noise studies are shown (section 3.5). The chapter concludes with a short review on the rate-behaviour of VMM3a/SRS using test pulses (section 3.6).

It should be noted that the calibration procedures were subject to various optimisations over the scope of this thesis. While here the latest version of the calibration is presented, not all the measurements shown in this thesis contain the most optimised calibration results.

## 3.1 DAC CALIBRATION

Each VMM contains three kinds of Digital-to-Analogue Converters, two global 10-bit DACs and 64 local 5-bit DACs. While one global DAC serves as pulser DAC to set the voltage level that is sent to each channel's test capacitor to generate the internal test pulses, the other global DAC is used to set the discriminator level that is applied

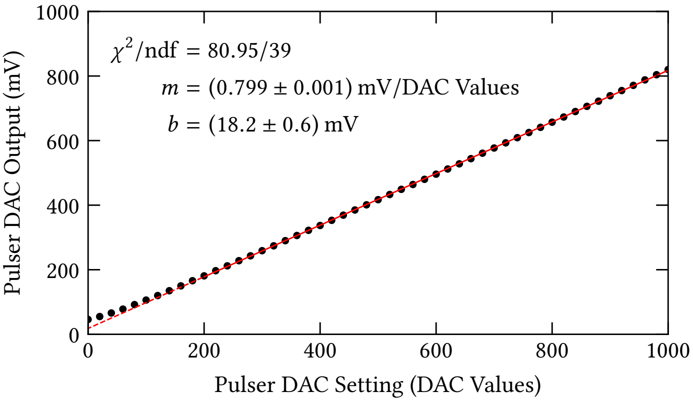

*(a)* – Pulser DAC calibration.

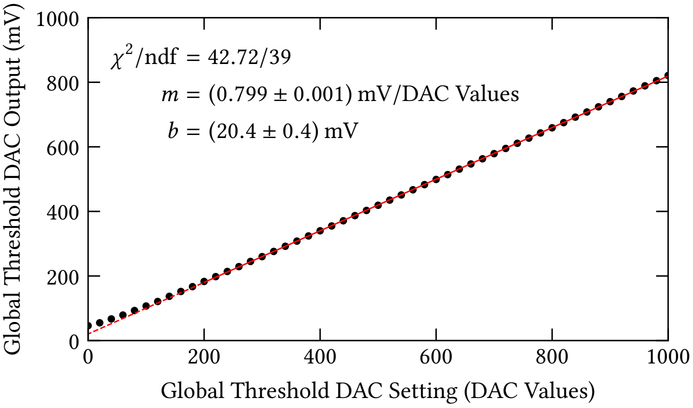

*(b)* – Global threshold DAC calibration.

*Figure 3.1* – Examples for the pulser and global threshold DAC calibration. The data points represent a single measurement without error bar. However, a repetition of the measurement did not show any variation, especially on the fit of the linear calibration function.

to all channels. The local DACs are individual to each channel and are used to trim/fine-tune the threshold level on each read-out channel.

The calibration of the global DACs relates the applied DAC value to a voltage that is measured on the analogue monitoring output of the VMM via the external ADC on the Hybrid. The measurement procedure is automatised in the slow control software, with one value being set, read back and then the next value being set and so on. Here, the examples of the 10-bit DAC calibration are shown for the internal test pulser (figure 3.1a) and the global chip threshold level (figure 3.1b). The data

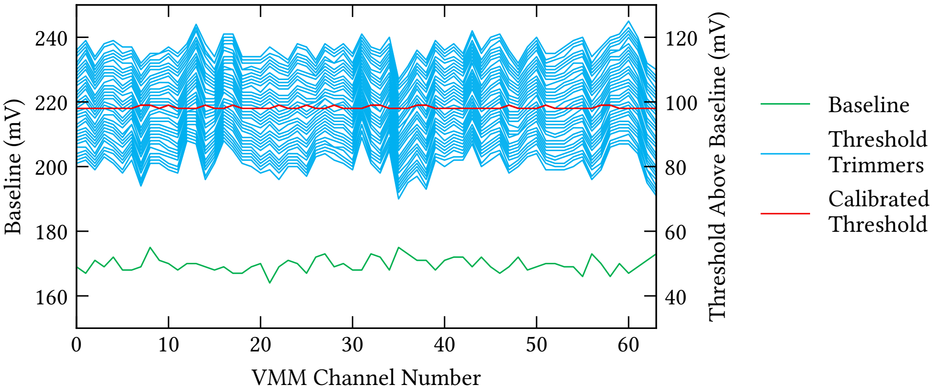

*Figure 3.2* – Illustration of the baseline fluctuations between the channels of a VMM3a, measured via the analogue monitoring output (left $y$-axis). In addition, the difference between the threshold and the baseline $\Delta U_i = U_{\mathrm{DAC},i} - U_{\mathrm{baseline},i}$ per channel $i$ is plotted for each of the 5-bit trimmer settings (right $y$-axis). Also, the result of the calibrated threshold per channel, meaning that each channel is triggered by the same amount of charge, with a flat $\Delta U_i$ response is shown.

are fitted with a linear calibration function $f(x) = mx + b$, starting with DAC values larger than 200. At lower values, the measured DAC output deviates from the linear behaviour. This is however of no concern as the threshold and the pulse height are measured from 0 mV, while the baseline of the VMM is around 170 mV. With this difference considered, the DACs behave linearly in the region of interest.

For the 5-bit threshold trimming DACs, the setting and the corresponding voltage are measured for each channel (figure 3.2). To fine-tune the threshold level and to minimise the threshold dispersion, the baseline of each channel is measured via the analogue monitoring output. With this, the distance between baseline and threshold level can be equalised, such that the read-out of each channel is triggered by the same amount of charge. For the equalisation itself, first, the global threshold DAC is calibrated. Afterwards any threshold level above baseline, e.g. 100 mV, can be selected on which the equalisation is performed. The 5-bit trimmers operate only in one direction, reducing the global THL per channel. Hence, the global THL DAC is calibrated such that the intended threshold level is approximately equally surrounded by the range of the trimmers, so e.g. around 115 mV. After having measured all the DAC values for each channel, the trimmer value that is closest to the desired THL is selected. As a result, the threshold distribution gets much narrower compared to the situation with the trimmer bits set to the maximum or minimum (figure 3.3). It should be noted though that this describes only the threshold setting and trimming. The threshold optimisation is discussed in the electronics noise part (section 3.5).

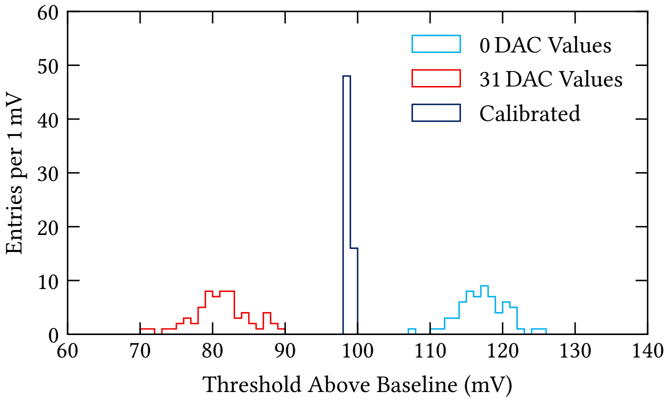

*Figure 3.3* – Illustration of the effect of the threshold trimming procedure. The channel-by-channel thresholds are histogrammed for the case with all trimmers at the maximum setting (0 DAC values), the minimum setting (31 DAC values) and for the case of the trimmed/calibrated thresholds. The reason why the largest DAC value corresponds to the minimum setting is that the trimmers only work in the negative direction, i.e. they reduce the global threshold level.

## 3.2 Charge ADC Calibration

The calibration of the charge ADCs relates the 10-bit ADC output to the input charge of each channel. Each VMM3a channel is equipped with a 0.3 pF test capacitor, with the optional flag to switch it to 3 pF. Using the pulser DAC, each capacitor can be charged up and then discharges into the preamplifier, leading to a calibration pulse. The calibration procedure starts by pulsing the VMM3a channels, making use of the previous pulser DAC calibration (section 3.1). Pulses with increasing pulse height and known voltage are injected into the test capacitor (figure 3.4). The test pulses are injected once every Offset, for a previously set amount of time[1]. For each channel $i$, the mean ADC value $\bar{A}_i$ is extracted from the ADC distribution per previously set pulser DAC height $U_{\mathrm{DAC}}$ (set per ASIC). The results are fitted by a linear calibration function (figure 3.5):

$$\bar{A}_i = m_{\mathrm{cal},\,i}\, U_{\mathrm{DAC}} + b_{\mathrm{cal},\,i} \ . \tag{3.1}$$

To then relate the ADC values to the input charge, the pulser DAC voltage could be e.g. multiplied by the test capacitance, which was found to vary by less than 10 % between channels [20].

---

[1] Typically data are acquired for 1 s per pulse height, which corresponds with a CKBC of 40 MHz to an Offset time (the time it takes for the BCID counter to overflow) of 102.4 µs and thus leads to about $10^4$ acquired pulses. This was considered to be sufficient in terms of statistics to extract a reasonably accurate mean ADC value.

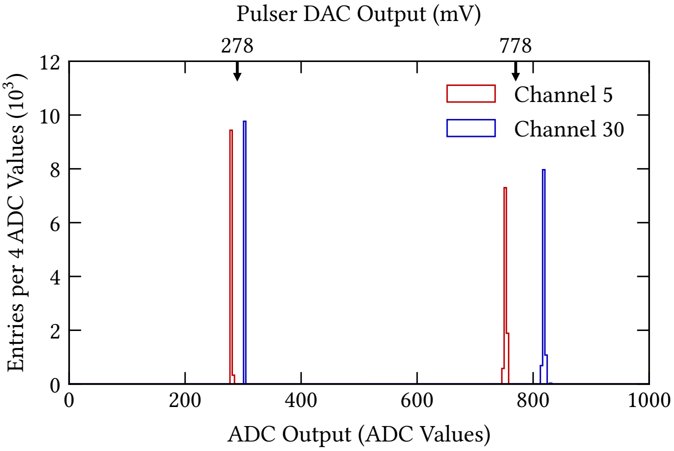

*Figure 3.4* – Exemplary ADC distributions for two read-out channels at two different pulse heights.

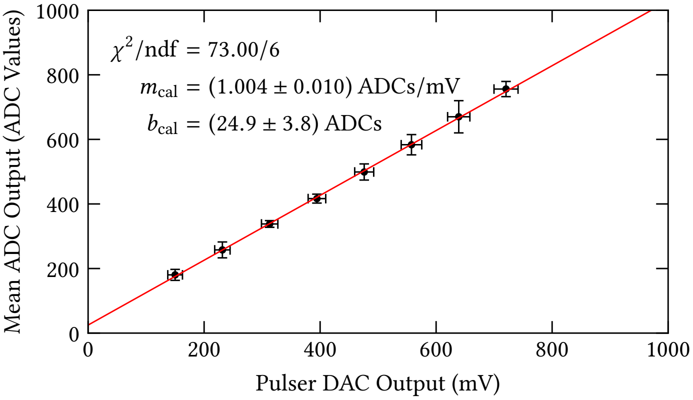

*Figure 3.5* – Example for a single channel calibration and its linear relation between the measured pulser DAC output and the measured charge ADC value. The error bars, which are enlarged by a factor of 20, originate from the DAC calibration fit error and the standard deviation of the ADC distribution.

This method has however not been applied as the main goal of the ADC calibration is to correct the VMM's ADC response behaviour. The charge ADCs exhibit a peculiarity, where for the same input charge the central channels of the VMM provide larger ADC output values than the outer ones, following an inverse-U shape (figure 3.6). The corrected ADC value $A_{\text{corr},\,i}$ is calculated from the measured ADC value $A_i$ via [55]

$$A_{\text{corr},\,i} = n_{\text{corr},\,i}\,(A_i - p_{\text{corr},\,i})\ . \tag{3.2}$$

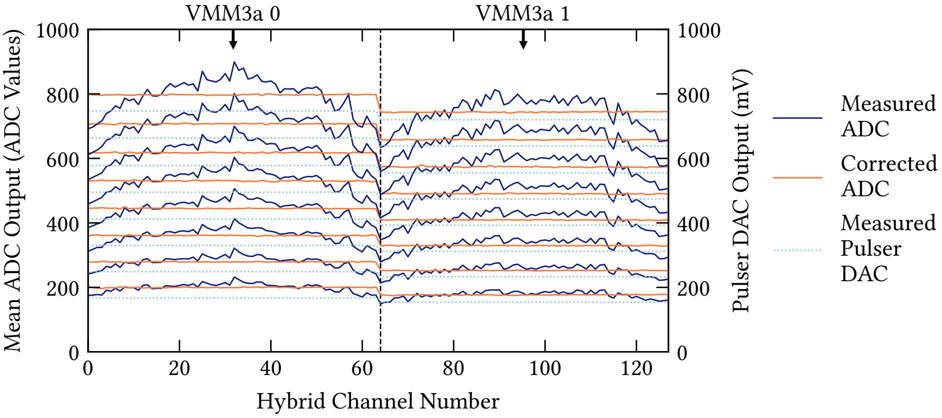

*Figure 3.6* – Example of the ADC response depending on the read-out channel. The case of the measured ADC values before the calibration and correction procedure is shown, as well as the case of the corrected ADC values. In addition, the measured height of the pulser DAC is indicated. In the given example, where a gain of 3 mV/fC was used, it almost coincides with the ADC response. At other detector gains, this is not the case.

To calculate the correction parameters $n_{\text{corr},\,i}$ and $p_{\text{corr},\,i}$, the mean calibration slope $\bar{m}_{\text{cal}}$ and offset $\bar{b}_{\text{cal}}$ are calculated from the channel slopes[2]. This is done for each VMM. The correction slope is then given by

$$n_{\text{corr},\,i} = \frac{\bar{m}_{\text{cal}}}{m_{\text{cal},\,i}} \,, \tag{3.3}$$

while the correction offset is given by

$$p_{\text{corr},\,i} = b_{\text{cal},\,i} - \bar{b}_{\text{cal}} \frac{m_{\text{cal},\,i}}{\bar{m}_{\text{cal}}} \,. \tag{3.4}$$

The fraction in equation (3.4) is a result of the definition of the correction formula in equation (3.2), to compensate for the multiplication of $p_{\text{corr},\,i}$ with $n_{\text{corr},\,i}$. Once the correction is applied for the measured ADC value on each channel, the ADC response gets uniform for a constant input charge (figure 3.6).

---

[2] The ADC response has to be corrected based on a reference. Due to the inverse U-shape of the ADC response per VMM channel number (figure 3.6), the true ADC value per input pulse height is not evident. One choice could be to use the maximum measured ADC per input pulse, but this is heavily affected by channel-by-channel fluctuations. Hence, it is assumed that the true ADC response is described by the mean calibration slope and offset for each VMM. This assumption allows to reduce the channel slopes $m_{\text{cal},\,i}$ that have a too steep slope (steeper than the mean slope) and to increase the slopes that are too flat.

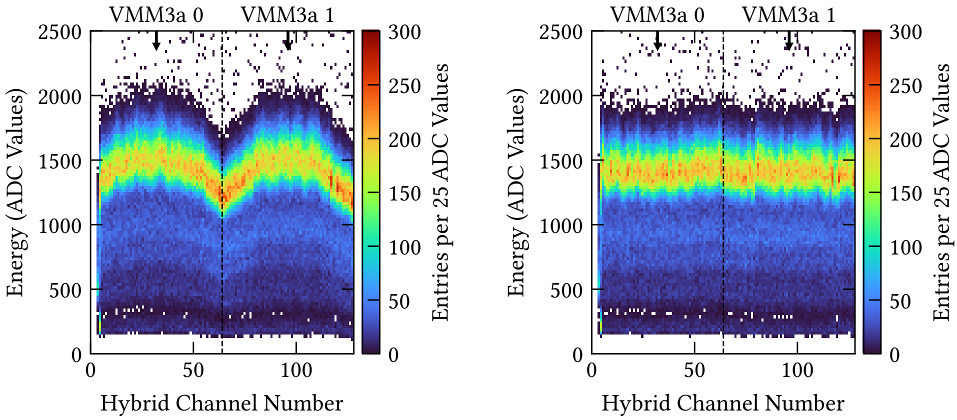

*(a)* – No correction applied.
*(b)* – With applied correction.

*Figure 3.7* – Examples the X-ray spectrum of an $^{55}$Fe radioactive source per read-out channel, without applied ADC correction (a) and with correction (b).

The effect can not only be illustrated with test pulses, but also with particle interactions recorded with a detector[3]. Here, the spectrum of an $^{55}$Fe radioactive source is plotted per detector read-out channel, without correction (figure 3.7a) and with the applied ADC correction (figure 3.7b). Knowing that the ADC correction flattens the response remarkably well (figure 3.6), only after the applied correction detector-related features in the acquired data, as visible around detector channel 150, become visible.

## 3.3 TDC and BCID Calibration

Similar to the ADC calibration, the goal of calibrating the TDC is not only to relate the 8-bit TDC output to a time in nanoseconds but mainly to perform the necessary corrections through a calibration procedure. Like the ADC, the TDC suffers also from channel-by-channel variations. Important to the timing is, however, that the TDC is intrinsically coupled to the BCID (figure 2.6), where the CKBC itself may have some slight shifts between individual channels. This requires calibrating and correcting the chip time, which is both quantities combined.

The calibration is performed with the internal calibration pulse[4], making use of the adjustable skew of the test pulse clock CKTP relative to the base clock. The skew

---

[3] To illustrate the calibration effect, no detailed detector description is needed. Nonetheless, it is referred to the experimental methods (chapter 4), where the detector and its response are described.

[4] Similar to the ADC calibration, also here the calibration pulses are sent once every Offset for a total time of typically 1 s.

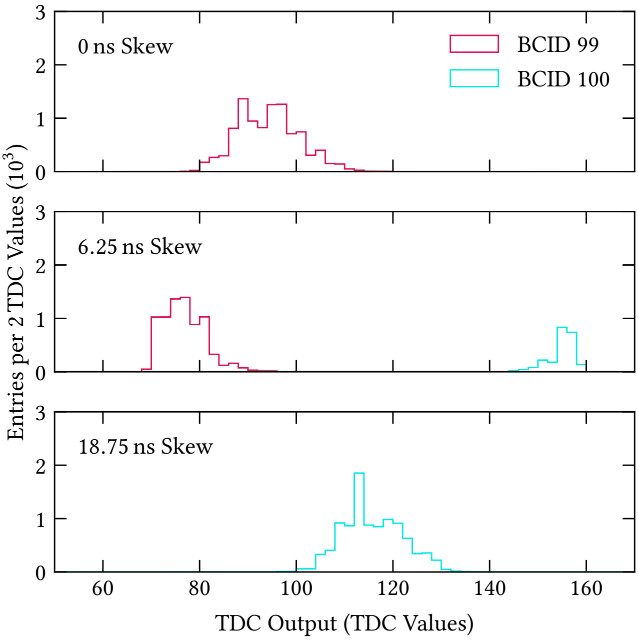

*Figure 3.8* – Example of the occurrence of a pulse (here an internal test pulse) at different BCID values, depending on the relative shift between pulse and CKBC. Despite the different TDC values, the pulses get the correct time assigned due to the corresponding different BCID values.

steps are $T_{\text{skew}} = 3.125\,\text{ns}$, which is defined by a 320 MHz clock of the Spartan-6 FPGA on the Hybrid [57]. This well-defined skew of the CKTP relative to the CKBC leads to different pulse arrival times and thus to different TDC and BCID outputs (as different pulse heights lead to different ADC outputs).

It is important to point out a peculiarity of the BCID/TDC combination, on which the calibration and correction procedure relies. Depending on the shift between any sort of analogue signal and the CKBC, it may happen that sometimes the signal is measured at a BCID of $B$ and sometimes at $B + 1$ (figure 3.8). However, the TDC behaves then accordingly, meaning a large TDC value is measured for the larger BCID[5] and a small TDC value for the smaller BCID, such that in the end the chip time, as defined in equation (2.4), remains the same. These occurrence-fluctuations of the pulses between different BCIDs allow to calculate the time, where 50 % of the pulses would occur at $B$ and the other 50 % at $B + 1$ (figure 3.9). The reason for this is that no reference time exists and hence this unique transition point is used as the

---

[5] The TDC output is subtracted from the BCID (section 2.1.3)

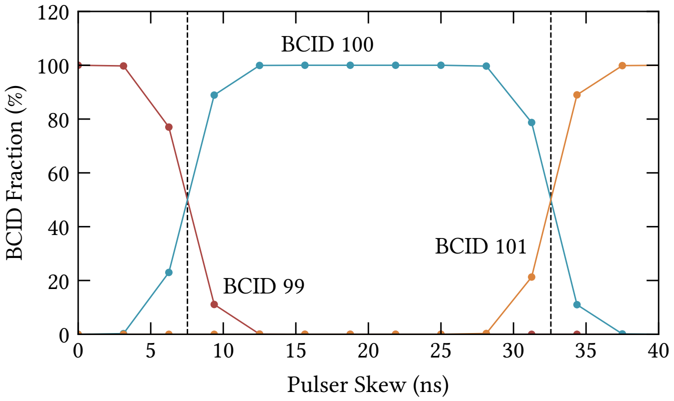

*Figure 3.9* – Illustration of the fraction of how many acquired hits contained a specific BCID depending on the skew of the test pulses.

reference time of the correction fit. The time of the 50 % transition is calculated via

$$t_{50} = t_{\text{skew}+1} + \frac{0.5 - k_{\text{skew}+1}}{k_{\text{skew}+1} - k_{\text{skew}}} \times T_{\text{skew}} \,, \tag{3.5}$$

where $t_{\text{skew}+1}$ is the skew time of the first test pulse skew after the 50 % transition, which in practice is the first skew where the fraction of BCID counts for the reference BCID $B + 1$ is larger than 50 %. The corresponding BCID fraction is given by $k_{\text{skew}+1}$. To find $t_{50}$, then the relative amount of $t_{\text{skew}+1}$ beyond the 50 % transition needs to be subtracted from $t_{\text{skew}+1}$, as $k_{\text{skew}+1}$ is larger than 50 %.

Having calculated the reference time of the 50 % transition, the data are shifted by this time, such that $t_{50} = 0\,\text{ns}$, with the time difference being $\Delta t_i = t_{\text{skew}} - t_{50}$. This leads to a linear correction fit (figure 3.10), which is given by

$$\tau_i = m_{\text{cal},\,i}\,\Delta t_i + b_{\text{cal},\,i} \,, \tag{3.6}$$

where $\tau_i = t_{\text{chip},\,i} - t_{B+1}$ is the mean measured chip time[6] per read-out channel $i$ minus $t_{B+1}$, the time of the reference BCID, and $m_{\text{cal},\,i}$ and $b_{\text{cal},\,i}$ are the calibration slope and offset, respectively. It is important to note, that the fit does not contain all data points within the reference BCID. The data points adjacent to the 50 % transition are excluded. Hence, in the given example (figure 3.9), the start and end points of the fit are the ones with a skew between 12.5 ns and 28.125 ns.

---

[6] The mean measured chip time is calculated via equation (2.4), but using the mean TDC from all acquired calibration pulses and the reference BCID as input parameters.

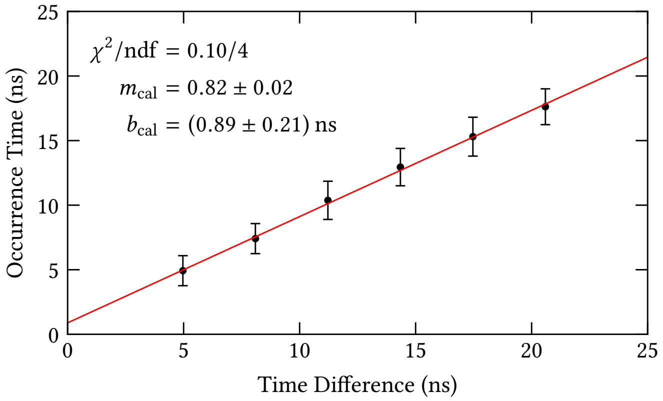

*Figure 3.10* – Example for a single channel calibration and its linear relation between the measured occurrence time of a signal hit and its supposed occurrence time, given as time difference to the reference time $t_{50}$. The error bars are not enlarged, but they represent the standard deviation of the occurrence time, which is close to the electronics' time resolution (section 3.4.1).

From the calibration fit, the correction of the time is calculated similarly to the correction of the ADC, via

$$\tau_{\mathrm{corr},\,i} = n_{\mathrm{corr},\,i}\left(\tau_i - p_{\mathrm{corr},\,i}\right)\,, \tag{3.7}$$

with the correction slope being

$$n_{\mathrm{corr},\,i} = \frac{1}{m_{\mathrm{cal},\,i}} \tag{3.8}$$

and the correction offset being

$$p_{\mathrm{corr},\,i} = b_{\mathrm{cal},\,i} - \Delta t'_i\, m_{\mathrm{cal},\,i}\,, \tag{3.9}$$

where $\Delta t'_i$ is the time difference between $t_{\mathrm{skew}} = 0\,\mathrm{ns}$ and $t_{50}$. Similar to the ADC correction, also the TDC/BCID correction leads to a flat and uniform time response of the read-out channels over the whole Hybrid (figure 3.11).

Similar to the ADC correction, also here the effect of the time calibration on the detector data is shown (figure 3.12). With the detector containing two layers of read-out electrodes (figure 4.4), with one measuring along the $x$-direction and the other one along the $y$-direction, it is possible to measure the time difference of the cluster signals[7] arriving on each layer. It can be seen that with the calibration the kink

---

[7] For the definition of a cluster it is referred to the cluster reconstruction (section 4.2.2).

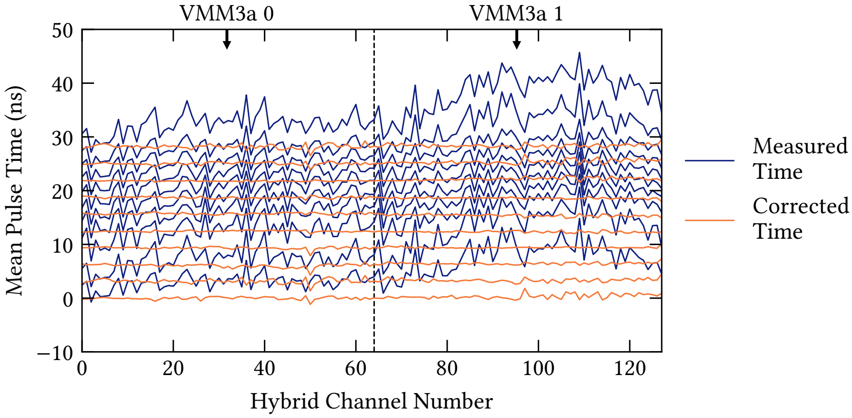

*Figure 3.11* – Example of the TDC/BCID response depending on the read-out channel before and after the applied time calibration and correction.

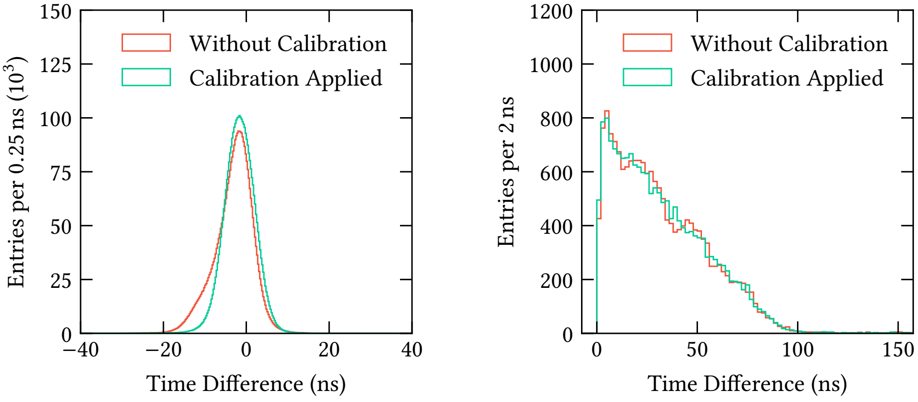

*(a)* – Time difference between $x$- and $y$-layer.

*(b)* – Consecutive interactions.

*Figure 3.12* – Examples of the effect of the time calibration on detector data, here generated with an $^{55}$Fe X-ray source, showing the time difference of the signal time in the detector's $x$-layer and $y$-layer (a) and the distribution of time differences between consecutively recorded X-ray interactions (b).

in the time difference distribution disappears (figure 3.12a). Another measurement to illustrate the effect of the time calibration is by calculating the time difference between consecutively recorded X-ray interactions. Without time correction, a wave structure with the periodicity of the CKBC can be observed in the distribution (figure 3.12b), while with the time correction applied, this structure disappears.

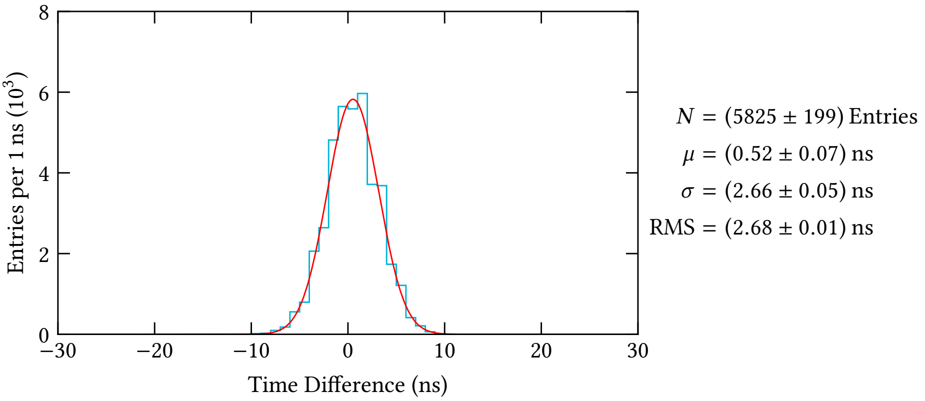

*Figure 3.13* – Example of the distribution of time differences between test pulses on two VMM read-out channels.

## 3.4 TIMING MEASUREMENTS

With its 60 ns TAC slope being sampled into 8-bit (even though effectively just 6.5-bit [11]), the VMM3a provides an excellent theoretical time resolution of around 500 ps. To confirm this number and investigate if it changes depending on other parameters, time resolution studies on the electronics using test pulses have been performed (section 3.4.1). From this point it is continued with understanding the VMM3a's timing behaviour in terms of time walk (section 3.4.2). As last part, the timing-at-threshold of the VMM3a is discussed (section 3.4.3).

### *3.4.1 Time Resolution*

The electronics time resolution $\sigma_{\text{time}}$ is expressed as differential time resolution, as defined in [58]. Two channels are pulsed with the internal test pulser and the time difference $\Delta t = t_2 - t_1$ between the two channels is calculated. The width $\sigma_t$ of the resulting distribution (figure 3.13) gives access to the time resolution. In case the time resolution of the channels is assumed to be the same, the final time resolution is given by [58]

$$\sigma_{\text{time}} = \frac{\sigma_t}{\sqrt{2}} \, . \tag{3.10}$$

This measurement was performed for different electronic gains and peaking times (figure 3.14) while investigating the amplitude dependence. It can be seen that the time resolutions for shorter peaking times, so for a peak which is easier to find,

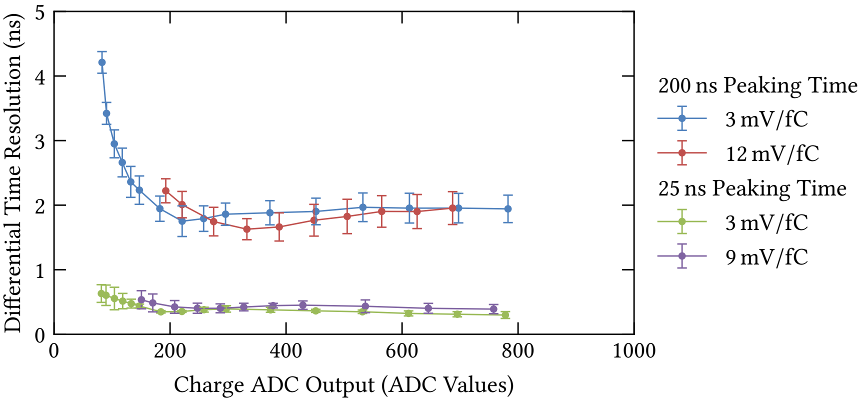

*Figure 3.14* – Illustration of the charge dependence of the differential time resolution as defined in equation (3.10). The time resolutions in the given examples are shown for two peaking time values of 200 ns and 25 ns, as well as for three different electronics gain levels of 3 mV/fC, 9 mV/fC and 12 mV/fC. The error bars on the time resolution are enlarged by a factor of 5, while the error bars on the ADC output are not plotted as the fluctuations are smaller than 2 ADC Values for each data point.

are better than the ones for longer peaking times. And while a charge dependence can be observed with lower time resolutions at smaller ADC values, the results are compatible for different electronic gains. In general, it should be noted that the measurements presented here are compatible with the measurements presented in the VMM3a reference [11]. A possible explanation for the observed behaviour is the use of timing-at-peak. In the case of 25 ns peaking time, the peak is well defined and less affected by signal fluctuations. Hence the time of the peak can be precisely determined and the time resolution is better than for 200 ns, where the peak is less pronounced and hence the peak finder is more sensitive to signal fluctuations.

### *3.4.2 Time Walk*

It was noticed that the time of the found peak shows an amplitude-dependent behaviour, meaning that the higher the amplitude of the signal, the lower the digitised timestamp with respect to the reference clock. This is illustrated by plotting the time difference $\Delta\tau = \tau_{\text{corr}} - t_{\text{B+1}}$ between the calibrated chip time $\tau_{\text{corr}}$ and the reference BCID $t_{\text{B+1}}$ (figure 3.15). This behaviour is more pronounced for larger peaking times (figure 3.15a) than for shorter ones (figure 3.15b). Similar to the time resolution results, also these results are compatible with the measurements presented in the VMM3a reference [11]. For the measurement itself, again the internal test pulser was used with different pulser DAC settings. From the output, the mean ADC and chip time values were extracted, with the corresponding corrections applied.

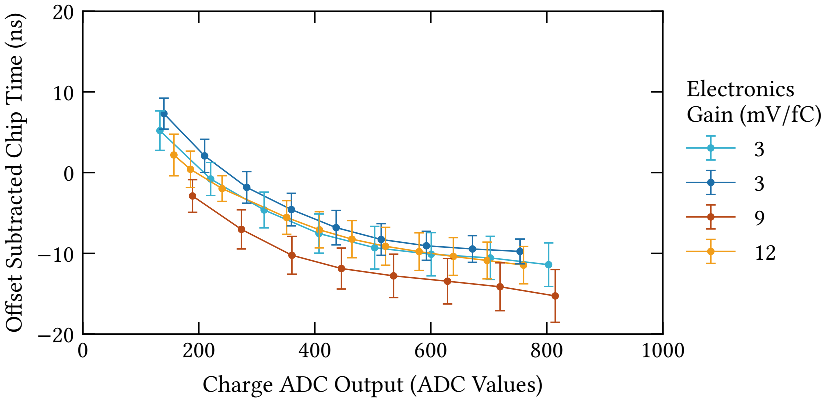

*(a)* – Time walk with 200 ns peaking time.

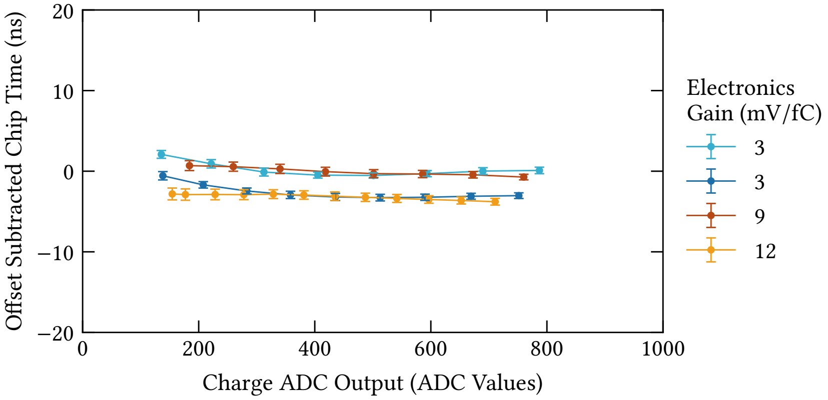

*(b)* – Time walk with 25 ns peaking time.

*Figure 3.15* – Examples of the time walk for different peaking times and electronics gains. The chip time of the pulse, as defined in equation (2.4) with the correction defined in equation (3.7) applied, is plotted against the pulse's amplitude. The chip time of the reference BCID (section 3.3) is subtracted as an offset. The error bars on the chip time reflect its standard deviation, so effectively the time resolution. The error bars on the ADC output are not plotted as the fluctuations are smaller than 2.5 ADC Values for each data point.

While the time walk does not affect the differential time resolution measurement, it does affect the general time response of the entire ASIC. Hence, a correction procedure exists, which works as follows. First, the time walk relation (figure 3.15) is measured for each individual read-out channel, with the corresponding ADC and TDC/BCID corrections applied. With the data recorded, the chip times $\tau_{\mathrm{corr},i}$ are

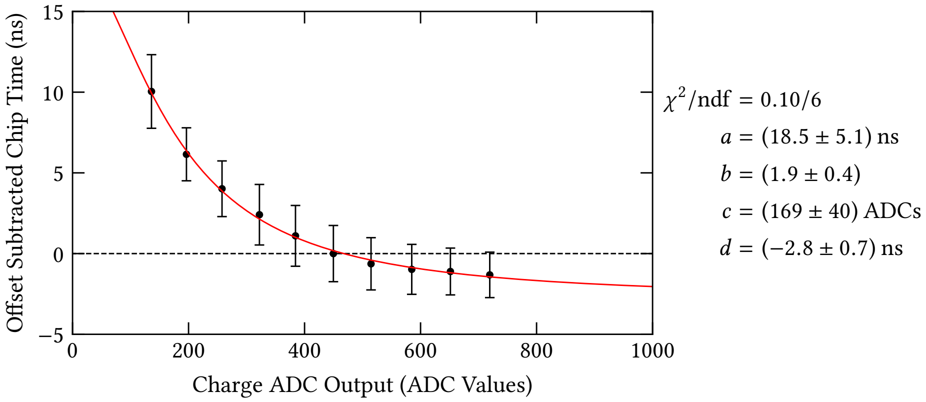

*Figure 3.16* – Example of the time walk correction fit, with the shifted corrected chip time $\tilde{\tau}_{\mathrm{corr},\,i}$ plotted against the corrected ADC output $A_{\mathrm{corr},\,i}$.

shifted per channel $i$, with the time at the central pulse height $A'_{\mathrm{corr},\,i}$ (the sixth from ten data points, at around 450 ADC Values) considered as reference (figure 3.16), such that

$$\Delta\tau_{\mathrm{corr},\,i}(A_{\mathrm{corr},\,i}) = \tau_{\mathrm{corr},\,i}(A_{\mathrm{corr},\,i}) - \tau_{\mathrm{corr},\,i}(A'_{\mathrm{corr},\,i}) \;. \tag{3.11}$$

Fitted to the data is a 4-parameter logistic function, which can be expressed as in [59]:

$$\Delta\tau(A) = d + \frac{a-d}{1+\left(\dfrac{A}{c}\right)^{b}} \;. \tag{3.12}$$

For the purpose of the time walk correction, it serves as a surrogate function that describes the data reasonably well, while at the same time providing a stable fit[8]. With equation (3.11) giving access to the time difference between the reference chip time and the amplitude-dependent chip time, the correction to the measured chip time is then applied via

$$\tilde{\tau}_{\mathrm{corr},\,i}(A_{\mathrm{corr},\,i}) = \tau_{\mathrm{corr},\,i}(A_{\mathrm{corr},\,i}) - \Delta\tau(A_{\mathrm{corr},\,i}) \;, \tag{3.13}$$

shifting the measured time towards the reference time (figure 3.17).

---

[8] Also other potential models, like a polynomial function or a Gaussian error function were tested, with the issue that sometimes the fit did not converge with the given start parameters, especially with the Gaussian error function. In the case of the 4-parameter logistic function this issue did not occur.

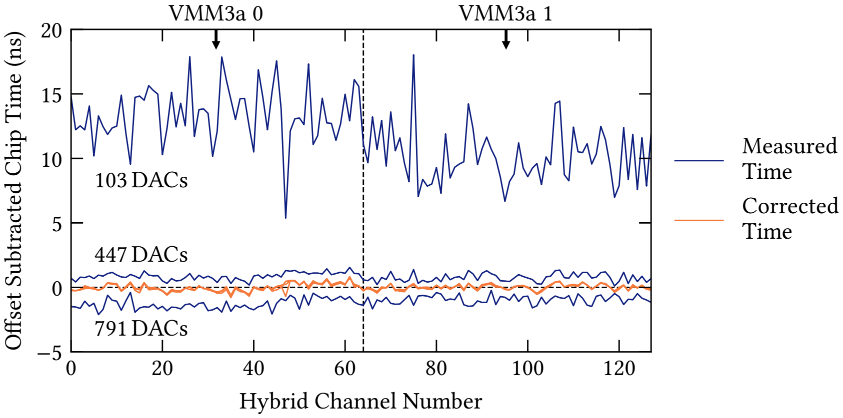

*Figure 3.17* – Example of the time walk depending on the read-out channel before and after the applied correction for different pulser DAC values.

### *3.4.3 Timing-at-Threshold*

With all measurements so far being performed with timing-at-peak, the last part of the timing measurements focuses on the timing-at-threshold. During one of the measurement campaigns at the test beam (section 4.3), it was first observed by colleagues reading out straw tube detectors with VMM3a/SRS [60–62], that the timing-at-threshold mode does not work as intended. Over time, more and more hits seem to be lost when the VMM is operated in the timing-at-threshold mode, while when using timing-at-peak all hits are recorded. The observations were later verified with measurements in the laboratory (figure 3.18) Afterwards, it was confirmed by the chip designers that the timing-at-threshold does not perform as planned [11].

What happens is the following. In timing-at-threshold mode, the TAC stop signal (figure 2.5) has to occur within a time window defined by the threshold crossing and the time of the peak. If this is not the case, the signal processing cannot be completed and the channel locks. However, the channel will also lock when the TAC slope goes into saturation before the peak is reached. This is, in particular, the case for small signals that just barely cross the THL or the case for short TAC slopes at long peaking times [57, 63]. A workaround to reset the channels exists, meaning however that the signal on this channel is lost [11]. It was also found that the neighbouring-logic does not work together with timing-at-threshold. The reason for this is that due to the timing logic needed for timing-at-threshold, the stop signal of the TAC slope is not sent when the shaper output does not cross the threshold level [57, 63].

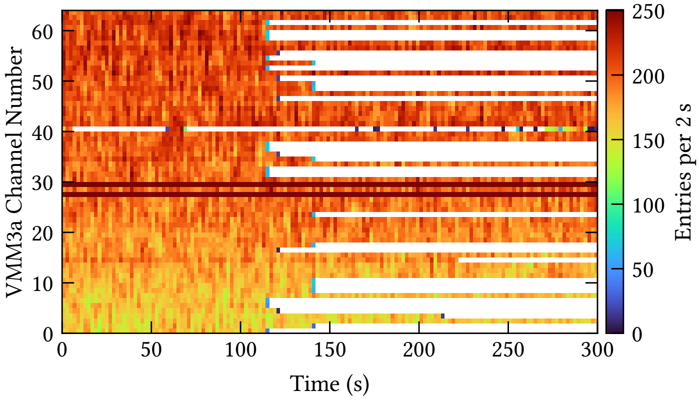

*Figure 3.18* – Illustration of the problem with timing-at-threshold in case of the VMM3a. For each VMM3a read-out channel, the number of hits is plotted depending on the run time. The measurement was performed with the laboratory set-up using an $^{55}$Fe radioactive X-ray source (chapter 4).

## 3.5 Electronics Noise and Threshold Level

Another aspect of the system characterisation is the understanding of electronic noise. The noise can originate from different sources [26], causing fluctuations in the signal amplitude and the baseline width. There are e.g. internal noise sources, such as thermal noise, shot noise or $1/f$ noise, which affect especially the detector signals and the analogue part of the read-out chain. Thermal noise means that the electrons follow a Brownian motion in the conductors of the read-out scheme, creating fluctuating voltage drops over resistors [26]. Shot noise is caused by the fact that the signal is generated by discrete charge carriers, with the arrival of the electrons being random and hence causing number fluctuations in a specific time interval [33]. $1/f$ noise comprises other frequency-dependent noise sources, where the noise amplitude increases with lower frequencies $f$ but where the origin is not necessarily known [33]. There are also external noise sources, specifically pickup noise where external periodic electric signals are picked up by the detector and/or the front-end electronics [26].

To quantify the noise, the ***E****quivalent* ***N****oise* ***C****harge* (ENC) is used, which relates the signal fluctuations on the shaper output due to noise to a charge that would be necessary to cause these fluctuations. With the shaper behind the preamplifier, the noise's impact can be partially reduced by optimising the shaping time $\tau$ with respect to the detector capacitance $C_{\text{det}}$ via [26]

$$\text{ENC} = k_{\text{shot}}\tau + k_{1/\text{f}}C_{\text{det}}^2 + k_{\text{therm}}\frac{C_{\text{det}}^2}{\tau} , \qquad (3.14)$$

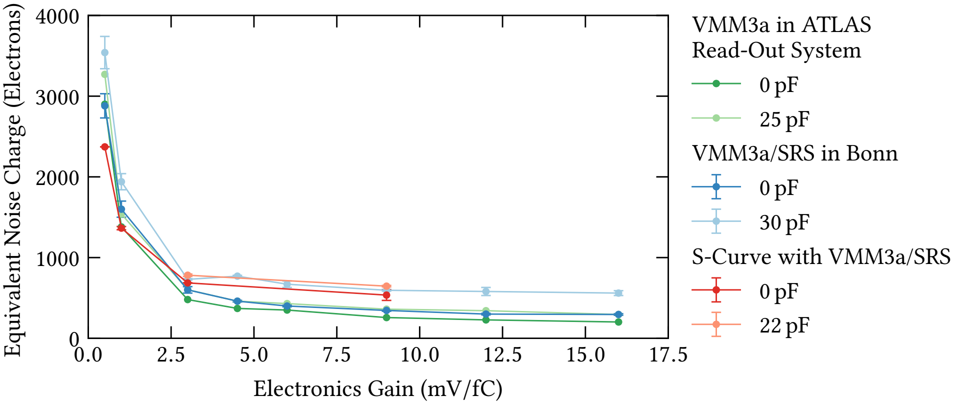

*Figure 3.19* – Dependence of the equivalent noise charge on the electronics gain measured for the VMM3a with different read-out and measurement methods, as well as for different detector capacitances. The data for the ATLAS read-out system are taken from [11], where no uncertainties are presented. The data for VMM3a/SRS from the colleagues from Bonn University are taken from [20]. The measurements for the S-curve at 22 pF were performed with the Hybrid connected to a test detector (chapter 4) and the VMMs operated at the mainly used electronics gains. All measurements have been performed with 200 ns peaking time.

where $k_i$ are the individual constants for the different noise contributions. This leads to an optimal shaping time of [26]

$$\tau_{\text{opt}} = \sqrt{\frac{k_{\text{therm}}}{k_{\text{shot}}} C_{\text{det}}^2} \, . \tag{3.15}$$

In addition, it is possible to reduce the impact of external noise sources e.g. by optimising the grounding scheme of the electronics or shielding the electronics [42]. Once the behaviour and the amplitude of the noise are known, this can be used to set the threshold level of the electronics.

### *3.5.1 Electronics Noise Measurements*

In the case of the VMM, extensive studies have been performed on the electronics noise by the chip designers and by colleagues, with results presented e.g. in [11, 20]. There, the dependence of the noise on the electronic gain (figure 3.19), the dependence of the noise on the detector capacitance including capacitances significantly larger than the ones of the typical test detectors, as well as e.g. the effect of the peaking time on the noise [20] are shown. In these studies, the noise was measured using the analogue monitoring output of the VMM and sampling the waveform e.g. with an

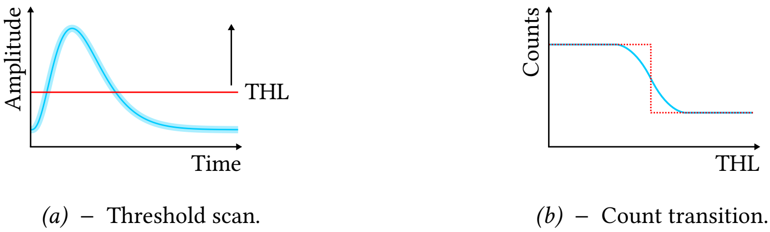

*(a)* – Threshold scan. *(b)* – Count transition.

*Figure 3.20* – Illustration of the working principle of the S-curve method, where the analogue pulse is scanned with the threshold level. Due to the electronic noise, the signal fluctuations can be pictured as an envelope around the actual pulse (a). This noise envelope leads to a broadening of the step-like transition (b). Adapted from Hans Muller [42].

oscilloscope. It can be e.g. seen that the noise decreases with increasing electronic gain. It should be noted that in the case of the colleagues from Bonn University VMM3a/SRS was used, while in the case of the chip designers the read-out system of the VMM3a for the ATLAS NSW was used [64].

In addition to these studies, which rely on the analogue monitoring output and external devices, a method was proposed in the scope of this thesis, using only the read-out system itself. Due to the analogue part of the VMM3a, the ASIC should be able to give access to the noise level by itself. The goal is however not to compete with the other measurement types, but to provide a simple method, which allows to estimate the noise level under working conditions, i.e. during the detector operation, and to support the noise optimisation process. For this, the S-curve method [26] is used[9] (figure 3.20), where internal test pulses of constant height are injected into the read-out channels while increasing the threshold level. Ideally, at the last threshold step before the pulse height, all pulses would still surpass the threshold level and at the first threshold step larger than the pulse height, no pulse would be recorded anymore. However, due to the electronic noise, the output height of the preamplifier is broadened, leading to an S-curve (figure 3.21). To extract the noise from the data points, a fit of the complementary error function should be used [26]:

$$N(\vartheta) = \frac{N_{\mathrm{max}}}{2}\,\mathrm{erfc}\left(\frac{\vartheta - \vartheta_{50}}{\sqrt{2}\sigma_{\mathrm{noise}}}\right) . \tag{3.16}$$

Here, $N_{\mathrm{max}}$ is the maximum number of pulse counts per threshold level $\vartheta$, the threshold level $\vartheta_{50}$ that is surpassed by 50 % of the pulses[10] and the width $\sigma_{\mathrm{noise}}$

---

[9] With the analogue capabilities of the VMM3a, in theory the fluctuations of any injected signal should be sufficient to estimate the noise. However, due to the value aggregation in the charge ADC leading to an equivalent number of bits of 8-bit, this option had to be discarded.

[10] It is effectively the mean of the error function.

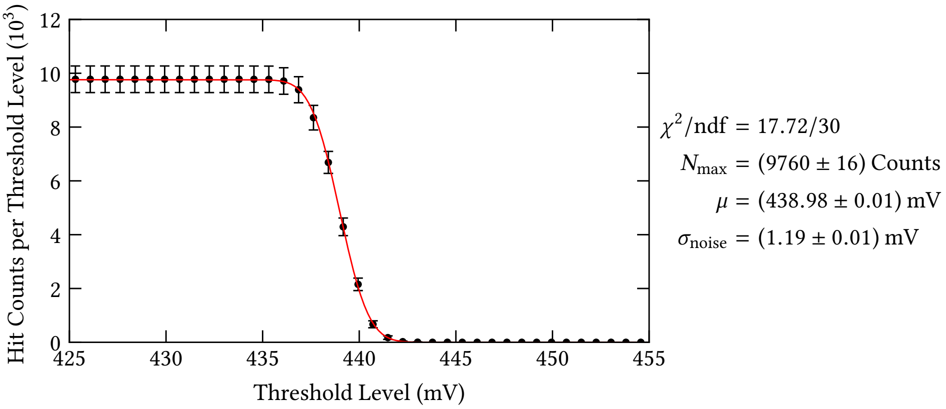

*Figure 3.21* – Example of the S-curve behaviour of the threshold scan over the internal test pulse, with the hybrid connected to one of tracking detectors in the test beam set-up (section 4.3). The measurement was performed with 200 ns peaking time at an electronics gain of 9 mV/fC.

giving direct access to the equivalent noise charge, using the electronics gain $G_{\text{el}}$ of the VMM3a via

$$\text{ENC} = 6242 \frac{\sigma_{\text{noise}}}{G_{\text{el}}} , \tag{3.17}$$

with 6242 being the number of electrons per 1 fC [25]. It can be seen that the results of the S-curve method are on average compatible with the other results (figure 3.19). At low gains ($\leq$ 1.0 mV/fC), the results yield slightly lower ENC values, which is likely to be caused by the roughness of the threshold step size of around 0.8 mV, meaning that in these discrete steps, the transition is almost step-like. As a result, the S-curve would underestimate the width of the transition.

With the goal of using the S-curve method to understand the noise level inside the experimental set-up, this was measured as well (figure 3.22). It allows not only to estimate the noise level but also to indicate the reproducibility of this method. In this particular case for example no effect is observed which could be caused by the ***High Voltage*** (HV), likely because of the HV filters that are used. What can be observed though are the fluctuations between the channels and the different ASICs, which are however compatible with the other measurements [20], where the fluctuations are of similar size. Another observation that can be made is that in the case of the shown VMMs number 0 and 10 (figure 3.22) the noise seems to increase towards larger channel numbers, while in the case of VMM 9 the noise seems to decrease. The same trend can be also observed in the data presented in [20], where the Hybrid was not connected to a detector, thus excluding a detector effect as a possible explanation.

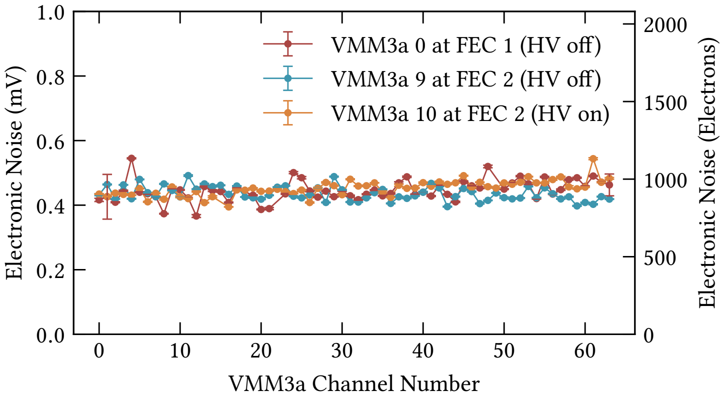

*Figure 3.22* – Illustration of the noise behaviour depending on the read-out channel for different VMMs in the test beam set-up (section 4.3), also with the ***High** Voltage* (HV) kept off or turned on. The measurements were performed with 200 ns peaking time at an electronics gain of 3 mV/fC.

While so far no explanation could be found, the behaviour was still accepted as within the general fluctuations the data are compatible with each other.

Despite these results and the implementation of the S-curve method in the control software [50], also the issues of the S-curve in VMM3a/SRS should be mentioned. The main issue is the method's stability, contradicting the original motivation. It happened rather frequently that the threshold scan over the pulse gets stuck at a certain point during the scan and hence does not finish. The longer the scan lasts, meaning the more threshold levels are set or data points are acquired, the more likely this is to happen[11]. So far, the issue could not be resolved, with the suspicion of its origin being the constant change of the system's configuration due to the increasing THL in combination with the fact that the data acquisition is turned on and off again in short time intervals over a longer duration. Another issue of the S-curve is its lack of sensitivity to external pickup noise. As the S-curve measurement is triggered by the internal test pulse with a fixed frequency, it is unlikely that pickup signals with different frequencies coincide with the test pulses.

### *3.5.2 Threshold Optimisation*

Despite the issues with the S-curve and its lack of sensitivity on external signals coupling into the detector, VMM3a/SRS still can be used by itself to optimise the

---

[11] The system got stuck in around one out of ten runs in case 20 data points needed to be acquired, while in case of 200 data points that needed to be acquired the system got stuck at least every second run.

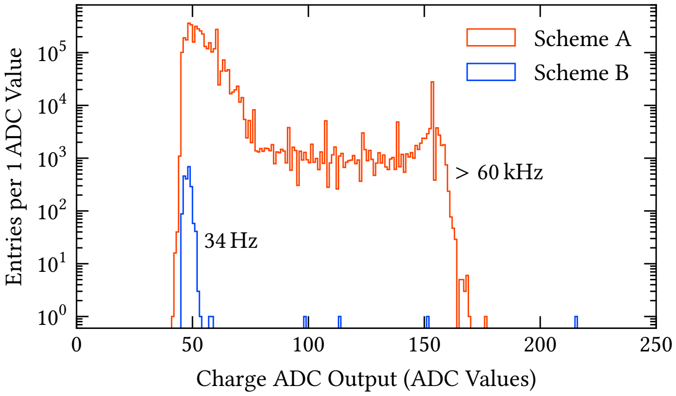

*Figure 3.23* – Illustration of the different number of acquired noise hits within 60 s acquisition time.

threshold level. This is illustrated in the following example. For the test beam measurements (section 4.3) it is essential to operate at as low thresholds as possible, due to the low number of primary ionisation electrons released by MIPs. Otherwise, charge information will be lost and the detection process becomes inefficient. However, in the case of the VMM3a front-end of the SRS, with its self-triggered continuous read-out, every signal above the threshold level will be processed and stored in the data stream. So even in case the noise level from the internal sources is low, external signals coupling into the detector or electronics can drive the need to operate the system at high threshold levels, depending on their frequency.

To reduce the effect of noise, good grounding and shielding of the entire experimental set-up are essential [42]. This requires a systematic approach of adding the components step-by-step to the set-up, measuring and understanding the noise level after each step and testing possible ways to reduce it. For the test beam set-up this procedure was pursued, where various elements to reduce the impact of external signals being picked up were introduced. The two main components in the case of this specific set-up were the introduction of a strong common ground reference (figure 4.10) and the additional grounding of the MPGD connector adapter to the detector ground (figure 2.8b).

For the measurement process itself, VMM3a/SRS was used. First, the threshold level on a read-out channel was set to a potentially low value, here 5 mV above the baseline. This corresponds to around 0.5 fC or around 3000 electrons at an electronics gain of 9 mV/fC, at which this measurement was performed. Then all the signals processed by the read-out channel were acquired for 60 s. The effect of the improved grounding can be clearly seen in terms of acquired noise hits (figure 3.23). In scheme A, a COMPASS-like triple-GEM detector (section 4.1) was equipped with four Hybrids, which were connected to the ground return of the SRS PowerCrate 2k (figure 2.17), with the crate itself being connected to the common ground. Nothing else, also no high voltage, was connected to the detector. For scheme B, where the high voltage power supply was connected to the and also powering the detector electrodes, the connection to the common ground of the detector was improved, but especially it contained an improved ground connection of the MPGD connector adapters to the detector. It should be noted that if the noise hit rate of 60 kHz, which was observed on a single read-out channel in scheme A, would be extrapolated to all read-out channels of a single ASIC, this would fill half of the available bandwidth of the read-out scheme of this ASIC. In the case of scheme A, another observation can be made, which is the peak at noise amplitudes of around 150 ADC Values. This is exactly due to an external signal being picked up, which was also observed with an oscilloscope connected to the analogue output of the VMM. In general, the oscilloscope was however not connected during the optimisation procedure, as this could affect again the grounding scheme which is supposed to be optimised for the measurement without an oscilloscope.

As a result of this optimisation procedure, the following can be concluded. Even though noise and threshold level are still connected to each other, the driving force for setting the threshold level in a self-triggered read-out system, like VMM3a/SRS, is not anymore purely the noise amplitude, but also the question of how much noise hits are accepted in the data stream by the user.

## 3.6 Rate-Capability with Test Pulses

One of the key features of the VMM is its high rate-capability. Hence, extensive studies on exploring the rate-capability and identifying possible limitations in the read-out chain have been performed within the scope of this thesis, both with well-defined test pulses as well as with X-rays and MIPs. While the measurements using particle interactions are presented later (section 5.1), for the test pulse measurements it is referred to [65]. The reason why the measurements with test pulses performed within the scope of this thesis are not presented in detail here is the fact that they have been performed with an outdated firmware version, which is not in use anymore. In fact, during the studies presented in [65], it was discovered that the main limitation of the outdated firmware was the way the data are read out from the VMM3a. This was confirmed by Patrick Schwäbig [47] who significantly modified and improved the Hybrid firmware, which is now known as *Bonn Firmware* (section 2.3.1). Hence, for the sake of completeness, some of the results from [47] are recalled in the following to illustrate the rate-behaviour of VMM3a/SRS with test pulses.

At first, it should be mentioned that if the data transmission clock of the VMM3a is operated at the initial design value of 200 MHz [12] and in dual edge transmission, the data transfers become corrupted, meaning that some bits in the 38-bit long hits are

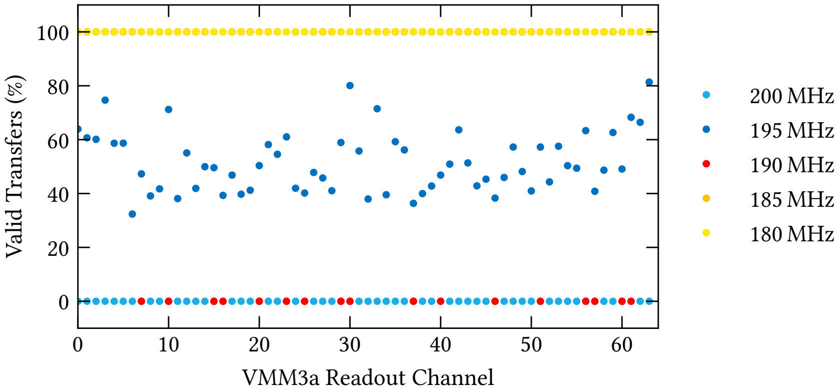

*Figure 3.24* – Percentage of good data transfers for different values of CKDT in dual edge transmission. The behaviour is shown only for one VMM3a as an example, with the behaviour being reproduced also for other VMMs. Adapted from [47]. Data kindly provided by Patrick Schwäbig.

not correctly transferred (figure 3.24). Without dual edge transmission also a CKDT of 200 MHz works. The maximum possible frequency without data corruption in dual edge transmission is 180 MHz [47], which is the one used in the *Bonn firmware*.

Secondly, it should be mentioned that until the bandwidth limit due to the token passing is reached, the measured output rate follows linearly the input rate in a one-to-one relation (figure 3.25). However, as it can be seen in the given example with five active channels, the maximum achievable rate is below the expected limit of 8 Mhits/s from the CKTK. This is due to the token passing, as it was observed on another occasion (figure 3.26). There, the maximum rate where the received hit rate saturates is plotted against the number of active read-out channels. As it can be seen, the received hit rate gets larger with increasing numbers of active channels, with the theoretical maximum in the asymptotic limit. This is due to the fact that in the token read-out scheme of the VMM3a, after having looped over all read-out channels, a reset token is needed to restart the loop [47]. So the fewer channels have to be read out, the more reset tokens are sent, limiting slightly the rate-capability.

Something else should be noted for the presented results. Even when considering the mentioned effect of the reset token, this does not explain why the expected limit of 8 Mhits/s is not reached. The reason for this is that at the time of the measurements shown in [47], the FEC firmware still contained a so-called *acquisition window*, meaning that only in a specified BCID window the hits were actually acquired. Here, the window was 3700 BCID values, so the theoretical limit is 8 Mhits/s × 3700/4095 = 7.2 Mhits/s. This acquisition window was later removed by Dorothea Pfeiffer for ESS and replaced by the latency logic [41] (section 2.3.3), allowing the acquisition of data over the full BCID cycle.

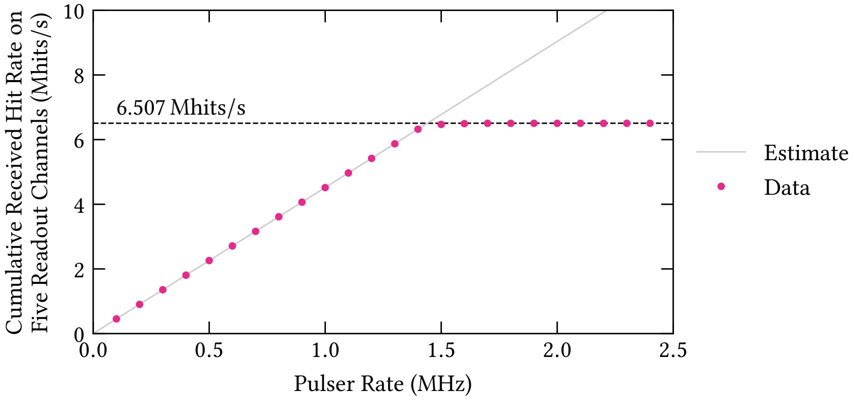

*Figure 3.25* – Hit rate measured on the DAQ computer compared to the input rate applied with an external pulse generator. Here, five read-out channels have been pulsed at the same time. The estimated rate increase is not a fit but corresponds to the assumption that all data on each channel can be read out. The dashed line indicates the saturation of the hit rate due to the limits in the read-out scheme. Adapted from [47]. Data kindly provided by Patrick Schwäbig.

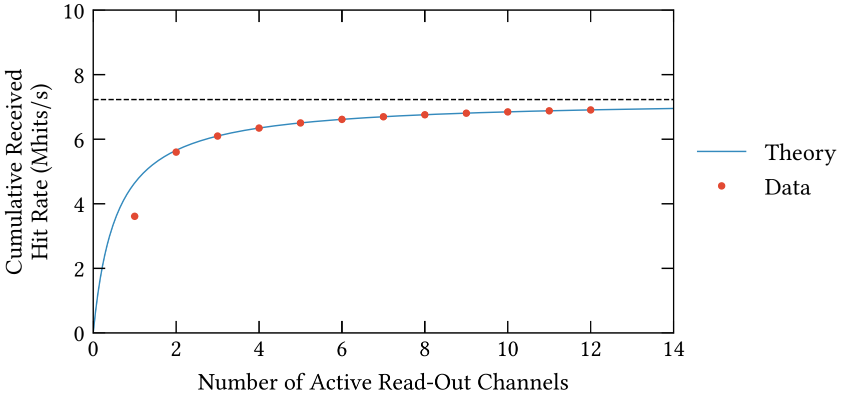

*Figure 3.26* – Dependence of the measured hit rate on the number of active read-out channels per VMM. The formula for the theoretical prediction is given in [47]. The dashed line indicates the saturation of the hit rate due to the limits in the read-out scheme. The reason for the deviation between theory and data at one active channel is that a single channel cannot reach rates larger than 4 Mhits/s, with the channel in this particular case being limited to 3.6 Mhits/s. Adapted from [47]. Data kindly provided by Patrick Schwäbig.

## 3.7 FEATURE SUMMARY

Having described VMM3a/SRS in the previous chapter and its characterisation measurements in the present chapter with its details, in the last section of this chapter the most important results from both chapters are summarised. This includes also a list of VMM3a properties, where the chip performance deviates from the intended design, as it was also provided by the chip designers themselves [11].

*Amplifier and Shaper:* The analogue part of the VMM3a contains 64 read-out channels, with each containing a charge-sensitive amplifier and a third-order shaper. The CSA is able to handle both positive and negative input signals. The electronics gain of the CSAs can be adjusted to values of 0.5, 1.0, 3.0, 4.5, 6.0, 9.0, 12.0 and 16.0 mV/fC per VMM. The shapers have adjustable peaking times of 25, 50, 100 and 200 ns, which again can be adjusted per VMM.

*Baseline Stabilisation:* It was observed that on some VMMs, especially at the highest electronics gain of 16 mV/fC, the baseline holder circuit works not as intended. With enabling bipolar shaping (SBIP flag of the VMM3a settings, done by default in the VMM3a/SRS control software) the effect is mitigated and the baseline is kept stable at around 170 mV.

*Electronics Noise:* With the noise level depending on the amplifier's gain and the detector capacitance connected to channel input, it was found that the intrinsic equivalent noise charge is not larger than 500 electrons and that connected to a typical $10 \times 10\,\mathrm{cm}^2$ test detector the ENC is not larger than 1000 electrons for gains $\geq 3\,\mathrm{mV/fC}$.

*Setting the Threshold:* The VMM3a front-end of the SRS operates in a continuous self-triggered read-out mode, with the read-out of the channel triggered by the shaper signal crossing an adjustable threshold value (10-bit for the global ASIC DAC and 5-bit as individual channel trimmers). So in order to be able to operate at THLs as low as possible and not acquire only noise hits, it is essential to optimise the grounding and shielding of the detector and the electronics.

*Pulser:* Each VMM channel contains a calibration pulser, with the voltage value of the pulser being adjustable with a 10-bit DAC for the entire ASIC. With this, a 0.3 pF capacitor is charged (alternatively also 3 pF), which gives a charge pulse to the CSA.

*Neighbouring-Logic:* The VMM3a has the possibility to enable a trigger-logic, which allows to read out channels below the threshold, if the adjacent read-out channel detected a signal above the threshold level.

*Bunch Crossing Clock CKBC:* Various clock frequencies have been tested, but not all of them work reliably. For frequencies up to $44.\bar{4}$ MHz, a stable operation was found. Typical operation frequencies have been between 20 MHz and $44.\bar{4}$ MHz. At a CKBC of 160 MHz, BCIDs were lost. The exact frequency at which the system becomes unstable was not determined.

*Timing-at-Threshold:* The VMM3a provides two different timing modes in VMM3a/SRS: timing-at-peak (default) and timing-at-threshold. For timing-at-threshold it was found that, depending on the electronics settings, the read-out channel can lock and lose data, making the timing-at-threshold mode in the VMM3a difficult to use. Also the neighbouring-logic does not work together with timing-at-threshold.

*Charge ADC:* Each read-out channel contains a clock-less 10-bit charge ADC. It suffers from a value aggregation, reducing the effective number of bits to 8-bit. The ADC provides only the baseline-subtracted peak amplitude of the shaper output.

*Timing ADC (TDC):* Each read-out channel contains an 8-bit timing ADC, which suffers from the same value aggregation as the charge ADC, reducing its effective number of bits to 6.5-bit. The reference time for the TDC can be adjusted to values of 60, 100, 350 and 650 ns.

*ADC and TDC Calibration:* The ADCs contains channel-by-channel fluctuations, meaning that the central channels give larger ADC outputs at the same input charge than the outer ones. For the TDC a similar situation exists however it does not follow necessarily the inverse U-shape of the ADC. For both cases, correction procedures are implemented in the VMM3a/SRS control software.

*Time Resolution:* Depending on the amplitude of the shaper output and the selected peaking time, the time resolution of the VMM3a can vary. The differential time resolution is around 2 ns at 200 ns peaking time and 0.5 ns at 25 ns peaking time.

*Channel FIFO:* Each read-out channel of the VMM3a contains a 4-bit deep FIFO. However, in the continuous read-out mode, which is e.g. implemented in VMM3a/SRS, this FIFO is not accessible, meaning that on a read-out channel only a new hit can be stored after a hit has been previously read out.

*Read-Out Clocks:* The maximum data transmission clock that the VMM3a can operate with, in dual edge transmission, is 180 MHz. The maximum token clock that VMM3a/SRS could potentially be operated with is then 9 MHz. The actual values are slightly lower, due to the base clock of the Hybrid firmware.

*Table 3.1* – Maximum achievable data rates of VMM3a/SRS depending on the read-out stage with the existing firmware versions and hardware components. The maximum rate from the switch to the DAQ computer depends on the number $n$ of FECs and hence network ports used at the switch, the output bandwidth of the switch, as well as the input bandwidth of the network card (e.g. 10 Gbps as in the hardware used for the measurements in this thesis).

| | Readout stage | Quantity unit | Maximum rate | | Limiting factor |
|---|---|---|---|---|---|
| | | Rate per | (Mhits/s) | (Mbps) | |
| A.1 | VMM3a channel | Channel | 3.6 | 144 | ADC conversion time |
| A.2 | VMM3a to Spartan-6 | VMM3a | $8.\bar{8}$ | $355.\bar{5}$ | CKTK frequency |
| A.3 | Spartan-6 | SERDES | $17.\bar{7}$ | $711.\bar{1}$ | Combining 2 VMMs |
| B.1 | HDMI | Hybrid | $17.\bar{7}$ | $888.\bar{8}$ | 8b/10b encoding |
| B.2 | DVMM | DVMM card | $142.\bar{2}$ | $7111.\bar{1}$ | Combining 8 Hybrids |
| C | FEC and Ethernet | FEC | 20.8 | 1000 | Gigabit Ethernet |
| D | Switch and Computer | Switch | $20.8 \times n$ | $1000 \times n$ | Combining $n$ FECs |

*Data Rates:* The maximum number of hits that can be read out of a single ASIC within VMM3a/SRS is 8 Mhits/s for the *Bonn firmware* or 8.8 Mhits/s for the *ESS firmware* (chapter 2). Hence, a single hybrid with two VMMs is able to almost fill the entire bandwidth of the FEC which is 20.8 Mhits/s (table 3.1). The maximum rate of a single channel is theoretically 4 MHz derived from the ADC conversion time. The observation indicates that most channels seem to have a slightly lower rate capability of 3.6 MHz [47].

*Detector Specific Settings:* At the end, a table with different electronics settings, depending on the detector type or the detector's operating condition is presented (table 3.2). It should be recalled that the VMM3a provides only the peak amplitude and the time of the peak and no information about the waveform of the induced signal. For this, the analogue output would be required, which gives only access to a single channel per VMM.

*Table 3.2* – Electronics settings that were used, depending on the detector settings and type.

| Detector | Detector gain | Particle type | Electronics gain (mV/fC) | Peaking time (ns) |
|---|---|---|---|---|
| COMPASS-like triple-GEM detector | $10^4$ | Copper X-rays | 3.0 or 4.5 | 200 |
| | $10^4$ | $^{55}$Fe X-rays | 6.0 | 200 |
| | $4 \times 10^4$ | $^{55}$Fe or copper X-rays | 1.0 | 200 |
| | $10^4$ to $4 \times 10^4$ | MIPs | 9.0 or 12.0 | 200 |
| Resistive layer MicroMegas | $10^4$ | MIPs | 9.0 or 12.0 | 200 |
| NIM-logic signals to 0.5 pF capacitor | - | - | 1.0 | 25 |

## *Chapter 4*

# EXPERIMENTAL METHODS

In the following chapter, the experimental aspects that are common to the detector-based characterisation studies and applications (chapters 5 and 6) are described. First, the detector type used for the measurements is presented: a COMPASS-like triple-GEM detector filled with $Ar/CO_2$ (70/30 %) at ambient pressure and temperature (section 4.1). Thereafter, the laboratory set-up is described (section 4.2). The measurements were performed with a single detector using X-ray sources. Thus, the description includes also the presentation of the detector response to X-rays. As the cluster reconstruction is always performed on the single detector level, its explanation is also included in the laboratory set-up part, even though it is independent of the particle interaction type. In the last part, the set-up used for test beam measurements is described (section 4.3). With the beam telescope built in the scope of this thesis, consisting of multiple COMPASS-like triple-GEM detectors, the reconstruction of particle tracks based on the single detector clusters is described in this part. Further, the response to MIPs and the commissioning of the beam telescope are presented.

## 4.1 COMPASS-LIKE TRIPLE-GEM DETECTOR

The main components of a COMPASS-like triple-GEM detector [66] are the three ***Gas Electron Multiplier*** (GEM) [24] foils used for the amplification process. Each GEM consists of a 50 µm thick polyimide foil, coated with 5 µm copper on the top and bottom sides. The foil is structured with bi-conical holes, where the inner hole diameter is around 50 µm, the outer one 70 µm and the hole pitch 140 µm, with the holes arranged in a hexagonal pattern[1] (figure 4.1). To reach the high electric fields for the gas amplification (section 1.4), a high voltage $\mathcal{O}(350\,\mathrm{V})$ is applied between

---

[1] It should be noted that the mentioned dimensions are the ones of the so-called *standard GEMs* that were also used in this thesis. Other geometries with different foil thicknesses, hole sizes and hole pitch exist as well. For an overview with further references, it is referred to [67].

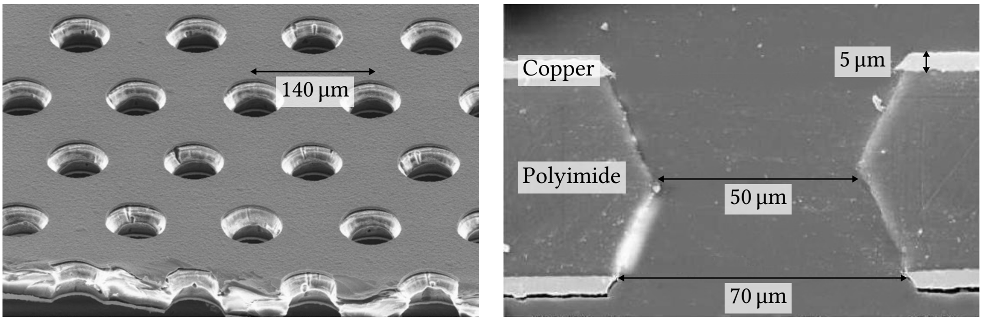

*(a)* – GEM hole pattern. *(b)* – GEM hole cutaway view.

*Figure 4.1* – Electron microscope images of a standard GEM (a) with the hexagonal hole pattern and the cut through one of these holes (b). Adapted from [66]. Courtesy of Fabio Sauli.

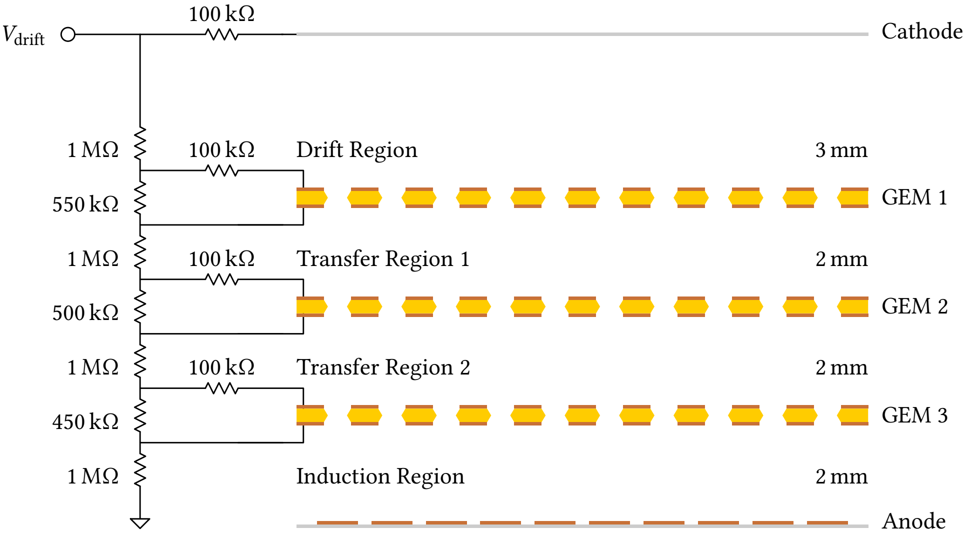

*Figure 4.2* – Schematics (not drawn to scale) of the triple-GEM detector used for the measurements in this thesis, with a particular focus on the voltage divider and the gap sizes.

the two copper electrodes of the GEM[2], with the electron avalanche taking place inside the holes (figure 1.1). In order to apply the high voltage, various schemes exist [68, 69], with a voltage divider being the one used here (figure 4.2). To achieve sufficiently high detector gains, multiple GEMs can be stacked on top of each other. The scheme used in this thesis adopts the one developed for COMPASS [66, 70],

---

[2] CAEN Mod. N470 high voltage power supply for the laboratory set-up and CAEN SY5527 mainframe with CAEN Mod. A1526N high voltage module.

where the GEM stack is composed of three foils, each with a distance of 2 mm from the neighbouring one. The entire stack has a distance of 2 mm from the read-out anode for the signal induction and 3 mm to the cathode for the drift region. The resistor in the voltage divider across the first GEM has the highest value, leading to the highest field and hence the largest amplification. With each following GEM, the resistor value is decreased, reducing the gain of each successive GEM, to decrease the discharge probability due to the higher electron density at the later GEMs.

During the process of amplifying, extracting, transferring and collecting the electrons between the different GEMs, some of the electrons are 'lost'. This can be e.g. due to attachment to the gas atoms or the (field dependent) electrical transparency[3]. Thus, the gain achieved with the detector is not simply the product of the three individual GEM gains. This leads to the definition of the total effective detector gain for such a multi-stage GEM detector [68]:

$$G = \frac{N_\mathrm{a}}{N_0} = \frac{I_\mathrm{a}}{N_0 \, e \, \nu_\mathrm{i}} \,, \tag{4.1}$$

where $N_0$ is the initial number of primary ionisation electrons, $N_\mathrm{a}$ the number of electrons reaching the anode, $e = 1.602 \times 10^{-19}\,\mathrm{C}$ the elementary charge, $\nu_\mathrm{i}$ the interaction rate, which is independent of the number of collected primary electrons and $I_\mathrm{a}$ the electron current measured on the anode. The gain shows the expected (section 1.4) exponential behaviour (figure 4.3).

After the amplification stage, the signal is induced on the read-out anode. In the case of COMPASS-like triple-GEM detectors, a segmented read-out anode is used, in order to be able to reconstruct the position of the incident particle. The segmentation consists of conducting copper strips of 5 µm thickness, separated by 50 µm thick polyimide wells. The 256 $x$-strips are on the top with a width of 80 µm, while the 256 $y$-strips are on the bottom with a width of 340 µm. In both cases, the pitch is 400 µm (figure 4.4). This defines the actively read out area of the detector of $10 \times 10\,\mathrm{cm}^2$.

## 4.2 Laboratory Set-Up

The laboratory set-up (figure 4.5) is a single detector, read out with four RD51 VMM Hybrids connected via HDMI cables to a single DVMM/FEC combination, which is mounted in a corresponding SRS Minicrate. It is important to note that this set-up started as a prototype, meaning that the components evolved and were partially replaced (with the exception of the Hybrids and the FEC) with the final production versions of them (chapter 2) in the scope of this thesis. Hence, for example, the use

---

[3] It should be noted that the electrical transparency is field-dependent. For the typical operation fields, as in this thesis, the situation is close to a fully transparent state [68].

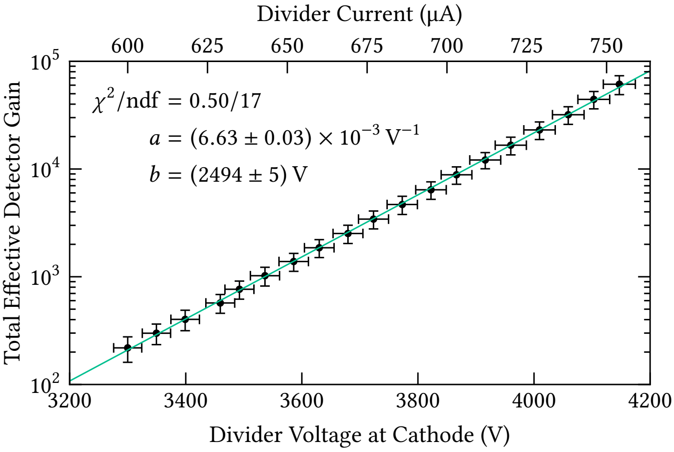

*Figure 4.3* – Total effective detector gain of a COMPASS-like triple-GEM detector, depending on the divider voltage $V_{\text{divider}}$. The error bars on the gain are enlarged by a factor of 5 for better visibility. The main contribution to the gain error arises from the current measurement, where the standard deviation of $I_{\text{a}}$ is used. The data are fitted with an exponential function $G(V_{\text{divider}}) = \exp[a(V_{\text{divider}} - b)]$. The measurements have been performed with an $^{55}$Fe source, for which $N_0 = 193$ (section 4.2.1).

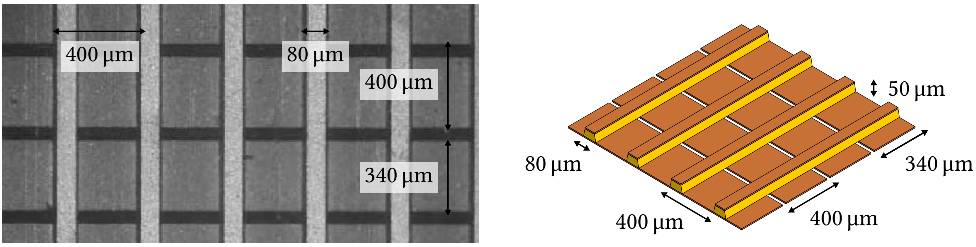

*(a)* – Read-out board SEM image.

*(b)* – Read-out board sketch.

*Figure 4.4* – Electron microscope images of a read-out anode for a COMPASS-like GEM detector (a). Adapted from [66]. Courtesy of Fabio Sauli. Drawing of the corresponding board to illustrate the height difference between the $x$-strips on the top and the $y$-strips on the bottom (b).

of an SRS Minicrate and an external powering scheme for the Hybrids, instead of the SRS PowerCrate 2k and the provision of the power via the HDMI cables.

The read-out strips traverse the detector housing, such that the Hybrids can be directly connected to the read-out board. In the case of the utilised detector, this made the use of adapters mandatory, as the read-out board contained the old-style connectors[4] instead of the new connectors[5] used on the Hybrid. The read-out strips

---

[4] Panasonic AXK6SA3677YG (130 contacts)

[5] Hirose FX10A-140P/14-SV1 (140 contacts with additional ground contacts)

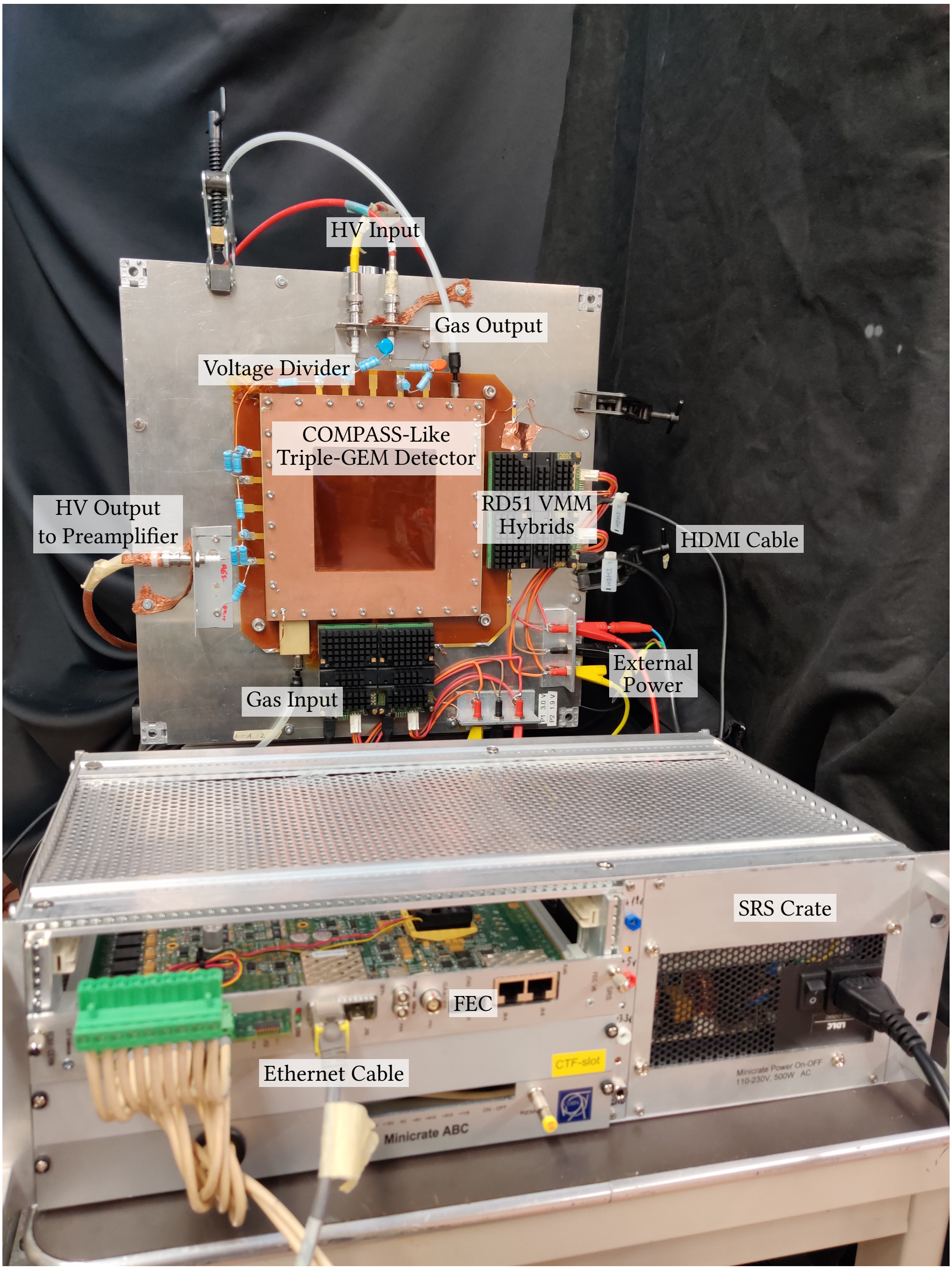

*Figure 4.5* – Photograph of the experimental set-up used in the laboratory, mainly for X-ray studies.

and the Hybrid's input channels are connected with a one-to-one mapping, where strip $s_i$ is mapped to hybrid channel $i$.

In addition to the read-out scheme with VMM3a/SRS, it is also possible to read out the detector with other electronic devices, which were for example used to characterise the basic detector performance. One of them is a picoammeter[6], with which the anode current $I_\mathrm{a}$ on the read-out strips was measured. For this, all strips were joined together and connected to ground through the picoammeter. At the same time, it was possible to read out the bottom of the last GEM with a signal processing chain consisting of preamplifier[7], shaper[8] and ***M**ulti**C**hannel **A**nalyser*[9] (MCA), with the latter being effectively a fast ADC for the signal digitisation. The signal reading on the bottom of the last GEM allowed to monitor the shaper signals on an oscilloscope[10].

### *4.2.1 X-Ray Sources and Typical Spectrum*

The measurements with the laboratory set-up involved two kinds of X-ray sources. On the one hand a passive $^{55}$Fe radioactive source[11] and on the other hand an active copper target X-ray tube[12], with both emitting soft X-rays. The $^{55}$Fe source emits photons with energies of $E_{\mathrm{K}_\alpha} = 5.9\,\mathrm{keV}$ and $E_{\mathrm{K}_\beta} = 6.5\,\mathrm{keV}$ [25], which have relative intensities of 89.8 % and 10.2 % respectively [36]. The copper target X-ray tube emits a continuous Bremsstrahlung spectrum with peaks at $E_{\mathrm{K}_\alpha} = 8.0\,\mathrm{keV}$ and $E_{\mathrm{K}_\beta} = 8.9\,\mathrm{keV}$, which have almost the same relative intensities as the $^{55}$Fe photons [36]. In order to suppress the Bremsstrahlung part of the spectrum, the opening of the X-ray tube was usually covered with three layers of copper tape.

The emitted X-rays interact predominantly via the photoelectric effect (figure 1.4). In the following, the different de-excitation processes and hence event signatures after the photoelectric ionisation of an argon atom through a soft X-ray photon are presented. First, the photoelectron is liberated from an inner shell, the K-shell, of the argon atom. The electron interacts with the surrounding gas atoms, ionises them and creates a charge cluster. This is common for all de-excitations processes of the initial argon atom (figure 4.6). The most probable one[13] is a photon-less de-excitation via an Auger cascade (figure 4.6a). There, the energy difference between the K-shell

---

[6] Keithley Model 6487 Picoammeter

[7] ORTEC® 142PC Preamplifier

[8] ORTEC® Model 474 Timing Filter Amplifier

[9] Amptek® MCA-8000D Pocket MCA

[10] Rohde & Schwarz® RTB2004 Digital Oscilloscope

[11] $^{55}$Fe decays via electron capture into $^{55}$Mn, which emits then characteristic X-rays, due to the de-excitation of the atomic shell levels [25].

[12] Ital Structures Compact 3K5 X-ray Generator

[13] From the integrals of the peaks in the recorded spectrum (figure 4.7) it is estimated that this takes place in around 85 % of the cases.

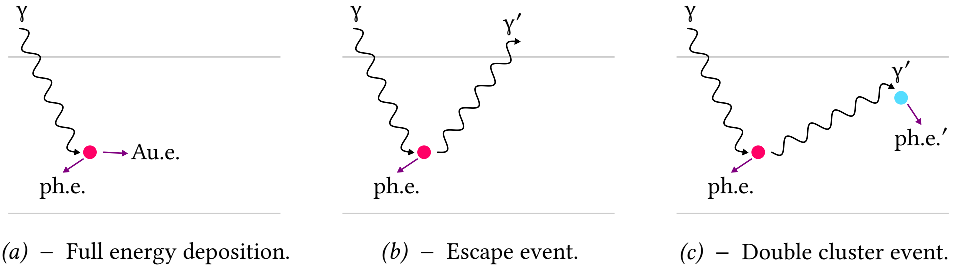

*(a)* – Full energy deposition. *(b)* – Escape event. *(c)* – Double cluster event.

*Figure 4.6* – Illustration of the different event characteristics after the photoelectric interaction of an X-ray photon γ with a gas atom. The full energy deposition in a single cluster is illustrated in (a), where after the liberation of a photoelectron (ph.e.) one or more Auger electrons (Au.e.) are emitted close to the initial interaction. Another single cluster event is illustrated in (b), where the initial ionisation is followed by the emission of a fluorescence photon γ′ that escapes the active detector volume. In (c), a double cluster event is shown, where γ′ does not escape the detector but interacts in the gas volume and liberates a second photoelectron (ph.e.′). Published in [71].

level $E_\mathrm{K}$ and higher shells $E_\mathrm{h}$ is transferred to other shell electrons, which are then emitted and ionise themselves surrounding gas atoms. This happens directly next to the ionisation track of the photoelectron, keeping the single charge cluster structure, containing almost the entire photon energy (so-called *photopeak* of the spectrum). Alternatively, a characteristic argon fluorescence X-ray photon, with energy $E_\mathrm{h} - E_\mathrm{K}$ can be emitted. This photon however often leaves the active area of the detector and thus *escapes* its detection (figure 4.6b). This leads to the so-called *escape peak* of the spectrum, where only the energy of the photoelectron is contained. In addition, it can happen that the characteristic X-ray photon does not leave the active detection area and interacts with another argon atom, leading to the liberation of a second photoelectron and thus a second charge cluster, separated in space (figure 4.6c).

Numerically this means the following. In the case of the photopeak, the charge cluster contains the full photon energy. The liberated shell electron ($E_\mathrm{b}^\mathrm{K} = 3.2\,\mathrm{keV}$) has a kinetic energy of $E_\mathrm{kin} = 2.7\,\mathrm{keV}$ in the case of $^{55}$Fe or $E_\mathrm{kin} = 4.8\,\mathrm{keV}$ in the case of the copper target X-ray tube. This corresponds to the always present charge cluster and at the same time to the energy of the escape peak, in case of the emission of an argon fluorescence photon. This photon has an energy of $E_\gamma = 3\,\mathrm{keV}$ [36]. During the interaction with an L-shell electron of another argon atom, this would lead to another cluster with about 2.7 keV [36].

It should be noted that the mentioned energy values for the photoelectron correspond only to interactions of $\mathrm{K}_\alpha$ photons. Due to the intensity differences between the $\mathrm{K}_\alpha$ and $\mathrm{K}_\beta$ line and the energy resolution of gaseous detectors, which is typically 10 % to 20 % at ***Full Width at Half Maximum*** (FWHM), it is not possible to distinguish

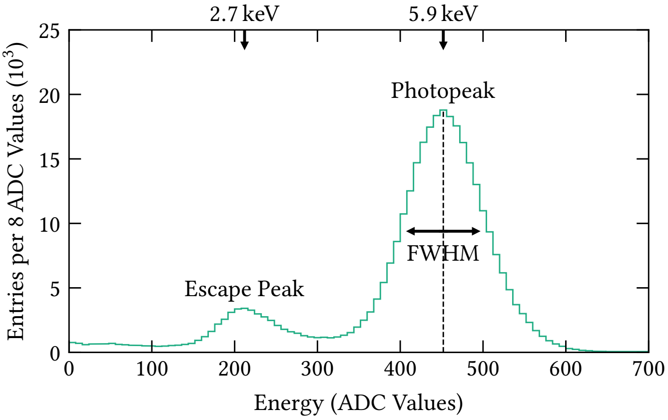

*Figure 4.7* – Example of an $^{55}$Fe spectrum, including the indication of the photopeak and the escape peak with its corresponding main energies. Further, the FWHM of the photopeak is indicated. The spectrum was recorded by reading out the bottom of the last GEM and using the discrete electronics with MCA.

the $\mathrm{K}_\beta$ line from the $\mathrm{K}_\alpha$ line, with the energy resolution being defined as [28]

$$R = \frac{\Delta E}{E} = \frac{2.35\sigma_E}{E} , \tag{4.2}$$

where $\Delta E$ is the FWHM of the peak with energy $E$ (figure 4.7).

Taking both, the escape and the photopeak into account, and recalling the average ionisation potentials for argon ($W_\mathrm{i} = 26\,\mathrm{eV}$) and carbon dioxide ($W_\mathrm{i} = 34\,\mathrm{eV}$), the number of created electron-ion pairs can be calculated:

$$N_0 = \frac{E_\mathrm{dep}}{\tilde{W}_\mathrm{i}} . \tag{4.3}$$

Here, $\tilde{W}_\mathrm{i} = 28.4\,\mathrm{eV}$ is the weighted ionisation potential, where the weights are derived from the mixing ratio in the gas compound. The deposited energy in the gas, $E_\mathrm{dep}$, contains the ratio between photopeak and escape peak, where the weights are derived from the peaks' integrals, so the relative amount of interactions:

$$E_\mathrm{dep} = 0.85\left(I_{\mathrm{K}_\alpha} E^\mathrm{photo}_{\mathrm{K}_\alpha} + I_{\mathrm{K}_\beta} E^\mathrm{photo}_{\mathrm{K}_\beta}\right) + 0.15\left(I_{\mathrm{K}_\alpha} E^\mathrm{escape}_{\mathrm{K}_\alpha} + I_{\mathrm{K}_\beta} E^\mathrm{escape}_{\mathrm{K}_\beta}\right) . \tag{4.4}$$

Here, $I_i$ describes the relative intensities of the $\mathrm{K}_\alpha$ and $\mathrm{K}_\beta$ lines [36]. With this, it is found that $N_0 = 193$ for $^{55}$Fe and $N_0 = 268$ for a copper target X-ray tube in $\mathrm{Ar/CO_2}$ (70/30 %).

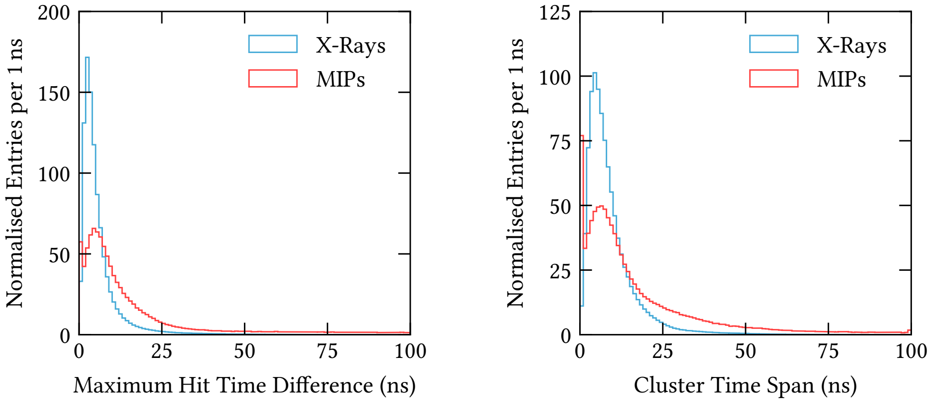

*(a)* – Time difference between hits.

*(b)* – Cluster span.

*Figure 4.8* – Distribution of the maximum time difference between the two hits within a cluster (a) and distribution of the time span of a cluster (b). The behaviour is illustrated for X-rays and MIPs at a total effective detector gain of around $3 \times 10^4$.

### *4.2.2 Cluster Reconstruction*

Following the interaction of the initial particle, the initial charge cloud and the following electron avalanche are spread over multiple read-out strips, due to diffusion, leading to a so-called *cluster*. With a cluster corresponding to an incident particle, it contains information about the particle's interaction point, the interaction time and the deposited energy. To get access to this information, the clusters have to be reconstructed from the acquired hit data. The VMM3a front-end of the SRS is operated in a self-triggered continuous read-out mode. This leads to the situation that no additional information exists, e.g. external trigger signals or a frame-based read-out, to assist the cluster identification.

In order to reconstruct clusters from the hit data stream, the following procedure, based on the hit time, is implemented in the reconstruction software [55]. First, the hits are sorted in time, using the full timestamp given in equation (2.7). Then *time clusters* have to be found. A time cluster means any accumulation of hits, which has to fulfil two conditions, defined by the user: the time between two consecutive hits must be equal to or smaller than $\Delta t_{\text{hits}}$ and the time between the first and the last strip of the accumulation must not be larger than $\Delta t_{\text{span}}$. Typical values used in this thesis are $\Delta t_{\text{hits}} = 100\,\text{ns}$ and $\Delta t_{\text{span}} = 500\,\text{ns}$. It can be seen that these values are a conservative choice (figure 4.8). For the hit time difference, only the maximum value from all the time differences between the strips within a cluster is shown (figure 4.8a). Both distributions peak well before the defined clustering values.

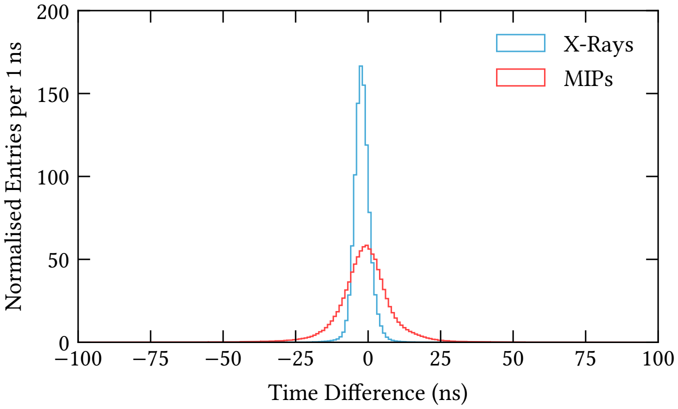

*Figure 4.9* – Distribution of the time difference between the cluster time (section 4.2.3) recorded in the $x$-plane and in the $y$-plane.

However, the choice was motivated by not losing cluster information, because of too strict clustering conditions. It was further motivated by the fact that after the time clustering, geometrical clustering is applied to identify the *plane clusters*. So even if multiple particle interactions are clustered together within a time cluster, they would be separated by the geometrical clustering. For this, all adjacent strips are considered as a plane cluster, if they are larger than a previously defined minimum cluster size $s_\mathrm{c}$ and there is no gap between two adjacent strips larger than $s_\mathrm{mis}$, called *missing strip*. Typical values used in this thesis are $s_\mathrm{c} = 1$ strip (usually for charged particles), $s_\mathrm{c} = 2$ strips (often for X-rays) and $s_\mathrm{mis} = 0$ strips or 1 strip. This choice was driven by the interaction behaviour and charge deposition of the particles.

Having found the plane clusters, an option exists to find the *detector clusters*. For one-dimensional strip detectors or detectors with pad read-out, the plane clusters are identical to the detector clusters, while for detectors with $x$-$y$-strip read-out, a matching of the clusters between $x$-plane and $y$-plane can be performed in order to obtain detector clusters. In that case, the plane clusters are matched in time again, using the cluster timestamp (section 4.2.3). This means that the time difference between an $x$-plane cluster and a $y$-plane cluster must not be larger than the previously defined value of $\Delta t_\mathrm{plane}$. Typical values used in this thesis are $\Delta t_\mathrm{plane} = 100$ ns or $\Delta t_\mathrm{plane} = 150$ ns. Also this choice is conservative (figure 4.9). It was driven by the case of individual read-out planes of the same detector being read out by different FECs, which despite the CTF card may have a time offset of up to 75 ns, which needs to be considered within $\Delta t_\mathrm{plane}$. It should be further noted that an option exists to match the correct plane cluster by respecting the charge sharing ratio, to reject possible mismatches. Usually, the read-out boards have a charge sharing ratio of 50/50 % or 60/40 % between the $x$- and $y$-plane, depending on the production series[14]. For this, the cluster ADC charge (sum of all hit ADC values of the cluster) is used.

### *4.2.3 Cluster Parameters*

For each found cluster, various quantities are saved. Starting with an identifier, the detector and the detector plane the cluster was found in, this is followed by the fundamental quantities size, charge, time and position. The cluster size refers to the number of strips a cluster is made up of. The cluster charge sums up all ADC values $Q_i$ from the strips $i$ within a cluster

$$Q_{\mathrm{c}} = \sum_i Q_i . \tag{4.5}$$

The position of the cluster is calculated with a position reconstruction algorithm, as it allows to achieve spatial resolutions much smaller than the electrode pitch. This is due to the spread of the charge cloud over several read-out strips because of diffusion. A popular choice as position reconstruction algorithm is the ***Centre-Of-Gravity*** (COG) method with

$$x_{\mathrm{c}} = \frac{\sum_i Q_i x_i}{\sum_i Q_i} . \tag{4.6}$$

Here, $x_{\mathrm{c}}$ is the calculated centre of the cluster found with vmm-sdat, $x_i$ the position of read-out strip $i$ and $Q_i$ the charge that was induced on this strip making up the cluster. Other methods exist as well, for which it is referred to the characterisation studies (section 5.2.2). In addition to the position of the cluster, also its timestamp is calculated. The default method is the COG method, with the strip position being replaced by the strip time $t_i$:

$$t_{\mathrm{c}} = \frac{\sum_i Q_i t_i}{\sum_i Q_i} . \tag{4.7}$$

Other methods are the usage of the earliest hit timestamp of the cluster, which is the µTPC-method [72, 73], or using the timestamp of the hit with the largest amplitude. For their comparison, it is also referred to the characterisation studies (section 5.3).

In addition to these already calculated quantities, the ROOT file generated with vmm-sdat contains also the raw information making up the clusters, meaning each $t_i$ or $x_i$ for each identified cluster. Furthermore, the reconstruction quantities are

---

[14] Both kinds of production series have been used in this thesis. For the tracking detectors of the beam telescope (section 4.3), the charge sharing ratio is 50/50 %, while for the laboratory detector, which is also one of the detectors under test in the beam telescope, the ratio is 60/40 %.

saved, such as the time span of the cluster or the maximum time difference between strips, the number of missing strips per cluster or the time difference of the plane clusters that could be matched to a detector cluster.

## 4.3 TEST BEAM SET-UP

The RD51 collaboration organises up to three times per year common test beam campaigns at the H4 beam line of the ***S**uper **P**roton **S**ynchrotron* (SPS) at CERN. This includes the provision of common test beam infrastructure, for instance, the permanent installation of a gas supply or the provision of two (movable) beam telescopes. As part of this thesis, a third beam telescope was equipped with VMM3a/SRS read-out with the main goal of commissioning the electronics and providing a new common front-end for future test beam campaigns.

A key point in this activity was to confirm that VMM3a/SRS, due to its rich feature set, is a fully integrated read-out system. This means that all the required information which is needed to characterise the ***D**etectors **U**nder **T**est* (DUT) is provided by a single common front-end. The data from the detectors for the track reconstruction are read out by the same system as the DUTs and are part of the same data stream, reducing the overhead in the event reconstruction. With the high rate-capability, it is possible to operate with short acquisition times and still acquire large statistics, while the charge and position sensitivity allow a precise scanning of the detector response. At the same time, due to the electronic time resolution in the nanosecond regime, it is possible to study the time resolution of the DUTs[15] without requiring further dedicated hardware, like for example external TDCs.

This leads to another important point in providing a common read-out system for test beam campaigns, which is compatibility with different detector technologies. Even though the following description focuses on COMPASS-like triple-GEM detectors, it should be noted that during the three test beam campaigns that took place over the course of this thesis, various other detector types have been successfully read out with VMM3a/SRS. Not all were tested in the new RD51 beam telescope, but also by other RD51 groups within their own set-ups[16]. Among the tested detectors are different kinds of triple-GEM detectors, different kinds of MicroMegas detectors, including a ***T**ime **P**rojection **C**hamber* (TPC) with a MicroMegas amplification stage, as well as detectors outside of the MPGD family, specifically straw tubes for the DUNE experiment, as well as NIM signals from a coincidence unit which received signals from scintillators connected to ***P**hoto**M**ultiplier **T**ubes* (PMTs).

---

[15] Typically of the order of $\mathcal{O}(10\,\text{ns})$.

[16] For a more detailed description of the mentioned technologies and in particular their application in the RD51 test beams, it is referred to the dedicated test beam reports during the RD51 collaboration meetings [60–62].

The specific beam telescope used for this thesis consists of three COMPASS-like triple-GEM detectors for track reconstruction and varying numbers and types of DUTs. The DUT with which most of the measurements have been performed is the COMPASS-like triple-GEM detector that was also used for the X-ray studies. The detectors are all mounted on a support frame (figure 4.10), which contains for example also the common electronics ground bar or the mounts for the optional scintillators and PMTs. In addition, a support rack next to the beam telescope is required that contains e.g. the low and high voltage power supplies or additional NIM electronics to pre-process the PMT signals for VMM3a/SRS.

Inside the telescope, the detectors have roughly the same distance to each other (figure 4.11), with the DUTs placed in between the tracking stations. The detectors themselves are all rotated by 90° with respect to each other, in order to avoid systematic errors in the coordinate system mapping. The coordinate system of the beam telescope is aligned with the first tracking station, which was mounted in such a way that the $x$-strips of the detector measure along the $x$-direction of the beam telescope and the $y$-strips measure along the $y$-direction, such that the origin of the detector is the origin of the beam telescope. However, to keep a right-handed coordinated system, all the other detectors are then placed along the negative $z$-coordinate within the beam telescope coordinate system.

The measurements themselves were mainly performed with muons with 80 GeV/$c$ momentum (figure 4.12) and around $10^5$ particles per spill[17] (sections 5.2.6 and 5.3). To measure with higher intensities of up to $10^7$ particles per spill, pions with 80 GeV/$c$ momentum were used (section 5.1.2). In addition to the test beams at the H4 beam line, the beam telescope was also operated at the H2 beam line with 31 GeV/$c$ protons, with maximally $10^5$ particles per spill (section 6.3).

### *4.3.1 Track Reconstruction*

In order to characterise the DUTs with a beam telescope, the tracks of the beam particles traversing the active area of the telescope have to be reconstructed. For this, the track reconstruction software *anamicom* [74, 75] was used, which is also used for other RD51 set-ups [7]. In the following, the principal working scheme of the tracking software using VMM3a/SRS data is recalled.

The starting point is the event-building. Usually, the event definition is provided by an external triggered signal. However, as the beam telescope is operated in the self-triggered continuous read-out mode, identical to the cluster reconstruction in a single detector (section 4.2.2), no external trigger signals are used for the event

---

[17] The beams at the secondary beam lines of the SPS originate from the extraction of the primary beam in so-called *spills* of around 5 s length towards the experiment halls.

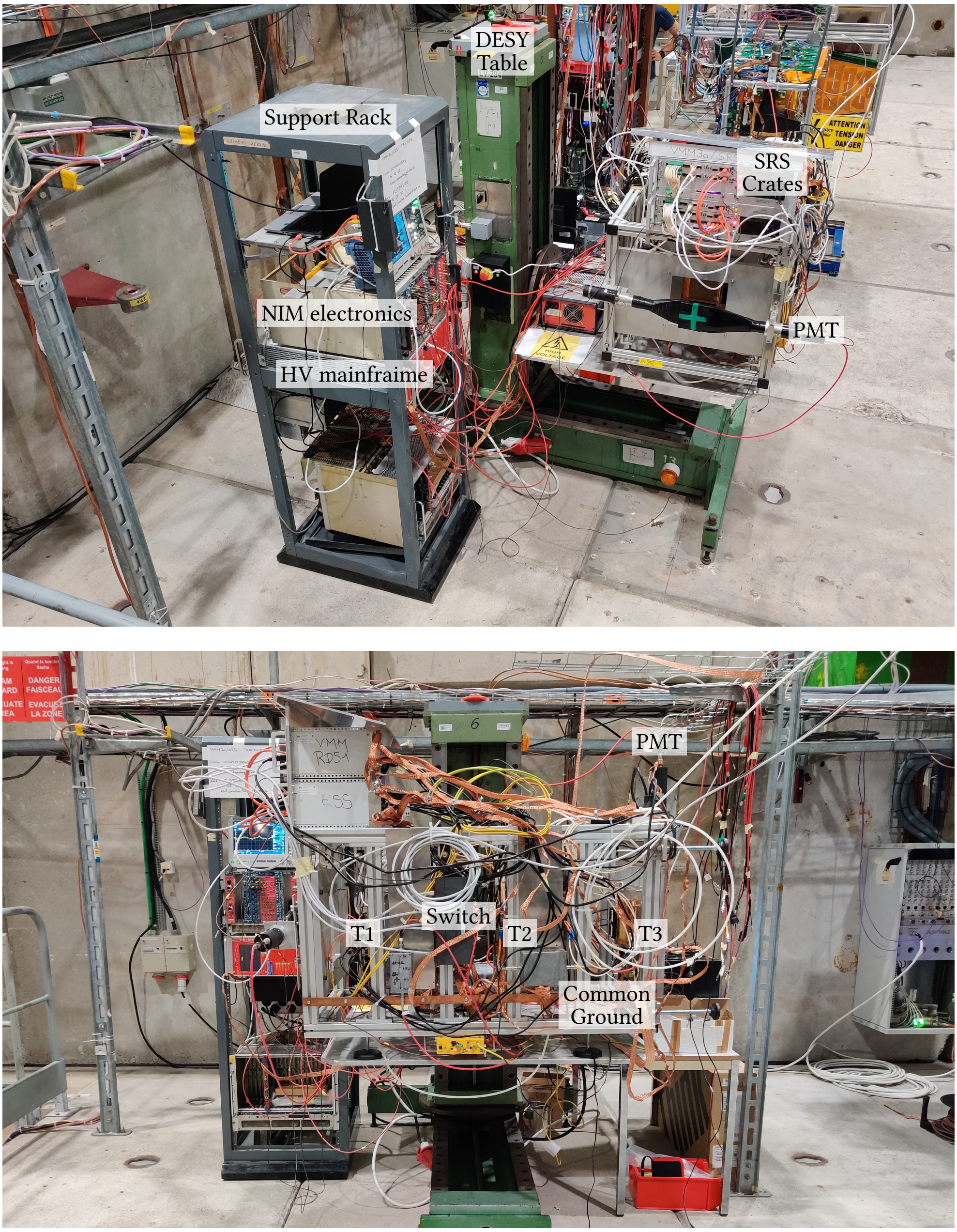

*Figure 4.10* – Photographs of the experimental set-up used in the RD51 test beam in May 2022. The beam telescope with its components (detectors, electronics, grounding, etc.) as well as the rack with its components (oscilloscope, HV mainframe, NIM electronic) are shown. In the bottom image, the positions of the three tracking detectors are indicated (T1, T2 and T3). The DUTs are placed between the tracking detectors, with DUT-A being hidden behind the switch.

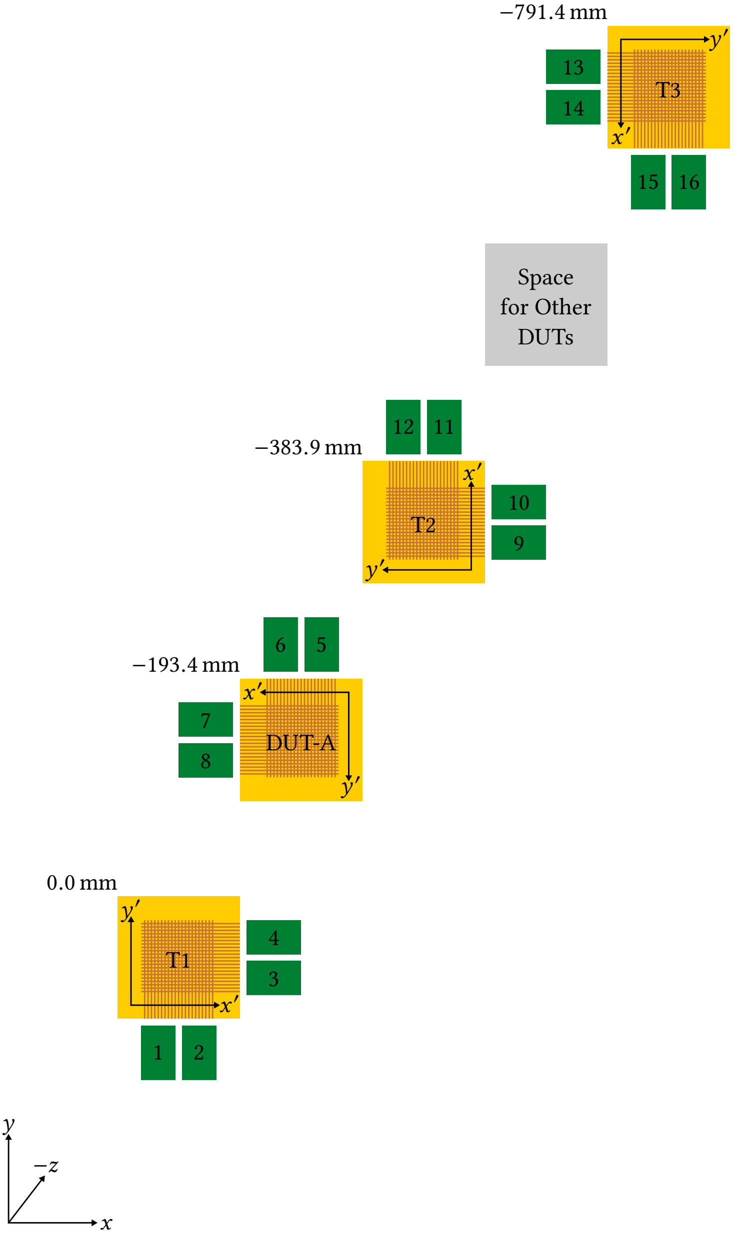

*Figure 4.11* – Sketch of some of the detectors used in the beam telescope with their distances to each other, their rotations and the orientation of the detector coordinates ($x'$ and $y'$) in the beam telescope coordinate system ($x$, $y$ and $-z$). It shows the three tracking detectors (T1, T2 and T3), as well as one detector under test (DUT-A). Connected to the detectors are the Hybrids, which are numbered from 1 to 16.

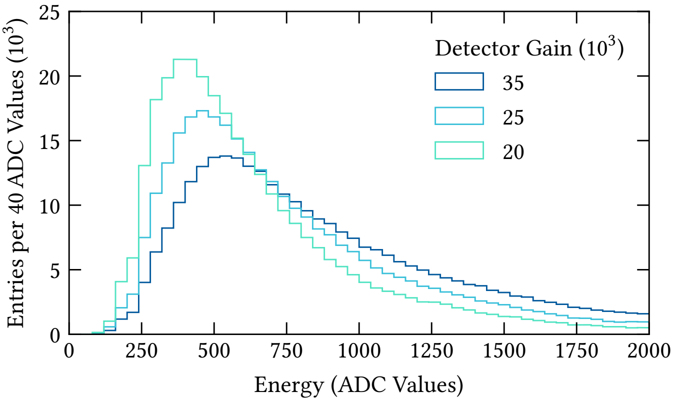

*Figure 4.12* – Example of the energy loss spectrum, the Landau distribution, of muons recorded with a COMPASS-like triple-GEM detector using VMM3a/SRS at different total effective detector gains.

definition. Hence, the signals are built from the plane clusters[18] reconstructed with vmm-sdat. At first, a coincidence window has to be found, containing a sufficiently large number[19] of coincident clusters from different planes. For this, the earliest timestamp of each detector read-out plane is stored in an $n$-tuple, with $n$ being the number of planes. If the time difference $\Delta t_{\mathrm{clusters}}$ between the earliest $t_0$ and the latest accepted timestamp[20] is smaller than a previously defined time interval, here $\Delta t_{\mathrm{coinc}} \leq 1000\,\mathrm{ns}$, the coincidence window was found. If the time difference is larger than $\Delta t_{\mathrm{coinc}}$, it is iterated over the read-out planes and the next earliest timestamp is taken until the coincidence condition is met. Once a coincidence window $\Delta t_{\mathrm{clusters}}$ is found, the event is defined: it contains all clusters from all read-out planes for which holds $t_{\mathrm{c}} - t_0 < \Delta t_{\mathrm{clusters}}$, with $t_{\mathrm{c}}$ the cluster timestamp. Similar to the cluster reconstruction, the chosen value for $\Delta t_{\mathrm{coinc}}$ may be considered as conservative (figure 4.13). It was driven by the fact that anamicom is able to reconstruct multiple tracks per event and hence the geometrical tracking would disentangle all the clusters contained within the event.

Having defined the event, the cluster information is transferred to the tracker. For this, the basic cluster information on the strip level (ADC value per strip, strip

---

[18] The track reconstruction software is specifically designed to work with detectors with strip read-out structures. As this includes also detectors that measure only along a single dimension, this structure was kept for VMM3a/SRS as they are provided within the plane clusters.

[19] It is possible to allow inefficient planes in the track reconstruction. The same inefficiency condition is also allowed in the event-building.

[20] Accepted due to the inefficiencies. Even though it is possible to allow inefficient planes, this is something, which was not allowed for the analysis performed in this thesis.

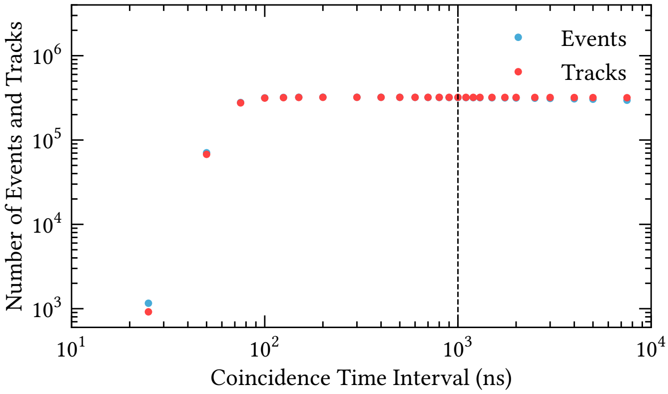

*Figure 4.13* – Number of built events and reconstructed tracks, depending on the length of the coincidence interval $\Delta t_{\text{coinc}}$. In this case, the detectors were operated at a gain of around $3 \times 10^4$. The beam conditions were muons with around 10 kHz particle rate (around 50 000 particles per spill) recorded over six spills.

position, time of the signal) is used to be compatible with the data from other readout electronics. The resulting cluster parameters are however the same as those used by vmm-sdat (section 4.2.3). The tracker itself is based on a Kalman filter [76]. With a detailed description of the Kalman track fitting algorithm used being given in [77], in the following only the general working principle is recalled (figure 4.14). This assumes no inefficient layers, which was in fact required for the three tracking stations. The starting point is the cluster with the highest charge in the first plane of the telescope, which has to be matched with the cluster with the highest charge in the second plane. If this works, the track extrapolation continues, if no matching is possible, the clusters with the next highest charge in the first plane is used, and the procedure for the second layer is repeated. Based on the position of the clusters found in the first two planes, the position of the cluster in the next plane is estimated. Once a cluster is found around the estimated position the extrapolation of the position towards the next layer continues until the last layer is reached. If at some point no matching cluster is found in the next layer, but there are other clusters in the current layer of the event available they will be used. This procedure is repeated until no clusters from the event can be matched and the track finding in the event gets terminated. When the track is found in the forward direction, the procedure is repeated in the backwards direction on the assigned cluster to smooth the track fit.

An important aspect of correctly reconstructing the particle tracks is to ensure that the detectors are precisely aligned with each other. This means to include shifts between the detectors in the $x$-$y$-plane of the beam telescope coordinate system

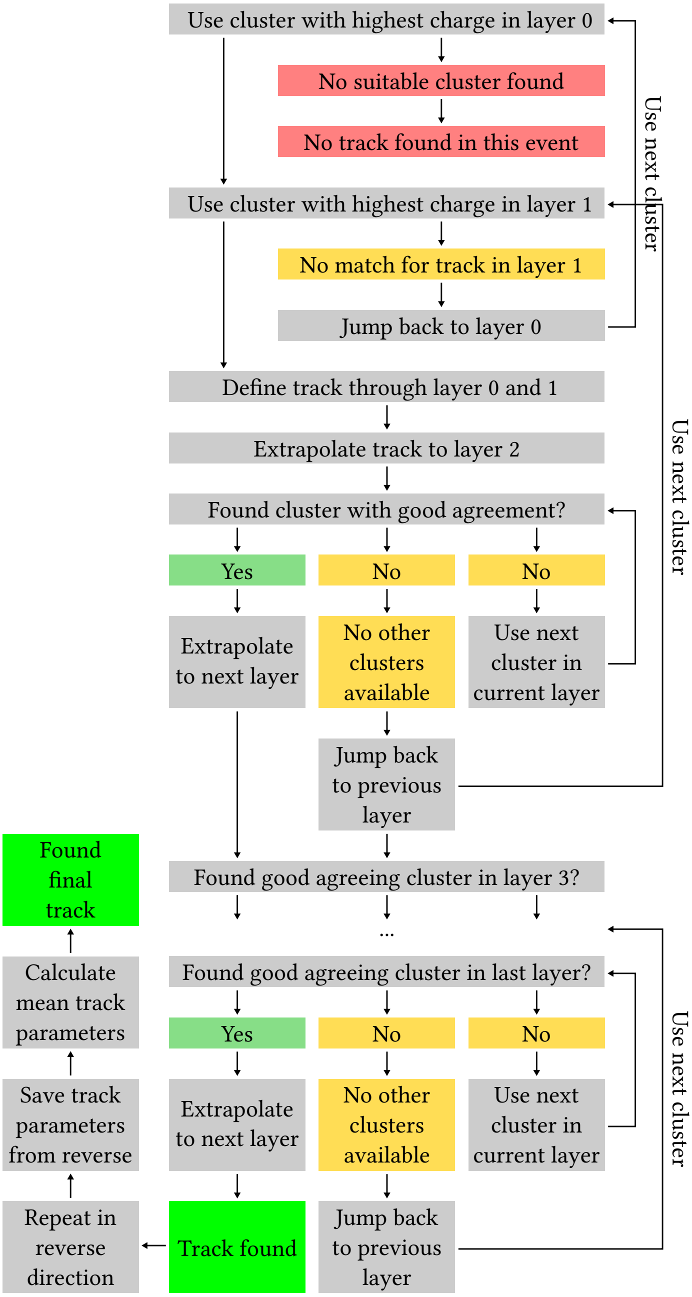

*Figure 4.14* – Working principle of the track finding and fitting algorithm based on a Kalman filter used in anamicom. Adapted from [77].

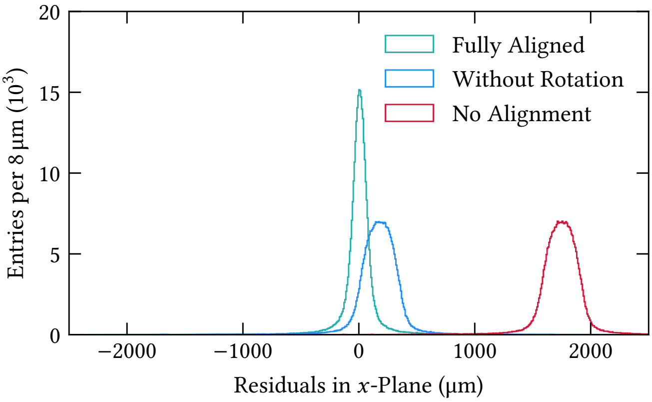

*Figure 4.15* – Example of a residual distribution in the $x$-direction of the DUT for various alignment conditions. While the tracking stations are already aligned, the situations for the DUT shown here are without any rotational and translational alignment, without any rotation around the $z$-axis and then with both transformation operations applied.

in the track reconstruction, as well as rotations of the detectors around each axis. With anamicom, the corresponding translations and rotations can be extracted via an iterative process from the particle tracks. A detailed description of how the parameters for the geometric transformations are extracted from the data and then applied in anamicom can be found in [75, 77]. Here, only an example of the residual distribution[21], after various alignment steps is shown (figure 4.15). This indicates the importance of a correctly aligned tracking system, as the residual distribution should always peak around 0 µm as this is the reference position of the particle tracks.

### *4.3.2 Commissioning of the Beam Telescope*

Being able to reconstruct particle tracks, the next step is to characterise the performance of the beam telescope and the DUTs. The main parameter for this is the *detector efficiency*, which is defined as the ratio between the number of times when a detector recorded a particle interaction that is part of a track $N_{\text{det}}$ and the number of particle tracks reconstructed with the beam telescope $N_{\text{tracks}}$, using only the tracking detectors:

$$\varepsilon_{\text{det}} = \frac{N_{\text{det}}}{N_{\text{tracks}}} \; . \tag{4.8}$$

Effectively it describes, how likely it is that a cluster in a detector can be matched to a track. Another quantity that can be useful to describe the performance of the

---

[21] See equation (5.13) for the definition.

beam telescope is the *tracking efficiency*, which can be understood as how likely it is to reconstruct the track of a particle. This requires precise knowledge of the true number of particles, which would require a second beam telescope as a reference, in order to determine the combined performance of tracking detectors, read-out electronics and track reconstruction software. For the track reconstruction itself, it would be possible to estimate the performance with Monte Carlo methods. Because at the time of the test beam campaigns it was not possible to either use a second reference beam telescope or to match the data from two telescopes, the tracking efficiency is not determined in the following and the focus is kept on the detector efficiency.

The starting point is to determine the efficiency of the tracking detectors. For this, a slightly adjusted efficiency definition is used, compared to equation (4.8). Instead of relying on the other GEM detectors which are also read out with VMM3a/SRS, the three scintillators with connected PMTs[22] that are also mounted on the beam telescope are used. Their signals are processed by a NIM coincidence unit, and it is assumed that the coincidence unit only sends signals in case a particle interacted inside the scintillators[23] The coincidence signals are matched with the GEM detector clusters, such that if a GEM detector recorded at least one potential particle interaction within a time difference of ±500 ns compared to the coincidence signal[24] it is assumed that this detector is part of the particle interaction and hence allows to reconstruct tracks. This means that the likelihood that a tracking detector is part of an event is investigated[25] (figure 4.16). It can be seen that all three tracking stations behave similar, with an increasing efficiency for higher detector gains. To reach efficiencies $\gtrsim 95\,\%$, it is necessary to operate the tracking detectors at gains $> 10^4$. Hence, to be as efficient as possible during the test beam measurements, the tracking stations were operated at gains between 20 000 and 30 000. The electronics threshold level is set to 15 mV above baseline for each channel in each tracking detector, which corresponds to 1.5 fC or $10^4$ electrons[26].

After investigating the tracking detectors, in the following the efficiency of the COMPASS-like triple-GEM detector under test (figure 4.17) is investigated, using

---

[22] Two scintillators are placed in front of the first tracking detector (T1) and the third one is placed behind the last tracking detector (T3).

[23] The assumption was later validated as in the time in between the particle spills, so when it is impossible that beam particles interact in the scintillators, no output signals from the coincidence unit were observed.

[24] The value of ±500 ns may seem again very wide. The choice is motivated by the goal to use the same time interval of 1000 ns as used for the event building.

[25] Ideally it would be investigated if a track or an event found with anamicom can be matched with the coincidence signals. This would however require a trigger counter [75], which was not available in the standard test beam set-up and only later integrated for VMM3a/SRS (section 6.3). However, to get an estimation of the tracking capabilities, the approach used here is considered sufficient.

[26] The determination procedure of the threshold level is described in the next paragraph.

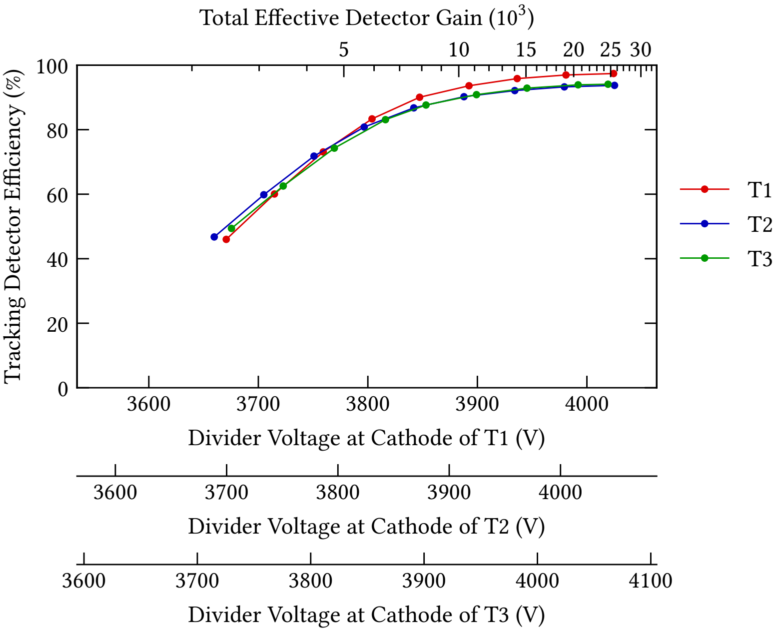

*Figure 4.16* – Efficiency of the three tracking stations T1, T2 and T3 depending on the total effective detector gain and the voltage applied to the voltage divider of the detectors. In terms of gain, the detectors behave similar, while in terms of voltage needed to achieve the corresponding gains, the detectors behave slightly different. Due to the overlap of the data series and to still distinguish the data points, the uncertainties of them are not shown; the uncertainties on the voltage are of the order of 2 % of the voltage value, while the uncertainty on the efficiency is of the order of around 3 %.

equation (4.8) and the particle tracks reconstructed with the tracking detectors. The plot combines the efficiency of the different read-out plane settings. This means that the cluster being part of the track counted for $N_{\mathrm{det}}$ is either part of the $x$-plane, the $y$-plane or both planes at the same time. Common to the plane settings is the difference between the $x$-plane on the one hand and the $y$-plane and both planes combined on the other hand. This is due to a charge sharing of 60/40 % between the $x$ and $y$-coordinate for this particular detector, with less charge collected in the $y$-coordinate. Requiring then, that a cluster is found in both coordinates means that this process is dominated by the $y$-plane, which explains the overlap between the $y$-plane efficiency and the one for both planes. In addition to the splitting between the planes, a strong threshold dependence can be observed. The larger the threshold, the more charge information is not accessible and the lower the efficiency. In case of the lowest operation threshold of around 1.5 fC (figure 4.17) the procedure to set the threshold should be recalled. First, the threshold levels for each read-out channel were equalised such that they are triggered at the same input charge. Afterwards, the

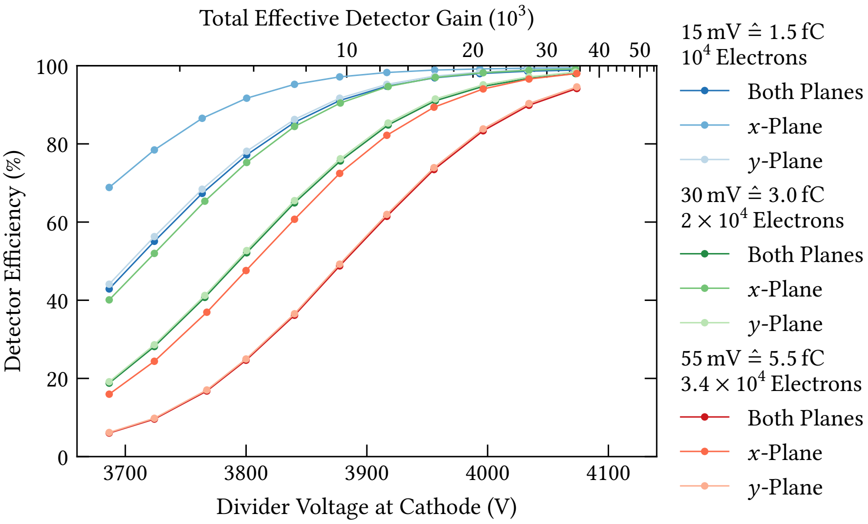

*Figure 4.17* – Plot of the detector efficiencies of the DUT, depending on the voltage applied to the voltage divider, the corresponding detector gain and the threshold level per read-out channel. The error bars are not shown for the sake of better distinguishing the different data series. However, the uncertainties on the detector efficiency are of the order of 3 %, while the uncertainties on the voltage are of the order of 2 %, similar to the gain plot (figure 4.3).

THLs were adjusted to values as low as possible, while pursuing in parallel further grounding to reduce external signals coupling into the detector as well as masking[27] particularly noisy channels. For this the following rough condition was applied: the hit rate in the data stream of the entire system of three tracking stations and the corresponding DUT should not be larger than around $\mathcal{O}(500)$ hits per network package[28], for 100 recorded packages. The recording time for the packages should be around 3 s. This choice[29] may seem arbitrary, however, it was driven by the decision to not acquire too many hits in the time in between SPS spills to avoid excessive data storage. While during the spill the network packages contain mainly hits and almost no Markers (section 2.3.3) due to the higher data rate, outside of the spill the Markers make up two-thirds of the data[30]. However, as the Markers are needed for a correct time calculation, an increased noise rate would reduce the relative contribution of the Markers to the data storage, but the absolute storage would

---

[27] Often it was sufficient to not mask the channel entirely but to increase the individual channel threshold with the trimmers by a few mV.

[28] This means around $\mathcal{O}(500)$ packages per FEC, as each FEC sends its own network packages.

[29] In fact, this was the choice for this particular test beam. Depending on the experimental conditions also different THLs can be selected based on how many noise hits are accepted.

[30] Each network package stores 1500 hits or Markers, so in case 500 noise hits are allowed per package, two-thirds of the data are Markers.

increase. Thus, the problem of data storage described in the following is purely based on the hits that are stored. The hit rate is about 16 kHz of noise (from three tracking detectors and one DUT combined) compared to the hit rate of around $\mathcal{O}(500\,\mathrm{kHz})$ (again for four detectors combined) generated by the interacting particles during the spill. Calculating the ratio between these two numbers gives that less than 5 % of the stored hits originate from noise.

If more noise hits can be accepted[31] or the detector grounding is further optimised, even lower THLs should be possible. For the medium threshold level of around 3 fC, the noise hits already disappeared, while for the large threshold of around 5.5 fC (figure 4.17) it should be remarked that this value was mainly picked for academic purposes as it is not a reasonable choice for MIPs anymore. The strong threshold dependence shows that an important part of the beam telescope's commissioning has to be spent on threshold optimisation.

The commissioning process of the beam telescopes shows that VMM3a/SRS allows to read out particle detectors for minimum ionising interactions. Efficiencies of $\gtrsim$ 95 % can be reached with detector gains of $10^4$ and more, while at the same time operating at a threshold of 1.5 fC per read-out channel. Higher efficiencies at lower gains might be reached when accepting more noise hits or when it is managed to further decrease the noise level of the detector. This might not be considered ideal, however, the values are not too far off from the numbers found for the original COMPASS triple-GEM detectors which reached the efficiency plateau at a gain of around 8000 [66]. Another important aspect of the efficiencies should be recalled: VMM3a/SRS operates in its self-triggered continuous read-out mode. This means for the case of an efficiency of 95 %, that 95 % of the interactions from all particles contained in the beam spill are recorded and reconstructed[32].

---

[31] Here it should be noted that during the test beam also lower threshold levels of 1.25 fC and 1.0 fC were tested. Runs with these thresholds were in the end discarded due to a large amount of recorded noise. In the case of 1.5 fC THL, the raw data `.pcapng` file had typically a size of around 100 MB recorded with four detectors. When lowering the THL only on the DUT to 1.25 fC, the file size increased to 200 MB, while in the case of 1.0 fC the file size increased to around 1 GB due to the additionally acquired noise hits.

[32] This requires though that no hit information is lost due to bandwidth limitations (section 5.1), which for the case of the muon beam with which most of the presented measurements were performed is a valid assumption (section 5.1).

*Chapter 5*

# LABORATORY AND TEST BEAM MEASUREMENTS

In the following chapter, the various measurements to characterise the detector and electronics performance, either with X-rays or with MIPs, are presented. The measurements focus each on a different quantity (flux, position, time and energy), which can be measured with the detector and the electronics. The starting point is the high rate-capability. Triple-GEM detectors can operate at rates up to several MHz/mm$^2$ [67, 69], and are thus an ideal device to investigate the rate-capability of VMM3a/SRS and explore its rate limits (section 5.1). Afterwards, spatial resolution studies and position reconstruction methods are presented (section 5.2), as this is of particular interest for imaging applications as well as for particle tracking over large areas with tens of micrometre spatial resolution. For this, calculations, X-ray imaging studies and measurements with the beam telescope are used. The latter is also used to determine the time resolution of the detectors (section 5.3). With the time resolution of GEM detectors being of the order of ten nanoseconds, it allows to demonstrate that VMM3a/SRS provides an integrated read-out system with which many parameters of a detector can be characterised. The energy resolution is the parameter, that the last part focuses on (section 5.4).

## 5.1 RATE-CAPABILITY

One of the VMM3a's key features is its rate-capability, especially in combination with its self-triggered continuous read-out. Particularly for imaging applications with X-rays or neutrons, this is advantageous as it allows to record the signals from the interacting particles without requiring any external trigger logic or frame-based read-out. To understand the limits of the read-out capabilities, various studies with randomly occurring hits from X-ray interactions have been performed (section 5.1.1), also to enhance the rate-capability studies with test pulses (section 3.6). Afterwards, measurements performed with charged particles during the test beam campaigns are shown (section 5.1.2). For both cases, application examples are given (section 5.1.3).

### *5.1.1 Studies with X-Rays*

The rate-capability studies with X-rays were performed with the laboratory set-up[1] (section 4.2). The sufficiently high particle rates in the $O(10\,\text{MHz})$ regime that are needed for the studies can be only achieved with the X-ray generator. It was operated at an acceleration voltage of 20 kV. The hardware configuration of VMM3a/SRS was optimised to achieve the highest possible data rates: since one Hybrid can almost saturate the bandwidth of the FEC's gigabit Ethernet transceiver, only a single hybrid was connected to one FEC, with a total of two FECs used. One FEC was used to read the $x$-strips of the detector and the other one to read the $y$-strips. Thus, the actively read out detector area was reduced to $5 \times 5\,\text{cm}^2$. To ensure that the photons interact only in this area, the rest of the detector was shielded with absorbers. For the measurements, the neighbouring-logic was enabled, as it is beneficial for the position reconstruction, when performing X-ray imaging applications (section 5.2).

The first goal is to find the rate saturation limits. For this, the active detector area was uniformly irradiated with X-rays. The anode current of the X-ray tube was increased, while at each current setting data were acquired for 10 s; the larger the X-ray tube current, the larger is the number of generated and thus interacting photons in the active detector area, leading to an increased data rate in the read-out system. The extracted hit rate saturates (figure 5.1), with the saturation level being very close to what is expected from the token clock, with 8 MHz for the Bonn firmware and $8.\bar{8}$ MHz for the ESS firmware (section 2.3.1). Each hit is driven out of a VMM3a with the token passing scheme (section 2.3.1), with the maximum possible hit rate being the CKTK frequency. With two Hybrids and thus four VMMs, the saturation levels should be the sum of the four VMMs, as no other bandwidth limit (should) exist in the chosen electronics configuration. At this point, almost every read-out channel, despite receiving signals randomly in position and time, contains a hit in its buffer, which has to be read out via the token, meaning that this is the limiting factor.

From the recorded hits, the clusters were reconstructed to understand the limit in terms of particle interaction rates and how the hit saturation affects the clustering procedure (figure 5.2). It can be seen that the plane cluster rate saturates, similar to the hit rate, and hence being explained by the bandwidth limits of the read-out electronics. However, the measured rate for the detector clusters decreases after reaching a maximum. The maximum rate is also lower than the plane cluster rate at the same X-ray tube current. It is a result of the bandwidth limit in combination with the cluster matching between the read-out planes and can be illustrated in terms of matching probabilities between the two read-out planes (figure 5.3). Due to rate

---

[1] Detector gain of around $10^4$, electronics gain of 3.0 mV/fC and 4.5 mV/fC, peaking time of 200 ns, TAC slope of 60 ns and a threshold level of around 40 mV, without channel-by-channel equalisation. Unless further specified, the neighbouring-logic was enabled.

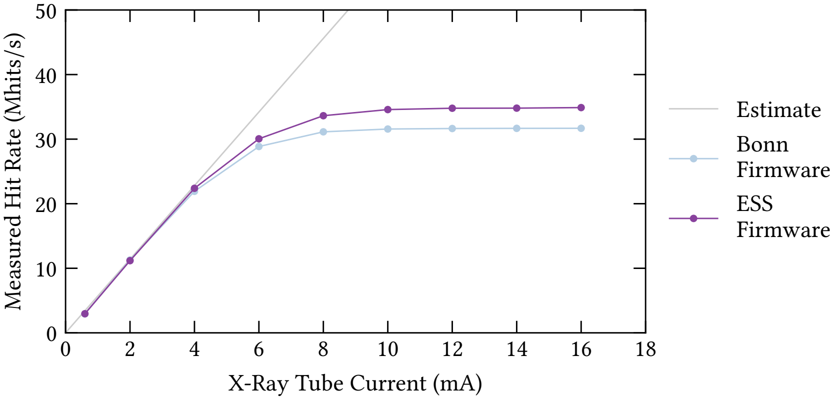

*Figure 5.1* – Dependence of the measured hit rate, so the number of read out VMM channels per second, on the anode current of the X-ray tube for the two Hybrid firmware versions. The estimate indicates the expected hit rate if there would be no bandwidth limit in the read-out chain. Each data point corresponds to an acquisition time of 10 s. The error bars on the data points are $< 0.2$ ‰ of the value and thus so small that they would not be visible and are hence not plotted. Data published in [41].

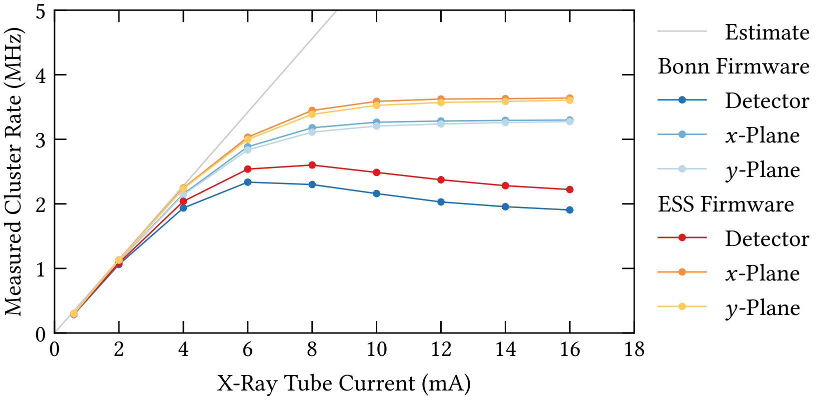

*Figure 5.2* – Dependence of the measured cluster rate on the X-ray tube's anode current for the two Hybrid firmware versions. The estimate indicates the expected measured interaction rate if there would be no bandwidth limit. Each data point corresponds to an acquisition time of 10 s. The error bars on the data points are $< 0.6$ ‰ of the value and thus so small that they would not be visible and are hence not plotted. For both firmware versions, the saturation of the cluster rate in the individual read-out planes can be seen, while for the detector cluster with a matching between $x$-plane and $y$-plane, a decrease in the measured rate can be observed. Data published in [41].

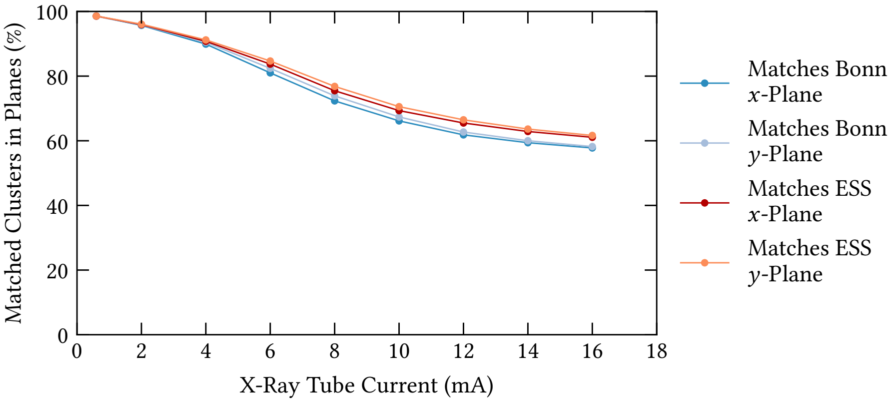

*Figure 5.3* – Fraction of plane clusters that are part of a detector cluster, so where the clusters in the $x$-plane and the $y$-plane could be matched, depending on the X-ray tube's anode current. The error bars on the data points are $< 0.08\,\%$ and thus so small that they would not be visible and are hence not plotted. Data published in [41].

saturation in each plane, the data that would lead to a cluster is lost and not processed. Then, a plane cluster can be for example reconstructed from the hit information on the $x$-plane, but the corresponding hits in the $y$-plane are not processed due to the bandwidth limit and thus no detector cluster can be matched. The larger the X-ray currents, the less efficient becomes the plane matching, as the probability to lose/not process the hits belonging to an X-ray interaction increases. It should be noted that the described behaviour for the cluster rate saturation, both for the plane and the detector clusters is related to the fact that a two-layer strip read-out anode with a 1:1 strip-to-channel mapping is used and that this behaviour may be different when other read-out geometries are used.

In both plots of the measured rate (figures 5.1 and 5.2), also an estimate of the expected rate is given. From previous measurements [69] with this X-ray generator, it is known that the photon flux depends linearly on the anode current for the chosen operating conditions. For the low X-ray anode current regime $I_\mathrm{a} \leq 4\,\mathrm{mA}$ the cluster rates are compatible with rate measurements performed by reading out the signals induced on the bottom side of the last GEM, using a pre-amplifier, a shaper and an oscilloscope (section 4.2). The estimated cluster rate $\nu_\mathrm{c}$, calculated from the VMM3a/SRS data, follows an expected linear fit to the first three data points, giving $\nu_\mathrm{c}(I_\mathrm{a}) = 0.57\,\mathrm{MHz/mA} \times I_\mathrm{a}$. It is assumed that in this regime the measured rate corresponds to the expected rate without significant hit losses. This is further confirmed by the two firmware versions that give the same cluster rates in this regime despite their different rate behaviour.

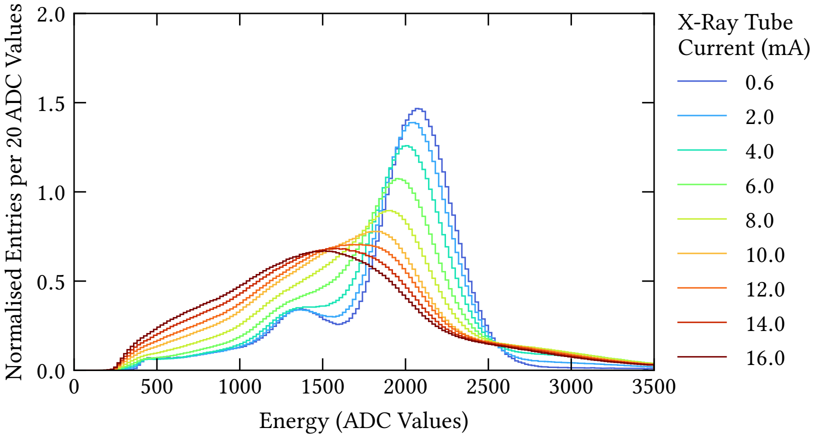

*Figure 5.4* – Recorded X-ray spectra depending on the X-ray tube current. Here recorded with the Bonn firmware. The X-ray tube currents lead to particle fluxes between 14 kHz/cm$^2$ for 0.6 mA and 365 kHz/cm$^2$ for 16 mA. The values were calculated with the formula for the rate estimation, $\nu_c(I_a) = 0.57\,\text{MHz/mA} \times I_a$ and an irradiated area of 25 cm$^2$. Data published in [41].

The investigation of the rate behaviour is continued with the study on the effects that the bandwidth limitation has on the data quality. For that purpose, the energy spectrum of each data point is plotted (figure 5.4). With increasing photon flux, the quality of the spectra gets worse, particularly for X-ray tube currents $\geq$ 8 mA, where the bandwidth limit is reached. The explanation for this is found in the CKTK and the round-robin token passing, where each channel is read after one another, going over each channel with raised data flag. As each channel can buffer only a single hit and is only able to store a new hit, after the previously buffered hit is read out, this means that some hits can be lost. The higher the irradiation density and the more channels are available that could potentially store a hit, the more likely it is to happen that a hit is not stored within the same channel. This is because more hits need to be read out in one token round and hence it takes more time to read out the same channel twice.

To confirm the explanation, the distributions of the time differences between acquired hits (figure 5.5) are studied, depending on the number of ***Active Channels per Hybrid*** (ACPH). The idea is that the more channels are active and have to be read out, the longer it takes to pass the token again to the same channel and to read out the next hit. By reducing the ACPH, the token passing for one round takes less time, meaning that the channels blocked with data are freed earlier. Hence, fewer hits are likely to be lost, resulting in the time difference between two consecutively read out hits on the same channel becoming smaller.

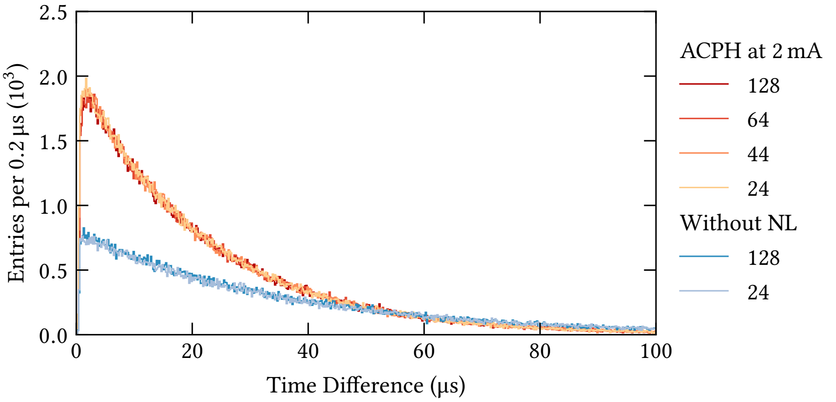

*(a)* – 2 mA X-ray tube anode current.

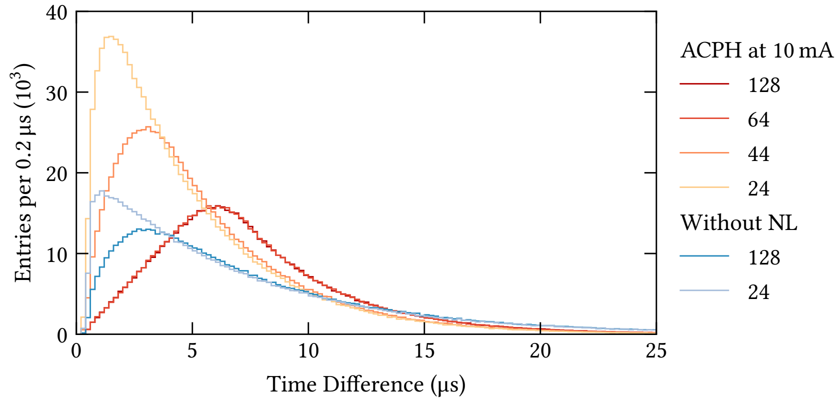

*(b)* – 10 mA X-ray tube anode current.

*Figure 5.5* – Time difference distributions for an X-ray tube anode current of (a) 2 mA and (b) 10 mA, recorded with the Bonn firmware. The plotted time differences are the ones between two consecutive hits on the same read-out channel, but for a different number of ***A****ctive* ***C****hannels* ***p****er* ***H****ybrid* (ACPH). Data published in [41].

For these studies, the detector and X-ray set-up remained the same, while more and more adjacent VMM channels were masked to reduce the ACPH. In the case of a low X-ray tube current (2 mA), all time difference distributions have the same shape, independent of the number of channels that had to be read out. When turning off the neighbouring-logic, only the absolute number of hits changed, but not the general behaviour. At a larger X-ray tube current (10 mA), where the bandwidth limitation is evident (figure 5.1), the expected effect becomes visible. First, no difference is observed between 128 ACPH to 64 ACPH, so masking the channels from an entire ASIC, while when reducing the number of active channels on a single VMM, a difference is observed. This confirms that the responsible bandwidth limit has to be on the ASIC and not on the read-out chain afterwards. Second, there is the expected effect observed of the peak in the time difference distribution moving towards smaller time differences when fewer channels are active and have to be read out. The same is observed, when the NL is disabled, so also when fewer channels have to be read out. This confirms that the round-robin-like token passing limits the bandwidth, affecting the data quality at high rates.

Having established these results, it can be seen that the ESS firmware is around 11 % faster than the Bonn firmware, which is exactly the difference in the CKTK and SERDES clocks. However, even if the maximum achievable hit rates are affected by this, the problem of information loss and degraded energy resolution occurs already below the maximum where the recorded data rates between the two firmware versions are comparable. Hence there is effectively, in terms of data rate, no relevant difference between the two versions.

### *5.1.2 Test Beam Results*

In addition to the X-ray studies, the rate-performance of VMM3a/SRS was also tested during the test beam campaigns. The electronics set-up was again optimised for rate studies, meaning that only a single detector was read out per FEC, so four Hybrids per FEC. Similar to the X-ray studies, the rate of the particle beam, here 80 GeV/$c$ pions, was increased over various steps. Different to the X-ray studies, an expected number of particles per spill could be easily provided by the beam instrumentation of the H4 beam line, specifically the scintillator particle counters. In terms of rate, it is important to note that here the number of particles per spill is studied, with each spill having a length of around 5 s.

For studying the rate-behaviour, the number of reconstructed clusters per spill is compared with the number of particles per spill recorded with the beam counters (figure 5.6). This comparison is done for two detectors, one of the tracking stations and a COMPASS-like triple-GEM detector under test[2]. It can be seen that at lower rates, with $\mathcal{O}(10^6)$ particles per spill or less, the number of reconstructed clusters agrees with the expected numbers of particles or even exceeds them. As the noise hit rate is below $\mathcal{O}(100\,\mathrm{Hz})$ this can be excluded as a possible explanation for the deviation to higher hit values. However, during the test beam campaign, other set-ups were located in front of the RD51 VMM3a/SRS beam telescope, meaning that

---

[2] The detector was operated at a gain of around 30 000, the electronics gain was 9 mV/fC, the peaking time was set to 200 ns and the TAC slope was set to 60 ns. The neighbouring-logic was enabled, with a threshold of 55 mV above baseline without channel-by-channel equalisation.

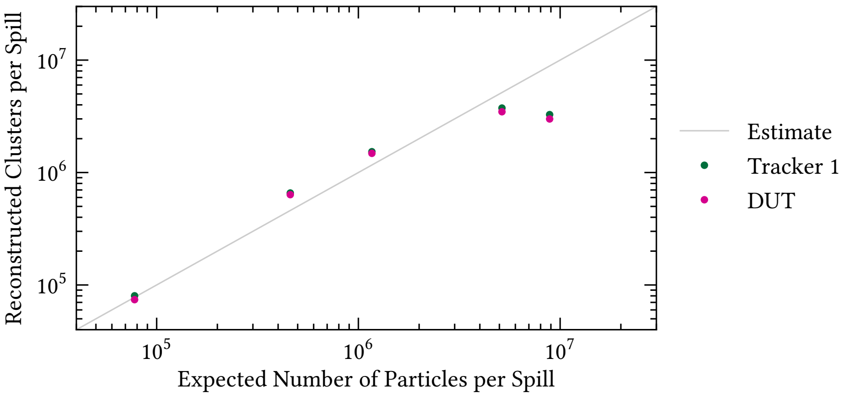

*Figure 5.6* – Number of reconstructed clusters per beam spill versus the expected number of beam particles for two different detectors in the beam telescope. The estimate indicates the unity relation from the expected number of particles. The error bars are smaller than < 3 ‰ of the values and are hence not plotted for visibility purposes.

the pions could create showers in those set-ups, leading to multiple particles, which are then detected by the detectors in the beam telescope. For the spills with $5 \times 10^6$ particles or 1 MHz of particle rate or more, it can be seen (figure 5.6) that the number of reconstructed clusters drops below the expectation. This can be explained with the same data loss per VMM caused by the token loop.

The earlier start of this behaviour in terms of absolute interaction rates (around 1 MHz for the pion beam versus several MHz for the X-ray studies) is caused by the irradiation density. While in the case of X-rays an area of 25 $\text{cm}^2$ was read out, the centre of the pion beam covers an area between around 1 $\text{cm}^2$ and 3 $\text{cm}^2$, depending on the rate[3]. Hence, the rate per area or read-out channel can be even higher for a localised pion beam than for a uniformly irradiated area, while the hit loss still takes place at a lower total particle rate.

As a result, it can be concluded from the X-ray and beam measurements, that the exact particle rate that can be recorded with VMM3a/SRS depends both, on the irradiation density and the number of channels in the irradiated area that have to be read out. For the case of the RD51 test beams at the H4 beamline of the SPS, it is possible to record pion beams with close to $5 \times 10^6$ particles per spill. In terms of order of magnitude, this would become also the limit for muon beams, here

---

[3] In order to change the particle rate of the secondary beam during the test beam, not the intensity of the primary beam on the target is changed, but the collimator, absorber and magnet settings of the secondary beam line are changed. As a result, not only the particle rate increases, but also the area of the beam spot, especially in the case of pions.

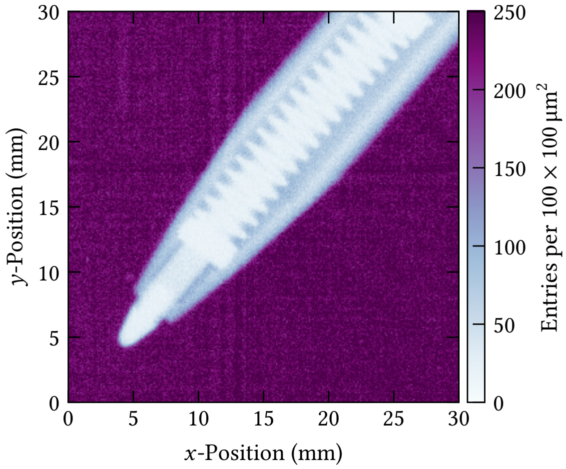

*Figure 5.7* – X-ray image of the tip of a pen. While the full data run contains $50 \times 10^6$ reconstructed clusters, the image consists only of $17 \times 10^6$ reconstructed clusters, with an acquisition time of 30 s. Published in [41].

however driven by the gigabit Ethernet of the FEC. With the muon beams being much wider in diameter (around 8 cm), the irradiation density is much lower. As each FEC handles up to 20 Mhits/s, the interaction rate could be maximally around 2.5 MHz with muons, using a cluster size of around 4 strips per read-out plane and assuming that only one detector with $x$-$y$-strip anode is read out per FEC. If more detectors are read out, the maximum would be further reduced (table 3.1).

### 5.1.3 *Examples of High-Rate Applications*

After the numerical studies, some measurements to highlight the application of the rate-capability of VMM3a/SRS are shown in the following. At first, two examples of X-ray imaging are shown. The measurements were performed with the same set-up as for the limitation studies with X-rays (section 5.1.1), but with the acceleration voltage set to 18 kV and the X-ray tube current being fixed to 5 mA. The first image shows a pen, with the image consisting of $17 \times 10^6$ clusters (figure 5.7), which is only an excerpt of the fully irradiated area, where $50 \times 10^6$ clusters have been recorded within 30 s. Analogous, an X-ray image of a bat was recorded (figure 5.8). The $279 \times 10^6$ clusters have been acquired in 3 minutes, with the image containing here the entire irradiated area. It should be noted that both images contain the raw position information extracted from the reconstructed clusters. No further image optimisation and processing (e.g. filtering or correcting for detector non-uniformities) was applied.

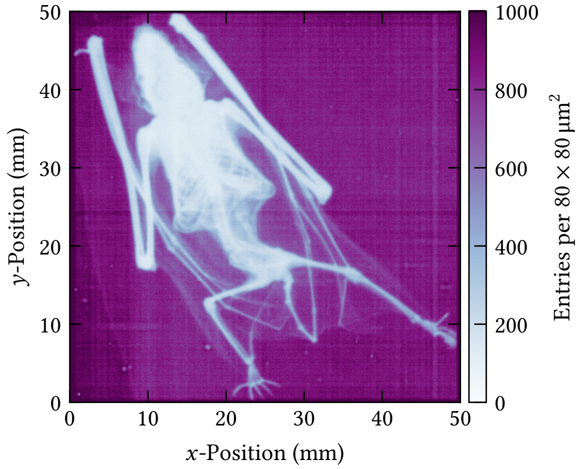

*Figure 5.8* – X-ray image of a bat. It consists out of $279 \times 10^6$ reconstructed clusters, with an acquisition time of 180 s. Published in [41].

In addition to the radiography, providing stationary images, the high rate-capability of VMM3a/SRS in combination with the continuous self-triggered read-out allows also to perform fluoroscopy, i.e. the imaging of moving objects. For this, on the one hand, the opening of the X-ray tube's shutter[4] was recorded (figure 5.9a) and on the other hand, the rotating blades of a fan (figure 5.9b). In both cases, the continuous data stream was sliced into frames of 2 ms length. For the fan, where each frame contains about 4000 clusters, the X-ray tube voltage was reduced to 16 kV, to decrease the higher energy Bremsstrahlung part of the spectrum. This in combination with copper tape that has been added to the fan's blades was done to increase the photon absorption.

The continuous self-triggered read-out provides also advantages for the operation with MIPs. In this particular example, it was possible to record around $10^6$ particles of the secondary beam in the H4 beam line of the CERN SPS. This allows to reconstruct the time profile of the beam spill, as well as, by integrating the time profile, the structure of the extraction of the primary beam from the SPS towards the North Area (figure 5.10a). The latter is confirmed by the beam monitoring provided for the CERN SPS (figure 5.10b). The observed structure is a result of the SPS operation, which at the time of the measurement (July 2021), was still in its beam tuning phase after resuming operation a week before the measurement. However, due to

---

[4] For this measurement it should be noted that e.g. for studying immediate charging up effects directly after the start of the irradiation, it is important to know the opening time of the X-ray tube's shutter, which could be provided with VMM3a/SRS.

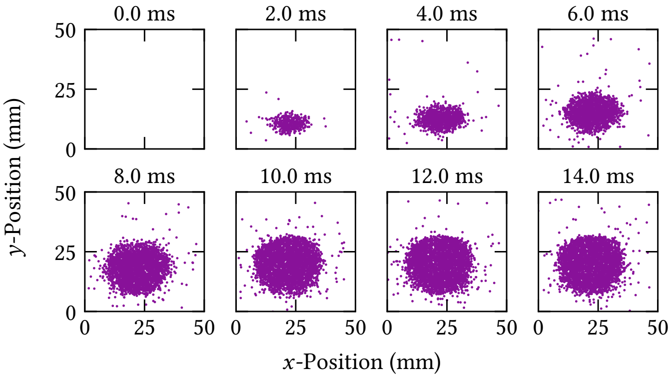

*(a)* – Opening of the X-ray tube's shutter.

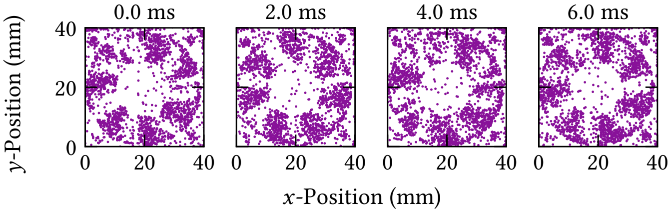

*(b)* – Rotating fan.

*Figure 5.9* – Examples of the capabilities of recording moving processes with VMM3a/SRS due to the continuous self-triggered read-out. Published in [41].

this measurement, the RD51 VMM3a/SRS beam telescope was then also used in the following test beam campaigns to provide live feedback on the beam structure, especially in terms of the geometrical beam profile and the time profile of the spill (figure 5.11).

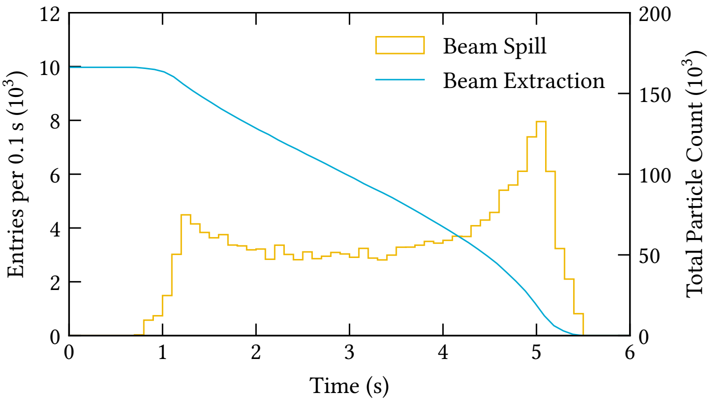

*(a)* – Measured SPS spill structure.

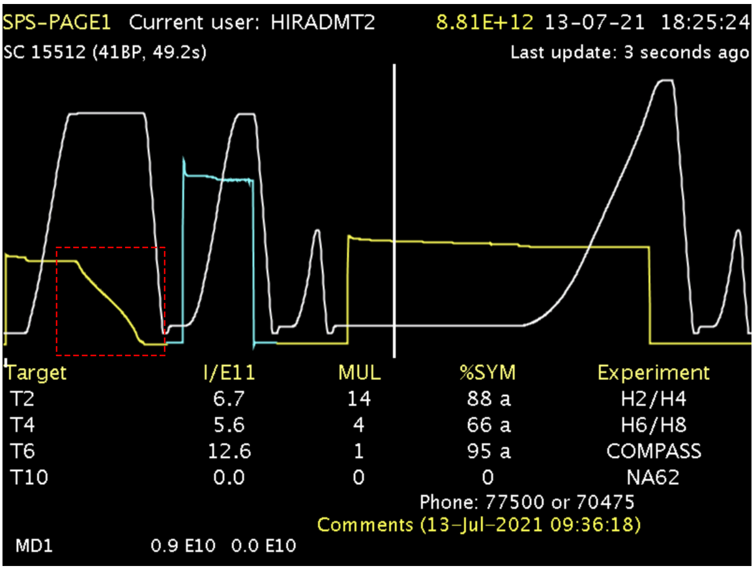

SPS-PAGE1 Current user: HIRADMT2 8.81E+12 13-07-21 18:25:24

SC 15512 (41BP, 49.2s) Last update: 3 seconds ago

| Target | I/E11 | MUL | %SYM | Experiment |
|---|---|---|---|---|
| T2 | 6.7 | 14 | 88 a | H2/H4 |
| T4 | 5.6 | 4 | 66 a | H6/H8 |
| T6 | 12.6 | 1 | 95 a | COMPASS |
| T10 | 0.0 | 0 | 0 | NA62 |

Phone: 77500 or 70475

Comments (13-Jul-2021 09:36:18)

MD1 0.9 E10 0.0 E10

*(b)* – Screenshot of the SPS status monitor (SPS Page 1).

*Figure 5.10* – Time profile of a spill from the SPS extracted to the CERN North Area and the corresponding extraction profile generated from the spill structure (a). The extraction profile is compatible with the observations from the SPS status monitor surrounded by the dashed line (b).

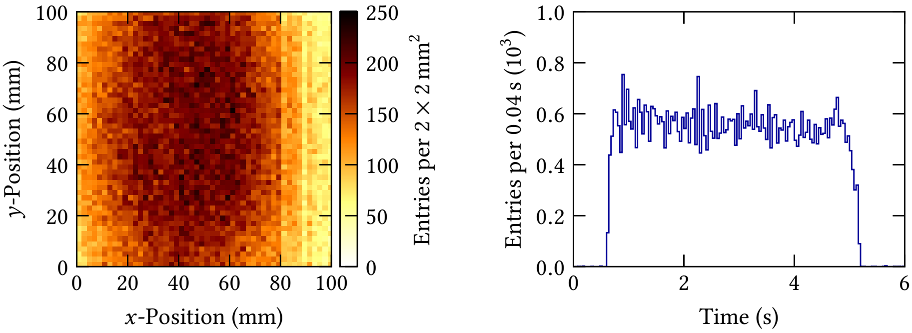

*(a)* – Muon beam image. *(b)* – Muon spill profile.

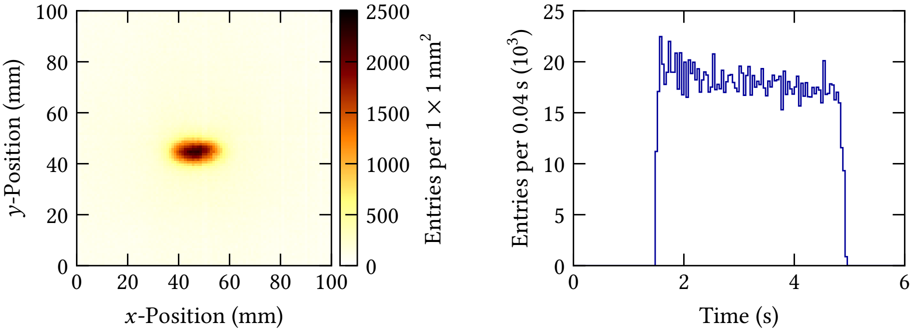

*(c)* – Pion beam image. *(d)* – Pion spill profile.

*Figure 5.11* – Examples for the 2D image of the muon (a) and the pion (c) beams and their corresponding spill time profiles for muons (b) and pions (d), with the beam extraction being a bit shorter than the typical 5 s in this particular situation (d).

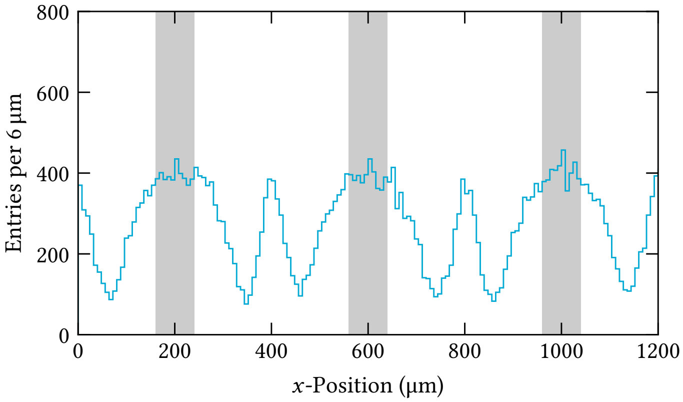

*Figure 5.12* – Example of the read-out modulation effect's on the reconstructed cluster position. The histogram is a projection of the reconstructed cluster positions on the $x$-axis, with the vertical bars indicating the position and the width of the anode strips in the $x$-plane. While here only the result for X-rays is shown, the behaviour is similar for MIPs.

## 5.2 SPATIAL RESOLUTION STUDIES

Having demonstrated that the capabilities of VMM3a/SRS are well suited for imaging applications, the next step is to study the image quality. For this, it is essential to understand the accuracy of the particle's reconstructed incidence position, which is not only important for imaging but also for tracking applications. The starting point is the observation of a well-known effect, where the distribution of the reconstructed positions contains a repeating pattern that follows the structure of the read-out electrodes (section 5.2.1). Afterwards, various methods to mitigate the effect are proposed (section 5.2.2). It is then investigated, if the mitigation is due to smoothing or because of more accurately reconstructed positions. For this, modelling studies (section 5.2.3), X-ray imaging methods using copper X-rays (sections 5.2.4 and 5.2.5) and position resolution measurements with a beam telescope are used (section 5.2.6).

### *5.2.1 Read-Out Modulation Effect*

When the position of a particle is reconstructed with the COG method as shown in equation (4.6) and the corresponding distribution of the calculated cluster centres is visualised with a fine binning, a periodic pattern can be observed (figure 5.12). The underlying behaviour was already observed with ***M****ulti-****W****ire* ***P****roportional* ***C****hambers* (MWPCs) [78]. Its origin is a combination of a segmented read-out structure, a threshold-based read-out system and using COG position reconstruction (figure 5.13).

*(a)* – Odd cluster size count.

*(b)* – Even cluster size count.

*Figure 5.13* – Illustration of the origin of the read-out modulation. The charge distribution is discretised due to the integration of the charge over the read-out strips, with the height of the vertical bars indicating the charge amplitude recorded per strip. Only the solid bars surpass the threshold level (THL) and are hence used for the position reconstruction. The vertical solid line indicates the actual centre position of the charge cluster, while the vertical dashed line indicates the cluster's reconstructed position $x_c$. Published similarly in [79].

Despite consisting of discrete charge carriers, the charge cloud can be assumed as continuous distribution, due to the large number of electrons $\mathcal{O}(10^6)$. Because of the spreading of the charge cloud over several read-out strips and the integration of the charge signal along each strip, the charge information of the cloud gets discretised. Combining this with a threshold-based read-out system, where only signals above the threshold level are processed and accessible for the position reconstruction, this means that charge and position information are missing in the COG formula. Thus, small signals that only surpass the THL by a little amount, represent a slightly larger charge fraction compared to their actual charge fraction from the original charge cloud. As a result, the reconstructed position of the cluster gets forced in the direction of the central strip in case the cluster size has an odd strip count (figure 5.13a) or in between the two central strips in case of an even strip count cluster (figure 5.13b). This explains the repeating double peak structure observed in the position distribution, with one peak being aligned with the read-out strip and the other peak being centred between two strips.

A few remarks should be made on the given example for the modulation effect and the related investigations presented in the following. First, the modulation behaviour is not only observed with X-rays as in the example but also with MIPs. While in the case of X-rays, the detector area was uniformly irradiated, for MIPs this was not the case, due to the density profile of the particle beam. Second, for the X-ray measurements an energy cut is applied to reduce the effect of noise clusters in the position reconstruction (figure 5.14). For MIPs this is not necessary, as here only the clusters that are contained within a particle track are used, meaning that noise hits are strongly suppressed. The third remark is related to the threshold level, as the observed modulation is also a threshold effect. While the studies with MIPs have been performed with equalised threshold levels, including a threshold optimisation

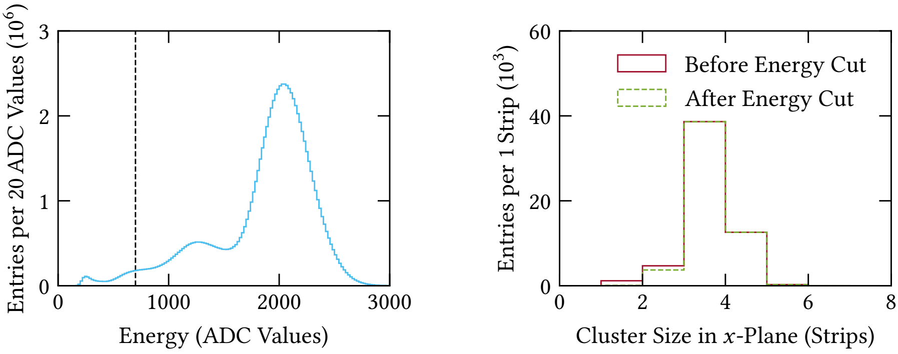

*(a)* – Energy cut.

*(b)* – Cluster size distribution.

*Figure 5.14* – Illustration of the energy spectrum from the copper target X-ray tube (a). The vertical dashed line indicates the position of the energy cut applied to the data for the X-ray imaging analysis. The distribution plot (b) shows the effect of the energy cut on the cluster size. Data published in [79].

to as low values as possible, this was not done for the X-ray studies. For the latter, the THL was chosen to record as few noise hits as possible without equalising the threshold levels, leading to a threshold of around 70 mV above the baseline. With an electronics gain of 3 mV/fC, this corresponds to a charge of 23 fC or around 10 % of the selected dynamic range. Although this can be regarded as a very high threshold level, the choice was accepted due to the high detector gain of around $10^4$ and the preserved good quality of the X-ray spectrum.

### *5.2.2 Mitigation of the Read-Out Modulation*

In the following, various approaches to mitigate the modulation effect by improving the position reconstruction and hence the spatial resolution are presented. A particular focus is put on a hardware approach, the ***N**eighbouring-**L**ogic* (NL) of the VMM3a (section 2.1.2), as it targets the problem of missing charge information. The NL allows to recover charge information below the threshold level, as a channel which surpasses the THL triggers the read-out of the left and right adjacent channel, even if they are below the threshold level (figure 5.15). It should be noted that, despite being triggered by the signal from an interacting particle, the neighbouring-logic may also acquire noise or signals with a bad signal-to-noise ratio. The consequences of this and how to potentially handle these situations are discussed in the classification of the results (section 5.2.7). So far, however, it can be seen that the position response for X-rays gets more uniform (figure 5.16), as it is expected for uniform irradiation. For MIPs, the modulation effect is still strongly visible, but nonetheless reducing the effect of single strip clusters, which are the spikes in the position distribution

*(a)* – Without NL. *(b)* – NL enabled.

*Figure 5.15* – Illustration of the neighbouring-logic's effect on the recorded charge distribution. With NL enabled, the adjacent channels below THL are read-out as well. Published similarly in [79].

that are aligned with the read-out strips (figure 5.16b). One of the main goals of the studies presented in the following sections is to understand if the NL recovers the charge information correctly. As the NL works on the VMM3a's channel level, it is important to note that a successful use of the NL with a particle detector requires that adjacent read-out electrodes are connected to adjacent VMM3a channels, as it is the case for COMPASS-like triple-GEM detectors.

With the read-out modulation problem already well-known before the existence of a hardware approach [78], various position reconstruction algorithms exist to mitigate the modulation effect and to improve the position reconstruction. It is important to note that the position reconstruction algorithms and the neighbouring-logic should not be considered as interchangeable alternatives, as they target different parts of the origin of the modulation effect. While the NL is supposed to recover missing charge information, the position reconstruction algorithms aim for an optimal handling of the existing charge information for the most accurate position determination. One of these algorithms, the $\eta$-method [75, 80], is recalled in the following, as it also allows to explore the read-out modulation from another point of view. The $\eta$-method is an iterative approach, where first the positions are reconstructed with COG. Afterwards, correction distributions are generated, for which first the difference between the cluster centre $x_\mathrm{c}$ and the centre of the nearest strip $s$ is calculated:

$$\eta = x_\mathrm{c} - s \; . \tag{5.1}$$

With the results being histogrammed (figure 5.17a), the number of expected entries $N_{b,\mathrm{exp}} = N_\mathrm{tot}/n$ is calculated for each bin $b$ from the total number of histogram entries $N_\mathrm{tot}$ and the number of bins $n$. This uses the assumption of a uniform position response. The correction functions are then calculated from the entry count difference $\Delta_b = N_b - N_{b,\mathrm{exp}}$ via

$$\delta\eta_b = \frac{\sum_{i=1}^{b} \Delta_i}{N_\mathrm{tot}} \; , \tag{5.2}$$

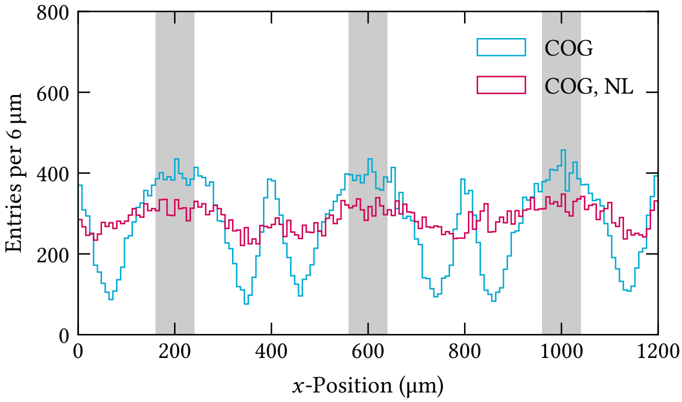

*(a)* – X-ray data.

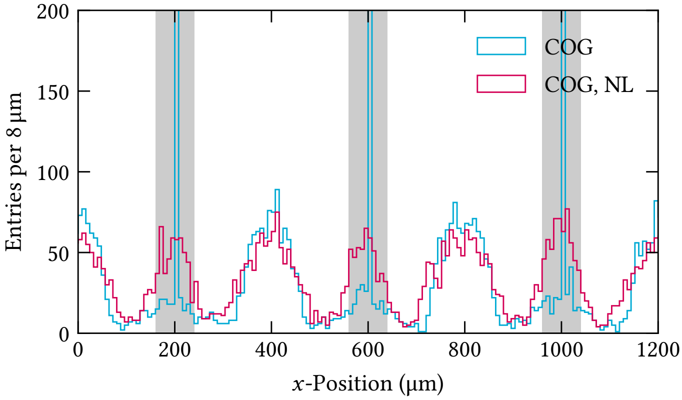

*(b)* – MIP data.

*Figure 5.16* – Position distributions for clusters reconstructed from X-rays (a) and MIPs (b), comparing the pure COG reconstruction and COG with enabled neighbouring-logic. The vertical bars indicate the positions of the anode strips. The spikes in the MIP data, which are aligned with the anode strips originate from single-strip clusters.

where $\delta\eta_b$ is the correction term for the position found in the corresponding $\eta$-bin (figure 5.17b). The corrected position of the cluster $x'_\mathrm{c}$ is calculated via

$$x'_\mathrm{c} = x_\mathrm{c} + \delta\eta_b \ . \tag{5.3}$$

When applied to the data, it can be seen that the position distribution gets completely uniform (figure 5.18).

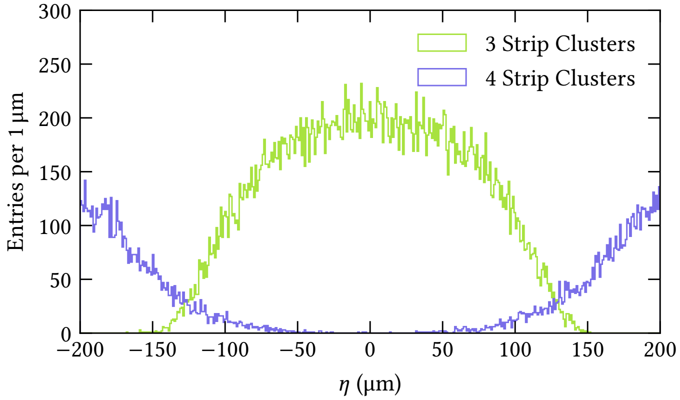

*(a)* – Examples of the $\eta$-distribution.

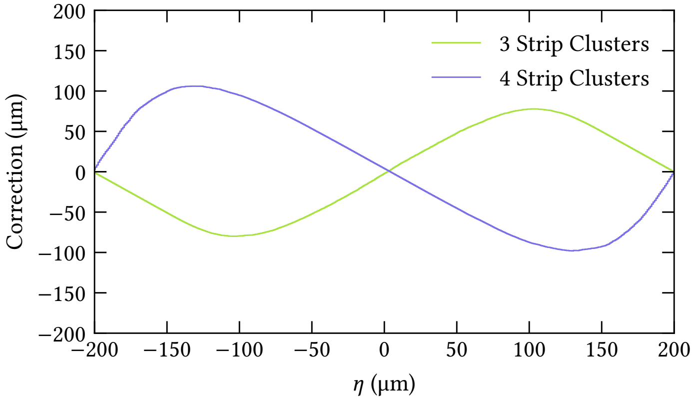

*(b)* – Examples of correction distributions.

*Figure 5.17* – Illustration of the $\eta$-method, with the initial distributions that illustrate the distance of the reconstructed cluster centre from the centre of the closest strip for two different cluster sizes (a) and the resulting correction functions (b) to flatten the position distribution.

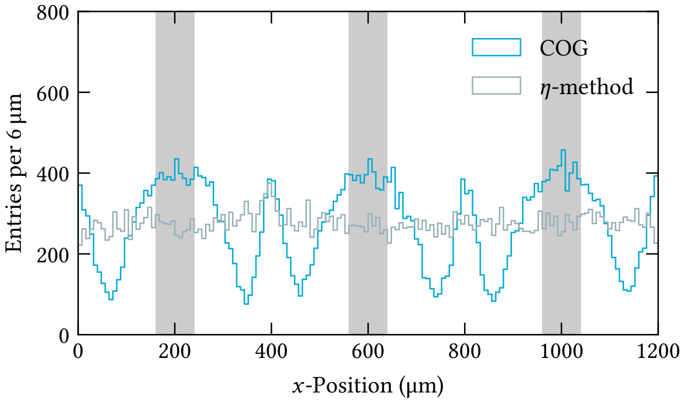

*Figure 5.18* – Comparison of the position distribution from the COG method without enabled NL, with the position distribution from the COG method after applying the $\eta$-correction. The vertical bars indicate the positions of the anode strips.

Another algorithm, originally proposed in a CERN Summer Student project [81], which is tested in this thesis, is the modification of the COG method. Instead of using an iterative algorithm which is based on the measured detector response, the modification of COG allows to keep an event-based algorithm without requiring previous data processing. It targets a different part of the read-out modulation's origin: the tails of the charge distribution which are just slightly above the THL. In order to give less weight to them, the COG formula is modified to

$$x_\mathrm{c} = \frac{\sum_i Q_i^n x_i}{\sum_i Q_i^n}\,, \tag{5.4}$$

with $n = 2$ being the parameter investigated in this thesis, while other values of $n$ have not been further studied. Despite the simplicity of this purely empirical approach, the $Q^2$ weighting reduces the read-out modulation (figure 5.19). The following studies focus mainly on the $Q^2$ method, intended to confirm that the flattening of the position distribution is a result of improved position reconstruction and not the consequence of a smoothing effect.

Both approaches to mitigate the modulation effect aim at different parts of the cause of the read-out modulation, with the NL being supposed to recover missing charge information below THL, and the $Q^2$ method being supposed to handle the existing charge information that surpasses just slightly the THL differently. Nonetheless, also their combination was studied, showing that the modulation effect gets even further reduced (figure 5.20).

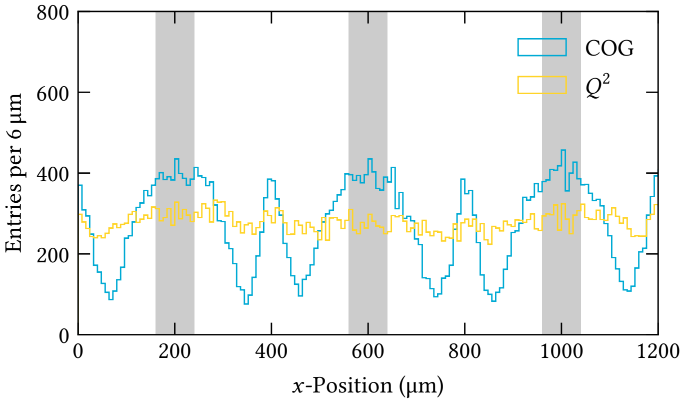

*(a)* – X-ray data.

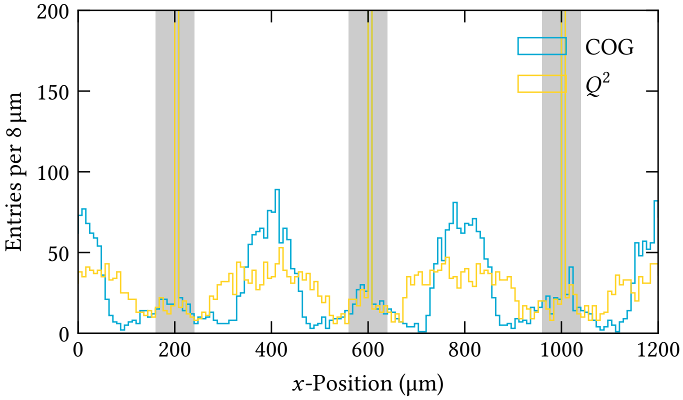

*(b)* – MIP data.

*Figure 5.19* – Position distributions for clusters reconstructed from X-rays (a) and MIPs (b), comparing the COG reconstruction with the $Q^2$ reconstruction, without enabled NL. The vertical bars indicate the positions of the anode strips. For the MIP data, it should be noted that the spikes, which originate from single-strip clusters, are contained in both data sets, with the $Q^2$ data overlapping the COG data.

It is important to note that among the presented data analysis approaches to mitigate the modulation effect only the $Q^2$ weighting method is further pursued. This is because the improvements in terms of flattening the position distribution when applying the $\eta$-method are not reflected by the improvements in terms of spatial resolution. On the one hand, there are results from other works [75], where the improvement by applying the $\eta$-correction was 'on the order of 10 %' [75] for some measurements, while other measurements showed 'improvements [that] are consid-

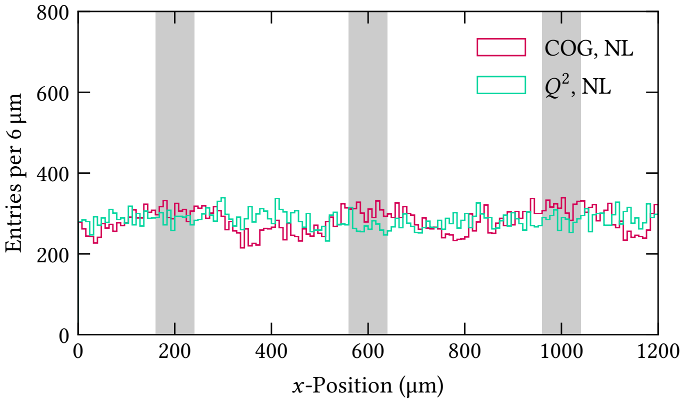

*(a)* – X-ray data.

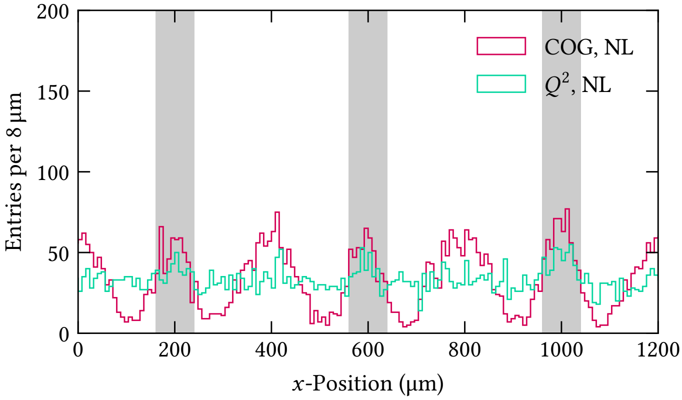

*(b)* – MIP data.

*Figure 5.20* – Position distributions for clusters reconstructed from X-rays (a) and MIPs (b), comparing the COG reconstruction with the $Q^2$ reconstruction, but with the neighbouring-logic being enabled in both cases. The vertical bars indicate the positions of the anode strips.

erably smaller' [75]. On the other hand, the two methods have been applied to a data set from a previous test beam campaign (pions with 150 GeV/$c$ momentum) presented in [7]. The data were taken with a different front-end electronics (APV25/SRS [10]), but using the same detector type and the same track reconstruction software as in this thesis. In the position distribution (figure 5.21), it can be seen that both methods flatten the distribution compared to the COG method. However, in terms of spatial resolution, it improves from $\sigma_{\mathrm{COG}} = (47 \pm 1)$ µm to $\sigma_{Q^2} = (42 \pm 1)$ µm when using $Q^2$ weighting, but decreases to $\sigma_\eta = (54 \pm 1)$ µm when using the $\eta$-method.

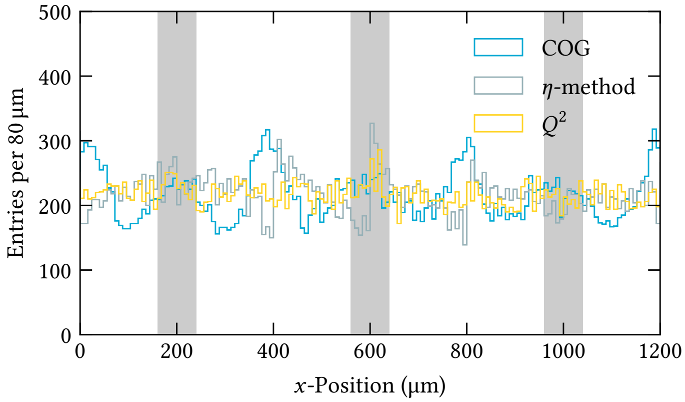

*Figure 5.21* – Position distribution recorded with MIPs (150 GeV/*c* pions), using a beam telescope read out with APV25/SRS. The vertical bars indicate the positions of the anode strips. Published in [79].

### *5.2.3 Modelling Studies*

In the following, modelling studies on the position reconstruction are presented. The goal is to understand the applicability and limitations of the previously presented approaches, particularly the $Q^2$ weighting method. Monte Carlo methods and numerical calculations were applied, using a simplified detector model close to the experimental set-up used in this thesis. Compared to the two-dimensional $x$-$y$-read-out of the detector, the Monte Carlo model contains only a one-dimensional read-out, representing one layer of the triple-GEM anode strips, with strip length not being kept at 10 cm but assumed to be infinitely long. The strip pitch is kept at 400 µm, while the strip width is increased. Instead of 80 µm wide $x$-strips of the detector, the strips in the model have a width of 240 µm, as the charge collection is performed geometrically. This effective strip width originates from the charge sharing ratio of the test detector, which is not 50/50 %, but 60/40 %.

To be able to perform the position reconstruction with COG or $Q^2$, it is necessary to calculate the induced charge $Q_i$ per strip $i$, for which a double Gaussian distribution was used which represents the diffusing charge cloud:

$$\begin{aligned} Q_i &= \frac{1}{2\pi\sigma_x\sigma_y}\int_{s_i-\frac{w}{2}}^{s_i+\frac{w}{2}}\int_{-\infty}^{\infty}\exp\left[-\left(\frac{(x-\mu_x)^2}{2\sigma_x^2}+\frac{(y-\mu_y)^2}{2\sigma_y^2}\right)\right]\mathrm{d}y\,\mathrm{d}x \\ &= \frac{1}{\sqrt{2\pi\sigma_x^2}}\int_{s_i-\frac{w}{2}}^{s_i+\frac{w}{2}}\exp\left[-\frac{(x-\mu_x)^2}{2\sigma_x^2}\right]\mathrm{d}x\,. \end{aligned} \tag{5.5}$$

Here, $\mu$ is the centre of the charge cloud, $\sigma$ its transverse width and $s_i$ the centre of strip $i$.

In order to reproduce the modulation pattern (here focussing on the X-ray data) with this model, the transverse width has to be matched with the recorded data. As the X-ray measurements contain not only effects from the diffusion, but also the photoelectron track[5], the charge cloud is wider than what would be expected from pure diffusion. For determining the charge cloud width for the modelling, the value of $\sigma_x$ was increased, until the average cluster size without NL reached the measured value of 3.1 strips (figure 5.14b), while a threshold of 10 % of the used dynamic range, as in the measurements, was applied. The result is $\sigma_x = 320\,\mu\mathrm{m}$.

To mimic the interaction behaviour of the X-rays in the 3 mm drift gap, the interaction depth $l$ is sampled from an exponential distribution $f(l) \propto \exp(-l/\lambda)$, as described in equation (1.7). As a result, the actual charge cloud width is different for each simulated interaction. To get the width for each interaction, equation (1.19) is used. This requires to calculate the transverse diffusion coefficient $D_\mathrm{T}$ from the average charge cloud width $\sigma$ via

$$\sigma_x = D_{\mathrm{T,\,sim}} \sqrt{L_\mathrm{max} - \langle l_\mathrm{int} \rangle}\,, \tag{5.6}$$

where $L_\mathrm{max} = 9\,\mathrm{mm}$ is the maximum drift length of the electron cloud and $\langle l_\mathrm{int} \rangle$ is the average interaction depth. The latter is

$$\langle l_\mathrm{int} \rangle = \int_{0\,\mathrm{mm}}^{3\,\mathrm{mm}} l \frac{1}{n} \exp\left(-\frac{l}{\lambda}\right) \mathrm{d}l = 1.49\,\mathrm{mm}\,, \tag{5.7}$$

for a 3 mm wide drift gap, with $n$ being a normalisation constant and $\lambda = 68\,\mathrm{mm}$ being the absorption length of 8.0 keV photons in $\mathrm{Ar/CO_2}$ (70/30 %). The value of $\lambda$ is calculated from the mass absorption coefficient $\mu_\mathrm{m} = 85.5\,\mathrm{cm^2/g}$ [34] and the density $\rho = 1.716\,\mathrm{g/l}$ [25] of $\mathrm{Ar/CO_2}$ (70/30 %) at NTP. As a result, it is found that $D_{\mathrm{T,\,sim}} = 369\,\mu\mathrm{m}/\sqrt{\mathrm{cm}}$ in the here shown Monte Carlo studies compared to the value calculated with Magboltz [37, 38] of $D_\mathrm{T} = 239\,\mu\mathrm{m}/\sqrt{\mathrm{cm}}$.

In addition to the interaction depth, also the initial position of the charge cloud is sampled with Monte Carlo methods, this time from a uniform distribution. The result is a reproduction of the read-out modulation (figure 5.22), which behaves also similarly in the terms of NL and $Q^2$. The reproduction is not perfect, which is likely to be caused by the simplification of the model e.g. in terms of charge collection, but it is considered to be sufficient for the purposes of the simulation studies. As such, the simulation allows to compare the known initial position $x_\mathrm{ini}$ with the reconstructed position $x_\mathrm{c}$ and to calculate the displacement $\delta_\mathrm{pos} = x_\mathrm{ini} - x_\mathrm{c}$ (figure 5.23). From this it can be seen that the displacement between the initial and reconstructed position for $Q^2$ weighting becomes smaller, indicating that the flatter position distribution is a

---

[5] In the presented conditions, for 8.0 keV photons, the track length is about 500 µm according to equation (1.10).

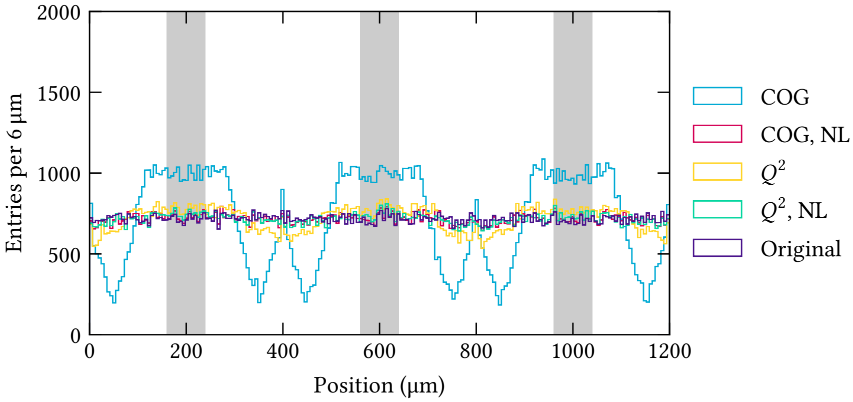

*Figure 5.22* – Position distribution for COG and $Q^2$, also with NL enabled, in case of the simulated position reconstruction. In addition, the distribution of the initial/original cluster positions is indicated. The vertical bars indicate the positions of the anode strips. Data published in [79].

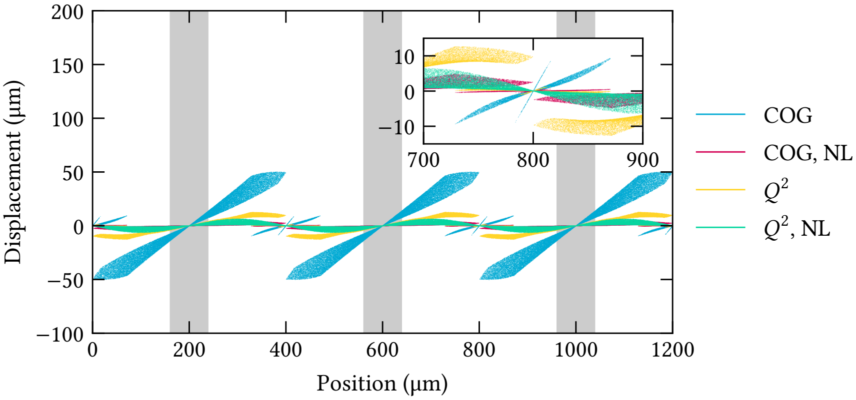

*Figure 5.23* – Displacement between the initial cluster position and the reconstructed one in the simulation. The vertical bars indicate the positions of the anode trips. Data published in [79].

result of better position reconstruction. In the displacement plot, especially for COG, also two structures with different slopes can be observed, which are highlighted in the inset. This is the result of considering different interaction depths leading to different cluster sizes, with the steeper structure being caused by clusters with 2 strips and the flatter one by clusters with 4 strips.

The next step is to find conditions under which the $Q^2$ weighting is not applicable anymore. For this, the Monte Carlo simulation is further simplified to pure numerical

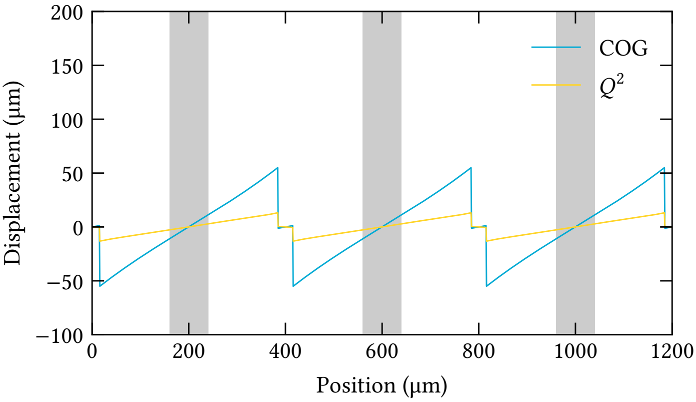

*Figure 5.24* – Example of the displacement calculation for a charge cloud width of $\sigma_x = 320\,\mu\mathrm{m}$ and a normalised threshold of 5 %. The vertical bars indicate the positions of the anode strips. Data published in [79].

calculations, meaning that the interaction depth is not considered anymore but purely the charge cloud width. As the read-out modulation is a consequence of the discretisation of the charge cloud by being spread over several read-out strips in combination with a threshold-based read-out, the displacement $\delta_{\mathrm{pos}}$ is calculated for different charge cloud widths and different THLs. For the calculations, the threshold level per strip is expressed in fractions of the total charge, with the charge distribution given in equation (5.5) having a total normalised charge of 1.

The displacement behaves symmetrically and is periodic (figure 5.24), hence, the quantity used for the calculation is the mean value of the absolute value of the displacement. When this quantity is calculated for various threshold levels, it can be observed (figure 5.25a) that $Q^2$ provides a more accurate position reconstruction (on average) than COG except for low threshold levels ($< 1\,\%$). In addition to this, a peak structure can be observed, where the positions of the peaks can be related to the cases where the cluster size has its minimal variation (figure 5.25b). Effectively, the read-out modulation gets maximised in these cases, resulting in a maximisation of the average displacement: when the reconstructed position is always forced towards the central strip or in between the two central strips, depending if the strip count is odd or even, the average difference between initial and reconstructed position becomes maximal. This behaviour (at least in such a strong pronunciation), is probably an artefact of the simplified calculation process because other effects which would smooth out the peak structure are missing, e.g. the different drift lengths, different energy depositions, slightly asymmetric charge cloud distributions, signal variations due to noise or fluctuations in the channel-by-channel threshold. It was nonetheless

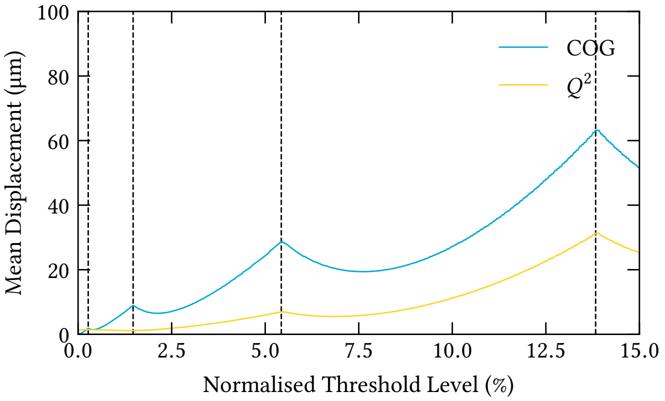

*(a)* – Threshold dependence of the mean displacement.

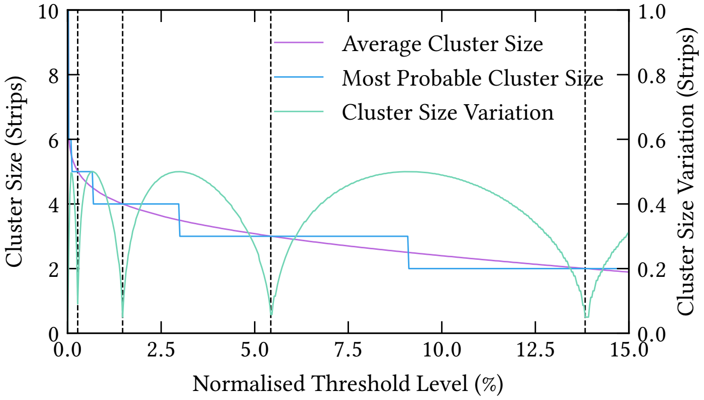

*(b)* – Threshold dependence of the cluster size.

*Figure 5.25* – Illustration of the threshold dependence of the mean displacement (a), the average ***C**luster **S**ize* (CS), the most probable cluster size and the cluster size variation (b) for $\sigma_x = 320\,\mu\text{m}$. Data published in [79].

accepted as the main interest lies in the general trend of the mean displacement, which stays preserved.

In addition to the threshold dependence, the calculations were repeated for different charge cloud widths (figure 5.26). From the results it is deduced that as long as the charge cloud width is not much smaller than the anode pitch or the threshold is very low (< 1 % of the total charge within the charge cloud), $Q^2$ weighting helps to improve the position reconstruction. Another observation is the sometimes nearly threshold-independent mean displacement. It cannot be excluded that this is an

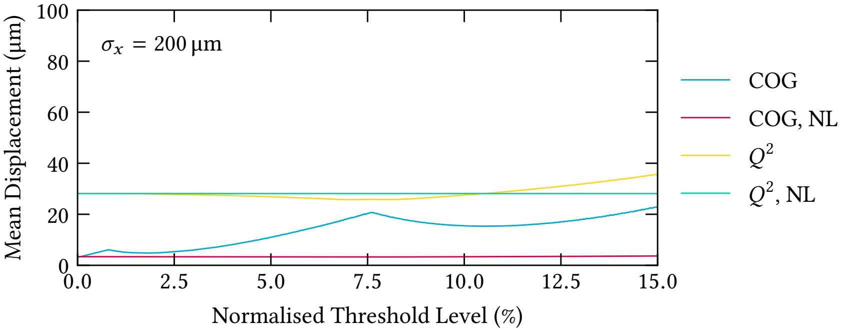

*(a)* – Charge cloud width of $\sigma_x = 200$ µm.

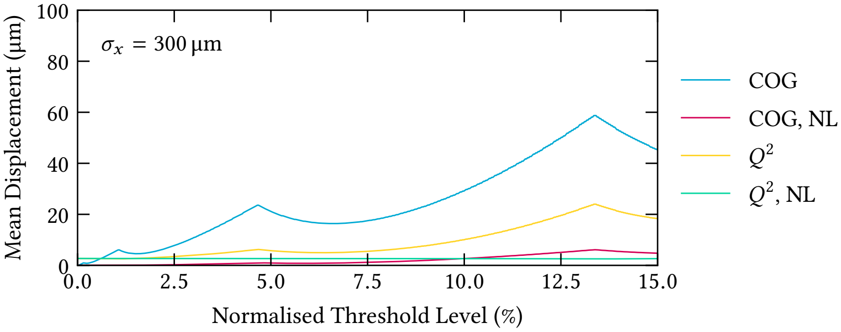

*(b)* – Charge cloud width of $\sigma_x = 300$ µm.

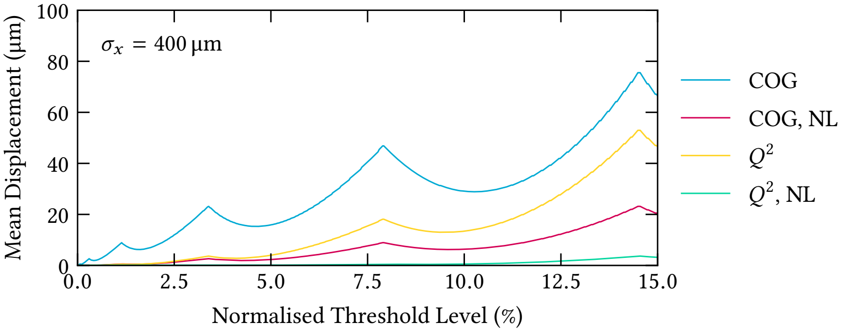

*(c)* – Charge cloud width of $\sigma_x = 400$ µm.

*Figure 5.26* – Threshold dependence of the mean displacement for various charge cloud widths and position reconstruction methods. Data published in [79].

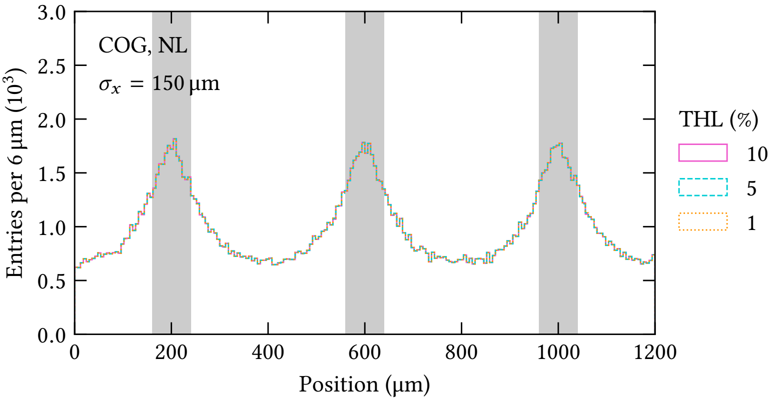

*(a)* – Position reconstruction with COG and NL enabled.

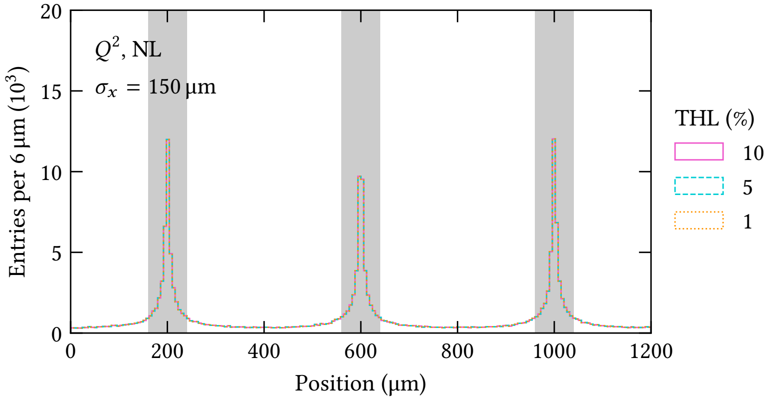

*(b)* – Position reconstruction with $Q^2$ weighting and NL enabled.

*Figure 5.27* – Calculated position distributions for very small charge cloud widths of 150 µm at different threshold levels, to illustrate the observed threshold independence of the mean displacement in the calculations in some cases. The vertical bars indicate the positions of the anode strips. Data published in [79].

artefact of the simplified calculation model, using geometrical charge collection. However, it still allows to conclude when $Q^2$ is not applicable anymore. For this, the position distribution was calculated for different charge cloud widths, showing here the most extreme example (figure 5.27), with $\sigma_x = 150$ µm. The average cluster size remains at 3 to 4 strips, but most of the charge is collected on one strip. Even with COG, the reconstructed cluster position will be forced towards this strip, but with a higher power weighting, as in $Q^2$, this behaviour gets enhanced. As a result, $Q^2$

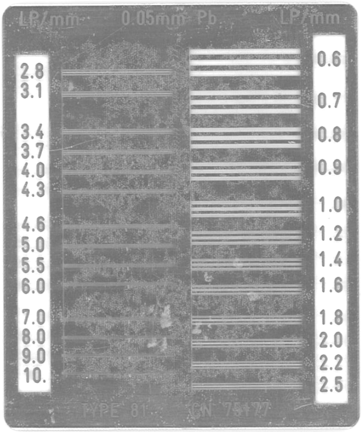

*Figure 5.28* – Image of the line phantom used for the X-ray imaging studies on the spatial resolution.

weighting over-corrects the reconstructed position in case a single strip contains a large fraction of the total charge, which is especially the case for small charge cloud widths. This explains then also the threshold-independent behaviour of the calculated position distribution (figure 5.27) and thus also the behaviour of the average displacement.

### *5.2.4 Modulation Transfer Function*

After modelling the modulation effect and obtaining an insight on possible limitations of the $Q^2$ weighting method, the focus is now shifted to X-ray imaging methods, to confirm experimentally that $Q^2$ is not a smoothing effect and that the neighbouring-logic recovers the charge correctly[6]. The X-ray imaging methods are used to determine the spatial resolution, as an improved spatial resolution would be the result of a more accurate position reconstruction.

The first method is the ***M**odulation **T**ransfer **F**unction* (MTF), where a line phantom is used (figure 5.28). The particular line phantom used, is a 50 µm thick lead layer within two layers of transparent plastics. The lead contains slits with varying width and pitch, representing a spatial frequency $f$, whose unit is ***L**ine **P**airs per **Millim**etre* (LP/mm) [82]. A line phantom is generally used to determine the imaging capabilities of an imaging system. The basis is the contrast, defined as the ratio between the

---

[6] It is possible that NL might record electronics noise instead of the induced signal or that the induced signal whose read-out is triggered by the signal above THL is dominated by noise. The noise aspect was however not included in the modelling.

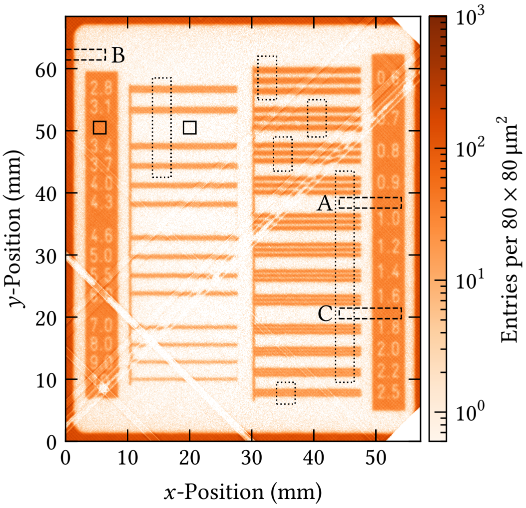

*Figure 5.29* – X-ray image of the line phantom. The regions contained within the dotted lines are used for the MTF studies, with the two regions in the solid lines being used for the normalisation with the maximum contrast. The three regions within the dashed lines, A, B, and C, are the regions used for the edge spread function measurements. Due to the rotation of the line phantom with respect to the read-out strips, the diagonal lines are dead electronics and detector channels. Data published in [79].

transparent and the covered areas of the phantom [83]:

$$c = \frac{I_{\text{max}} - I_{\text{min}}}{I_{\text{max}} + I_{\text{min}}} . \tag{5.8}$$

As each spatial frequency corresponds to a group of slits, the maximum intensity $I_{\text{max}}$ and the minimum intensity $I_{\text{min}}$ are here defined as the mean intensities over all maxima/minima per spatial frequency. The concept behind this is that with increasing spatial frequency the contrast decreases, allowing to determine the smallest structure size that remains resolvable.

An X-ray image of the line phantom (figure 5.29) is used to generate a transmission profile (figure 5.30), to obtain the intensity values. The diagonal lines in the X-ray image correspond to issues on the read-out board (e.g. two strips were connected together on the detector connector), dead channels of the prototype Hybrids and masked channels of the VMM. The reason for their diagonal nature is that the line phantom was rotated by 45.1° when it was mounted on the detector. This was done, due to unavoidable Moiré patterns when two grid patterns (the line phantom and the two-dimensional read-out grid) are overlayed. With the goal of getting the best average and not giving any preference to a read-out direction, the line phantom was supposed to be rotated by 45°. In the X-ray image, all the cluster positions have been

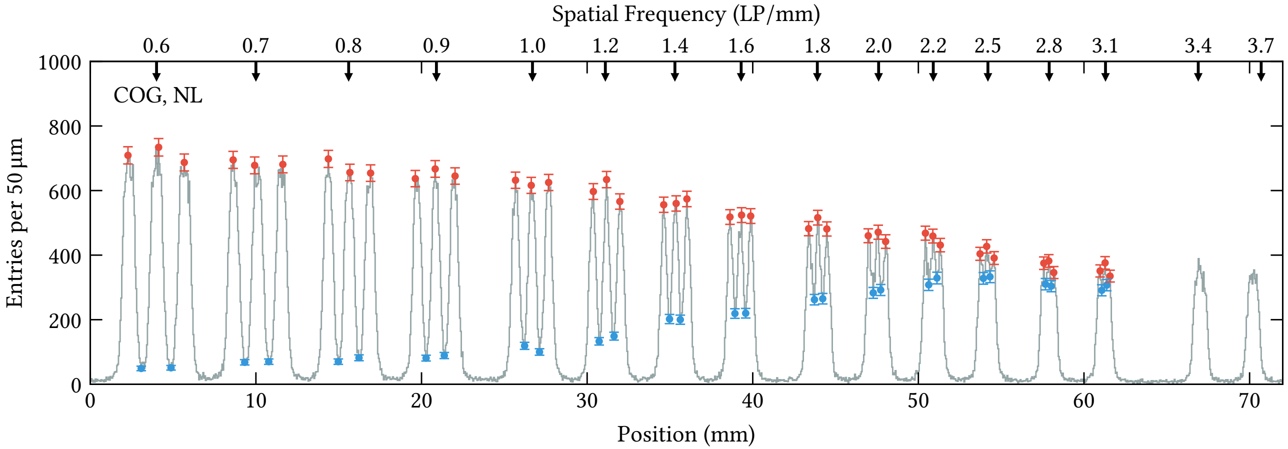

*Figure 5.30* – Illustration of the transmission profile obtained from the image of the MTF line phantom (figure 5.29). The data points indicate the intensity maxima and minima, with the error bars being a $\sqrt{N}$-error, with $N$ the number of entries per corresponding bin. Data published in [41].

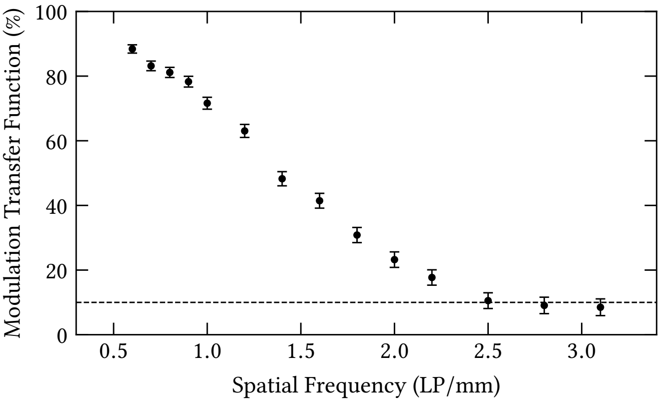

*Figure 5.31* – Illustration of the modulation transfer function, calculated from the transmission profile (figure 5.30) and the normalisation of the corresponding contrast levels as given in equation (5.9). The dashed horizontal line indicates the 10 % MTF value, and hence the estimate of the spatial resolution. Data published in [79].

rotated accordingly to allow the generation of the transmission profile. For this, the cluster positions within the dotted areas (figure 5.29) have been projected onto the $y$-axis[7]. The intensities which can be extracted from the transmission profile are given in terms of cluster entries $N$ per bin. The corresponding error of this counting is then given by $\sqrt{N}$. After the extraction of the contrast for each line pair group, the values have to be normalised by the maximum contrast $c_{\mathrm{max}}$, in order to determine the MTF:

$$\mathrm{MTF}(f) = \frac{c(f)}{c_{\mathrm{max}}} \,. \tag{5.9}$$

The maximum contrast is calculated from the intensities in a fully covered and a fully open area, illustrated by the solid lined areas in the X-ray image (figure 5.29). The resulting MTF (figure 5.31) illustrates the imaging capabilities and allows also to compare different imaging systems. A common choice to extract a spatial resolution value from the MTF is the inverse of the spatial frequency when the MTF is at 10 % [82]:

$$r_{\mathrm{MTF}} = f^{-1}\Big|_{\mathrm{MTF}=10\,\%} \,. \tag{5.10}$$

In the given example (figure 5.31) this means that the spatial resolution is about 400 µm.

---

[7] The selection is a consequence of the diagonal lines in the image.

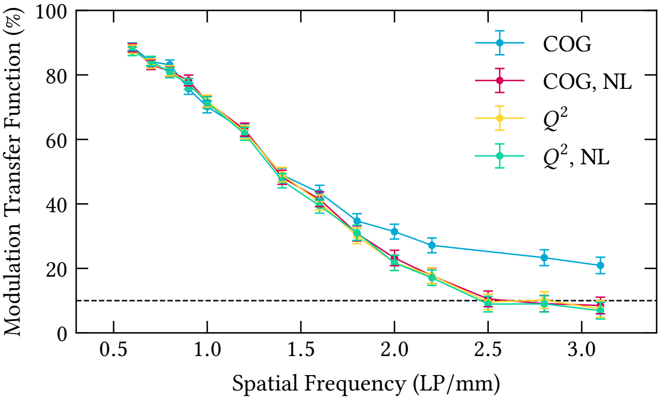

*Figure 5.32* – Comparison of the modulation transfer functions for different reconstruction methods. Data published in [79].

This procedure is repeated for the different reconstruction methods, allowing to compare them (figure 5.32). The resulting MTF seems to indicate that the position reconstruction and spatial resolution with the COG method are the best. However, as the line phantom and the transmission profile allow to describe the imaging capabilities of a system, even without specifically determining a numerical MTF value, it becomes evident that this statement has to be treated with care. When investigating the transmission profile in more detail (figure 5.33), it can be seen that the profile generated from the positions reconstructed with COG is affected by the read-out modulation. At low spatial frequencies (figure 5.33a) the profiles of the three slits have each three intensity maxima, reflecting the modulation pattern. When enabling the neighbouring-logic or using $Q^2$ weighting, this behaviour disappears. The convolution of the read-out modulation into the transmission profile explains then also the larger MTF values for higher spatial frequency, as the MTF is calculated from the contrast, which itself is calculated from the intensity. If now the intensity values get artificially enhanced because of spikes caused by the modulation pattern, also the contrast and the MTF values get artificially enhanced. At higher spatial frequencies (figure 5.33b), the same behaviour can be observed, as well as the occurrence of a fourth 'fake' peak in the COG profile, which is likely to be caused by the read-out modulation; with three slits only three peaks should be observed. The fourth peak disappears when enabling the NL or when using $Q^2$. This particular case at 2.5 LP/mm is another indication that the NL recovers the charge correctly as well as that $Q^2$ is not a smoothing effect and as such improve the position reconstruction. The corresponding spatial frequency corresponds to a spatial resolution of 400 µm FWHM or the limit of what is possible to resolve (10 % MTF). While all three slits can be resolved with NL or $Q^2$, this is not the case for COG.

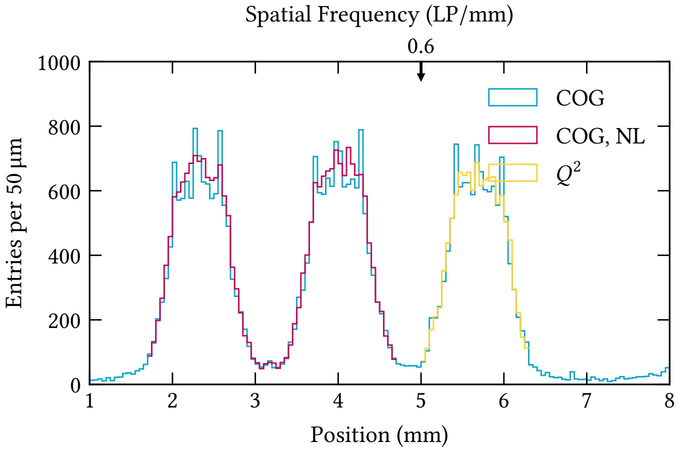

*(a)* – Region with low spatial frequency.

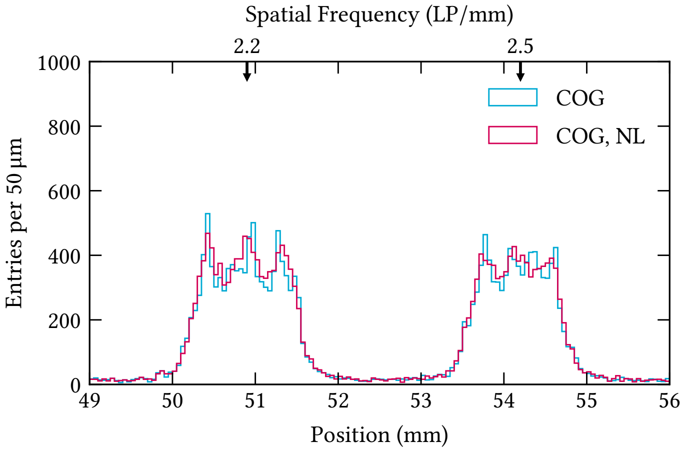

*(b)* – Region with higher spatial frequency.

*Figure 5.33* – Comparison of the MTF transmission profiles for different spatial frequencies and position reconstruction methods. In the case of a low spatial frequency (a), the NL and the $Q^2$ weighting remove the additional peaks in the intensity profile, while at higher spatial frequencies (b), the fourth peak at 2.5 LP/mm disappears when using the NL. It also disappears when using $Q^2$, which is not shown for the sake of visibility, but the result is almost identical to the one of COG with NL. Data partially published in [79].

*Table 5.1* – Resulting spatial resolutions, obtained with the ESF for the three different regions and the four different methods.

| Method | $\sigma_A$ (µm) | $\sigma_B$ (µm) | $\sigma_C$ (µm) |
|---|---|---|---|
| COG | 172 ± 10 | 180 ± 13 | 194 ± 17 |
| COG, NL | 170 ± 8 | 181 ± 5 | 194 ± 10 |
| $Q^2$ | 169 ± 9 | 180 ± 6 | 190 ± 10 |
| $Q^2$, NL | 164 ± 9 | 182 ± 5 | 189 ± 10 |

### 5.2.5 Edge Spread Function

In addition to the MTF, a second X-ray imaging method is used to determine the spatial resolution. For the ***E**dge **S**pread **F**unction* (ESF), a sharp edge is resolved, which in practice means the transition between a fully irradiated and a fully covered area of the detector, both directly adjacent to each other. Within an ideal imaging system, the transition between the two areas would be almost like a step function, only affected by X-ray diffraction on the object with the sharp edge covering one part of the detector. In reality, the step-like transition gets smeared out by processes within the imaging system, i.e. the track of the photoelectron or diffusion of the charge cloud [84].

For the ESF measurements, the edges of the line phantom were used, within the three regions A, B and C (figure 5.29). To get the edge spread function, the cluster positions within a region (figure 5.34) are projected on the long axis and then fitted (figure 5.35) with a function based on the Gaussian error function:

$$I(x) = \frac{I_{\mathrm{max}}}{2}\mathrm{erf}\left(\frac{x - x_0}{\sqrt{2}\sigma}\right) + I_0 \ . \tag{5.11}$$

It describes the position dependence of the intensity (again given in cluster counts), where $I_{\mathrm{max}}$ is the maximum intensity from the fully irradiated area, $x_0$ is the position of the sharp edge, $\sigma$ is the width of the intensity transition, being the spatial resolution, and $I_0$ describes an offset[8]. The obtained spatial resolutions (table 5.1) are compatible with each other for all three regions within their uncertainties. The resolution measured with the COG method has the largest uncertainty, which is likely to arise from the read-out modulation (figure 5.36), similar to the transmission profile (figure 5.33).

It is possible to relate the obtained resolution from the ESF, with the one from the MTF [85]. The relation is however not exact and depends also on the frequency behaviour of the MTF. With the 10 % value of the MTF, defined in equation (5.10),

---

[8] It does not describe the minimum intensity as the Gaussian error function $\mathrm{erf}(x) \in [-1, 1]$.

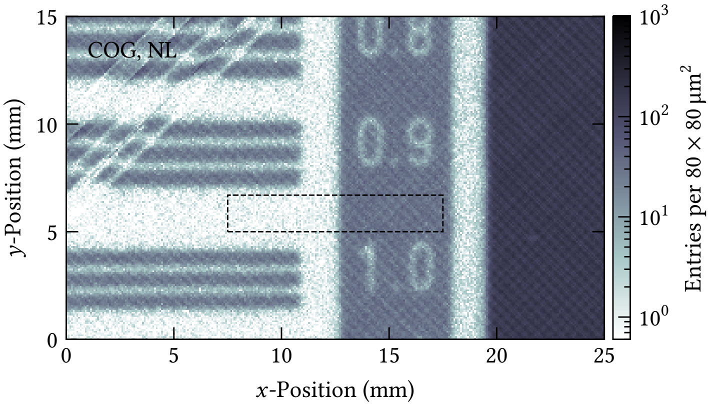

*Figure 5.34* – Highlight of one of the regions (region A) used for the ESF studies. The cluster positions used for the studies are taken from the area within the dashed line and are projected on the long edge of the rectangle. Data published in [79].

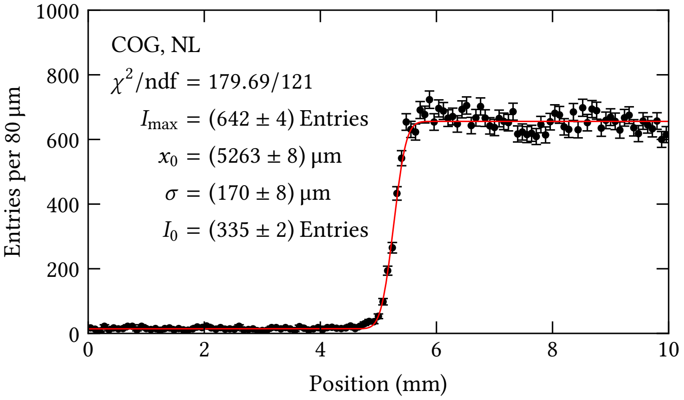

*Figure 5.35* – Example of the edge spread function fit (region A). The error bars represent a $\sqrt{N}$-error, with $N$ being the number of entries per bin. Data published in [79].

the following is used:

$$2.35\sigma \approx r_{\mathrm{MTF}} . \tag{5.12}$$

It means that the resolution extraction from the MTF should be approximately similar to the FWHM of the ESF. With the here measured numbers of $\sigma = (170 \pm 8)\,\mu\mathrm{m}$ and $2.35\sigma = 400\,\mu\mathrm{m}$, this is the case. Within this rough approximation, the relation is also valid for the other regions and all other position reconstruction approaches (table 5.1).

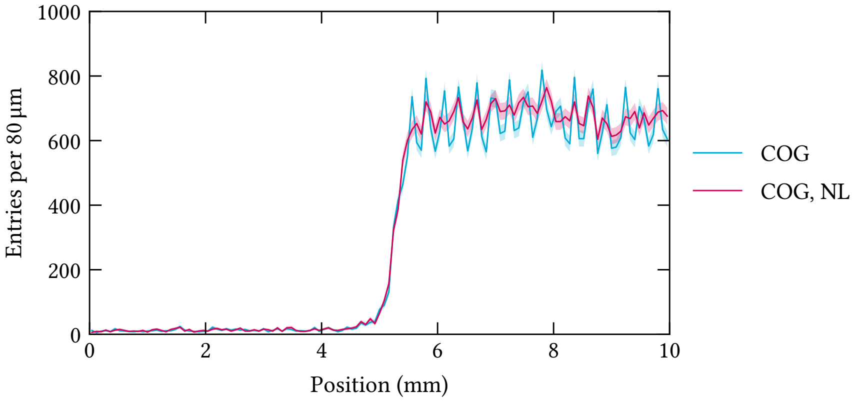

*Figure 5.36* – Comparison of the edge spread function (region C) without NL and with enabled neighbouring-logic for COG position reconstruction. Here, the bin entries are represented by the solid line, with the band around each line representing the error bars. The peaks in the high-intensity region are caused by the read-out modulation. With each peak being around 280 µm apart, this is expected, due to the 45° rotation and a peak appearing every half pitch of 400 µm: 400 µm/2 × $\sqrt{2}$ = 283 µm. Data published in [79].

*Table 5.2* – Fit results for the ESF slices (figure 5.37).

| Method | $\chi^2$/ndf | $I_{\max}$ (Entries) | $x_0$ (µm) | $\sigma$ (µm) | $I_0$ (Entries) |
|---|---|---|---|---|---|
| COG | 626.41/97 | 20.1 ± 1.6 | 5187 ± 115 | 25 ± 104 | 11.3 ± 0.8 |
| COG, NL | 126.77/92 | 30.7 ± 0.9 | 5278 ± 30 | 122 ± 32 | 16.6 ± 0.5 |
| $Q^2$ | 93.57/94 | 30.8 ± 0.8 | 5291 ± 25 | 118 ± 24 | 16.7 ± 0.4 |
| $Q^2$, NL | 80.81/93 | 31.6 ± 0.7 | 5298 ± 28 | 164 ± 28 | 17.0 ± 0.4 |

It should be noted that the presented resolutions are average values, as the cluster positions are integrated by the projection. Hence, the sensitivity and accuracy of the position reconstruction might suffer, which is why a study on the local level was performed. For this, each region is sliced into 20 equal-sized parts, with the ESF being measured for each slice. The examples of the slices illustrate the impact of the modulation effect on the intensity behaviour (figure 5.37 and table 5.2), where particularly for the COG method no uniform intensity behaviour is observed for the high-intensity region of the ESF. In fact, the fit to the data points for the COG method (figure 5.37a and table 5.2) is highly questionable, which is also reflected by the goodness of the fit (table 5.2). Thus, the subsequent studies are focussing only on the case of an enabled neighbouring-logic or the impact of $Q^2$ on the position reconstruction. For this, the spatial resolution $\sigma$ (figure 5.38) and the edge position $x_0$ (figure 5.39) are plotted against the central position of each slice. For both, position-

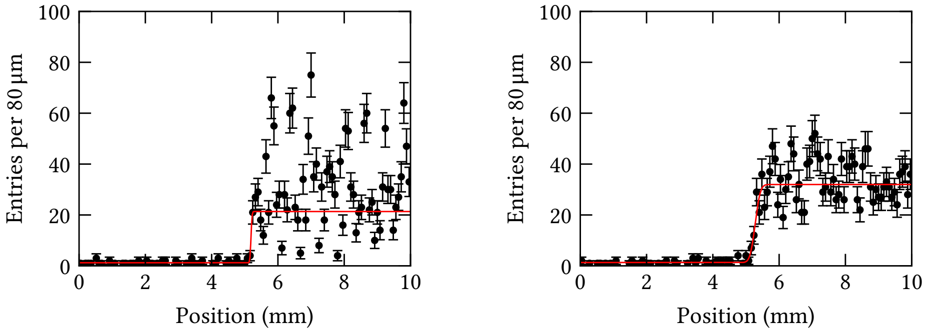

*(a)* – COG.

*(b)* – COG, NL.

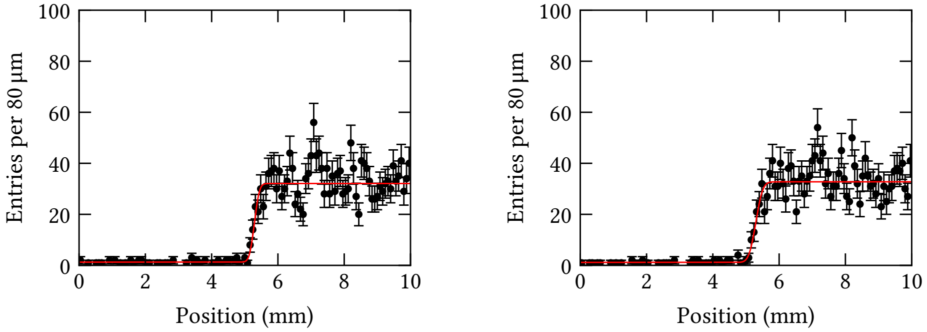

*(c)* – $Q^2$.

*(d)* – $Q^2$, NL.

*Figure 5.37* – Example of an ESF slice (slice 10, meaning $y \in [764, 849]$ µm) for the local analysis of the spatial resolution, once reconstructed with COG (a), once with COG and enabled NL (b), once with $Q^2$ (c) and once with $Q^2$ and NL combined. Data partially published in [79].

dependent fluctuations can be observed. While the fluctuations in edge position seem to be independent of the reconstruction method, the fluctuations in the spatial resolution seem to become smaller when using $Q^2$, especially when combined with the NL. When the fluctuations of the spatial resolution are overlaid with the image of the edge, it can be seen that it coincides with intensity fluctuations (in the case of COG and NL), probably caused by the read-out modulation. When using $Q^2$ and NL, this behaviour is reduced as also the intensity fluctuations from the modulation effect are reduced. As the spatial resolution should not depend on the reconstructed position, this is a further indication that $Q^2$, where the dependence is the smallest, helps to reconstruct the interaction position of an interacting particle with higher accuracy.

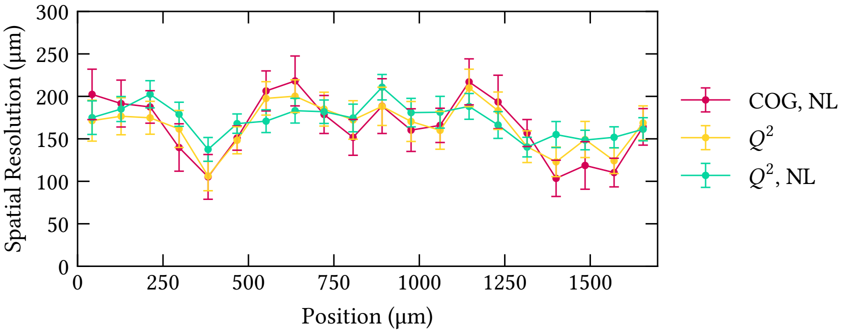

*(a)* – Spatial resolution versus slice position.

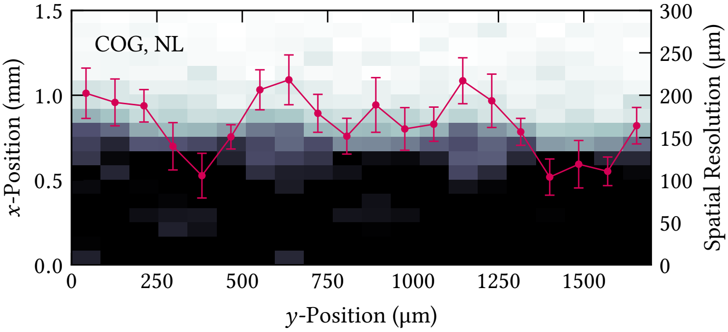

*(b)* – Overlay of the spatial resolution with the image of the edge for COG reconstruction with NL.

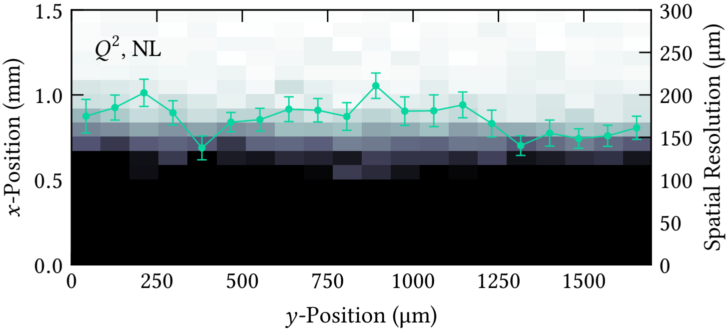

*(c)* – Overlay of the spatial resolution with the image of the edge for $Q^2$ reconstruction with NL.

*Figure 5.38* – Position dependence (ESF slice) of the spatial resolution determined via the edge spread function. While in (a) different reconstruction methods are compared, in (b) the COG and in (c) the $Q^2$ weighting are overlaid with the reconstructed image of the sharp edge. The image is rotated by 90° compared to the original image (figure 5.29). The brighter the image, the fewer entries contains the bin, meaning low intensity. Data published similarly in [79].

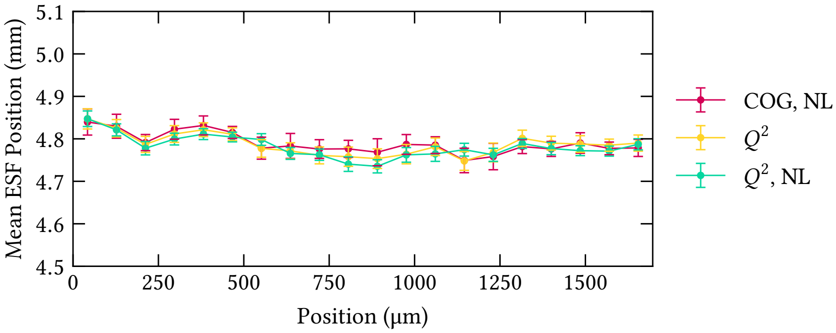

*(a)* – Edge position versus slice position.

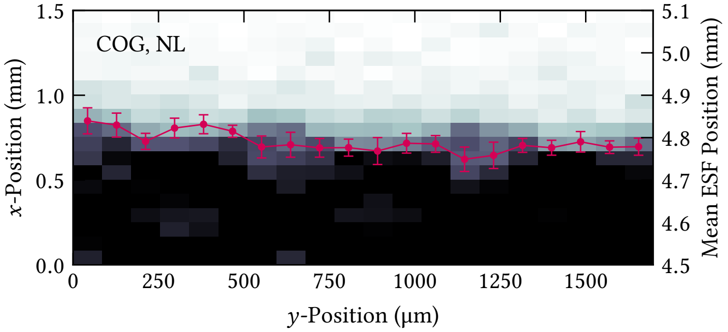

*(b)* – Overlay of the edge position with the image of the edge for COG reconstruction with NL.

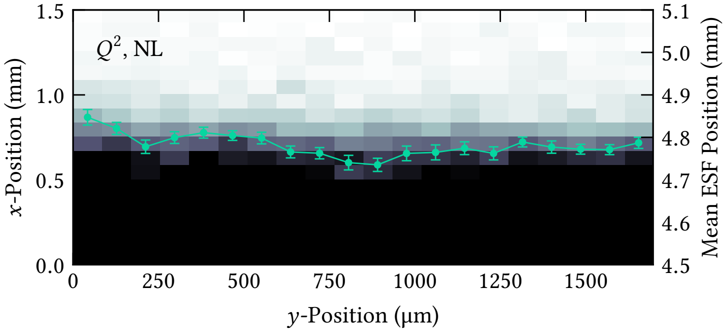

*(c)* – Overlay of the edge position with the image of the edge for $Q^2$ reconstruction with NL.

*Figure 5.39* – Position dependence (ESF slice) of the ESF edge position $x_0$. While in (a) different reconstruction methods are compared, in (b) the COG and in (c) the $Q^2$ weighting are overlaid with the reconstructed image of the sharp edge. The image is rotated by 90° compared to the original image (figure 5.29). The brighter the image, the fewer entries contains the bin, meaning low intensity. Data published similarly in [79].

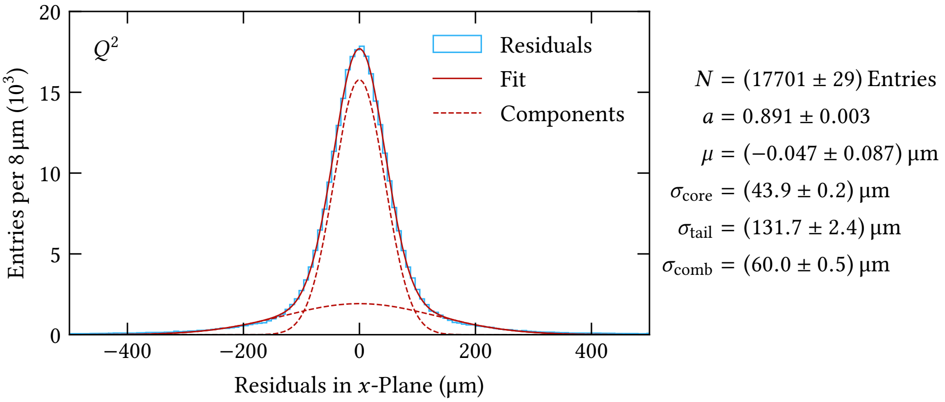

*Figure 5.40* – Example of a residual distribution, where the double Gaussian given in equation (5.14) is fitted to the data. The full function is represented by the solid line, while the two individual components for the core and the tail of the residual distribution are represented by the dashed lines.

### *5.2.6 Spatial Resolution in a Beam Telescope*

After the indications from the X-ray imaging methods that $Q^2$ weighting is not a smoothing effect in COMPASS-like triple-GEM detectors and that the neighbouring-logic recovers the charge correctly, the focus is now shifted towards MIPs in a beam telescope[9]. This is the ultimate method to determine the effect of $Q^2$ and NL on the spatial resolution, as the beam telescope provides a clear reference position.

The basis of determining the spatial resolution with a beam telescope is the residual distribution (figure 5.40). It contains the position differences

$$\Delta x = x_{\mathrm{track}} - x_{\mathrm{c}} \tag{5.13}$$

between the reconstructed cluster position in the detector $x_{\mathrm{c}}$ and the particle's expected interaction position $x_{\mathrm{track}}$ provided by the track fit. The distribution can be fitted by a double Gaussian function

$$f(\Delta x) = N\left[a\exp\left(-\frac{(\Delta x-\mu)}{2\sigma_{\mathrm{core}}^2}\right) + (1-a)\exp\left(-\frac{(\Delta x-\mu)}{2\sigma_{\mathrm{tail}}^2}\right)\right], \tag{5.14}$$

---

[9] The detectors were operated at various gains, with the tracking detectors being operated at around 30 000, in case they are needed as a reference for the DUT. The electronics gain was set to 9 mV/fC, the peaking time to 200 ns and the TAC slope to 60 ns. The threshold for the DUT was varied, while for the tracking detectors it was kept at 15 mV above baseline with channel-by-channel equalisation.

where $\mu$ is the mean of the distribution, $N$ is a scaling factor, $\sigma_{\text{core}}$ is the width of the core distribution and $\sigma_{\text{tails}}$ the width of the distribution used to describe the tails[10]. Further, a parameter $a$ is included in equation (5.14), which weights the two Gaussian functions with the condition that $a \in [0, 1]$. This parameter allows to extract the combined width of the residual distribution:

$$\sigma^2_{\text{comb}} = a\sigma^2_{\text{core}} + (1 - a)\sigma^2_{\text{tail}} \,. \tag{5.15}$$

The combined width does however not correspond to the spatial resolution of the detector under test. It still contains the uncertainty of the track fit itself. To get access to the detector and the track resolution, the procedure from [75] is followed, where itself the methods developed in [86] and [87] are recalled.

First, it is necessary to determine the spatial resolution of the reference detectors of the beam telescope, which is given by [87]

$$\sigma_{\text{pos},\,i} = \sqrt{\sigma_{\text{in},\,i}\sigma_{\text{ex},\,i}} \,, \tag{5.16}$$

with $\sigma_{\text{in},\,i}$ the width of the residual distribution with reference detector $i$ being included in the track fit and $\sigma_{\text{ex},\,i}$ the width of the residual distribution with reference detector $i$ being excluded from the track fit. With the exact derivation being found in [87], the idea behind this method is the following. The width of the residual distribution giving access to the spatial resolution gets too narrow if the detector that is investigated is included in the track fit as it also defines the track fit. Hence the spatial resolution would be overestimated. If it gets excluded from the track fit, the other detectors gain more weight on the track fit with their own uncertainty. Hence the spatial resolution would be underestimated. An accurate estimate of the detector resolution is given by the geometric mean of both scenarios.

Knowing the spatial resolution of the reference tracking detectors, the track resolution can be determined via [86]

$$\sigma_{\text{track}}(z) = \sqrt{\frac{\Lambda_{22} - 2z\Lambda_{12} + z^2\Lambda_{11}}{\Lambda_{11}\Lambda_{22} - \Lambda^2_{12}}} \,, \tag{5.17}$$

where $z$ is the position of the detector $i$ in the beam telescope along the beam axis. The other quantities are

$$\Lambda_{11} = \sum_{i=1}^{n} \frac{1}{\sigma_{\text{pos},\,i}} \quad , \quad \Lambda_{12} = \sum_{i=1}^{n} \frac{z_i}{\sigma_{\text{pos},\,i}} \quad \text{and} \quad \Lambda_{22} = \sum_{i=1}^{n} \frac{z_i^2}{\sigma_{\text{pos},\,i}} \,, \tag{5.18}$$

---

[10] A recurring explanation found for this behaviour, e.g. in [77], is the occurrence of delta electrons. They ionise gas atoms along their track, leading to a wider charge cluster and a shift of the cluster position away from the interaction point of the particle.

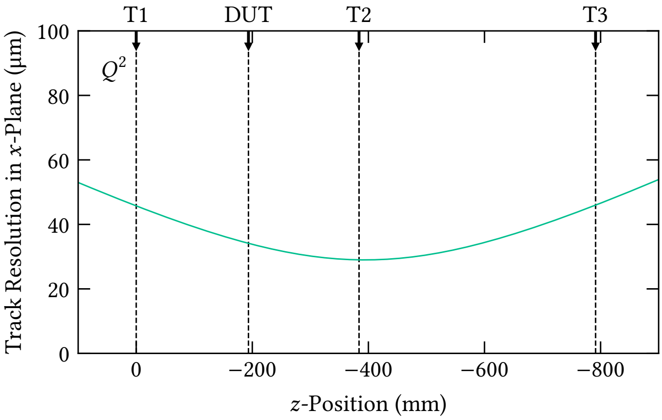

*Figure 5.41* – Position dependence of the track resolution in the RD51 VMM3a/SRS beam telescope, as defined in equation (5.17), with the positions of the three tracking stations and the detector under test used for the spatial resolution studies indicated.

where $n$ is the number of detectors involved in the track fit. For the derivation it is referred to [75, 86]. Having calculated all the corresponding quantities, the spatial resolution of the detector under test is given by [75]

$$\sigma_{\mathrm{DUT}} = \sqrt{\sigma_{\mathrm{ex}}^2 - \sigma_{\mathrm{track}}^2}\,, \tag{5.19}$$

with $\sigma_{\mathrm{track}}$ being the track resolution at the position of the DUT (figure 5.41) and $\sigma_{\mathrm{ex}}$ the width of the residual distribution of the detector under test excluded from the track fit.

The measurements with the beam telescope allow a deeper investigation of the effect of the neighbouring-logic and the $Q^2$ method on the spatial resolution, due to the reference position provided by the beam telescope. In addition, due to the much smaller charge deposition of MIPs inside the detectors compared to X-rays, the fraction of charge below the threshold is larger, allowing for better investigation of threshold effects. The results are shown in the following for three different threshold levels: 15 mV above baseline or around 10 000 electrons (figure 5.42), 30 mV above baseline or around 20 000 electrons (figure 5.43) and 55 mV above baseline or around 34 000 electrons (figure 5.44). In each case the spatial resolution is studied for each detector plane individually, depending on the voltage applied to the divider, leading to a dependence on the total effective detector gain.

It can be seen that the typical spatial resolutions of COMPASS-like triple-GEM detectors between 50 μm and 70 μm [66, 88] can be reached, however only in the fewest cases when using pure COG, which was used in the given references. Here,

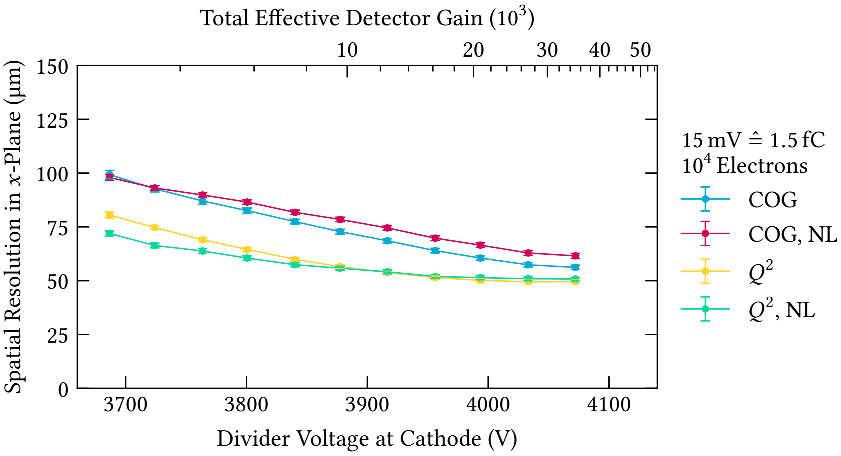

*(a)* – Spatial resolution in the $x$-plane.

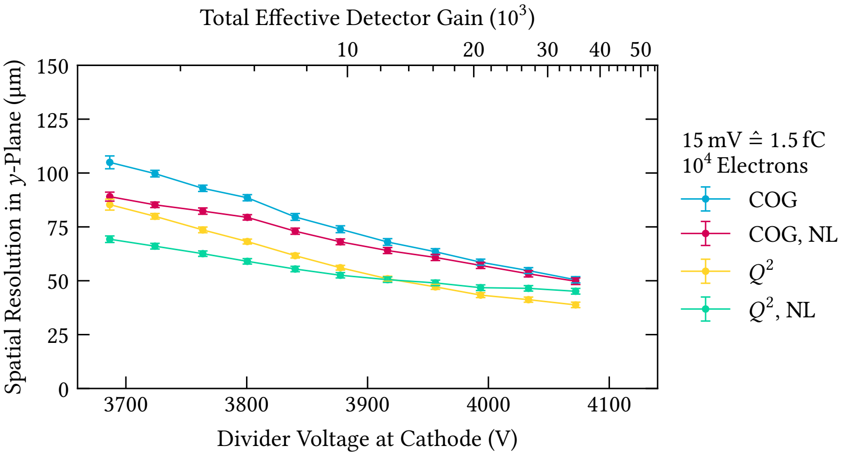

*(b)* – Spatial resolution in the $y$-plane.

*Figure 5.42* – Spatial resolution in the detector under test for both read-out planes individually. The applied threshold was around 15 mV above the baseline, which corresponds at the chosen electronics gain to around 1.5 fC or $10^4$ electrons.

this requires high detector gains $> 10^4$, low threshold levels and the usage of either the neighbouring-logic or $Q^2$ weighting. In some conditions, also spatial resolutions below 50 µm could be achieved, with $\sigma_{\text{DUT}} = (38.8 \pm 1.3)$ µm as the best result. However, it has to be remarked that, particularly in lower gain situations, the spatial resolution reaches sometimes values worse than 100 µm. Independent of the detector gain or the threshold level, $Q^2$ weighting obtains better spatial resolution results

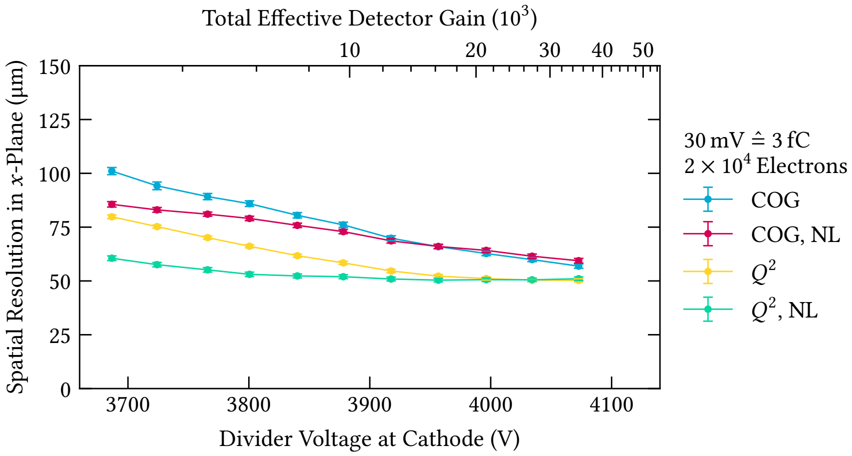

*(a)* – Spatial resolution in the $x$-plane.

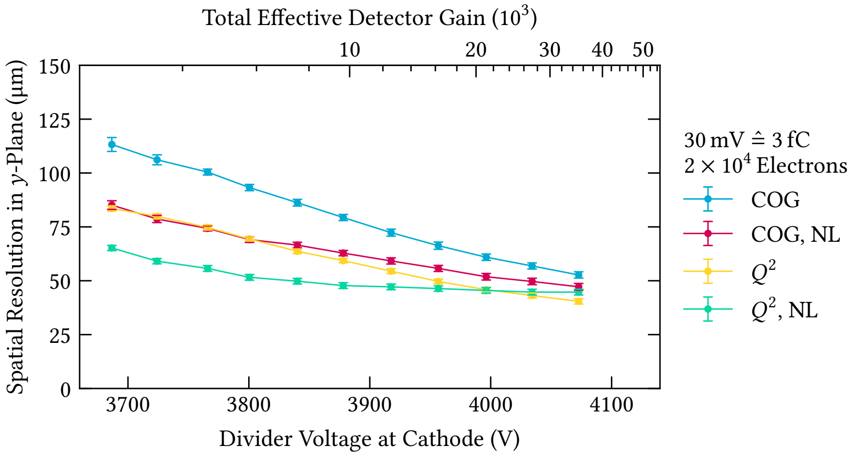

*(b)* – Spatial resolution in the $y$-plane.

*Figure 5.43* – Spatial resolution in the detector under test for both read-out planes individually. The applied threshold was around 30 mV above the baseline, which corresponds at the chosen electronics gain to around 3 fC or $2 \times 10^4$ electrons.

than centre-of-gravity, confirming that it is not a smoothing effect. At the same time, $Q^2$ gives in the high gain region ($G > 20\,000$) better results for the spatial resolution in the $y$-plane of the detector than in its $x$-plane. COG on the other hand gives worse spatial resolutions in the $y$-plane compared to the $x$-plane of the detector, independent of the investigated thresholds and detector gains. A possible explanation for this can be found in the 60/40 % charge sharing ratio between the

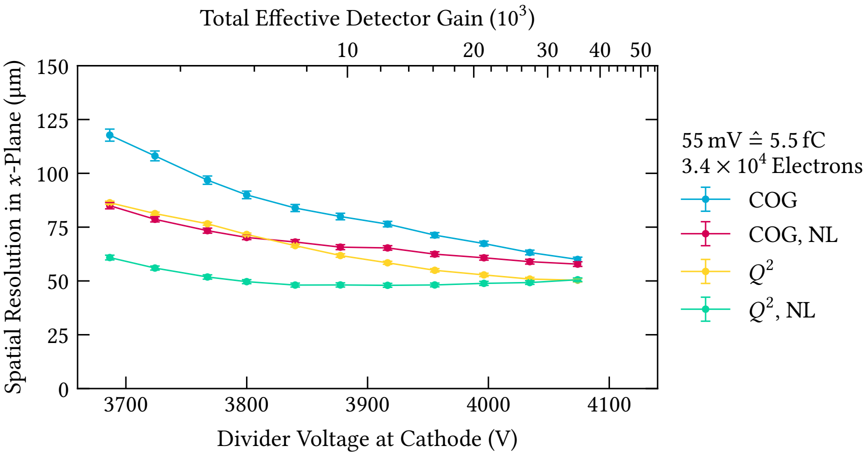

*(a)* – Spatial resolution in the $x$-plane.

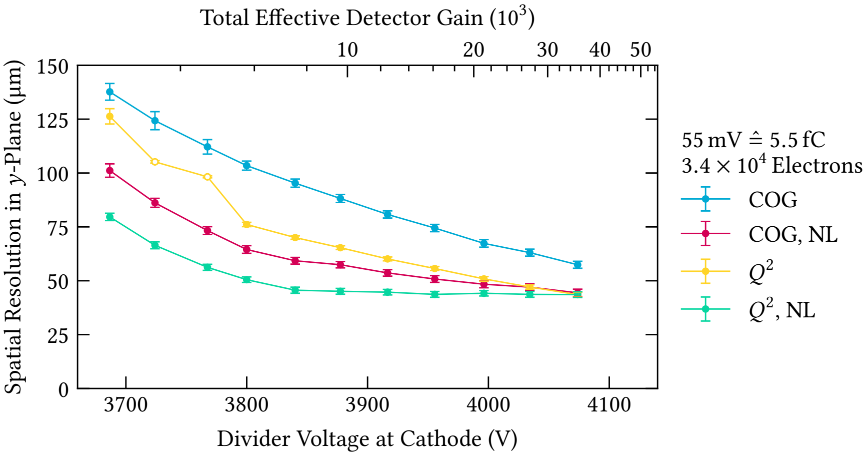

*(b)* – Spatial resolution in the $y$-plane.

*Figure 5.44* – Spatial resolution in the detector under test for both read-out planes individually. The applied threshold was around 55 mV above the baseline, which corresponds at the chosen electronics gain to around 5.5 fC or $3.4 \times 10^4$ electrons. It should be noted that for the two non-solid data points for the $y$-plane resolution the fit of the double Gaussian function of equation (5.14) did not converge, hence the RMS was used to determine the width of the residual distribution.

read-out planes. This means that less charge information is available in the $y$-plane, affecting the accuracy of the centre-of-gravity reconstruction. For the $Q^2$ weighting on the other hand, with its slightly different handling of the available charge, the accuracy of the reconstructed position can be affected differently.

The effect of less available charge information in the $y$-plane is also highlighted when the neighbouring-logic is considered. As it recovers parts of the missing charge information, the relative improvement of the spatial resolution from COG without neighbouring channels to COG with NL is larger in the case of the $y$-plane, where more charge is lost due to the THL, compared to the $x$-plane. In general, it can be seen that the larger the threshold level or the smaller the gain, i.e. the smaller the signal-to-threshold ratio, the larger the relative improvement of the spatial resolution with COG due to the recovered charge information. Only in the case of the $x$-plane at an investigated threshold of 15 mV above baseline, no improvement due to the neighbouring-logic is observed, but in fact a slight decrease.

Even though the neighbouring-logic and the $Q^2$ weighting target different parts of reducing the modulation effect and improving the spatial resolution, also their combination is studied. Especially in the regions of low detection efficiency (figure 4.17), meaning low signal-to-threshold ratio, the combination gives the best spatial resolution results. There are however a few occasions, at high signal-to-threshold ratios, where pure $Q^2$ weighting without NL gives better spatial resolution results. This indicates that if the tails of the charge distribution contain an additional small fraction of the total charge (recovered by the NL), the different weighting of the additional charge in the tail decreases slightly the spatial resolution.

### *5.2.7 Classification of the Results*

Following the various studies on the spatial resolution, the last part of this section is the classification of the results and the effect of the NL and the $Q^2$ on the position reconstruction. Both cases were motivated by the reduction of the modulation pattern in the position distribution (section 5.2.1).

The starting point is the $Q^2$ weighting method, which addresses one of the origins of the modulation pattern. By handling the available charge information differently by giving less weight to the tails of the charge distribution that just slightly crossed the THL, the position should be reconstructed more accurately and hence the position distribution becomes more uniform. The important point of this approach is that it is an event-based approach which can be directly applied to the data and not an iterative approach depending on the full detector-response as e.g. the $\eta$-method. If $Q^2$ weighting improves the accuracy of the position reconstruction, this should lead to an improved spatial resolution. Hence, different X-ray imaging methods (sections 5.2.4 and 5.2.5) as well as the results from a beam telescope (section 5.2.6) were used to determine if $Q^2$ improves the image quality and response as well as the spatial resolution for particle tracks. Independent of the employed method, the $Q^2$ method gave better results than the default centre-of-gravity method, confirming that it improves the position reconstruction, which is also the case for other electronics than VMM3a/SRS (figure 5.21).

However, to give the full picture, several aspects have to be considered regarding the $Q^2$ weighting. There is for instance the detector type and the read-out geometry. $Q^2$ weighting was only tested in a COMPASS-like triple-GEM detector with $x$-$y$-strip read-out. Any other read-out geometries for example pads or pixels were not tested. Also, other detector types with strip read-out, e.g. MicroMegas or GEM detectors with different drift or GEM configurations, were not investigated. Nonetheless, it is possible to illustrate some of the limitations of $Q^2$, due to the calculations performed with it (section 5.2.3). In case the charge cloud width becomes small with respect to the read-out pitch, i.e. if a large fraction of the total collected charge is acquired by one read-out channel, the modulation effect that is supposed to be reduced gets actually enhanced, as the weight on this single channel increases. In such a case, $Q^2$ weighting would decrease the position reconstruction capabilities and the spatial resolution. Hence, it might not be adopted as a general position reconstruction method for any particle detector.

In addition to the $Q^2$ weighting, also the VMM3a's neighbouring-logic was studied. The target of the NL in reducing the modulation pattern is to recover the charge information below the threshold level, to better describe the charge distribution and hence achieve a more accurate position reconstruction. Thus, the goal here is not to understand if the position reconstruction improves due to the additional charge, this is intrinsically the case, but to understand if the charge is recovered correctly. If most of the charge is acquired correctly the spatial resolution should improve, otherwise, it should decrease. In the case of the X-ray imaging studies the position reconstruction improves (figure 5.33) and reduces the introduced intensity fluctuations which do not reflect the actual intensity behaviour (figure 5.37). In the case of the beam telescope studies, the neighbouring-logic also helps to improve the spatial resolution, in particular in situations with a low signal-to-threshold ratio. There the fraction of charge below the threshold level that can be recovered is the largest. If this is not the case (figure 5.42a), the spatial resolution becomes slightly worse.

This indicates one of the possible problems with the NL. The neighbouring channel below THL will acquire any peaked signal, despite the fact that the read-out of the neighbouring channels is triggered by the signals above the THL which usually originate from interacting particles. So even though the neighbouring channel should contain the charge information from the charge cloud of the interacting particle, this information might contain also a considerable fraction of noise. If that is the case, the spatial resolution would decrease as in the given example. In such a case, additional cuts to reject the neighbouring channel could be in principle applied. One possible cut could be applied on the charge, which would define a software threshold below the set hardware threshold in the electronics. Another possible cut would be on the time of the neighbouring channel. If the neighbouring channel would contain pure noise information, the signal time should be uncorrelated with the time of e.g. the strip with the highest amplitude inside the charge cluster. Then the neighbouring channel could be removed from the cluster. Both types of cuts were not applied and are in case of the time cut not yet implemented in vmm-sdat. However, even without these potential cuts to improve the neighbouring-logic's impact, the experimental data show that the results with NL enabled are typically better in terms of spatial resolution, as well as in terms of energy resolution (section 5.4).

It should be also recalled that only one detector type was tested, which furthermore contained a one-to-one detector strip to read-out channel mapping. So unless adjacent read-out strips are mapped to the same adjacent read-out channels of the VMM3a, the use of the neighbouring-logic is not applicable. In addition, despite potentially providing an advantage for the position reconstruction, it increases the number of hits that have to be read out from the electronics, hence for some applications requiring high rates the neighbouring-logic should be kept turned off.

One of the goals of this thesis is to demonstrate that the combination of VMM3a and SRS is a read-out system which is well-suited to study the performance of particle detectors and to extract specific detector features. As such, the spatial resolution studies are a prime example where the read-out electronics were used to study the detector or, to be more precise, the reconstruction behaviour.

## 5.3 Time Resolution Studies

The VMM3a has an intrinsic time resolution between 0.5 ns and 2 ns (figure 3.14), which is better than the typical[11] detector time resolution of $\mathcal{O}(10\,\text{ns})$ [25, 67] for MPGDs. In the pursuit of providing a fully integrated read-out system, this is an important feature, as it allows to precisely determine the detector time resolution, without requiring additional external high-resolution timing electronics or event matching between different read-out systems. Despite being able to record all necessary data within a single data stream, the time resolution studies require a reference time signal. Hence, similar to the reference position in the beam telescope, the time resolution studies are only performed with MIPs, with the recorded time of each interacting particle traversing the beam telescope being the reference time.

First, the tracking detectors are studied by comparing the recorded time of a cluster in each detector $t_\text{c}$ with a reference time $t_\text{scint}$ that is here provided by the scintillator coincidence. While $t_\text{scint}$ is the timestamp recorded on a single read-out channel to which the output of the coincidence unit was connected, the time of the cluster in the tracking detectors, is defined as the average of the two plane timestamps via $(t_x + t_y)/2$, with each plane timestamp being given by the centre-of-gravity

---

[11] Typical for MPGD tracking detectors filled with gas mixtures containing large fractions of argon or $CO_2$ and not operated at gains $\geq \mathcal{O}(10^5)$.

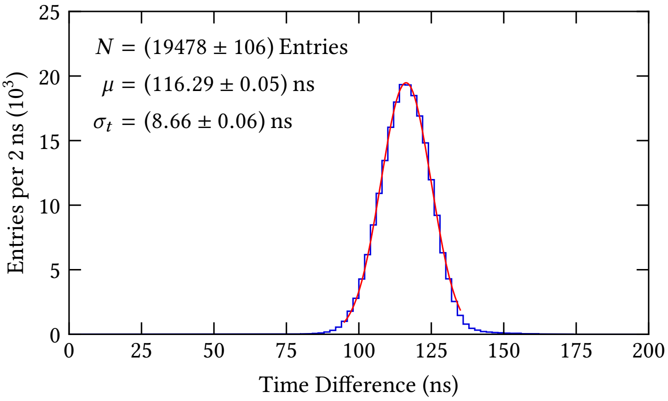

*Figure 5.45* – Example of a time difference distribution. Here, the time difference $\Delta t = t_c - t_{\text{scint}}$ between the signals from scintillators connected to a NIM coincidence unit $t_{\text{scint}}$ and the ones from the clusters in the triple-GEM detectors $t_c$ is plotted. Both signals have been obtained within a single data stream via VMM3a/SRS.

time, as in equation (4.7). To compare the timestamps, $t_c$ has to lie within a time interval of ±500 ns around $t_{\text{scint}}$, such that the cluster and the scintillator event are considered as a matched event. The time interval was chosen like this, to match the 1000 ns time interval of the event-building (section 4.3.1). From the distribution of the corresponding time difference $\Delta t = t_c - t_{\text{scint}}$ in the matched events (figure 5.45), it is possible to extract the width $\sigma_t$ of the distribution. The width is the convolution of the intrinsic detector resolution, the time resolution of the electronics on the tracking detectors $\sigma_{\text{el}}$ as well as the one of the scintillators and the NIM logic $\sigma_{\text{scint}}$:

$$\sigma_t^2 = \sigma_{\text{det}}^2 + \sigma_{\text{el}}^2 + \sigma_{\text{scint}}^2 \,. \tag{5.20}$$

With values of around 2 ns for the tracking detector electronics[12] and an estimated value of below 1 ns for $\sigma_{\text{scint}}$ [25], their contribution to the total width is almost negligibly small in the case of triple-GEM detectors filled with $Ar/CO_2$ (70/30 %) but nonetheless included in the calculations.

As for their efficiency (figure 4.16), the tracking detectors have to be operated with different divider voltages to reach the same gain. Once this is considered, the three tracking detectors behave similarly in terms of time resolution (figure 5.46). All detectors have resolutions of around 10 ns, which get better with higher voltages applied to the divider. This is expected as a higher divider voltage leads to a higher

---

[12] The VMMs connected to the detectors were operated with a peaking time of 200 ns and a TAC slope of 60 ns, which results in the given resolution (section 3.4).

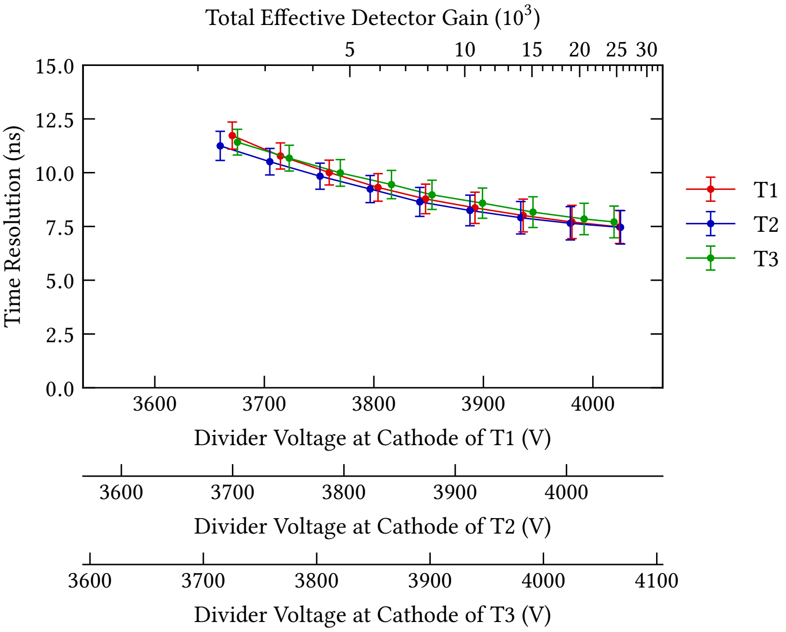

*Figure 5.46* – Time resolution of the three triple-GEM tracking detectors, depending on the voltage applied to the divider. The cluster timestamps are determined via the centre-of-gravity method as given in equation (4.7). The error bars are enlarged by a factor of 5 for better visibility.

drift and induction field, so a faster charge collection. Also, the gain is higher, meaning that more charge is collected, which also improves the time resolution [26]. The obtained values and the behaviour is compatible with previous measurements on the time resolution of COMPASS-like triple-GEM detectors [88, 89].

In parallel to the study on the detector resolution, also the different methods of defining the cluster timestamp $t_c$ are investigated. The three methods in question are the COG time as in equation (4.7), the timestamp of the strip with the highest amplitude or the µTPC-method, where the strip with the earliest timestamp is used to define the cluster time. The comparison measurement is identical to the time resolution measurement of the tracking detectors. The time resolution of the tracking detectors is measured for each method (figure 5.47) Even though only the example of one tracking detector is shown, the behaviour is the same for the two other tracking detectors: within the error bars, the time resolution for MIPs is the same for all three reconstruction methods. This indicates that the measured time resolution reflects the intrinsic detector resolution and is not affected by the reconstruction method.

Afterwards, the time resolution of the detector under test is determined, with the goal of studying the effect of the electronics threshold on the time resolution.

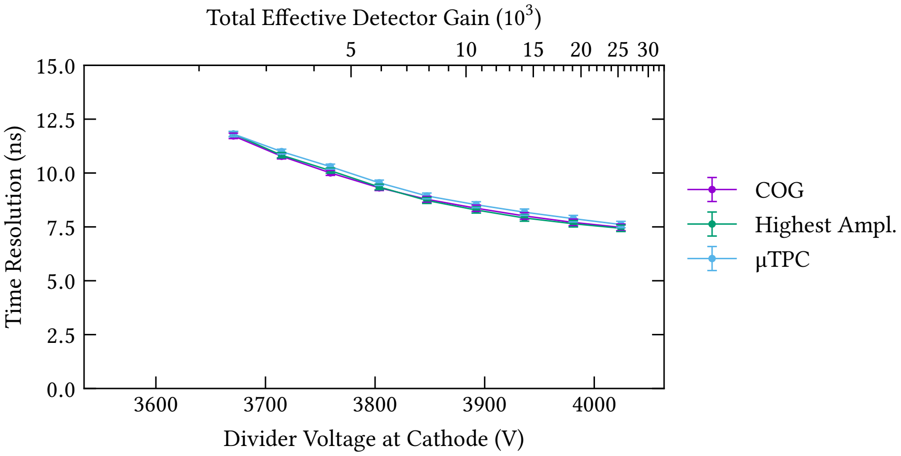

*Figure 5.47* – Time resolution of a COMPASS-like triple-GEM tracking detector (T1 of the beam telescope), depending on the voltage applied to the divider. The three methods indicate the way how the timestamps of the clusters are defined.

The time resolution is again determined from the width of the distribution of time differences between the cluster timestamp in the DUT and the event timestamp. Here, the event timestamp is however not provided by the scintillators but by the tracking detectors themselves. Both timestamps are calculated via the COG method. For the event, it is required that within a time interval of 1000 ns each tracking detector contains a cluster. Due to this requirement, it is assumed that using a single tracking detector as a time reference for the event is sufficient as all of them have a similar time resolution and timing behaviour. In this particular case, tracker T1 was selected to be the time reference. Hence, the time resolution of the detector under test is given by

$$\sigma_{\mathrm{DUT}} = \sqrt{\sigma_t^2 - \sigma_{\mathrm{T1}}^2 - 2\sigma_{\mathrm{el}}^2} \, . \tag{5.21}$$

In addition, also the time resolution of the electronics $\sigma_{\mathrm{el}}$ has to be considered, now for both the DUT and the tracking detector.

The observed timing behaviour (figure 5.48) is similar to the tracking detectors, with increasing time resolution for larger voltages applied to the divider. The measured time resolution of the DUT is slightly worse compared to the tracking detectors, as a higher total effective detector gain is needed to reach the same time resolution. However, the values are still close enough to be considered compatible, especially when compared with the previous measurements from [88, 89]. From the measurements it is further obtained that the measured time resolution behaviour is almost threshold independent. The only exception is observed for high thresholds (here

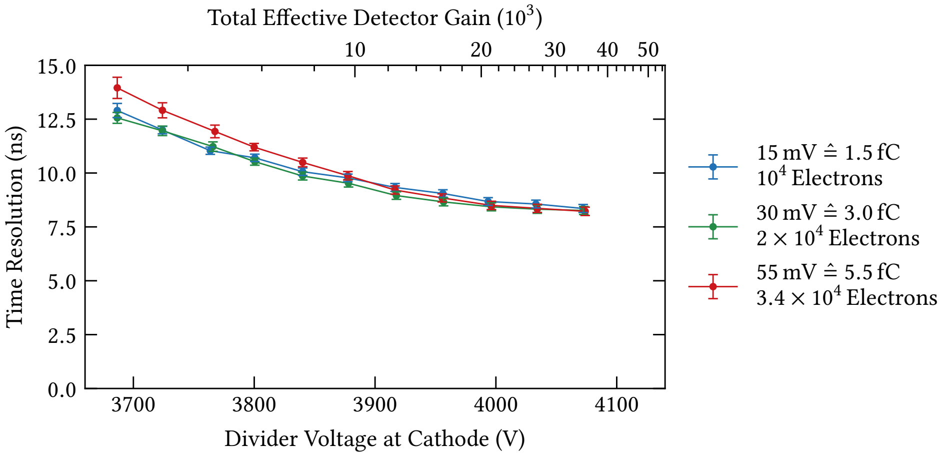

*Figure 5.48* – Time resolution of the COMPASS-like triple-GEM detector under test, depending on the voltage applied to the voltage divider and the electronics THL. The cluster timestamps are determined via the centre-of-gravity method as given in equation (4.7).

55 mV) towards lower detector gains, so regions of detector efficiencies below 50 % (figure 4.17). However, the obtained time resolutions are within their uncertainties still compatible with the other measurements. This all demonstrates that VMM3a/SRS is well suited for studying the time resolution of particle detectors as part of being an integrated read-out system.

## 5.4 Energy Resolution Studies

After using VMM3a/SRS to investigate the detector behaviour in space and time, the last step is to study the energy behaviour. This involves measurements of the neighbouring-logic's effect on the energy resolution and energy-resolved X-ray imaging. The starting point however is the illustration of the threshold equalisation's effect on the energy behaviour. The effect became particularly evident during the test beam, where the energy correlation between the $x$-plane and the $y$-plane was studied (figure 5.49). At first, a strong charge splitting between the two read-out planes was observed (figure 5.49a). The splitting in the given example represents a medium case, with other runs containing a more pronounced deviation from a linear correlation than in the example and others being more linearly correlated. The behaviour was observed in all detectors, including a gain dependence with the behaviour becoming more pronounced at lower gains. Hence, the origin was assumed to be related to the charge collection and processing, specifically the threshold which is needed to trigger the read-out of each channel. Thus, the measurement was repeated in a later test

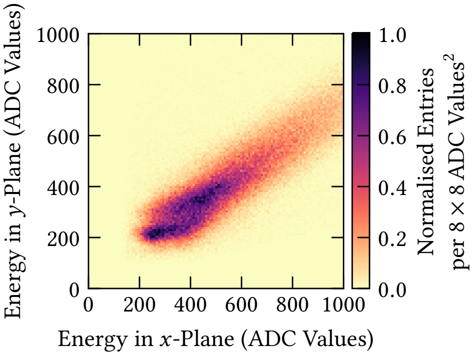

*(a)* – Threshold of 55 mV, not equalised.

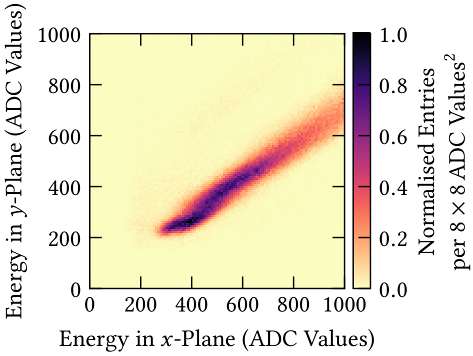

*(b)* – Threshold of 55 mV, equalised.

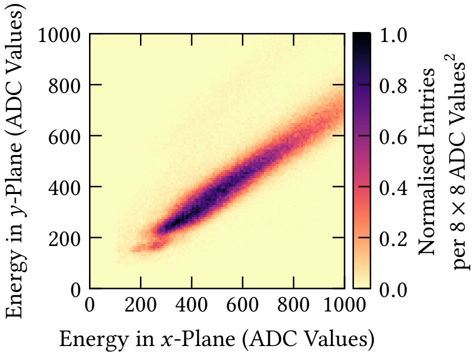

*(c)* – Threshold of 15 mV, equalised.

*Figure 5.49* – Charge correlation plots with the cluster charge measured in ADC values in the $y$-plane plotted versus the charge in the $x$-plane for different threshold levels and equalisation conditions.

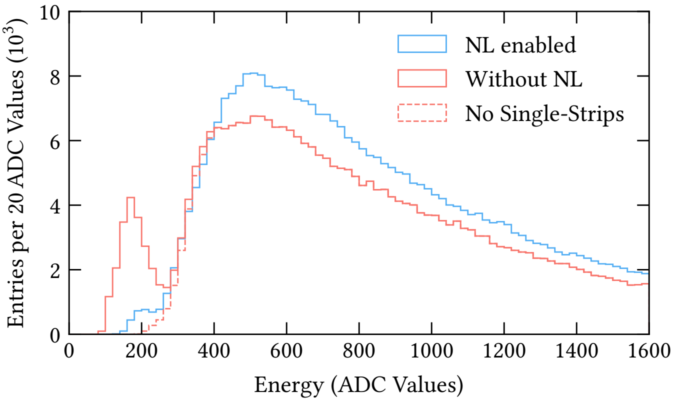

*Figure 5.50* – Landau distribution for the cases with and without neighbouring-logic enabled, as well as with the single-strip clusters excluded from the energy spectrum for the case without NL.

beam at the same global THL, but with the channel-by-channel thresholds equalised (figure 5.49b). It is still possible to observe a deviation from the linear correlation but the fluctuations became smaller. When further reducing the threshold level with equalised thresholds, the observed deviation almost disappears (figure 5.49c). This demonstrates once more the importance of the threshold level in VMM3a/SRS and its impact on the data quality.

A similar effect of the threshold on the data quality is observed, when comparing the Landau distribution for the cases with and without NL enabled (figure 5.50). For the case without NL, a peak at low energies is observed, which almost disappears for the case of enabled neighbouring-logic. As this peak appears in the clusters that can be matched to a particle track, it is considered unlikely that the peak contains noise events. With the peak disappearing, when excluding single-strip clusters from the events, the assumption is that these particular single-strip clusters correspond to low amplitude events which just cross slightly the threshold level, while the neighbouring strips are still below the threshold level and hence not processed. With NL enabled, these two strips can be recovered and the peak with the former single-strip clusters disappears. This indicates that the neighbouring-logic helps to improve the measured energy resolution.

To better study the possible improvements of the measured energy resolution, the effect of the NL on the X-ray spectra is studied (figure 5.51). In the case of soft X-rays, three different event signatures exist (figure 4.6). While for the copper target X-ray tube, the photopeak is located at 8.0 keV, the argon fluorescence events[13] are

---

[13] With VMM3a/SRS it is possible to resolve these particular interactions. For the exact procedure it is referred to the next chapter (section 6.1).

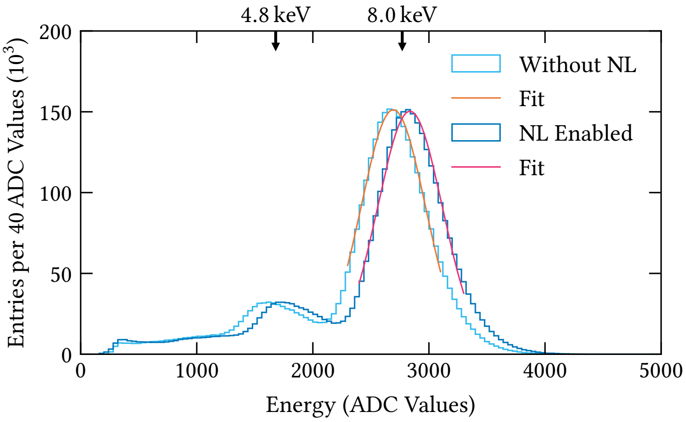

*(a)* – Full copper X-ray spectrum.

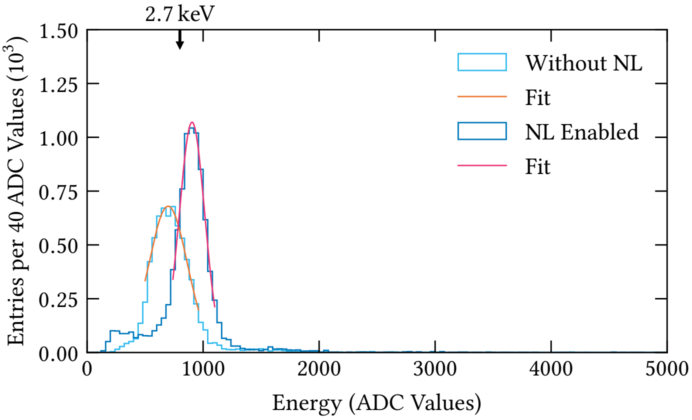

*(b)* – Argon fluorescence spectrum.

*Figure 5.51* – Measured energy spectra for the full spectrum of the copper target X-ray tube (a) and the resolved argon fluorescence interactions (b). It should be noted that the annotated energy values serve only for indication purposes, but within a 10 % variation interval, the ratios between the annotated energies and the measured ADC values are compatible.

located at 2.7 keV. With the goal of being able to reconstruct events over this larger dynamic range, the energy resolutions with and without neighbouring-logic enabled are compared. As before, the main effect is introduced by the threshold level, but with the neighbouring-logic improving the energy resolution due to the additional charge that is recovered from below the THL. In the case of a high signal-to-threshold ratio as for the photopeak, the improvement in the energy resolution is marginal,

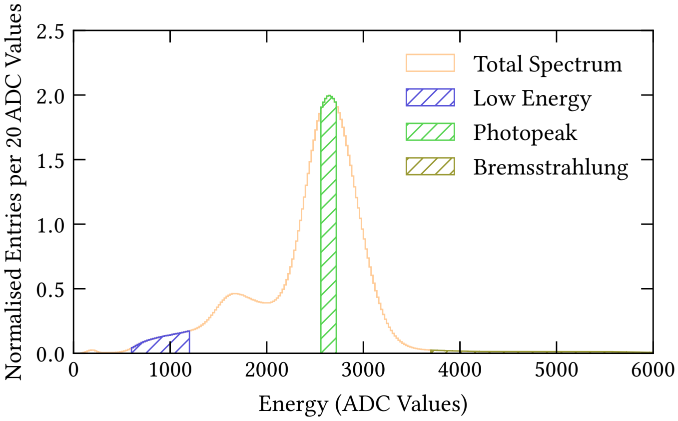

*Figure 5.52* – Spectrum of the copper target X-ray tube, with the different energy regions used for the energy-resolved X-ray imaging being highlighted.

from $R = (24.2 \pm 0.3)\,\%$ to $R_{\mathrm{NL}} = (23.1 \pm 0.3)\,\%$ for the case with NL enabled. This is mainly caused by the shift of the photopeaks position, due to the additional amount of recovered charge, as the width of the peak remains with around 280 ADC Values the same for both cases (within their uncertainty). The relative shift of the photopeak itself is in addition rather small, as the relative amount of charge recovered is small. In the case of argon fluorescence photons, the situation is slightly different. Here, the relative amount of charge recovered from below the THL is much larger, hence the impact of the peak's position shift is much more significant. However, also the width of the peak itself gets much narrower, improving the energy resolution from $R = (56.1 \pm 1.5)\,\%$ to $R_{\mathrm{NL}} = (28.3 \pm 0.6)\,\%$. The reduced width of the peak with NL enabled can be explained by the fluctuations of the lost charge below THL. Depending on the cluster position, a different number of strips have a signal above the threshold. However, with the total signal being rather small, losing charge below THL has a large relative impact on the measured charge. Hence, the fluctuations of the measured charge are much larger when the individual strip charge cannot be recovered from below the THL. This is reflected by the measured width of the argon fluorescence peak and hence impacts also the measured energy resolution, which improves when enabling the neighbouring-logic.

The last part of studying the energy behaviour with VMM3a/SRS is to select specific energy regions of the X-ray spectrum, to perform energy-resolved X-ray imaging. Three different regions are selected from the spectrum (figure 5.52): a low energy region with photons of around 3 keV energy, the region within the photopeak of around 8 keV and the higher energetic Bremsstrahlung region of around 12 keV and more. For each region, the image of the bat's torso was generated (figure 5.53), with the number of entries per bin being normalised to the total number of entries per region, as the latter varies. The resulting images indicate the energy and density-dependent interaction cross sections of the photons with matter. While in the photopeak region (figure 5.53b), a distinction between bones and tissue is possible, the intensity response gets much more uniform for the Bremsstrahlung region (figure 5.53c), meaning that most photons are not absorbed anymore. In the case of the low energy region (figure 5.53a), the distinction between tissue and bones becomes also worse, however here because the photons are already absorbed by the tissue. However, here it is also seen that fewer photons are measured in the lower left corner of the image, where neither bones nor tissue of the bat is located. This is likely to be caused by the plastic bag, in which the bat was contained during the measurements, absorbing also the low energetic photons. The results indicate that energy-resolved imaging with VMM3a/SRS is possible, also at high interaction rates (section 5.1.3), however, the quality of the different energy regions would have profited from a wider covered energy range. This would however require an X-ray tube with a different target, e.g. tungsten.

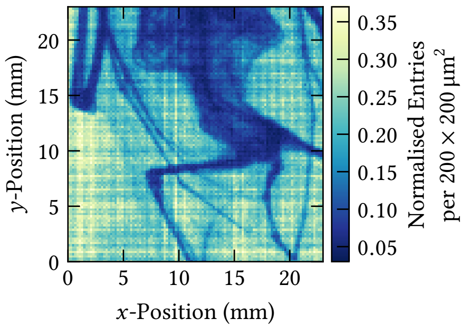

*(a)* – Low energy region.

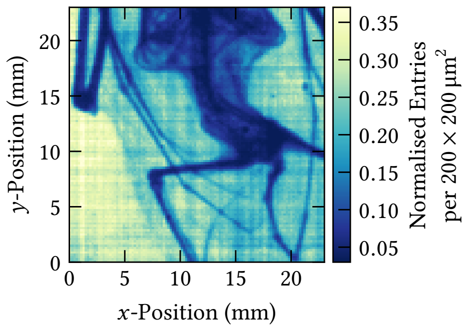

*(b)* – Photopeak region.

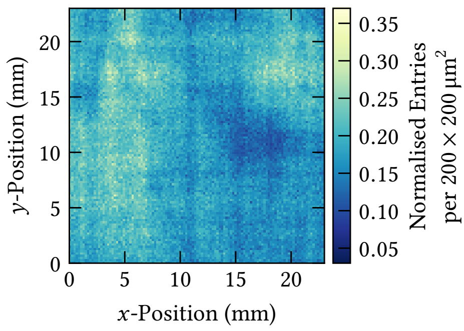

*(c)* – Bremsstrahlung region.

*Figure 5.53* – Images of the bat's torso at different photon energies. Data published in [79].

## Chapter 6

# APPLICATIONS

Following the exploration of detector properties and how the electronics affect their measurement (chapter 5), the last part of this thesis is dedicated to making use of these results for other applications. At first, it is shown how to resolve argon fluorescence interactions with VMM3a/SRS and how these interactions can be used to determine the electron drift velocity (section 6.1). In the second section it is illustrated how the system can be used for quality assurance measurements on particle detectors (section 6.2). In the last part, the application of VMM3a/SRS in the NA61/SHINE experiment [13, 14] is shown (section 6.3).

## 6.1 RESOLVING FLUORESCENCE INTERACTIONS

The spectra of soft X-rays recorded in argon-based gas mixtures are the result of three interaction types (section 4.2.1), with the full energy deposition (figure 4.6a) and the escape events (figure 4.6b) peaking out. In addition, the spectra contain events which are here called *double cluster events*, where after the liberation of the photoelectron an argon fluorescence photon is emitted in the de-excitation process which then ionises another gas atom (figure 4.6c). Due to their unique event structure with two correlated clusters which are separated in space, where the separation along the drift direction corresponds to a separation in time, it is possible to resolve these events with VMM3a/SRS, making use of most of its features at once. After presenting how the events can be resolved (section 6.1.1), the events are used to determine the electron drift velocity in the utilised particle detector (section 6.1.2).

For the measurements, the laboratory set-up was used, both with the $^{55}$Fe radioactive source and the copper target X-ray generator. The detector was operated at a gain of around 40 000, with the electronics settings being 200 ns peaking time, 60 ns TAC slope and an electronics gain of 1.0 mV/fC The threshold was set to 25 mV above the baseline without channel-by-channel equalisation and the neighbouring-logic was enabled. It should be noted that the results of this section have been published in [71], but there without applied time calibration.

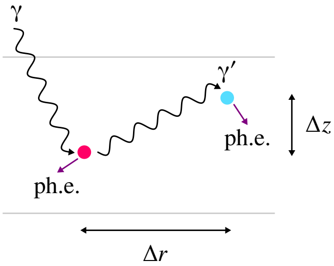

*Figure 6.1* – Illustration of the separation of the two charge clouds in $z$-direction and in the $x$-$y$-plane, where $\Delta r^2 = \Delta x^2 + \Delta y^2$ and $\Delta z = w\Delta t$, with $w$ the drift velocity and $\Delta t$ the difference in the signal arrival time due to the particle drift.

### *6.1.1 Identifying Argon Fluorescence Interactions*

The identification procedure of the double cluster events starts with the fact that both clusters are effectively generated at the same time[1]. This means that the spatial separation of the clusters along the drift direction, here the $z$-direction, is defined by the drift gap, with the maximum possible separation being here $\Delta z_{\mathrm{max}} = 3\,\mathrm{mm}$. Due to the particle drift, the two clusters will arrive at different times at the read-out anode, with the maximum time difference being $\Delta t_{\mathrm{max}} = \Delta z_{\mathrm{max}}/w$, where $w$ is the drift velocity (figure 6.1). The drift velocity in $\mathrm{Ar/CO_2}$ (70/30 %) at a typical drift field of 2.5 kV/cm is expected to be 6.7 cm/μs according to Magboltz calculations [37, 38], leading to a maximum difference in the signal arrival time at the read-out anode of $\Delta t_{\mathrm{max}} = 45\,\mathrm{ns}$.

Thus, the double cluster events should be identified by taking the time difference $\Delta t$ between consecutive clusters and then looking at the corresponding distribution of the values, with $\Delta t$ of the same order of magnitude as calculated from Magboltz (figure 6.2). In this time difference region, various events are found. It is further observed that the distribution stretches towards larger time differences at half of the drift field[2], where $\Delta t_{\mathrm{max}} = 69\,\mathrm{ns}$ is expected from the Magboltz calculations. Important features to perform this measurement are the self-triggered continuous read-out in combination with the nanosecond time resolution of the VMM3a. Without them, neither every charge cluster could be recorded nor could it be assigned with a precise timestamp in the continuous process of the electron drift. It should be noted that the measurements were performed at low recorded interaction rates of $\lesssim 1\,\mathrm{kHz}$. This was done to reduce the probability of two X-ray photons being emitted by the X-ray generator or the radioactive source in time intervals comparable to $\Delta t_{\mathrm{max}}$.

---

[1] Compared to the time resolution of the electronics, the de-excitation time and the time it takes to ionise the gas atoms are negligibly small.

[2] To half the drift field, the 1 MΩ resistor in the voltage divider to define the voltage applied to the drift region (figure 4.2), was replaced with a 0.5 MΩ resistor.

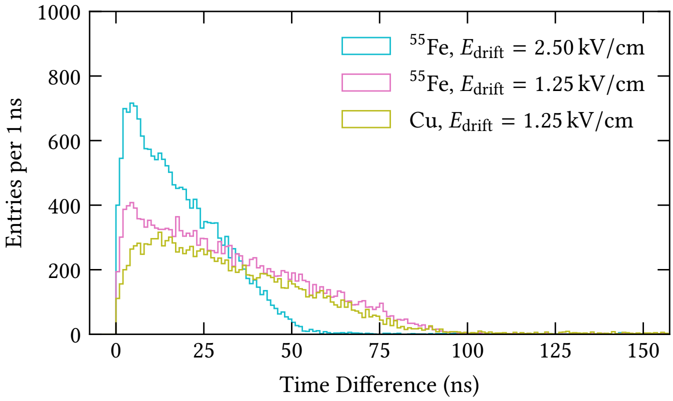

*Figure 6.2* – Distribution of time differences between consecutively recorded X-ray interactions.

The next step is to confirm that the recorded interactions are the ones containing the argon fluorescence interactions. For this, the time information is combined with the energy information, meaning that the energy spectra of the clusters with time differences $\Delta t < 100$ ns are compared with the full energy spectra (figures 6.3 and 6.4)[3]. In the case of the $^{55}$Fe spectra, a prominent peak can be observed in the double cluster spectrum, being aligned with the escape peak of the full energy spectrum (figure 6.3). This is compatible with the expectation (section 4.2.1), where for $^{55}$Fe the initial photoelectron has an energy of 2.7 keV and the photoelectron liberated by the argon fluorescence photon has also an energy of 2.7 keV. As the interaction and emission processes do not depend on the electric drift field, the observed behaviour for the two different fields is similar.

For the case of X-rays from the copper target X-ray tube, where the photon energy is different (8.0 keV for the $K_\alpha$-line instead of 5.9 keV), the position of the photopeak and the escape peak shift towards larger values, while the argon fluorescence interaction remains at 2.7 keV. As a result, the escape peak, which is now at around 4.8 keV, and the peak from the argon fluorescence interaction do not coincide anymore. This explains the two prominent peaks that can be observed in the double cluster spectrum of the copper X-rays (figure 6.4a).

Even though this should be sufficient to confirm that VMM3a/SRS can resolve the argon fluorescence interactions, another step is added, meaning the position sensitivity (figure 6.4b). For this, a geometrical position cut is applied to the double

---

[3] It is important to note that the energy values given in keV in the spectra correspond to the expected values. No Energy calibration was performed. However, the ratios of the corresponding ADC values are compatible with the ratios of the expected energy values, with maximum 10 % deviation.

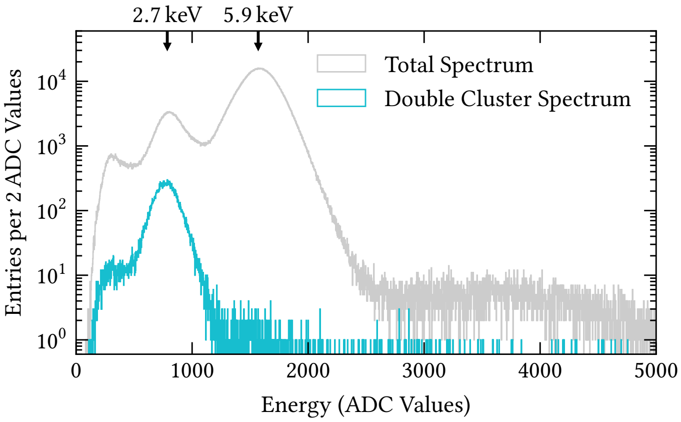

*(a)* – Electric drift field of 2.5 kV/cm.

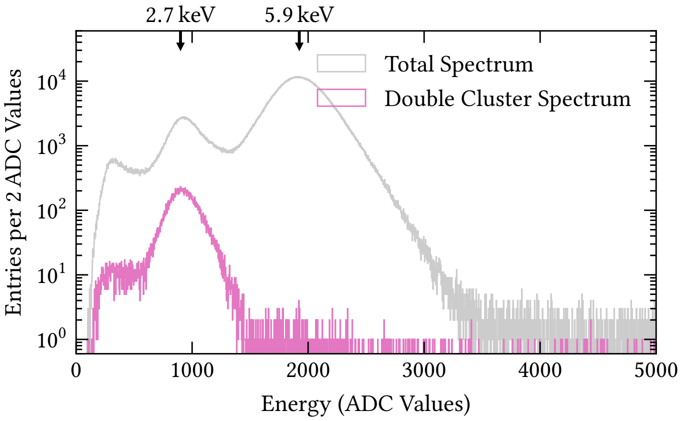

*(b)* – Electric drift field of 1.25 kV/cm.

*Figure 6.3* – Recorded energy spectra of the X-ray photons emitted from an $^{55}$Fe source, with the spectra of the double cluster events overlaid.

cluster events: from all the clusters being part of the time difference distribution (figure 6.2), only the ones with a position outside of the area of the X-ray photon beam spot are considered (figure 6.5). Due to the localised beam spot, the liberation of the 4.8 keV photoelectron can take only place inside this area, while the interactions of the argon fluorescence photons can then take place also outside of this area. Thus, only these clusters should remain as part of the double cluster spectrum, which can be observed in the corresponding spectrum (figure 6.4b). As such, it is confirmed that VMM3a/SRS enables the possibility to resolve argon fluorescence interactions.

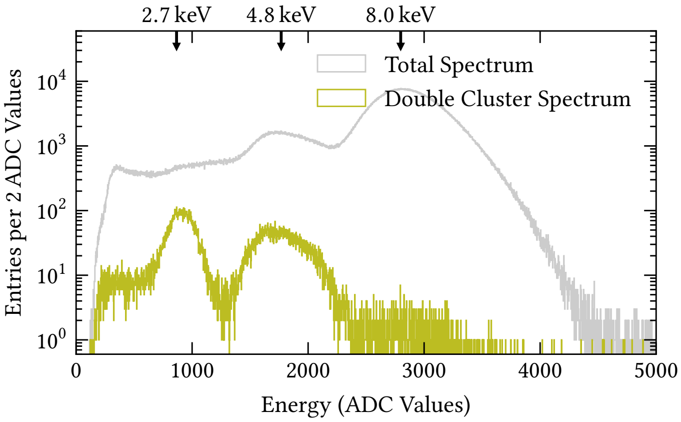

*(a)* – Without position selection.

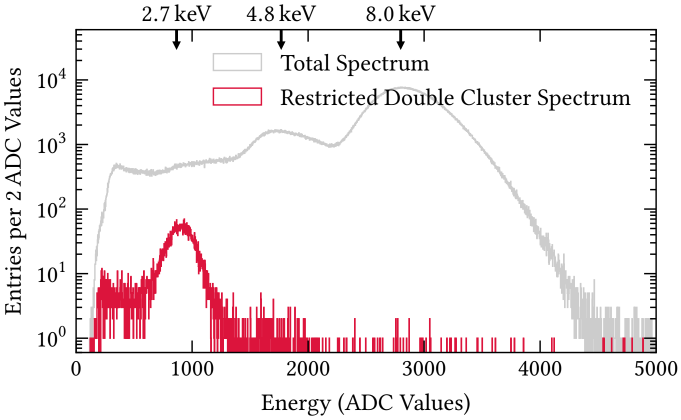

*(b)* – Position selection applied.

*Figure 6.4* – Recorded energy spectra of the X-ray photons emitted from the copper target X-ray tube, with the spectra of the double cluster events overlaid. The electric drift field was 1.25 kV/cm.

### *6.1.2 Drift Velocity and Absorption Length*

Being able to identify the double cluster events, the underlying interactions are used in the following to study the electron drift velocity inside the detector. In addition, also the absorption length of argon fluorescence photons inside $Ar/CO_2$ (70/30 %) is determined. While the determination of the absorption length is performed with the data from the measurements with the copper target X-ray tube, the drift velocity measurements were performed using an $^{55}$Fe source. In addition, to be able to scan over various drift fields, the 1 MΩ resistor in the voltage divider, defining the voltage

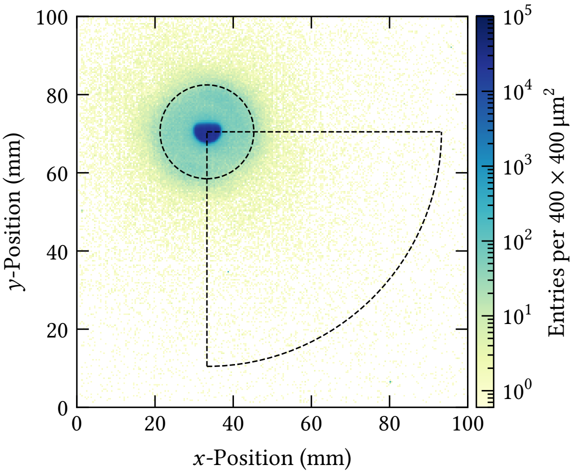

*Figure 6.5* – Image of the beam spot of the copper X-rays. The areas contained by the dashed lines indicate the position selections. The X-rays with reconstructed positions inside the circle are excluded for the generation of one of the double cluster spectra (figure 6.4), while the X-ray interactions recorded within the wedge region are the ones used to determine the absorption length (figure 6.11).

to generate the drift field (figure 4.2), was taken out of the voltage divider. Instead, the high voltage was applied separately to the drift cathode and the GEM stack, with the latter being operated at the same detector gain of around 40 000 as before.

To determine the electron drift velocity, the procedure of identifying the double cluster events is effectively reverted. Instead of using the calculated drift velocity to establish the time difference range to be looked at, the cut-off-value of the time difference distribution has to be determined as this corresponds to $\Delta t_{\text{max}}$, which then allows to calculate the drift velocity, with $\Delta z_{\text{max}} = 3\,\text{mm}$. The first step to do so is the filtering of the time difference distribution. This means that an energy cut is applied to the data, selecting only cluster events where the measured energy of the clusters lies within a $2\sigma$ interval of the mean of the 2.7 keV peak (figure 6.6a). To determine the peak's mean and its width $\sigma$, a Gaussian function is fitted to the peak. Applying this energy selection leads to a time difference distribution with a much clearer defined cut-off-value (figure 6.6b).

However, the cut-off value that can be seen in the histogram is not the value of $\Delta t_{\text{max}}$. This is due to the fact that the time difference distribution gets broadened by the time resolution of both the detector and the electronics. This was reproduced with a simple Monte Carlo simulation (figure 6.7), were numbers between 0 ns and 60 ns where drawn from a uniform distribution, corresponding to the drift time of the charge clusters. This assumes that in a 3 mm wide drift gap the exponential

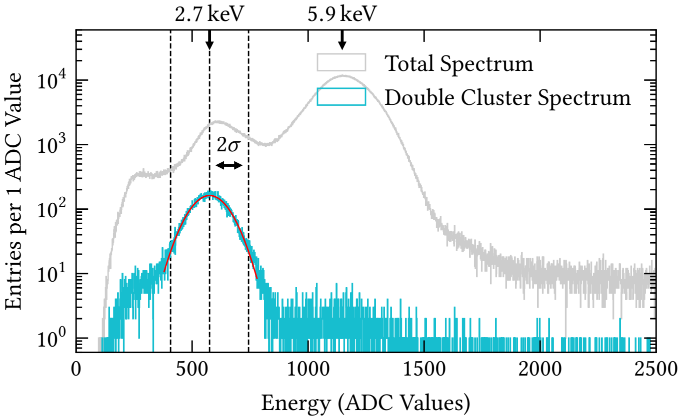

*(a)* – Energy selection.

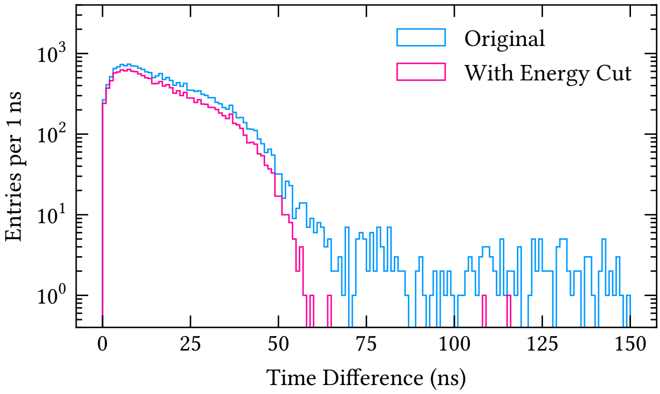

*(b)* – Effect of the energy selection on the time difference distribution.

*Figure 6.6* – Illustration of how the energy cut in the double cluster spectra is applied (a) and the effect of the cut on the time difference distribution (b).

intensity loss behaviour of the 5.9 keV X-ray photons and the emission behaviour of the argon fluorescence photons along the drift direction can be approximated as uniform behaviour. With the general trend of the resulting simulated time difference distributions (figure 6.7) behaving similar to the measurement (figure 6.2), the approximation might be considered as sufficient for the here needed purpose. This is further underlined once the time uncertainty, reflecting the time resolution, is added to the time difference distribution. For the Monte Carlo simulation, this means that the uniformly drawn time is convoluted with an uncertainty drawn from a Gaussian distribution with a standard deviation of here 5 ns.

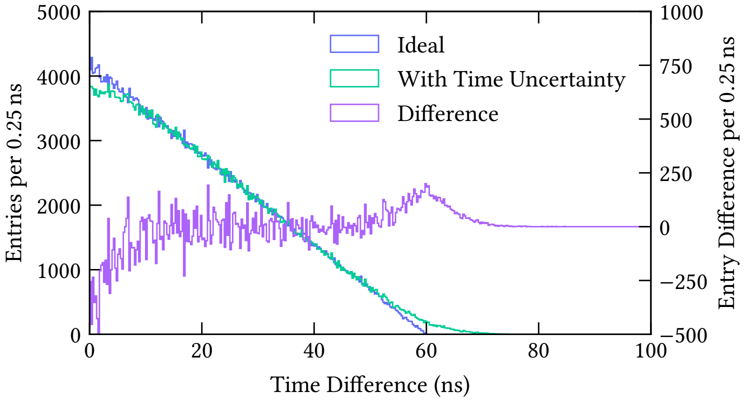

*Figure 6.7* – Time difference distribution generated with Monte Carlo methods for the ideal case without time uncertainty and the case where this uncertainty on the simulated drift time of the electron clusters is considered. In addition, the difference between these two cases is shown, where the different axis range on the right axis should be considered.

The comparison between the ideal case without time resolution effects and the case with time resolution effects considered allows to calculate the difference between the two cases. From this, the following function to describe the filtered time difference distributions could be derived:

$$f(\Delta t) = \begin{cases} -\frac{N}{2}\left[\operatorname{erf}\left(\frac{\Delta t-\mu}{\sqrt{2}\sigma}\right)+1\right] & \text{for } \Delta t \geq \mu \\ -\frac{N}{2}\left[\operatorname{erfc}\left(\frac{\Delta t-\mu}{\sqrt{2}\sigma}\right)+2\right]+m\Delta t+b & \text{for } \Delta t < \mu \end{cases} . \tag{6.1}$$

Here, $N$ is a scaling factor, $\sigma$ is the time uncertainty on the measurement, so the convolution of the electronics and detector time resolution, $\mu$ is the mean of the error functions, corresponding to $\Delta t_{\text{max}}$ and $m$ and $b$ are parameters of a linear function to describe the decrease of the distribution towards larger values of $\Delta t$. In the fit of the function to the data (figure 6.8), it is further imposed that $\mu = -b/m$. An important aspect of the fit procedure is the range of the fitted bins, i.e. the first bin used in the fit. Hence, a range of start values was scanned, from 10 ns to 40 ns, with the resulting values of $\mu$ slightly varying, but still being compatible with each other within their uncertainties (figure 6.9). Because the values of the reduced $\chi^2$/ndf to determine the goodness of the fit were all similar and all close to one, it was decided to calculate the error weighted average from the fit range scan results to determine the final value of the cut-off-value $\mu$.

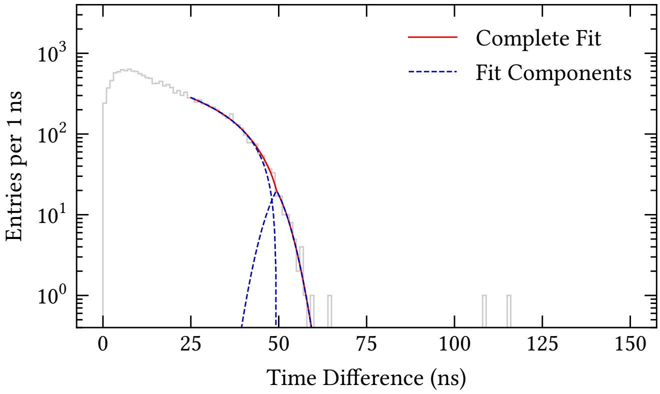

*Figure 6.8* – Example of a time difference distribution (here for an electric drift field of 2500 V/cm, starting the fit at 25 ns) fitted with the function derived from the Monte Carlo methods. On the one hand, the complete fit is shown and on the other hand the individual components, meaning the two error functions and the linear part.

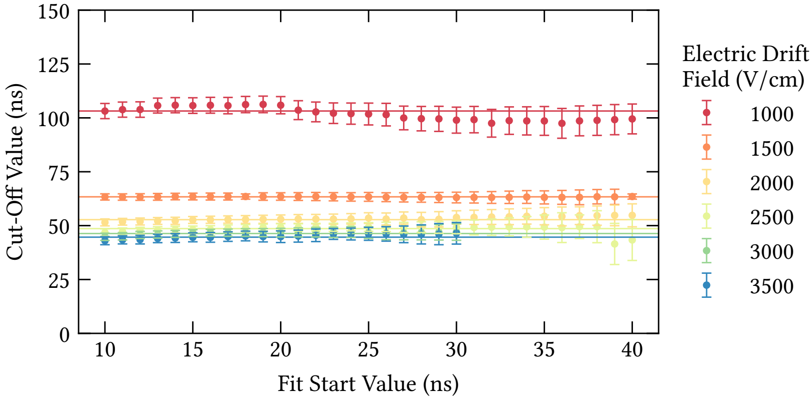

*Figure 6.9* – Illustration of the different cut-off values obtained for different start values of the fit. The results are shown for the six different drift fields, with the horizontal lines indicating the average cut-off value. In the case of the two highest drift fields, the fit of equation (6.1) to the data was already stopped at 30 ns, as there were otherwise not enough data points available for a stable fit.

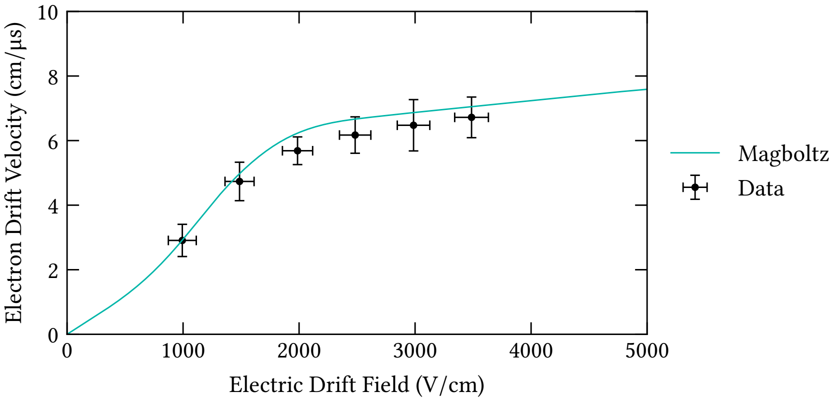

*Figure 6.10* – Comparison of the measured drift velocity and the expectation from Magboltz, depending on the electric drift field. The error bars on the data point contain the statistical error from the weighting, as well as the time uncertainty, so $\sigma$ from equation (6.1).

Having extracted the cut-off values via this method, the obtained value corresponds to the maximum possible time difference $\Delta t_{\text{max}}$ between the two clusters or 3 mm drift distance. So calculating $w_{\text{meas}} = 3\,\text{mm}/\mu$ gives then the measured drift velocity (figure 6.10). A reasonably good agreement between the measured drift velocity and the expectation from the Magboltz calculations can be seen. Even though the overlay is not perfect, within the uncertainties, the values are compatible with each other. Possible ways to achieve a better agreement, are to gain a better understanding of the drift gap's geometry (width and uniformity) as well as a more sophisticated method to determine the cut-off-value of the time difference distribution.

In addition to the drift velocity of electrons in $Ar/CO_2$ (70/30 %) at NTP, also the absorption length for the 3.0 keV argon fluorescence photons is determined. This requires determining the three-dimensional distance between the two charge clouds in the double cluster events. The distance in the $x$-$y$-plane can be directly reconstructed, due to the segmented read-out, while the $z$-distance is calculated from the time difference between the two reconstructed clusters.

For the measurement process, the X-ray tube was moved off the centre of the detector, as the absorption length $\lambda = 1/(\mu\rho)$ in $Ar/CO_2$ (70/30 %) at NTP is 3.35 cm, with $\mu = 174\,\text{cm}^2/\text{g}$ at 3.0 keV [34] and $\rho = 1.716\,\text{g/l}$ [25]. The resulting asymmetry is mitigated by considering only events in the analysis that are contained within a quarter of a circle with 60 mm radius around the centre of the X-ray beam spot. In the analysis itself an energy cut was applied, similar to the drift velocity measurements, meaning that only events with 4.8 keV photoelectrons in the beam spot and 2.7 keV photoelectrons outside of the beam spot area are used. In addition, only events

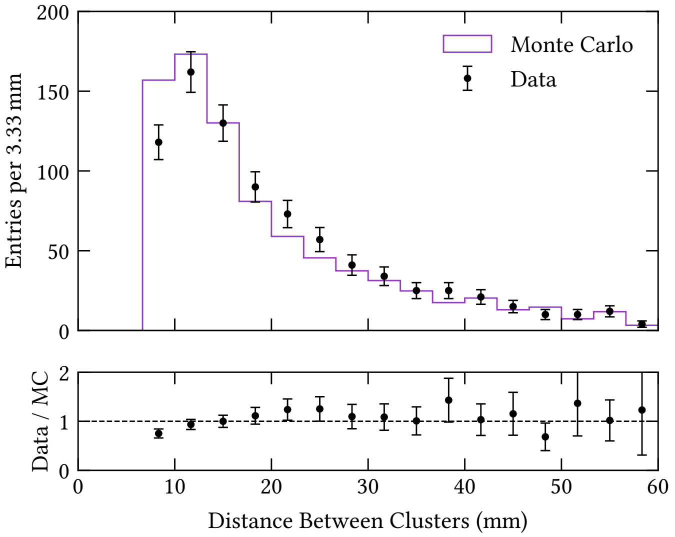

*Figure 6.11* – Distribution of the distances between the reconstructed interaction points of the initial X-ray photon and the argon fluorescence photon. The measured distribution is in addition compared with ***M**onte **C**arlo* (MC) data.

with a distance of more than 8 mm between the reconstructed interaction positions in the $x$-$y$-plane are taken into account for the analysis. This is due to the size of the clusters, which on average is around 6 strips or 2.4 mm. This means that, if the interactions happen too close to each other, the resulting clusters will overlap and are identified as a single cluster.

From the resulting distribution of distances between the clusters (figure 6.11), it can be seen that the number of entries decreases with increasing distance between the clusters, which corresponds to the expected intensity loss (section 1.2). However, the observed decrease of the entry numbers per bin is more rapid than what would be expected from $\lambda = 3.35\,\text{cm}$. This is due to a geometrical constraint, where the covered solid angle for the interaction of the fluorescence photons gets smaller for larger interaction distances in the cuboidal shaper drift region. Hence the data are compared with a Monte Carlo simulation. The simulated photon emission point from the X-ray beam spot is generated in the $x$-$y$-plane from a Gaussian distribution with an FWHM of 5 mm in order to match the observation (figure 6.5). The $z$-coordinate of the photon emission is sampled from a uniform distribution between 0 and 3 mm. The emission angle in the $x$-$y$-plane is again sampled from a uniform distribution, as well as the $z$-coordinate of the interaction. The interaction depth is sampled from an exponential distribution with $\lambda = 3.35\,\text{cm}$ as a parameter. Applying the same geometrical restrictions that apply in the drift gap, the resulting distribution of distances between the emission and the interaction point agrees well with the measurement (figure 6.11). This demonstrates that VMM3a/SRS can be used to determine fundamental physics properties in the experimental set-up as the electron drift velocity or the absorption length of photons.

## 6.2 Quality Assurance Measurements on MPGDs

During the development and production of new detectors for particle physics experiments, it is crucial to understand the detector performance and quality of the new detectors. This requires specific ***Quality Assurance*** (QA) procedures, which contain among other things also measurements of the gain uniformity with X-rays and cosmic rays [90]. One aspect during the uniformity measurements might be that the final electronics, which is supposed to be used in the experiment, is not yet available during the testing and QA phase of the first detectors. With APV25/SRS it was demonstrated that the system could be used for QA studies in the described situation [90]. Hence it was also investigated if VMM3a/SRS is suitable for these measurements.

The important aspect in this investigation is however not to understand if the VMM3a front-end of the SRS can be used for e.g. X-ray studies; this was already demonstrated (chapter 5). The goal is to demonstrate that VMM3a/SRS allows to perform complementary QA measurements to get a more precise understanding on the detector behaviour, specifically the behaviour of GEM detectors. The uniformity of a particle detector is typically described via a so-called *gain map*, where the position-dependent amplitude variations are shown (figure 6.14). In GEM detectors it was observed that the total effective detector gain depends almost linearly on the uniformity of the induction gap [68]. So to better understand the cause of potential non-uniformities in the gain map, the following method was proposed to disentangle effects that originate from the induction gap and other parts of the detector [91].

Due to the capacitive coupling between the bottom side of the third GEM and the read-out anode, it is possible to send voltage pulses with an external pulse generator to the bottom side of the third GEM and to read-out the induced signals on the read out strips with the same multi-channel electronics with analogue capabilities[4] that is used for the uniformity gain map. As the capacitance depends on the distance $d$ between two parallel-plate electrodes via $C_{\text{ind}} \propto 1/d$, the changes in the capacitance due to non-uniformities will result in changes in the induced signal $Q_{\text{ind}} = C_{\text{ind}}U$. The advantages that VMM3a/SRS could provide to this measurement are its capability to handle various detector capacitances and its self-triggered read-out, meaning that the experimental set-up becomes relatively simple.

---

[4] To be position-sensitive and get access to the charge and hence gain information.

To demonstrate the sensitivity of VMM3a/SRS to such variations, two large-area triple-GEM modules with an active area of about $1.0\,\mathrm{m}\times 0.5\,\mathrm{m}$ were used. The general structure of the two modules is the same. Each module contains a triple-GEM stack with a 3 mm wide drift gap, a first 1 mm wide transfer gap, a second 2 mm wide transfer gap, and a 1 mm wide induction gap. The read-out anode is segmented into $8 \times 3$ groups of 128 strips (1D read-out), meaning that each group was read out by one RD51 VMM hybrid. The strip segmentation takes place along the three columns.

The results show a position dependence of the recorded amplitude (figure 6.12a). This particular module was known for having an intrinsic outwards bending. It can be seen that the signal amplitude increases towards the outer strips, meaning that the capacitance in the centre of the module is smaller, as it would happen when the induction gap gets larger. In addition, it can be seen that the signal amplitude varies between different rows $\eta_i$. This can be explained with different strip areas depending on the row, leading to a change in the capacitance, as $C_{\text{ind}} \propto A$ in the case of a parallel-plate capacitor. To prove this statement, the recorded amplitude was normalised by the strip area, with the largest strip as a reference, which should correct for the observed behaviour (figure 6.12b). From the result it can be seen that the bending is the strongest in the centre of the module. The measurement type was repeated with another module, that was known to suffer less from intrinsic bending. Instead, a lead brick with a mass of around 5 kg was placed in the centre of the module (between $\eta_4$ and $\eta_5$), to actively bend the structure and study the relative signal variation $\Delta Q_s = (Q_{\text{no},s} - Q_{\text{weight},s})/Q_{\text{weight},s}$ between the case with weight $Q_{\text{weight},s}$ and the one without weight $Q_{\text{no},s}$ for each read-out strip $s$ (figure 6.13). With the weight placed on the read-out board, the board gets bent inwards, leading to a larger capacitance and thus a larger signal amplitude and hence also a larger signal variation. As the weight is placed in the centre, there the bending is the strongest.

The measurements show that using a pulser to understand the induction gap uniformity works. As the intention is to disentangle different sources of non-uniformities, now an example is shown, where both QA methods have been applied, the pulser method and the X-ray imaging for the gain map. The measurements have been performed on a novel neutron detector for the NMX experiment at the European Spallation Source with a low material budget read-out [15, 16]. The detector is constructed such that its components are not mounted on a solid bottom plane that contains also the read-out strips, but the other way around. This means that the detector is built up from a solid top/cathode plane, with the read-out anode being a thin foil stretched over the active area. Different to the measurements with the previous large area modules, the NMX detectors are COMPASS-like triple-GEM detectors with $x$-$y$-strip read-out but 10 mm drift gap. The results with the X-ray measurements, here only shown for one of the detector quadrants, indicate a strong non-uniformity (figure 6.14). When the observed variations are projected along one

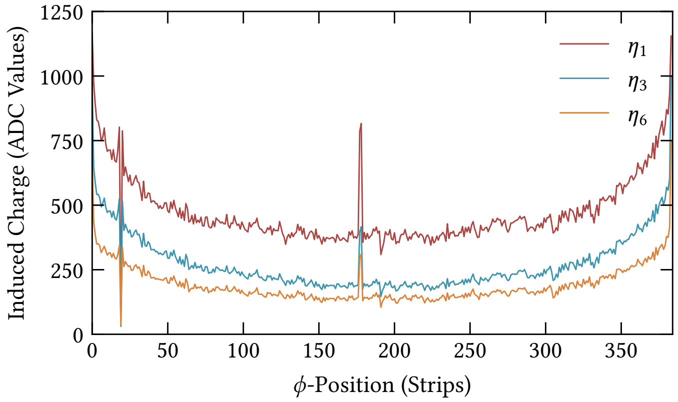

*(a)* – Without area normalisation.

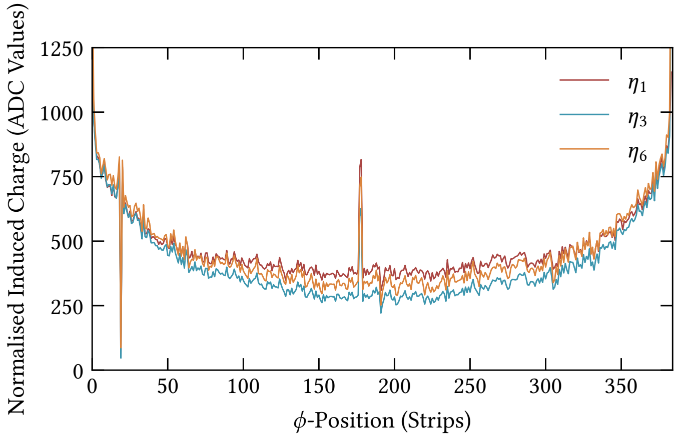

*(b)* – Normalisation by strip area applied.

*Figure 6.12* – Illustration of the position dependence of the induced signal charge $Q_{\text{ind}}$ for an intrinsically bent GEM module with a non-uniform induction gap, using the pulsing technique. In one case (a), the results are shown without correcting for the different-sized read-out strips, while in the other case (b), the measured signal charge is normalised by the strip area.

axis, the results of the X-ray measurements can be directly compared with the pulser method (figure 6.15). A good correlation between the two different measurements can be observed, confirming that VMM3a/SRS is well suited for QA studies and uniformity measurements of the induction gap in GEM detectors. The reason for the observed non-uniformity was found after the detector was opened. There, a wave structure in the read-out foil introduced through the stretching procedure can be observed (figure 6.16). To avoid this behaviour in future detectors, the design of the

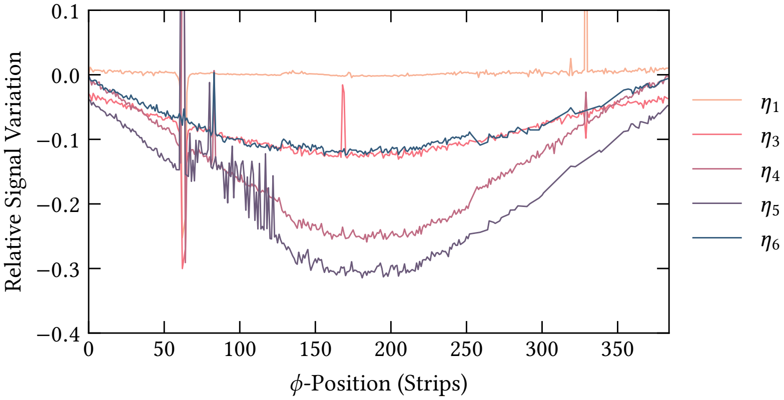

*Figure 6.13* – Relative variation of the signal amplitude between the case with additional weight and the one without weight. The fluctuations in the signal variation at $\eta_5$ for a $\phi$-strip position of around 100, are likely to be caused by problems with the specific connector on the read-out board of the detector module at this position.

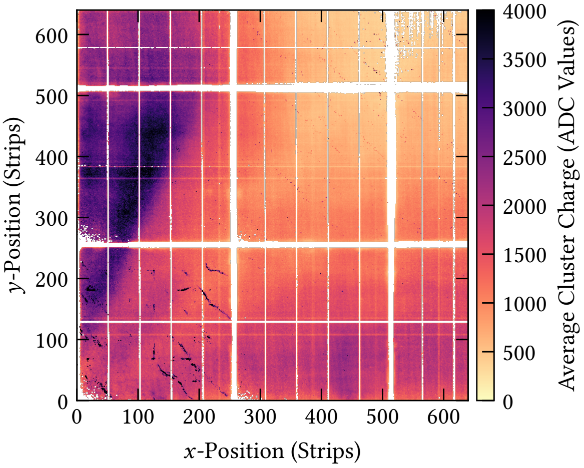

*Figure 6.14* – X-ray image of one of the detector's quadrants, with the colour corresponding to the average cluster charge. The thick white stripes originate from spacers between the GEM foils in the detector. The thin vertical lines originate from the sectorisation of the GEM foils. Data kindly provided by Jerome Samarati [92].

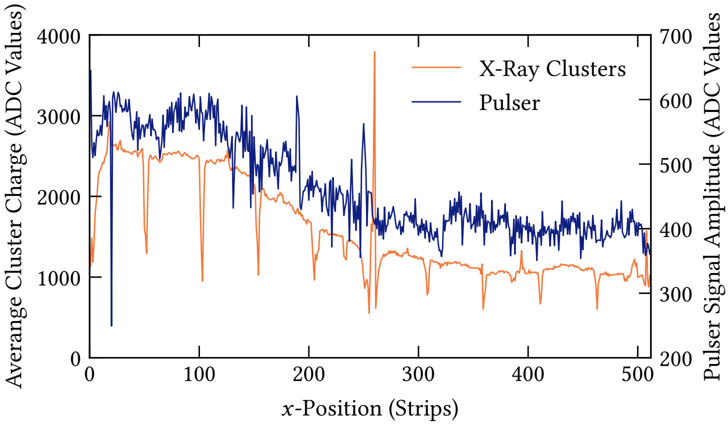

*Figure 6.15* – Overlay of the average cluster charge from the X-ray events along each read-out strip and the measured signal amplitude from the pulser method. Data kindly provided by Jerome Samarati [92].

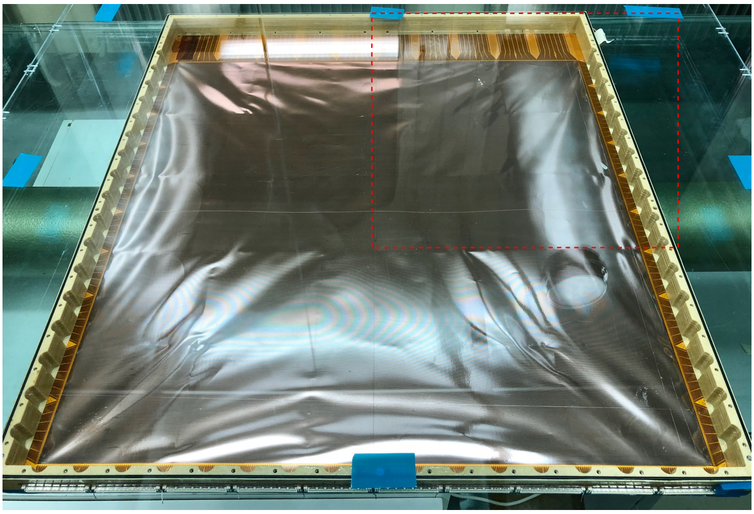

*Figure 6.16* – Photograph of the read-out foil, with the dashed-line square highlighting the quadrant whose X-ray image is shown (figure 6.14). The wave structure in the read-out foil, leading to variations in the induction gap size can be clearly observed. Photograph kindly provided by Jerome Samarati [92].

NMX prototype was optimised, such that the read-out foil is glued on a glass plate. With this, a high uniformity of the induction gap can be preserved.

These measurements indicate however one issue with the pulsing technique. The non-uniformities are integrated along the strips which does not allow a precise 2D position sensitive identification of irregularities as with the X-rays, making an exact and quantitative description of the non-uniformities difficult Nonetheless, it indicates if a potential problem occurs in the induction gap or another part of the GEM detector. The pulsing method remains further useful, as it is well suited for quality measurements during the detector production because it works without gas flow and does not even require a fully assembled detector.

## 6.3 Beam Position Detector of NA61/SHINE

The last part of this chapter focuses on the use of the RD51 VMM3a/SRS beam telescope in the NA61/SHINE experiment[5] [13, 14], located at the H2 beam line of the CERN SPS. The experiment is designed to study different kinds of hadron and nucleus interactions, with one of its main objectives being the study of the onset of deconfinement [13]. Also activities on neutrino physics are pursued, particularly studies with the target of the T2K experiment[6] [93]. The goal is to reproduce the beam conditions of the T2K experiment, using a 31 GeV/$c$ proton beam, and to study the production of hadrons in the proton-nucleus interactions in the target in order to better estimate the initial neutrino flux [94]. This requires a precise measurement of the particle tracks before and after the interactions of the proton beam with the target. The track measurement after the interaction is performed with the NA61/SHINE ***T**ime **P**rojection **C**hambers* (TPCs). To be able to calculate the scattering angle of the particles, the initial position of the proton beam before the interaction in the target needs to be known. For this, so-called ***B**eam **P**osition **D**etectors* (BPDs) are used. Originally operated with wire chambers [14], the BPDs are supposed to be upgraded, using scintillating fibres and silicon strip detectors [95]. In the meantime, until the upgrade is finalised, the RD51 VMM3a/SRS beam telescope with its COMPASS-like triple-GEM detectors (section 4.3) was used as an interim solution for the beam position detectors as so-called *GEM-BPDs* (figure 6.17).

To be operated as GEM-BPDs, a few adjustments had to be made to the RD51 VMM3a/SRS beam telescope. First, to have as little material budget as possible in the beam line, the scintillators and all DUTs were removed, with only the three tracking

---

[5] SHINE is the abbreviation for ***SPS H**eavy **I**on and **N**eutrino **E**xperiment* [14].

[6] The T2K experiment studies neutrino oscillations and aims on determining the mixing angles and precise measurements on the oscillation parameters [93]. To produce the corresponding neutrino beam, a proton beam is sent onto a 90 cm long carbon rod with 2.6 cm diameter and a density of 1.83 g/cm$^3$ [14].

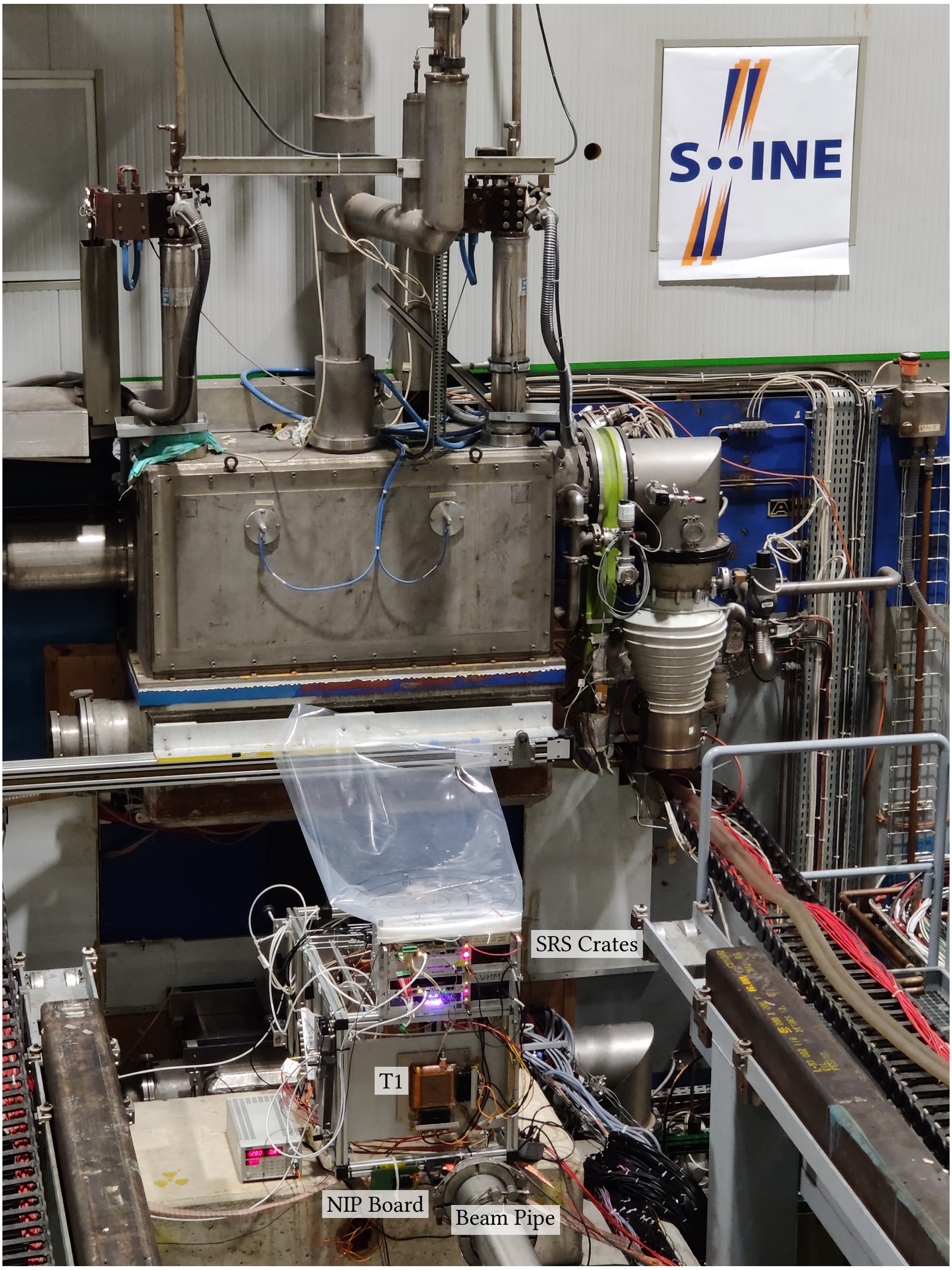

*Figure 6.17* – Photograph of the RD51 VMM3a/SRS beam telescope as GEM-BPDs at the NA61/SHINE experiment.

detectors remaining. Secondly, to slightly increase the angular resolution, the first tracking detector was moved 20 cm forwards, such that the distance between T1 and T3 is almost 1 m. As third and most important point, only one quadrant of each detector with an area of $5 \times 5\,\text{cm}^2$ was read out. This was possible because of the transversal profile of the proton beam, a circular shape with around 2 cm diameter, and hence allowed to use a single FEC/DVMM combination to read the signals from all GEM-BPDs. The motivation for a single FEC operation was to potentially increase the operation stability. Nonetheless, a second FEC/DVMM combination was used to power and configure the six remaining hybrids on the tracking detectors, as the read-out strips require a similar signal termination. In terms of operation settings, the tracking detectors were operated similar to the RD51 test beam, i.e. a gain of 30 000. The threshold level was slightly increased to 25 mV, including the channel-by-channel equalisation. The other electronics settings remained the same.

### *6.3.1 Integration of the GEM-BPDs into NA61/SHINE*

To integrate the RD51 VMM3a/SRS beam telescope into the NA61 experiment and turn it into the GEM-BPDs, various steps were necessary. The most crucial aspect for a successful integration was to combine two different read-out paradigms in order to match the recorded particle interactions from the beam telescope with the ones recorded by the other detectors of NA61. While the VMM3a/SRS beam telescope operates in a self-triggered continuous read-out mode, NA61 operates as a triggered experiment with trigger rates of up to 1 kHz [96]. With particle rates in the used proton beam of up to $5 \times 10^4$ particles per spill or 10 kHz and VMM3a/SRS recording almost all of their interactions in the GEM detectors, this requires a precise matching between the protons setting off the NA61 trigger signal and the protons recorded by the GEM-BPDs.

As the NA61 trigger-logic generates for each trigger event a 32-bit long event identifier [7] it became evident that the best solution to match the recorded interactions would be that the event-IDs from NA61 are acquired with VMM3a/SRS acquires, such that they are contained in its data stream. This allows the matching of the GEM-BPD clusters with the NA61 events in the offline data analysis. To inject the event-ID into the VMM3a/SRS data stream, it was decided that the event-ID bits would be decoded on the VMM3a input channels, with one channel corresponding to one bit. For this, the 32-bit event-IDs were split up onto 32 individual transmission lines, with the LVDS signals from the trigger-logic being converted into NIM signals, which was implemented by Piotr Podlaski. The NIM signals were then sent to the ***NI**M **P**attern Injector* (NIP) board for the VMM3a front-end of the SRS (figure 6.18), which was designed by Hans Muller. The NIP board contains 36 inputs for push-pull

---

[7] In the following also called *event-ID*.

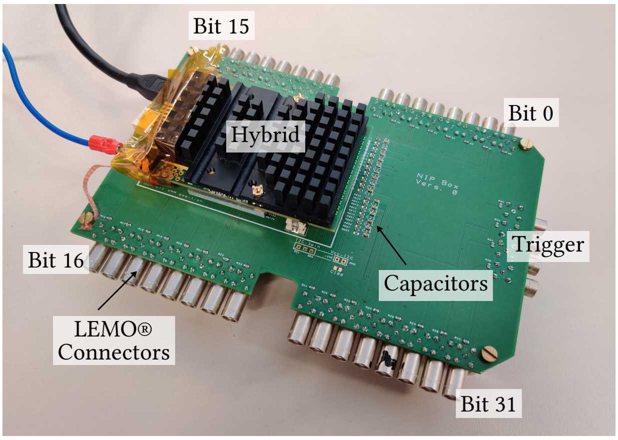

*Figure 6.18* – Photograph of the NIP board used to distribute the split event identifier bits to the individual VMM3a input channels.

connectors[8], of which 32 inputs are reserved for the event-ID and four for the trigger signal itself. With each of the push-pull connectors being connected to a VMM3a input channel via a 50 Ω termination resistor and a 0.5 pF capacitor, a bit set to one leads to a 400 fC charge pulse. As the pulses for the active bits arrive at almost the same time and knowing the channel-to-bit mapping, the combination of channels that recorded a charge pulse with the ones that did not record a charge pulse, allows decoding the NA61 event-IDs in the offline data analysis (figure 6.19).

However, instead of sending all 32-bits to the NIP board, only the first 24-bit were sent, with the eight least significant bits being doubled, meaning that these bits are sent to two of the push-pull connector inputs. This is done for redundancy purposes, as it was observed that when injecting NIM pulses to the VMM3a input channels some of the corresponding hits (less than 1 ‰) are lost in the read-out chain. So far it was not identified at which part of the chain, so if the hit is already lost at the pulse injection or at some point in the later data processing. This is also the reason why the trigger input was quadrupled. However, with doubling the last eight bits, more than 99.99 % of the event-IDs could be immediately and correctly[9] decoded.

Other parts of the integration of the GEM-BPDs into NA61 included the data acquisition and the stopping of a run. Neither the control software of VMM3a/SRS nor the online monitoring was integrated into the NA61 DAQ system. Instead, the

---

[8] Commonly known as *LEMO® connectors.*

[9] Correctly means here that the event-IDs are consecutive. So once an event-ID is smaller than the previous one, it is considered as not correctly reconstructed. Despite that, in the offline analysis, because the event-IDs before and afterwards are known, it is possible to recover the IDs with a missing active bit.

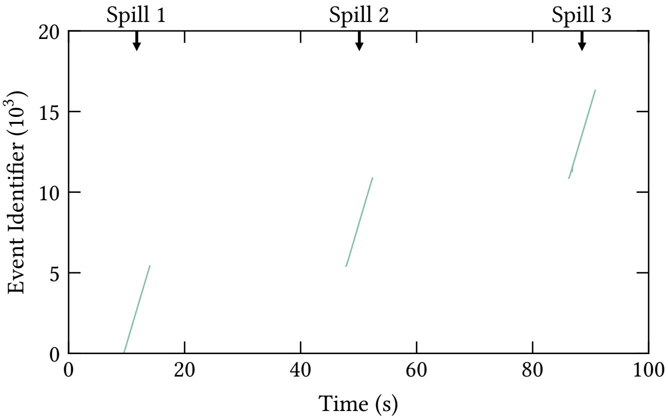

*Figure 6.19* – Example of the event-ID decoding, where the event identifier is plotted against the acquisition time. In this particular run, three spills have been recorded, with the event counter not increasing in between the spills. Data kindly provided by Brant Rumberger [97].

GEM-BPDs were operated separately, similar to the RD51 test beams. However, the data acquisition with tcpdump was connected to the DAQ start of NA61, meaning that once a data acquisition run was started for NA61, also the data from VMM3a/SRS would be saved to the hard drive. This was implemented by Brant Rumberger, who also wrote a quality assurance analysis which reads in the `.root` files from vmm-sdat to investigate the data quality, understand if the event-ID matching works and hence understand in an almost online[10] matter the data quality. This allows also to stop the data acquisition fast enough in case of problems. In case of immediate problems with the GEM-BPDs, i.e. high voltage instabilities at the detectors, a stop signal was generated with the high voltage power supply which could then be registered by the NA61 DAQ system, leading to an automatic stop of the data acquisition run. Here it should be noted that the detectors operated quite stable and the only occasions where the data acquisition was stopped due to issues with the high voltage stability, was due to a faulty high voltage filter. In general, it can be concluded that in terms of operation stability the GEM-BPDs operated for almost five weeks at NA61/SHINE without interruption or detector and VMM3a/SRS-related faults.

### *6.3.2 Tracking Performance and Event Matching*

With the stable operation of the GEM-BPDs confirmed and being able to decode the event-IDs contained in the VMM3a/SRS data stream, the next steps are to ensure that

---

[10] Considering the the reconstruction and analysis time the delay between data taking and receiving the results for the quality assurance check is around 1 minute.

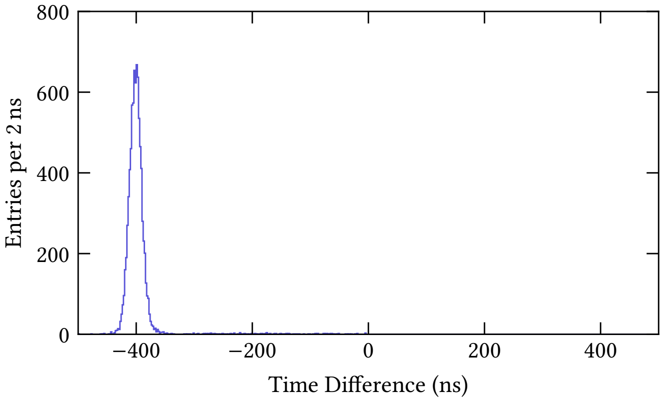

*Figure 6.20* – Distribution of the time difference between the recorded interaction time of the particle and the timestamp of the decoded event-ID. Data kindly provided by Brant Rumberger [97].

the interactions in the GEM detectors can be assigned to the event-IDs, to determine the tracking performance of the GEM-BPDs and to include the reconstructed particle tracks from the GEM-BPDs in the NA61 events.

At first, the matching between the recorded proton interactions from the GEM detectors and the event-IDs is shown. For this, an interaction is considered as matched, if the time difference between the interaction time of a particle in the GEM detectors and the arrival time of the event-ID at the NIP board is not larger than ±500 ns (figure 6.20). The observed offset in the time difference is due to the fact that the initial trigger signal in NA61 is sent with a delay of at least 200 ns to include also the information from other detectors in the final trigger signal. Combining this with the delays of the various signal transmission lines, an offset of around 400 ns between the interaction taking place and the trigger and hence event-ID signal being distributed is expected [98].

Managing to match the recorded interactions in the GEM-BPDs with the event identifiers, allows also to illustrate parts of the detectors involved in generating the trigger signal (figure 6.21). In one case (figure 6.21a) all the interactions recorded with the first tracking detector of the GEM-BPDs are shown, using only the self-triggered read-out of VMM3a/SRS. These clusters are then matched with the event-ID and trigger signal (figure 6.21b). In this image, the circular shape of one of the scintillators, which in this case was directly mounted in front of the target, can be seen. In addition to this, also the efficiency of the tracking detectors was studied. The efficiency is here defined as the ratio between the total number of event-IDs and the number of

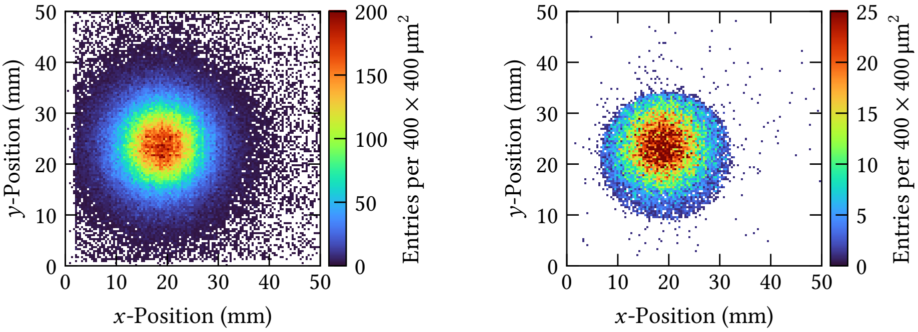

*(a)* – Only self-triggered. *(b)* – Matched with event-ID.

*Figure 6.21* – Illustration of the transversal structure of the proton beam, here only shown for the reconstructed interactions in the first tracking detector T1. In one case all the reconstructed clusters are shown (a) and in the other case only the clusters that could be matched with an event-ID (b). Note the different number of entries (b) due to the lower NA61 trigger and hence event-ID rate. Data kindly provided by Brant Rumberger [97].

interactions that can be matched with an event-ID:

$$\varepsilon = \frac{N_{\text{matched}}}{N_{\text{event-IDs}}} \, . \tag{6.2}$$

For the use of the GEM-BPDs no specific efficiency scan was performed, as operation conditions to achieve efficiencies as high as possible have been established before (section 4.3.2). Thus, the tracking detectors were operated at detector gains of 20 000 to 30 000 at a THL of around 25 mV or 2.5 fC or $15.6 \times 10^3$ electrons above the baseline. This allowed to achieve tracking detector efficiencies larger than 95 % throughout the entire data-taking period. Most of the time, the detectors could be operated with $\varepsilon_{\text{T1}} \approx 98\,\%$, $\varepsilon_{\text{T2}} \approx 97\,\%$ and $\varepsilon_{\text{T3}} \approx 97\,\%$, where the fluctuations are around 1 %.

The next step in studying the tracking performance is the determination of the track resolution. This is done with the same method as for the RD51 VMM3a/SRS beam telescope (section 5.2.6). The resulting track resolution (figure 6.22) is, as expected, similar in terms of values and behaviour as what has been observed before from the test beam results (figure 5.41). It should be noted that the reconstructed particle tracks are built up only by clusters which could be matched to an event-ID.

The last step in terms of matching event-IDs and reconstructed particle tracks is related to the detector alignment. The alignment of the GEM detectors with respect to each other is performed with anamicom, providing the position of the particle tracks inside the GEM-BPDs. However, to have the full information available for the

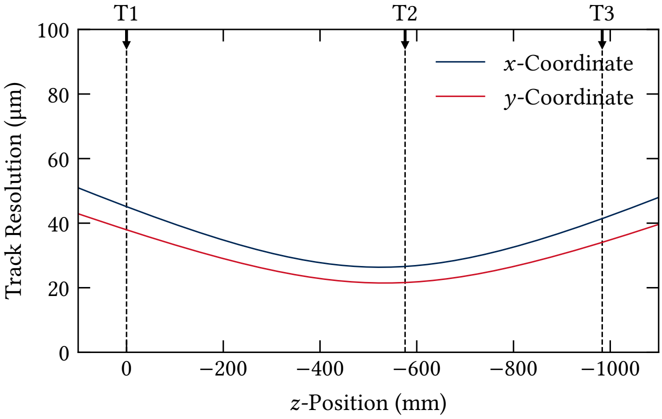

*Figure 6.22* – Track resolution of the GEM-BPDs, calculated via equation (5.17), presented in the GEM-BPD coordinate system. The method for the position determination is $Q^2$ weighting with enabled neighbouring-logic. For the determination, only tracks that could be matched with an event-ID were used, for which anamicom was modified by Jona Bortfeldt.

vertex reconstruction inside the target, the positions of the protons inside the experiment coordinate system need to be known. This means to use reference detectors, whose position in the experiment coordinates is well known and to match tracks that are reconstructed using the reference detectors with the ones reconstructed from the GEM-BPDs. From the geometrical offset between the two tracks, the absolute alignment of the GEM-BPDs can be performed. In the present case, to perform the alignment, the target was removed from the experiment and two ***Delay Wire Chambers*** (DWCs) of the H2 beam line, located before and after the NA61/SHINE experiment, were used as reference detectors. It can be seen that the tracks reconstructed with the GEM-BPDs and the ones with the DWCs, both matched via the event identifier can be well aligned with each other (figure 6.23). Also in terms of correlation, it can be seen that the reconstructed penetration point of the proton beam in the GEM-BPDs can be well correlated with the ones determined from the DWCs (figure 6.24). This confirms the stable and successful operation of the RD51 VMM3a/SRS beam telescope as NA61 GEM-BPDs. The position of the proton beam sent on the carbon target could be reconstructed with $> 90\,\%$ efficiency, it could be matched with the NA61 event counter and from this, the positions could be aligned with the experiment coordinate system. This means that the acquired data can be used in the analysis of the neutrino physics data for the NA61/SHINE and the T2K experiments.

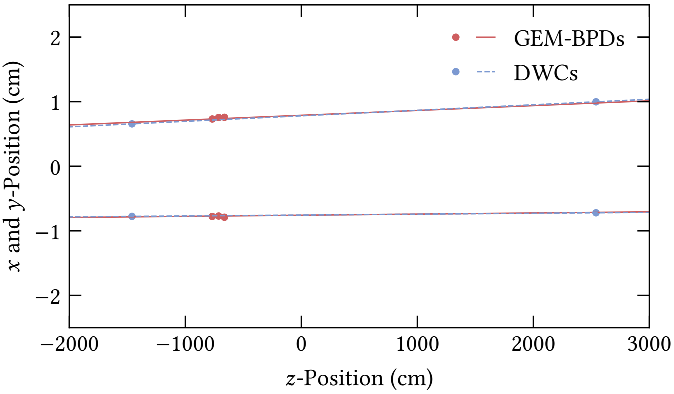

*Figure 6.23* – Examples of the particle tracks (for one track the $x$-position is shown and for the other one the $y$-position), individually reconstructed with the GEM-BPDs and the DWCs and then overlaid, in order to illustrate the matching of the GEM-BPD data with the data recorded in other parts of NA61, presented in the NA61 coordinate system. Data kindly provided by Brant Rumberger [97].

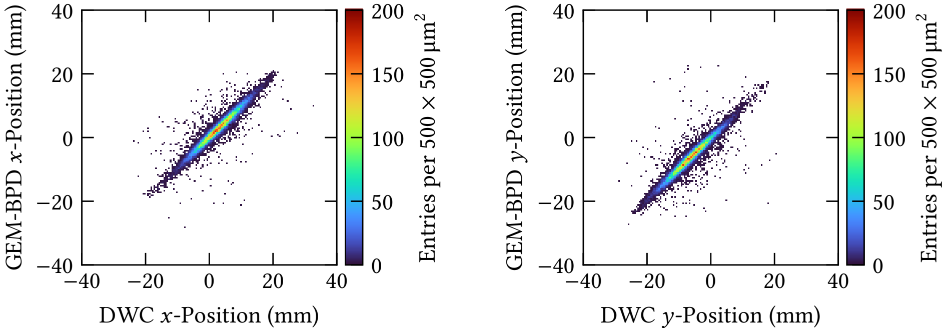

*(a)* – $x$-coordinate.

*(b)* – $y$-coordinate.

*Figure 6.24* – Correlation plots between the calculated penetrations points of the beam particles in the first tracking detector of the GEM-BPDs, comparing the position reconstructed with the data from the GEM-BPDs and the DWCs for both coordinates. Data kindly provided by Brant Rumberger [97].

# CONCLUSION AND OUTLOOK

The needs from new particle physics experiments require the use of modern detector technologies. As such, Micro-Pattern Gaseous Detectors are more and more used to provide a good spatial resolution (better than 100 µm), a good time resolution (better than 10 ns) and a high rate-capability (several MHz/cm$^2$) over a large area (up to hundreds of square metres). In order to cope with these requirements and process the signals from the detectors, new front-end electronics is needed. In case of the New Small Wheel upgrade of the ATLAS experiment, this lead to the development of the multi-channel ATLAS/BNL VMM3a front-end ASIC, which provides a MHz rate-capability, nanosecond time resolution and access to the charge and hence energy information of the interacting particle. At the same time it can operate with detectors of different size, handling detector capacitances between a few pF up to 1 nF. In order to use its feature set also in small-scale R&D detectors as well as medium-size experiments, the VMM3a was integrated into the RD51 Scalable Readout System.

In this thesis, the capabilities of the integrated VMM3a front-end and Scalable Readout System for the charge read-out of Micro-Pattern Gaseous Detectors were explored. Not only to characterise the performance of VMM3a/SRS, but also to help in improving its operation stability and turning it into a full-scale read-out system, in terms of hardware, firmware and software. These activities were carried out in a larger collaborative effort to further develop and improve the read-out system, the *Working Group 5.1* of the RD51 collaboration. Over the course of this thesis, it was possible to turn VMM3a/SRS from a small system with unstable operation into a large-scale, multi-purpose read-out system, which was ultimately operated for five weeks without interruption as part of the NA61/SHINE experiment at CERN.

At first, the electronic behaviour of the system was characterised. This includes the evaluation, testing and improvement of the calibration and correction procedures, but also studies on the rate-capability, electronics noise (less than 1000 electrons at a detector capacitance of 22 pF, i.e. when connected to a $10 \times 10\,\mathrm{cm}^2$ COMPASS-like triple-GEM detector) or the optimisation of the threshold level. Further, the time resolution and timing behaviour of VMM3a/SRS was characterised. With electronics time resolutions between 0.5 ns and 2 ns, depending on the front-end's settings, VMM3a/SRS is well suited to be used as an integrated read-out system for most R&D purposes, as well as particle physics experiments.

It was demonstrated that VMM3a/SRS allows characterising the performance of particle detectors, profiting highly from the VMM3a's high-rate, self-triggered continuous read-out used in the SRS implementation. It was shown, how VMM3a/SRS enables high-rate X-ray imaging with gaseous detectors, meaning radiography, but also fluoroscopy, where imaging of moving objects is performed. In an example measurement, $280 \times 10^6$ X-ray interactions were recorded in 180 s, giving access to the position of each interacting particle, its energy and its time of interaction. This allowed performing studies on energy-resolved imaging. The read-out system was also used for the RD51 VMM3a/SRS beam telescope, which was built throughout of this thesis, where in addition to COMPASS-like triple-GEM detectors, also other detector technologies were read out, i.e. MicroMegas and scintillators/PMTs via a NIM-logic output. As part of the studies with minimum ionising particles, VMM3a/SRS was used to provide a live response monitoring of the beam quality. A large fraction of the characterisation measurements, both with X-rays and MIPs, was spent on spatial resolution studies and how to improve the position reconstruction. Two different approaches were investigated. On the one hand a modification of the centre-of-gravity method, where the square of the charge is used as a weight, and on the other hand a hardware feature of the VMM3a, its neighbouring-logic. For both cases, but especially for the $Q^2$ weighting, it was found that the spatial resolution and hence the position reconstruction gets improved for COMPASS-like triple-GEM detectors. Spatial resolutions below 50 µm, using MIPs, could be achieved. In addition, the time resolution of the COMPASS-like triple-GEM detectors was precisely determined, profiting from the electronics' time resolution. Resolutions between 8 ns and 14 ns could be measured, depending on the total effective gain of the detector.

Also, different applications of VMM3a/SRS outside of the study of the typical detector resolution parameters have been investigated. It was shown how its continuous self-triggered read-out, allows to resolve argon fluorescence interactions, which can be used to determine the electron drift velocity inside the detector. The possible use case of VMM3a/SRS for quality assurance measurements was illustrated. Furthermore, the RD51 VMM3a/SRS beam telescope was successfully operated as Beam Position Detector in the NA61/SHINE experiment, where it was also shown that the data from VMM3a/SRS can be merged with the data from other read-out systems and experiments.

This successfully demonstrated that VMM3a/SRS works as an integrated read-out system for MPGDs and is able to cope with the requirements set by the experiments. As such, the integration of the VMM3a into the SRS, puts the SRS into its next era.

Nonetheless, there are still aspects left for the future, with potential improvements of the current system in terms of software, firmware and hardware to gain even more productivity and stability. An example for this is the planned replacement of the Spartan-6 FPGA on the Hybrid by a Spartan-7 FPGA in future production series of the RD51 VMM Hybrid. This would e.g. make the use of other read-out modes of the VMM easier. Other improvements would require more profound changes, for example, the repair of the non-working channel FIFO or the timing-at-threshold mode, which would need a new design and production iteration of the VMM ASIC. And while bandwidth limitation of the SRS FEC may be addressed by implementing a fully triggered read-out mode for the VMM3a in the SRS, the current proposal foresees the new *__e__xtended __F__ront-__E__nd __C__oncentrator* (eFEC) as part of the SRS-e with a higher bandwidth Ethernet transceiver of 2 × 10 Gbps [99].

Also from the measurement perspective, there exist several aspects, that have not been covered within this thesis, but which could profit from the capabilities of VMM3a/SRS. This includes e.g. fluorescence imaging as an evolution of the energy-resolved imaging. The read-out of negative-ion TPCs, where potentially each ion could be resolved may profit from the VMM3a's time resolution. In a similar direction points the application of a Frisch grid inside a GEM detector to improve the time resolution, which could be studied with VMM3a/SRS. An example of currently ongoing activities for future experiments is the read-out of *__Si__licon __P__hoto__m__ultipliers* (SiPMs) with VMM3a/SRS.

This concludes the exploration of next-generation electronics for the read-out of micro-pattern gaseous detectors, with the VMM3a front-end of the RD51 Scalable Readout System, being successfully tested, characterised and optimised for the use in R&D applications and future particle physics experiments.

# BIBLIOGRAPHY

[1] G. Aad et al. (The ATLAS Collaboration): *The ATLAS Experiment at the CERN Large Hadron Collider*, Journal of Instrumentation **3** (2008) S08003. doi: `https://doi.org/10.1088/1748-0221/3/08/S08003`.

[2] T. Kawamoto et al. (The ATLAS Collaboration): *New Small Wheel Technical Design Report*, CERN-LHCC-2013-006, ATLAS-TDR-020 (2013). url: `https://cds.cern.ch/record/1552862` (visited on 19/04/2022).

[3] S. Chatrchyan et al. (The CMS Collaboration): *The CMS Experiment at the CERN LHC*, Journal of Instrumentation **3** (2008) S08004. doi: `https://doi.org/10.1088/1748-0221/3/08/S08004`.

[4] D. Contardo et al. (The CMS Collaboration): *The Phase-2 Upgrade of the CMS Muon Detectors*, CERN-LHCC-2017-012, CMS-TDR-016 (2017). url: `https://cds.cern.ch/record/2283189` (visited on 05/09/2022).

[5] K. Aamodt et al. (The ALICE Collaboration): *The ALICE Experiment at the CERN LHC*, Journal of Instrumentation **3** (2008) S08002. doi: `https://doi.org/10.1088/1748-0221/3/08/S08002`.

[6] H. Appelshaeuser et al. (The ALICE Collaboration): *Upgrade of the ALICE Time Projection Chamber*, CERN-LHCC-2013-020, ALICE-TDR-016 (2013). url: `https://cds.cern.ch/record/1622286/` (visited on 05/09/2022).

[7] J. Bortfeldt et al.: *PICOSEC: Charged particle timing at sub-25 picosecond precision with a Micromegas based detector*, Nuclear Instruments and Methods in Physics Research A **903** (2018) 317–325. doi: `https://doi.org/10.1016/j.nima.2018.04.033`.

[8] M. Titov, L. Ropelewski: *Micro-Pattern Gaseous Detector Technologies and RD51 Collaboration*, Modern Physics Letters A **28** (2013) 1340022. doi: `https://doi.org/10.1142/S0217732313400221`.

[9] RD51 Collaboration: *Development of Micro-Pattern Gas Detectors Technologies.* url: `https://rd51-public.web.cern.ch/` (visited on 29/08/2022).

[10] S. Martoiu et al.: *Development of the Scalable Readout System for Micro-Pattern Gas Detectors and other applications*, Journal of Instrumentation **8** (2013) C03015.
doi: `https://doi.org/10.1088/1748-0221/8/03/C03015`.

[11] G. de Geronimo et al.: *The VMM3a ASIC*, IEEE Transactions on Nuclear Science **69** (2022) 976–985.
doi: `https://doi.org/10.1109/TNS.2022.3155818`.

[12] M. Lupberger et al.: *Implementation of the VMM ASIC in the Scalable Readout System*, Nuclear Instruments and Methods in Physics Research A **903** (2018) 91–98.
doi: `https://doi.org/10.1016/j.nima.2018.06.046`.

[13] M. Gazdzicki, Z. Fodor, G. Vesztergombi: *Study of Hadron Production in Hadron-Nucleus and Nucleus-Nucleus Collisions at the CERN SPS*, CERN-SPSC-2006-034 (2006).
url: `http://cds.cern.ch/record/995681`.

[14] N. Abgrall et al. (The NA61/SHINE Collaboration): *NA61/SHINE facility at the CERN SPS: beams and detector system*, Journal of Instrumentation **9** (2014) P06005.
doi: `https://doi.org/10.1088/1748-0221/9/06/P06005`.

[15] D. Pfeiffer et al.: *First measurements with new high-resolution gadolinium-GEM neutron detectors*, Journal of Instrumentation **11** (2016) P05011.
doi: `https://doi.org/10.1088/1748-0221/11/05/P05011`.

[16] K. H. Andersen et al.: *The instrument suite of the European Spallation Source*, Nuclear Instruments and Methods in Physics Research A **957** (2020) 163402.
doi: `https://doi.org/10.1016/j.nima.2020.163402`.

[17] T. Block et al.: *Particle Physics Readout Electronics and Novel Detector Technologies for Neutron Science*, Preprint submitted to Nuclear Instruments and Methods in Physics Research A (2022),
url: `https://arxiv.org/abs/2207.06470`.

[18] S. S. Caiazza et al.: *The MAGIX focal plane time projection chamber*, Journal of Physics: Conference Series **1498** (2020) 012022.
doi: `https://doi.org/10.1088/1742-6596/1498/1/012022`.

[19] S. Meyer et al.: *Optimization and performance study of a proton CT system for pre-clinical small animal imaging*, Physics in Medicine & Biology **65** (2022) 155008.
doi: `https://doi.org/10.1088/1361-6560/ab8afc`.

[20] E. Terzimpasoglou: *Investigations on ASIC for Triple-GEM Detectors*, Master Thesis, Rheinische Friedrich-Wilhelms-Universität Bonn (2021).
url: `https://arxiv.org/abs/2206.09968` (visited on 15/08/2022).

[21] S. Vahsen: *Dynamic range in MPGD-based directional neutron and dark matter detection*, RD51 Collaboration Meeting and Topical Workshop on 'Wide Dynamic Range Operation of MPGDs' (18/11/2021).
url: `https://indico.cern.ch/event/1071632/contributions/4551142/` (visited on 29/08/2022).

[22] I. Lázaro Roche: *A Compact Muon Tracker for Dynamic Tomography of Density Based on a Thin Time Projection Chamber with Micromegas Readout*, Particles **4** (2021) 333–342.
doi: `https://doi.org/10.3390/particles4030028`.

[23] V. Bautin: *VMM3 ASIC as a potential front end electronics solution for future Straw Trackers*, 15th Pisa Meeting on Advanced Detectors (27/05/2022).
url: `https://agenda.infn.it/event/22092/contributions/167837/` (visited on 29/08/2022).

[24] F. Sauli: *GEM: A new concept for electron amplification in gas detectors*, Nuclear Instruments and Methods in Physics Research A **386** (1997) 531–534.
doi: `https://doi.org/10.1016/S0168-9002(96)01172-2`.

[25] M. Tanabashi et al. (Particle Data Group): *Review of Particle Physics*, Physical Review D **98** (2018) 030001.
doi: `https://doi.org/10.1103/PhysRevD.98.030001`.

[26] H. Kolanoski, N. Wermes: *Particle Detectors: Fundamentals and Applications*, Oxford University Press, Oxford (2020).
isbn: `978-0-198-85836-2`.

[27] F. Sauli: *Gaseous Radiation Detectors: Fundamentals and Applications*, Cambridge University Press, Cambridge (2014).
isbn: `978-1-107-04301-5`.

[28] W. R. Leo: *Techniques for Nuclear and Particle Physics Experiments: A How-to Approach*, Springer-Verlag, Berlin Heidelberg (1994).
isbn: `978-3-540-57280-0`.

[29] H. Schindler: *Microscopic Simulation of Particle Detectors*, PhD Thesis, Technische Universität Wien (2012). CERN-THESIS-2012-208.
url: `https://cds.cern.ch/record/1500583` (visited on 02/03/2022).

[30] H. Schindler: *Garfield++*.
url: `https://garfieldpp.web.cern.ch/garfieldpp/` (visited on 02/03/2022).

[31] I. Smirnov: *Modeling of ionization produced by fast charged particles in gases*, Nuclear Instruments and Methods in Physics Research A **554** (2005) 474–493. DOI: `https://doi.org/10.1016/j.nima.2005.08.064`.

[32] I. Smirnov: *Modeling of ionization produced by fast charged particles in gases.* URL: `https://ismirnov.web.cern.ch/ismirnov/heed` (visited on 02/03/2022).

[33] W. Blum, W. Riegler, L. Rolandi: *Particle Detection with Drift Chambers*, Springer-Verlag, Berlin Heidelberg (2008). ISBN: `978-3-540-76683-4`.

[34] M. J. Berger et al.: *XCOM: Photon Cross Sections Database*, National Institute of Standards and Technology, Gaithersburg (2010). DOI: `https://dx.doi.org/10.18434/T48G6X`.

[35] W. Demtröder: *Experimentalphysik 2 – Elektrizität und Optik*, Springer-Verlag, Berlin Heidelberg (2013). ISBN: `978-3-642-29943-8`.

[36] A. C. Thompson et al.: *X-Ray Data Booklet*, Lawrence Berkeley National Laboratory, Berkeley (2009). URL: `https://cxro.lbl.gov/x-ray-data-booklet` (visited on 13/03/2022).

[37] S. F. Biagi: *Monte Carlo simulation of electron drift and diffusion in counting gases under the influence of electric and magnetic fields*, Nuclear Instruments and Methods in Physics Research A **421** (1999) 234–240. DOI: `https://doi.org/10.1016/S0168-9002(98)01233-9`.

[38] S. F. Biagi: *Magboltz - transport of electrons in gas mixtures.* URL: `https://magboltz.web.cern.ch/magboltz/` (visited on 02/03/2022).

[39] Y. Giomataris et al.: *MICROMEGAS: a high-granularity position-sensitive gaseous detector for high particle-flux environments*, Nuclear Instruments and Methods in Physics Research A **376** (1996) 29–35. DOI: `https://doi.org/10.1016/0168-9002(96)00175-1`.

[40] A. Abusleme et al.: *Performance of a full-size small-strip thin gap chamber prototype for the ATLAS new small wheel muon upgrade*, Nuclear Instruments and Methods in Physics Research A **817** (2016) 85–92. DOI: `https://doi.org/10.1016/j.nima.2016.01.087`.

[41] D. Pfeiffer, L. Scharenberg, P. Schwäbig et al.: *Rate-capability of the VMM3a front-end in the RD51 Scalable Readout System*, Nuclear Instruments and Methods in Physics Research A **1031** (2022) 166548. DOI: `https://doi.org/10.1016/j.nima.2022.166548`.

[42] H. Muller: *Personal communication.* 2022.

[43] G. de Geronimo et al.: *VMM1 – An ASIC for Micropattern Detectors*, IEEE Transactions on Nuclear Science **60** (2013) 2314–2321.
doi: `https://doi.org/10.1109/TNS.2013.2258683`.

[44] M. Raymond et al.: *The APV25 0.25 μm CMOS readout chip for the CMS tracker*, IEEE Nuclear Science Symposium Conference Record **2** (2000) 9/113–9/118.
doi: `https://doi.org/10.1109/NSSMIC.2000.949881`.

[45] X. Llopart et al.: *Timepix, a 65k programmable pixel readout chip for arrival time, energy and/or photon counting measurements*, Nuclear Instruments and Methods in Physics Research A **581** (2007) 485–494.
doi: `https://doi.org/10.1016/j.nima.2007.08.079`.

[46] M. Lupberger et al.: *Implementation of the Timepix ASIC in the Scalable Readout System*, Nuclear Instruments and Methods in Physics Research A **830** (2016) 75–81.
doi: `https://doi.org/10.1016/j.nima.2016.05.043`.

[47] P. Schwäbig: *Improving the performance of high-speed mutli-channel readout electronics: the VMM3a ASIC in the Scalable Readout System*, Master Thesis, Rheinische Friedrich-Wilhelms-Universität Bonn (2020).
url: `https://www.lhc-ilc.physik.uni-bonn.de/ergebnisse/dateien/t00000127.pdf` (visited on 20/04/2022).

[48] L. Scharenberg et al.: *VMM3a/SRS software, firmware and hardware guidance.*
url: `https://gitlab.cern.ch/rd51-slow-control/vmm-doc` (visited on 21/04/2022).

[49] L. Scharenberg: *VMM3a/SRS software installation and operation overview*, RD51 Collaboration Meeting and Topical Workshop on 'Wide Dynamic Range Operation of MPGDs' (2021).
url: `https://indico.cern.ch/event/1071632/contributions/4615369/` (visited on 21/04/2022).

[50] M. Guth, M. Lupberger, D. Pfeiffer et al.: *VMM3a/SRS Slow Control and Calibration Software.*
url: `https://gitlab.cern.ch/rd51-slow-control/vmmsc` (visited on 25/07/2022).

[51] G. Combs et al.: *Wireshark.*
url: `https://gitlab.com/wireshark/wireshark` (visited on 25/07/2022).

[52] The Tcpdump Group: *TCPdump.*
url: `https://github.com/the-tcpdump-group/tcpdump` (visited on 25/07/2022).

[53] M. Shetty et al.: *DAQuiri.*
url: `https://github.com/ess-dmsc/daquiri` (visited on 25/07/2022).

[54] M. J. Christensen et al.: *ESS DAQ: utilities for the EFU-based data acquisition system.*
url: `https://github.com/ess-dmsc/essdaq` (visited on 25/07/2022).

[55] D. Pfeiffer et al.: *vmm-sdat – VMM3a/SRS Data Analysis Tool.*
url: `https://github.com/ess-dmsc/vmm-sdat` (visited on 22/04/2022).

[56] R. Brun, F. Rademakers: *ROOT – An Object Oriented Data Analysis Framework*, Nuclear Instruments and Methods in Physics Research A **389** (1997) 81–86.
doi: `https://doi.org/10.1016/S0168-9002(97)00048-X`,
url: `https://root.cern/`.

[57] D. Pfeiffer: *Personal communication.* 2022.

[58] H. Muller et al.: *Configurable electronics with low noise and 14-bit dynamic range for photodiode-based photon detectors*, Nuclear Instruments and Methods in Physics Research A **565** (2006) 768–783.
doi: `https://doi.org/10.1016/j.nima.2006.05.246`.

[59] J. L. Sebaugh: *Guidelines for accurate EC50/IC50 estimation*, Pharmaceutical Statistics **10** (2011) 128–134.
doi: `https://doi.org/10.1002/pst.426`.

[60] RD51 Collaboration Meeting: *WG7 – Common Test Facilities (19/11/2021).*
url: `https://indico.cern.ch/event/1071632/` (visited on 22/07/2022).

[61] RD51 Mini Week: *WG7 – Common Test Facilities (10/02/2022).*
url: `https://indico.cern.ch/event/1110129/` (visited on 22/07/2022).

[62] RD51 Collaboration Meeting: *WG7 – Common Test Facilities (17/06/2022).*
url: `https://indico.cern.ch/event/1138814/` (visited on 22/07/2022).

[63] G. De Geronimo: *Personal communication.* 2021.

[64] T. Alexopoulos et al.: *The VMM readout system*, Nuclear Instruments and Methods in Physics Research A **955** (2020) 163306.
doi: `https://doi.org/10.1016/j.nima.2019.163306`.

[65] D. Pfeiffer, L. Scharenberg: *Studies on the Rate-Capability of the VMM3a within the SRS* (10/02/2020),
url: `https://indico.cern.ch/event/872501/contributions/3741492/` (visited on 21/08/2022).

[66] C. Altunbas et al.: *Construction, test and commissioning of the triple-GEM tracking detector for COMPASS*, Nuclear Instruments and Methods in Physics Research A **490** (2002) 177–203.
doi: `https://doi.org/10.1016/S0168-9002(02)00910-5`.

[67] F. Sauli: *Micro-Pattern Gaseous Detectors: Principles of Operation and Applications*, World Scientific, Singapore (2020).
ISBN: `978-981-122-221-4`.

[68] S. Bachmann et al.: *Charge amplification and transfer processes in the Gas Electron Multiplier*, Nuclear Instruments and Methods in Physics Research A **438** (1999) 376–408.
DOI: `https://doi.org/10.1016/S0168-9002(99)00820-7`.

[69] P. Thuiner: *Ion space-charge effects in multi-GEM detectors: challenges and possible solutions for future applications*, PhD Thesis, Technische Universität Wien (2016). CERN-THESIS-2016-199.
URL: `https://cds.cern.ch/record/2238855/` (visited on 29/07/2022).

[70] P. Abbon et al.: *The COMPASS experiment at CERN*, Nuclear Instruments and Methods in Physics Research A **577** (2007) 455–518.
DOI: `https://doi.org/10.1016/j.nima.2007.03.026`.

[71] L. Scharenberg et al.: *Resolving soft X-ray absorption in energy, space and time in gaseous detectors using the VMM3a ASIC and the SRS*, Nuclear Instruments and Methods in Physics Research A **977** (2020) 164310.
DOI: `https://doi.org/10.1016/j.nima.2020.164310`.

[72] G. Iakovidis: *The Micromegas project for the ATLAS upgrade*, Journal of Instrumentation **8** (2013) C12007.
DOI: `https://doi.org/10.1088/1748-0221/8/12/C12007`.

[73] D. Pfeiffer et al.: *The $\mu$TPC method: improving the position resolution of neutron detectors based on MPGDs*, Journal of Instrumentation **10** (2015) P04004.
DOI: `https://doi.org/10.1088/1748-0221/10/04/P04004`.

[74] J. Bortfeldt: *anamicom.*
URL: `https://gitlab.physik.uni-muenchen.de/Jonathan.Bortfeldt/anamicom` (visited on 16/07/2022).

[75] J. Bortfeldt: *Development of Floating-Strip Micromegas Detectors*, PhD Thesis, Ludwig-Maximilians-Universität München (2014).
DOI: `https://doi.org/10.5282/edoc.16972`.

[76] R. E. Kalman: *A New Approach to Linear Filtering and Prediction Problems*, Journal of Basic Engineering **82** (1960) 35–45.
DOI: `https://doi.org/10.1115/1.3662552`.

[77] F. Klitzner: *Development of Novel Two-Dimensional Floating Strip Micromegas Detectors with an In-depth Insight into the Strip Signal Formation*, PhD Thesis, Ludwig-Maximilians-Universität München (2019).
DOI: `https://doi.org/10.5282/edoc.24286`.

[78] F. Piuz et al.: *Evaluation of systematic errors in the avalanche localization along the wire with cathode strips read-out MWPC*, Nuclear Instruments and Methods in Physics Research **196** (1982) 451–462.
doi: `https://doi.org/10.1016/0029-554X(82)90113-6`.

[79] L. Scharenberg et al.: *X-ray imaging with gaseous detectors using the VMM3a and the SRS*, Nuclear Instruments and Methods in Physics Research A **1011** (2021) 165576.
doi: `https://doi.org/10.1016/j.nima.2021.165576`.

[80] M. Villa: *Developing and evaluating new micropattern gas detectors*, PhD Thesis, Rheinische Friedrich-Wilhelms-Universität Bonn (2013). CERN-THESIS-2013-284.
url: `http://cds.cern.ch/record/1666140` (visited on 31/08/2022).

[81] H. Pulkkinen: *Basic properties of Gas Electron Multipliers and different methods to determine the cluster characteristics*, Student Report Tfy-3.5111, Aalto University (2013).

[82] A. Maier et al. (Eds.): *Medical Imaging Systems – An Introductory Guide*, Springer International Publishing, Cham (2018).
isbn: `978-3-319-96519-2`.

[83] S. N. Ahmed: *Digital Signal Processing: a Practical Guide for Engineers and Scientists*, Elsevier, Amsterdam (2015).
isbn: `978-0-12-801363-2`.

[84] C. D. R. Azevedo et al.: *Position resolution limits in pure noble gaseous detectors for X-ray energies from 1 to 60 keV*, Physics Letters B **741** (2015) 272–275.
doi: `https://doi.org/10.1016/j.physletb.2014.12.054`.

[85] S. W. Smith: *Digital Signal Processing: a Practical Guide for Engineers and Scientists*, Newnes, Boston (2002).
isbn: `978-0-7506-7444-7`.

[86] S. Horvat: *Study of the Higgs Discovery Potential in the Process $pp \rightarrow H \rightarrow 4\mu$*, PhD Thesis, University of Zagreb (2005).
url: `https://cds.cern.ch/record/858509` (visited on 31/08/2022).

[87] R. K. Carnegie et al.: *Resolution studies of cosmic-ray tracks in a TPC with GEM readout*, Nuclear Instruments and Methods in Physics Research A **538** (2005) 372–383.
doi: `https://doi.org/10.1016/j.nima.2004.08.132`.

[88] B. KETZER ET AL.: *Performance of triple GEM tracking detectors in the COMPASS experiment*, Nuclear Instruments and Methods in Physics Research A **535** (2004) 314–318.
DOI: `https://doi.org/10.1016/j.nima.2004.07.146`.

[89] A. MARINOV: *Feasibility Study of a GEM Based Muon System for the CMS Detector at the Large Hadron Collider*, PhD Thesis, Universiteit Gent (2012).
URL: `http://hdl.handle.net/1854/LU-3091997` (visited on 09/08/2022).

[90] J. MERLIN: *Study of long-term sustained operation of gaseous detectors for the high rate environment in CMS*, PhD Thesis, Université de Strasbourg (2016). CERN-THESIS-2016-041.
URL: `https://cds.cern.ch/record/2155685` (visited on 25/08/2022).

[91] M. GOLA ET AL.: *A new technique to establish the uniformity of the induction gap in GEM based detectors*, Nuclear Instruments and Methods in Physics Research A **1019** (2021) 15826.
DOI: `https://doi.org/10.1016/j.nima.2021.165826`.

[92] J. SAMARATI: *Personal communication.* 2020.

[93] K. ABE ET AL.: *The T2K experiment*, Nuclear Instruments and Methods in Physics Research A **659** (2011) 106–135.
DOI: `https://doi.org/10.1016/j.nima.2011.06.067`.

[94] N. ABGRALL ET AL. (THE NA61/SHINE COLLABORATION): *Pion emission from the T2K replica target: Method, results and application*, Nuclear Instruments and Methods in Physics Research A **701** (2013) 99–114.
DOI: `https://doi.org/10.1016/j.nima.2012.10.079`.

[95] M. URBANIAK ET AL.: *Development of a new beam position detectors for NA61/SHINE experiment*, Proceedings of Science **PANIC2021** (2022) 085.
DOI: `https://doi.org/10.22323/1.380.0085`.

[96] A. ADUSZKIEWICZ ET AL. (THE NA61/SHINE COLLABORATION): *Study of Hadron-Nucleus and Nucleus-Nucleus Collisions at the CERN SPS: Early Post-LS2 Measurements and Future Plans*, CERN-SPSC-2018-008 (2018).
URL: `https://cds.cern.ch/record/2309890/`.

[97] B. T. RUMBERGER: *Personal communication.* 2022.

[98] P. PODLASKI: *Personal communication.* 2022.

[99] K. DEHMELT ET AL.: *Snowmass 2021 White Paper Instrumentation Frontier 05 – White Paper 1: MPGDs: Recent advances and current R&D* (2022),
DOI: `https://arxiv.org/abs/2203.06562`.

# LIST OF FIGURES

# LIST OF TABLES

# ACKNOWLEDGMENTS

At the end of this thesis, I want to express my deepest gratitude to many people that I had the pleasure to meet and call my colleagues and friends over the course of this thesis. Without your support, motivation and pushing me forward, the results that were achieved during this thesis would not have been possible.

First, I would like to thank Prof. Dr. Klaus Desch. Thanks for letting me be part of your group, for having confidence in my skills and for your valuable input when discussing results. Without you, I would be definitively not there, where I am now as a scientist.

I would like to say thousand thanks to Dr. Eraldo Oliveri. You have been an incredible supervisor. I enjoyed your input and your advice in our frequent conversations. Thanks for pushing me to try out new things and investigate any new problems.

I would like to express my gratitude to Prof. Dr. Ian C. Brock, PD Dr. Bastian Kubis and Prof. Dr. Jürgen Gall for accepting to be part of the review committee.

Another big thank you goes to Dr. Leszek Ropelewski, for letting me be part of the CERN Gas Detector Development team, for asking always the right questions, pointing me in the right directions and for calming me down in some not-so-easy situations.

I am very grateful to you, Dr. Dorothea 'Doro' Pfeiffer. With all your help on software and firmware and with all the things that you implemented on my request. Without you, VMM3a/SRS would not be there, where it is now. The time working together with you was always a great pleasure.

Many thanks to you, Dr. Hans Muller, the godfather of the SRS. Thanks for helping me to find and solve any problem that I encountered and for all your 'lectures' where you enlightened me with your knowledge of electronics

A big thank you goes to Dr. Florian Brunbauer. We shared so many brilliant moments, both at work and outside of CERN. With your support and friendship, you have been to me like a big brother.

Many thanks go to Dr. Michael Lupberger. With all the exchange that we had on VMM3a/SRS, with you teaching me how to operate it and your work both at CERN and Bonn University, my work profited significantly from your input.

Another big thank you goes to Dr. George Iakovidis. Any time I had a question on a specific VMM feature, you helped me and make me understand it.

I would also like to thank all my other colleagues from the GDD team for the fantastic time during my PhD studies. Starting with my fellow PhD students with whom I enjoyed many moments at work, as well outside of work during our 'PhD meetings'. Thank you Karl Flöthner, Djunes Janssens, Marta Liswoska, and Giorgio Orlandini. To Karl, I would like to thank you as well for your support in building up the RD51 VMM3a/SRS beam telescope and the time during the test beam campaigns. Then there are Dr. Jerome Samarati, Miranda van Stenis, Dr. Antonija Utrobicic, Dr. Francisco Garcia, Dr. Rob Veenhof and Prof. Dr. Fabio Sauli. Thanks for being such wonderful colleagues who supported me in many situations and with whom I always enjoyed the company.

I would also like to thank my colleagues and friends from Bonn, especially Markus Gruber, Sebastian Schmidt, Tobias Schiffer and Dr. Christoph Krieger. It was a pity that we could not see each other more often, but I enjoyed it every time when we managed it. Thanks also for proofreading (parts) of my thesis. I would also like to thank Dr. Jochen Kaminski. Without your idea of sending me to CERN to learn the operation of VMM and SRS, I would have probably never ended up in GDD. I am deeply grateful for this. Also a big thank you to Patrick Schwäbig for all the exchanges that we had on the Hybrid firmware.

I would like to thank you Dr. Jonathan 'Jona' Bortfeldt for all your help and support with anamicom and the discussions and input on spatial resolution studies. I have learned a lot during our conversations.

Another thank you goes to Dr. Hugo Natal da Luz. Thanks for helping me in understanding X-ray imaging methods and how to evaluate the results. From our meetings, I took valuable lessons home with me.

I would also like to thank the NA61/SHINE collaboration, for all the efforts in making VMM3a/SRS run the experiment. A particular thank you goes to Dr. Piotr Podlaski and Dr. Brant Rumberger. Without your firmware and software skills, the integration would have never been as smooth as it turned out.

To all the other colleagues from CERN, the RD51 test beams or the Working Group 5.1 who I met during my PhD studies, in particular Prof. Dr. Yorgos Tsipolitis, Alexandru Rusu, Marek Hracek, Prof. Dr. Spyros Tzamarias, Dr. Mohit Gola, Pepe Gülker, Dr. Stefano Caiazza, Gerardo Roque Romero, Vitalii Bautin, Dr. Temur Enik, Dr. Katerina Kuznetsova and Daniel Sorvisto: thanks for all the chats and nice discussions.

In the end, I would also like to acknowledge the funding that I received during my PhD studies.

This work has been sponsored by the Wolfgang Gentner Programme of the German Federal Ministry of Education and Research (grant no. 13E18CHA).

This project has received funding from the European Union's Horizon 2020 Research and Innovation programme under GA no 101004761.

The work has been supported by the CERN Strategic Programme on Technologies for Future Experiments. `https://ep-rnd.web.cern.ch/`

In this context, I would particularly like to express my thanks to Dr. Michael Hauschild and Dr. Dominik Dannheim from the Wolfgang Gentner Programme.

Last but not least, I would like to thank my family. Throughout my PhD studies, I went through many sorts of different situations. No matter what the situation, you were on my side, despite the physical distance to CERN. Thousand thanks for enabling me the opportunity to pursue my dream of being a scientist. Without your support, this would have never worked.